Cosmic simulations cook up realistic galaxies *p. 954*

Lessons from the glyphosate debate *p. 958*

Pluto's methane ice dunes *pp. 960 & 992*

Science

$15
1 JUNE 2018
sciencemag.org

AAAS

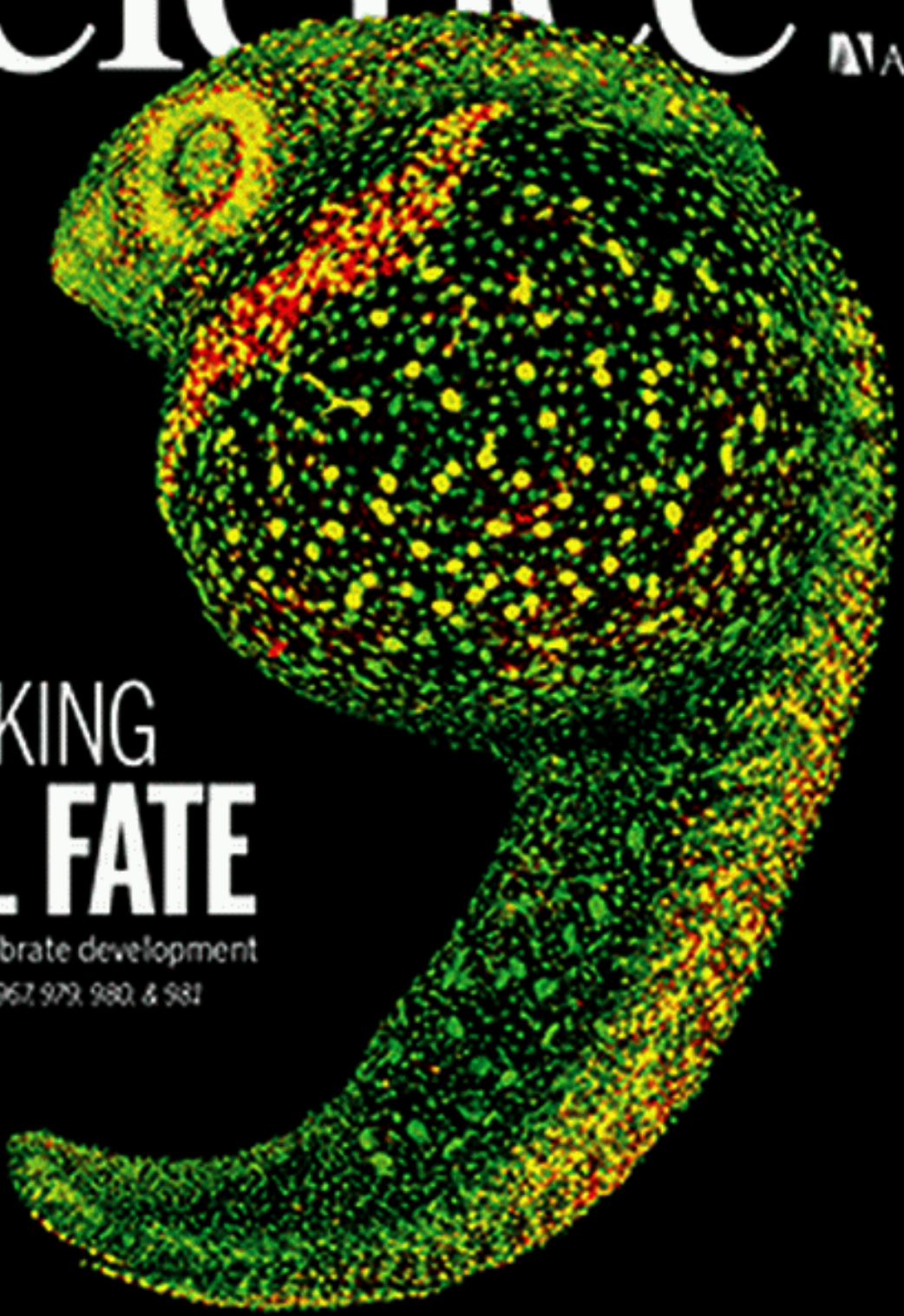

TRACKING CELL FATE

Mapping vertebrate development cell by cell *pp. 967, 979, 980, & 981*

CONTENTS

1 JUNE 2018 • VOLUME 360 • ISSUE 6392

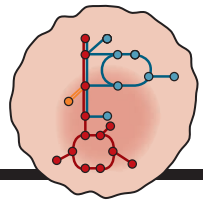

962 Metabolic microenvironments affect drug responses

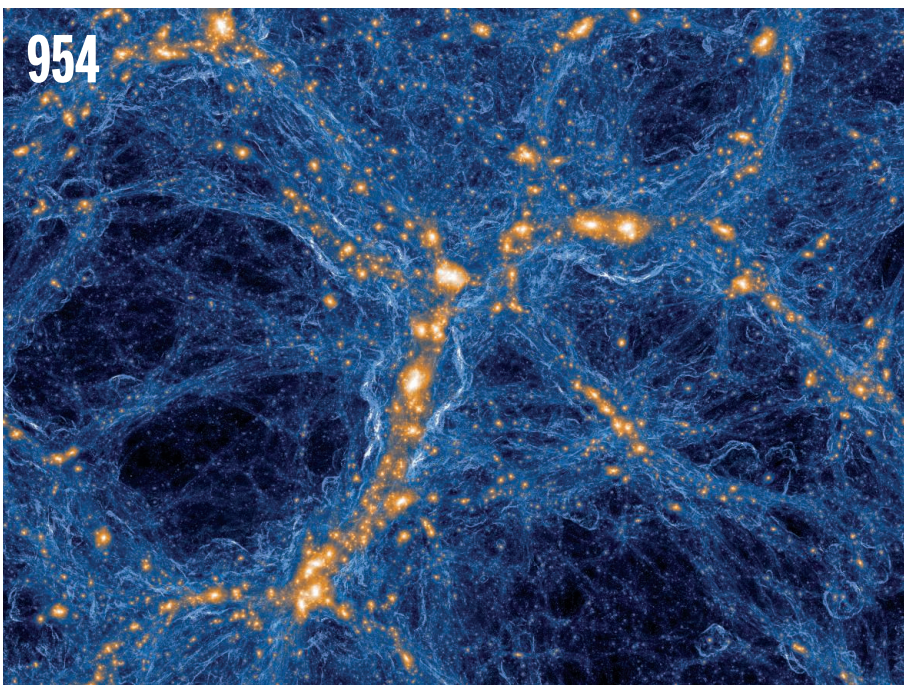

954

NEWS

IN BRIEF

IN DEPTH

FEATURE

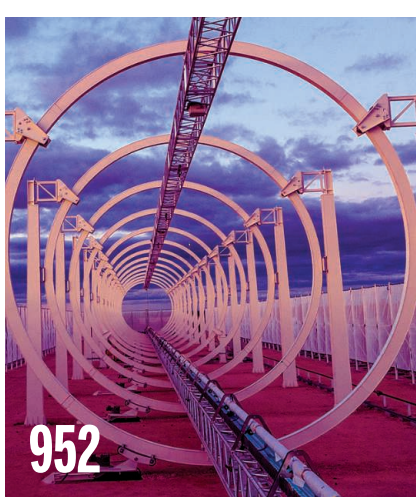

952

INSIGHTS

PERSPECTIVES

POLICY FORUM

Published by AAAS

CONTENTS

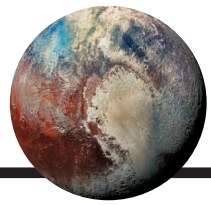

960 & 992
Pluto's dunes

1 JUNE 2018 • VOLUME 360 • ISSUE 6392

ON THE COVER

Tiled confocal microscopy image of a developing zebrafish embryo at single-cell resolution, less than 1 day after fertilization. Single-cell RNA sequencing can be used to generate high-resolution maps of gene expression activity as embryos develop into fish and amphibians. See pages 967, 979, 980, and 981. *Image: Frederique Ruf-Zamojski and Sean Megason*

SCIENCE (ISSN 0036-8075) is published weekly on Friday, except last week in December, by the American Association for the Advancement of Science, 1200 New York Avenue, NW, Washington, DC 20005. Periodicals mail postage (publication No. 484460) paid at Washington, DC, and additional mailing offices. Domestic individual membership, including subscription (12 months): $165 ($74 allocated to subscription). Domestic institutional subscription (51 issues): $1808; Foreign postage extra: Mexico, Caribbean (surface mail) $55; other countries (air assist delivery): $89. First class, airmail, student, and emeritus rates on request. Canadian rates with GST available upon request, GST #125488122. Publications Mail Agreement Number 1069624. **Printed in the U.S.A.**
Change of address: Allow 4 weeks, giving old and new addresses and 8-digit account number. **Postmaster:** Send change of address to AAAS, P.O. Box 96178, Washington, DC 20090–6178. **Single-copy sales:** $15 each plus shipping and handling; bulk rate on request. **Authorization to reproduce** material for internal or personal use under circumstances not falling within the fair use provisions of the Copyright Act is granted by AAAS to libraries and others who use Copyright Clearance Center (CCC) Pay-Per-Use services provided that $35.00 per article is paid directly to CCC, 222 Rosewood Drive, Danvers, MA 01923. The identification code for *Science* is 0036-8075. *Science* is indexed in the *Reader's Guide to Periodical Literature* and in several specialized indexes.

Science
AAAS
1200 New York Avenue, NW, Washington, DC 20005
Clarendon House, Clarendon Road, Cambridge, UK CB2 8FH

SUBSCRIPTION SERVICES For change of address, missing issues, new orders and renewals, and payment questions: 866-434-AAAS (2227) or 202-326-6417, FAX 202-842-1065. Mailing addresses: AAAS, P.O. Box 96178, Washington, DC 20090-6178 or AAAS Member Services, 1200 New York Avenue, NW, Washington, DC 20005

INSTITUTIONAL SITE LICENSES 202-326-6730 **REPRINTS:** Author Inquiries 800-635-7181 **COMMERCIAL INQUIRIES** 803-359-4578 **PERMISSIONS** 202-326-6765, permissions@aaas.org **AAAS Member Central Support** 866-434-2227 www.aaas.org/membercentral.

INFORMATION FOR AUTHORS See www.sciencemag.org/authors/science-information-authors

Published by AAAS

EDITORIAL

When facts are not enough

Katharine Hayhoe is a professor and director of the Climate Science Center at Texas Tech University, Lubbock, TX, USA. www.katharinehayhoe.com

Science is based on a shared respect for the scientific method—the principle that, by gathering and analyzing data and information, scientists and others can draw conclusions that are robust and generalizable across cultures and ideologies. Scientists furthermore assume that disagreements can be resolved by more facts. So when people object to the reality of climate change with science-y sounding arguments—"the data is wrong," or "it's just a natural cycle," or even, "we need to study it longer"—the natural response of scientists is simple and direct: People need more data. But this approach often doesn't work and can even backfire. Why? Because when it comes to climate change, science-y sounding objections are a mere smokescreen to hide the real reasons, which have much more to do with identity and ideology than data and facts.

For years, climate change has been one of the most politically polarized issues in the United States. Today, the best predictor of whether the public agrees with the reality of anthropogenic climate change is not how much scientific information there is. It's where each person falls on the political spectrum. That's why the approach of bombarding the unconvinced with more data doesn't work—people see it as an attack on their identity and an attempt to change their way of life.

I am a climate scientist who has spent a lot of time trying to make climate science more accessible. I've authored National Climate Assessments and numerous outreach reports; I host a YouTube show called Global Weirding; I tweet; I've even promoted knitting patterns that display rising temperatures. Yet the most important step I've taken to make my science communication more effective has nothing to do with the science. As uncomfortable as this is for a scientist in today's world, the most effective thing I've done is to let people know that I am a Christian. Why? Because it's essential to connect the impacts of a changing climate directly to what's already meaningful in one's life, and for many people, faith is central to who they are.

Scientists can be effective communicators by bonding over a value that they genuinely share with the people with whom they're speaking. It doesn't have to be a shared faith. It could be that both are parents, or live in the same place, or are concerned about water resources or national security, or enjoy the same outdoor activities. Instead of beginning with what most divides scientists from others, start the conversation from a place of agreement and mutual respect. Then, scientists can connect the dots: share from their head and heart why they care.

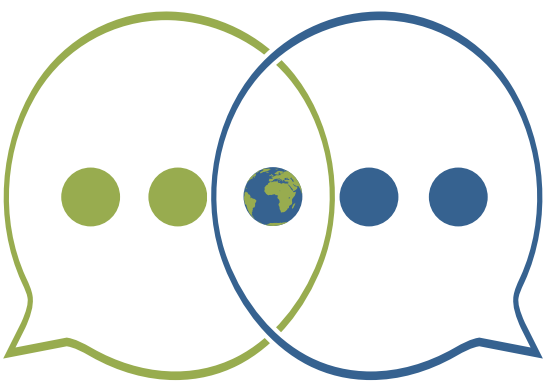

"...changing minds...requires... practical, viable, and attractive solutions that someone can get excited about."

Talking about impacts isn't enough, though. Sadly, the most dangerous myth that many people have bought into is, "it doesn't matter to me," and the second most dangerous myth is, "there's nothing I can do about it." If scientists describe the daunting challenge of climate change but can't offer an engaging solution, then people's natural defense mechanism is to disassociate from the reality of the problem. That's why changing minds also requires providing practical, viable, and attractive solutions that someone can get excited about. Concerned homeowner? Mention the amazing benefits of energy conservation. Worried parent? Bring up the practical steps to take to make outdoor play spaces safer for kids, even in the hot summer. Business executive? Talk about the economic benefits of renewables.

We all live on the same planet, and we all want the same things. By connecting our heads to our hearts, we all can talk about—and tackle—the problem of climate change together.

–Katharine Hayhoe

10.1126/science.aau2565

> “This shows how climate denial is a hothouse flower that doesn’t survive well outside of Congress.”
>
> **Senator Sheldon Whitehouse** (D–RI), on ex-Representative Jim Bridenstine (R–OK), now NASA administrator, who reversed himself and called humans the top cause of climate change.

IN BRIEF

Edited by **Jeffrey Brainard**

PLANETARY SCIENCE

Mars rover’s drill revived

Scientists will use the drill to continue searching for signs of ancient life on Mars.

Some 18 months after it first failed, the drill on NASA’s Curiosity rover is once again sampling rocks on Mars, the agency announced last week. Since December 2016, the drill on the SUV-size rover, located at the end of a robotic arm, could not reliably penetrate rock after first being stabilized against its target. Engineers at the Jet Propulsion Laboratory in Pasadena, California, have now tested a technique that forgoes stabilization, instead using the robotic arm to plunge the drill into rock. In May, the drill penetrated 50 millimeters into a veiny rock in a clay-rich formation. Scientists hope the revived drill will allow Curiosity to resume its chase for molecular evidence of ancient martian life using its most precise measure: mixing samples with thimbles of solvent, a technique it had yet to deploy when the drill failed (*Science*, 3 February 2017, p. 444).

Study charts health care gains

PUBLIC HEALTH | Cambodia, Equatorial Guinea, Ethiopia, Myanmar, and Rwanda were among the countries with the biggest gains in access to quality health care from 2000 to 2016. So says a new study published online in *The Lancet* this week by a massive group of researchers known as the Global Burden of Diseases group, led by the Institute for Health Metrics and Evaluation at the University of Washington in Seattle. The new assessment is based on mortality figures for 32 diseases that, if properly treated, should not be fatal. Most lower-income nations saw gains driven by expanded vaccination programs. Not surprisingly, nations with the highest quality overall were Iceland, Norway, and the Netherlands, whereas the much poorer Central African Republic, Somalia, and Guinea-Bissau were at the bottom of the list. Large countries such as India and China had enormous differences within their borders—Beijing scored high, for example, whereas Tibet was low. The United States ranked 29th out of the 195 countries and territories studied.

Weather satellite in peril

REMOTE SENSING | A balky cooling system has crippled the most recent multibillion-dollar U.S. weather satellite, the Geostationary Operational Environmental Satellite-17 (GOES-17), which stares fixedly at the western United States, the National Oceanic and Atmospheric Administration reported last week. The problem began a month ago on the satellite’s primary instrument, the Advanced Baseline Imager (ABI), used for forecasting and meteorological research. For half the day, while the ABI is exposed directly to the sun, the sensor must be cooled to record Earth’s emissions in the infrared, used for measuring wind speeds, moisture, and temperature. Launched on 1 March, GOES-17 is the second of four satellites in an $11 billion program. Although older satellites remain operational, the cooling failure could jeopardize planned gains in forecasting for the western United States and force a re-evaluation of systems, already built, for the two satellites set to follow GOES-17.

PHOTO: NASA/JPL-CALTECH

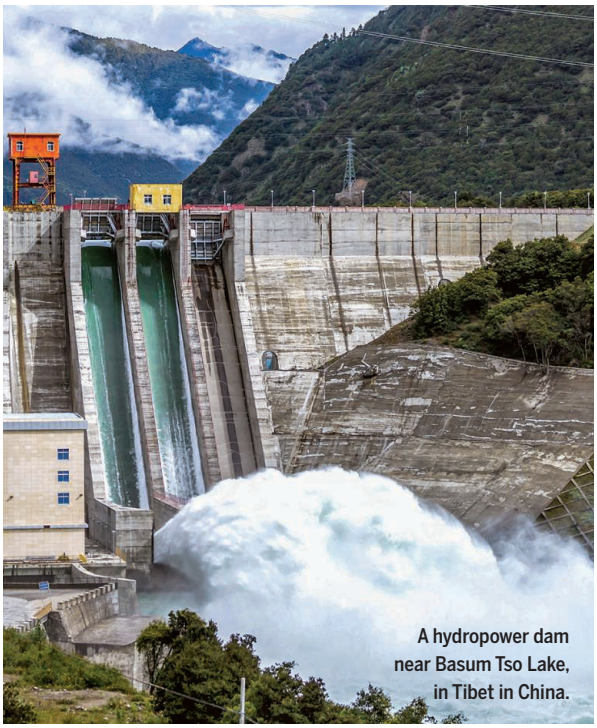

A hydropower dam near Basum Tso Lake, in Tibet in China.

RENEWABLE ENERGY

East Asia becomes a hydropower superpower

Hydropower is the largest source of renewable energy worldwide, and projects in East Asia, particularly China, have driven global growth in gigawatts of hydroelectric generating capacity since 2006. Planned projects in South Asia, especially India, could further boost capacity, according to a report by Oak Ridge National Laboratory in Tennessee for the U.S. Department of Energy. In China, new capacity could come from building large new dams in the nation's west. In the United States and Europe, where environmental concerns have made the construction of new dams more controversial, some of the planned expansion involves modifying existing dams to produce more power.

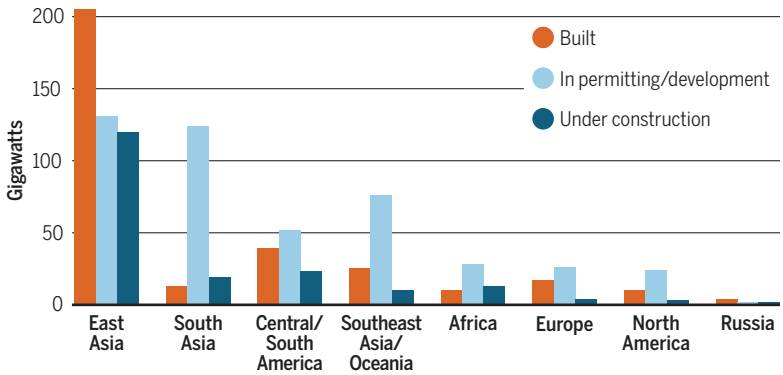

Court blocks Nobel Center design

SCIENTIFIC SOCIETIES | A Swedish court last week blocked plans for a controversial new headquarters building for the Nobel Foundation on central Stockholm's waterfront, saying its design would mar the harbor's historic character. The eight-story, bronze, glass, and steel Nobel Center would consolidate in one location the foundation's activities, including the annual December award ceremonies for the world's most prestigious science prizes, now held in Stockholm's concert hall. Besides an auditorium, the 1.2 billion Swedish krona ($140 million) center would house the Nobel Museum and space for exhibitions, educational programs, and a restaurant. The design, by the Berlin office of David Chipperfield Architects, has sparked controversy since it was unveiled in 2014. It was scaled back in 2015 and revised again in 2016. But on 22 May the Land and Environment Court said the revised plans would still damage the location's historic character, lacked an adequate traffic plan, and would block views of the harbor from neighboring buildings. Stockholm city officials said they will appeal the court's decision to the regional appeals court, which will have the final say.

Space station's cool study

PHYSICS | Low temperatures reached new heights when the automated Cold Atom Laboratory (CAL) arrived at the International Space Station on 24 May. The rig will use laser light and radio waves to trap clouds of atoms and chill them to within a billionth of a degree of absolute zero. At those temperatures, a macroscopic quantum wave called a Bose-Einstein condensate (BEC) emerges that can persist longer in the weightless environment than on Earth. CAL scientists will strive for record-low temperatures, look for novel quantum effects, and even blow BEC bubbles. An upgrade could follow in a few years.

Critics of the planned Nobel Center (center) oppose its impact on Stockholm's historic waterfront.

A 'right to try' unapproved drugs

DRUG DEVELOPMENT | A bill passed by Congress last week would give people with life-threatening illnesses a new means to petition drug companies to give them experimental treatments without the U.S. Food and Drug Administration (FDA) evaluating the request. The "Right to Try" bill, expected to get President Donald Trump's signature, permits terminally ill patients who have exhausted other treatment options to obtain an unapproved drug, as long as it is undergoing clinical trials and has completed an initial safety study. Patients can already make "compassionate use" requests to FDA; the agency says it grants nearly all of these, but supporters of the new alternative say it will be less cumbersome and time-consuming. Critics—including many patient advocacy groups—have warned that it could put people at risk of harmful drug side effects. The new legislation limits the liability of drug manufacturers and prescribers for providing unproven drugs, but does not oblige companies to do so. FDA Commissioner Scott Gottlieb, who raised concerns about previous versions of the bill, said he stands "ready to implement it

CREDITS: (PHOTOS, TOP TO BOTTOM) VLADIMIR ZHOGA/SHUTTERSTOCK.COM; © DAVID CHIPPERFIELD ARCHITECTS; (GRAPHIC) J. BRAINARD/*SCIENCE*; (DATA) 2017 *HYDROPOWER MARKET REPORT*, OAK RIDGE NATIONAL LABORATORY

in a way that achieves Congress's intent to promote access and protect patients."

Still no sign of dark matter

PHYSICS | The world's most sensitive dark matter detector, XENON1T, has failed to snare its quarry, researchers reported this week. Every galaxy sits shrouded in invisible dark matter whose gravity keeps it from flying apart, observations indicate. In the 1980s, physicists suggested that dark matter might consist of weakly interacting massive particles (WIMPs) that would interact only through gravity and the weak nuclear force and should linger from the big bang in the right amount to account for dark matter. However, the 165 XENON researchers report that during a year of observations, its latest detector, located in Italy's subterranean Gran Sasso National Laboratory, saw no evidence of WIMPs hitting atomic nuclei in 1300 kilograms of liquid xenon. The team plans to quadruple the detector's mass, even as physicists in South Dakota build a similar 7-metric-ton detector called LUX-ZEPLIN. If those efforts come up dry, the next step is uncertain.

THREE QS

White supremacists marching in Charlottesville, Virginia, in August 2017.

Twisting genetics for hate

A year ago, as graduate student Jedidiah Carlson at the University of Michigan in Ann Arbor searched online for a population genetics paper, one result stood out: a link to a forum post on the website Stormfront, one of the internet's most notorious hangouts for white supremacists and neo-Nazis. Curious, he clicked through and found forum users hosting "informal journal clubs," knowledgeably discussing details of population genetics—and badly mangling others—to find support for a white nationalist ideology. He has followed the evolution of this strange, racist trend on that website and "alt-right" forums, and he chatted with *Science* about what he's found. (A longer version of this interview is available at https://scim.ag/QApopgenetics.)

Q: Do people on these forums know what they're talking about?
A: There's a range of expertise. It behooves them to know the science so they can feel like they are going toe-to-toe with the people actually doing it. There are even some who have graduate degrees. They aren't population geneticists, but some of them are quite well educated, both formally and informally.

Q: How do they misappropriate the work?
A: They grab figures from scientific papers and edit them to make them look like they support the white nationalist ideology. In one example, researchers published a figure with a plot inferring regional ancestry of dozens of different populations based on hundreds of individuals and roughly divided them into clusters. [Some forum users] take this plot and add text like "The genetic reality of race," with no context showing what the scientists were actually looking at, and ignoring the fact that there's a continuum among the individuals. Then they turn these images into memes and try to make them go viral.

Q: What are they after?
A: They're interested in anything that would reinforce traditional, discrete racial categories. Intelligence is probably the No. 1 topic that they gravitate toward. And anything pertaining to history of human migrations, or things that play into traditional classifications of racial phenotypes like facial morphology or skin color. I don't think engaging them directly will help, but I think we need to think more carefully about how our work might be misinterpreted.

Taiwan replaces research ship

MARINE SCIENCE | Taiwan's marine researchers are celebrating the commissioning last week of *Legend*, a $30 million replacement for a ship sunk in an October 2014 accident that claimed the lives of two scientists (*Science*, 24 October 2014, p. 407). The island's marine research "really suffered" for the past several years, says Wang Chau-Chang, director of the Taiwan Ocean Research Institute in Kaohsiung. The 2600-ton, 76-meter-long *Legend* is smaller than its predecessor. But it has improved features, including updated sonar equipment for sea bottom profiling, coring capabilities, and the ability to deploy a remotely operated vehicle capable of diving to 3000 meters, all supporting "many different combinations of scientific experiments," Wang says. After training cruises, *Legend* will make its maiden scientific voyage in September.

EU ban on consumer plastics

CONSERVATION | To reduce marine pollution, the European Commission last week proposed to ban or increase recycling of consumer plastic items. Straws, cutlery, and plates would be removed from the market; EU member states would be required to collect 90% of single-use plastic drink bottles by 2025, using, for example, deposit refunds. Producers of plastic fishing gear would have to collect used material from ports and fund public education campaigns to encourage proper disposal. Plastics make up 85% of marine litter.

Down under, hordes look up

ASTRONOMY | Australians last week apparently set a Guinness World Record for the largest number of people stargazing across multiple venues at once—more than 40,000, smashing the previous record of 7960, also set by Australians, in 2015. A final tally of participants was still being made when *Science* went to press. The 23 May event featured more than 285 registered stargazing parties and thousands of telescopes deployed across the country, the Australian Broadcasting Corporation reported.

SCIENCEMAG.ORG/NEWS
Read more news from *Science* online.

PHOTO: SAMUEL CORUM/ANADOLU AGENCY/GETTY IMAGES

ENVIRONMENTAL RESEARCH

Scientists aim to smoke out wildfire impacts

U.S. campaign to study how plumes affect human health and environment

By **Warren Cornwall**

Emily Fischer is likely one of the few people whose summer plans were buoyed by a recent forecast that much of the western United States faces another worse-than-normal wildfire season. Unusually warm weather and drought, together with plenty of dry grass and brush, are expected to create prime conditions for blazes this summer, federal officials announced on 10 May.

The forecast has local officials bracing for the worst. But it represents an opportunity for Fischer, an atmospheric scientist at Colorado State University in Fort Collins who is preparing to spend the summer flying through plumes of wildfire smoke aboard a C-130 cargo plane jammed full of scientific equipment. The flights are the highlight of an unprecedented effort, costing more than $30 million, that involves aircraft, satellites, instrumented vans, and even researchers traveling on foot. Over the next 2 years, two coordinated campaigns—one funded by the National Science Foundation (NSF), and the other by NASA and the National Oceanic and Atmospheric Administration (NOAA)—aim to better understand the chemistry and physics of wildfire smoke, as well as how it affects climate, air pollution, and human health.

"This is definitely the largest fire experiment that has ever happened," says atmospheric chemist Carsten Warneke of NOAA's Earth System Research Laboratory in Boulder, Colorado, one of the lead scientists. Wildfire smoke, he adds, is "one of the largest problems facing air quality and climate issues going forward."

The problem is growing as the size and intensity of wildfires rise in the western United States, marinating communities in smoke. Wildfires account for more than two-thirds of the particulate matter in the West on days that exceed federal clean air standards, according to a 2016 study in the journal *Climatic Change*. And global warming is likely to stoke even more fire in coming years, by making wildlands more combustible. By midcentury, more than 80 million people living across much of the West can expect a 57% increase in the number of "smoke waves"—events that shroud a community for 2 days or more—according to the 2016 study. The consequences for public health could be sobering; smoke includes an array of noxious compounds and tiny particles that can complicate breathing and promote disease. Other parts of the Americas as well as Europe, Africa, Asia, and Australia are likely to experience the same climate-driven surge in wildfires, according to U.S. Forest Service researchers.

Despite the potential threat, wildfire smoke has received little sustained scientific attention. The two new campaigns aim

A smokier future

Forecasts suggest the western United States will see more wildfire smoke waves (events lasting 2 days or more) and longer periods when smoke waves occur.

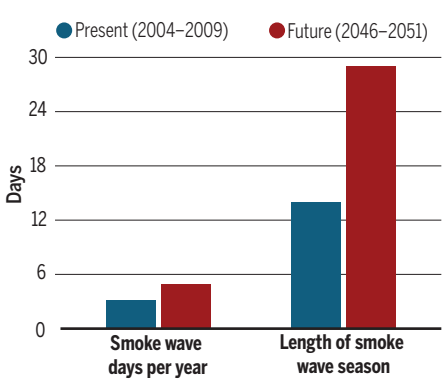

CREDITS: (PHOTO) KURT WILSON/*MISSOULIAN*; (GRAPH) D. MALAKOFF/*SCIENCE*; (DATA) J. LIU *ET AL.*, *CLIMATE CHANGE* 138, 655 (2016)

Smoke from a nearby wildfire blanketed Seeley Lake, Montana, for weeks in the summer of 2017.

to change that. This year, the NSF-funded team that includes Fischer aims to fly its instrumented C-130 through 15 to 20 wildfire plumes. And next year, researchers with NASA and NOAA will have access to a bigger aircraft—a DC-8 jet—that will scour smoky skies across the United States.

One goal is to inventory the chemicals released by wildfires, including nitrogen oxides and carbon monoxide, and a vast array of volatile organic compounds. Current models for predicting the chemical makeup of smoke, which rely largely on satellite observations, have a huge margin for error, Warneke says. In part, that's because of uncertainty about how much vegetation wildfires consume. New studies that combine data from satellites, aircraft, and ground-based researchers scrutinizing burn sites should help fine-tune those estimates.

Researchers will also use the C-130 to chase plumes during their first 24 hours aloft, to see how the chemistry of smoke changes as it wafts through the atmosphere. In particular, they hope to get a more precise picture of what happens to the nitrogen released by burned vegetation, including how much is converted into nitrogen oxides that can contribute to ground-level ozone, a regulated pollutant that can worsen breathing problems. Such data, Fischer says, could help answer questions like: "If wildfires are burning in the Pacific Northwest, what does that mean for Colorado air quality?"

> ***"If wildfires are burning in the Pacific Northwest, what does that mean for Colorado ... ?"***
>
> **Emily Fischer**, Colorado State University

Researchers also plan to track the evolution of aerosols—minute particles that can either scatter or absorb sunlight, and play a major role in shaping climate. And they want to observe plumes as they collide with clouds, to better understand how the two affect each other. Smoke particles can alter cloud formation by acting as nuclei for ice particles, potentially influencing the weather, and cloud moisture can alter smoke chemistry. The results could help improve weather forecasts.

At night, falling temperatures can cause smoke plumes to sink into valleys, worsening air quality there. NOAA and NASA researchers will track the plumes with aircraft, vans, and a drone. That initiative will also involve DC-8 flights beyond the West, into the Midwest and Southeast, tracking smoke from fires intentionally set to clear farm fields and prescribed burns in forests. The goal of collecting such a wide array of data, Warneke says, is "to do the whole picture at one time and understand how the whole thing plays together."

Beyond these projects, public health researchers are taking a growing interest in what happens when smoke blankets communities, sometimes for weeks at a time. Past studies have found that short-term smoke exposure can increase problems for people with asthma and other lung ailments, but "there's really not much information at all" about the effects of long-term, chronic exposure, says Curtis Noonan, an environmental epidemiologist at the University of Montana in Missoula.

Noonan was at the center of some of the worst smoke of the 2017 wildfire season, when Montana was hit by fires that burned 400,000 hectares. The biggest blow fell on Seeley Lake, a town of 1600 located 50 kilometers northeast of Missoula. The nearby Rice Ridge fire filled the town with smoke for much of August and early September 2017, driving levels of fine particulate matter to nearly 20 times the acceptable limit set by the Environmental Protection Agency.

Noonan is now working with colleagues to gather health information from residents of Seeley Lake and several other Montana towns. They aim to track how respiratory performance, mental states, and genetic markers related to inflammation change when smoke descends. Noonan is also seeking funding to sift through health records of wildland firefighters to understand how sustained smoke exposure has affected them.

Farther north, Sarah Henderson, an environmental epidemiologist and veteran smoke researcher at the British Columbia Centre for Disease Control in Vancouver, Canada, hopes to track the fate of children born during high-smoke events. One big question, she says, is: "If you're born into really smoky conditions with your extremely sensitive, newborn lungs, what does that mean for you?"

As scientists prepare to tackle such questions, health officials in Missoula are preparing for a possible repeat of last year's smoke waves. The health department is stockpiling indoor air filters for day care centers, schools, and other gathering spots.

Fischer, for one, hopes they aren't needed. Although she requires fire for her studies, she says, "I'm just wishing for an average wildfire year with wildfires in wilderness areas that don't cause any property damage." ■

MISCONDUCT

Will U.S. academies expel sexual harassers?

Prestigious bodies consider changing bylaws to eject members who offend

By **Meredith Wadman**

As high-profile sexual harassment cases fuel public criticism, the presidents of the U.S. National Academies of Sciences, Engineering, and Medicine announced last week they may adopt new policies allowing the prestigious bodies to eject members who have committed harassment and other forms of misconduct. Members of the academies—which serve as both honorific societies and advisers to the U.S. government—are elected by existing members to life-long terms, and the bodies currently lack mechanisms for removing them for harassment.

Because scientists and the public "place much trust" in the three Washington, D.C.–based academies, their leadership councils "have begun a dialogue about the standards of professional conduct for membership," the presidents said in a 22 May statement. "We want to be sure that we are doing everything possible to prevent sexual harassment, to instill a culture of inclusion and respect, and to reinforce that harassment is not tolerated." The statement was signed by Marcia McNutt, head the National Academy of Sciences (NAS); C. D. Mote Jr., head of the National Academy of Engineering (NAE); and Victor Dzau, head of the National Academy of Medicine (NAM).

Some researchers welcomed the announcement. "This may seem small, but as someone who's been working with them for 2 years, this is BIG for this organization," tweeted Kate Clancy, an anthropologist who studies sexual harassment in science at the University of Illinois in Urbana. Clancy helped author an NAS report on sexual harassment in science that will be released on 12 June.

But Clancy and others also expressed concern that the "dialogue" would not lead

to major changes, and criticized the academies for moving too slowly. "McNutt and other science society presidents have a moral imperative to get these knuckleheads out. Folks need to know women in science are done waiting for our societies to have our backs," says neuroscientist BethAnn McLaughlin of the Vanderbilt University School of Medicine in Nashville. On 6 May, angered by an article in *Science* detailing allegations of sexual harassment by scientist and NAS member Inder Verma of the Salk Institute for Biological Studies in San Diego, California (*Science*, 4 May, p. 480), McLaughlin launched an online petition asking NAS to eject members sanctioned for sexual harassment. (Verma has denied the allegations; Salk is investigating.)

McNutt argues that getting it right will take time at the staid and governance-laden academy she runs. NAS's 17-member governing council—which includes 11 women—will discuss the issue at its next meeting,

Marcia McNutt, head of the U.S. National Academy of Sciences, wants members to consider ejecting harassers.

McNutt tweeted, with an eye toward having the full NAS membership vote on amending its bylaws at its annual meeting next April. The outcome of that vote is not certain, McNutt suggested in a tweet. "Anyone who thinks it is easy [to change bylaws] has not tried to get a majority vote from an honorary society of more than 80 percent men over 70 years average age." (The average age of the 2382 NAS members is 72; 84% are men.)

NAM and NAE referred questions about how those two bodies will proceed to NAS, which said it is too early to know.

The effort comes as U.S. universities, scientific societies, and research funders are scrambling to respond to a wave of allegations of sexual harassment and scientific misconduct. One society, the American Geophysical Union, has expanded its definition of research misconduct to include sexual harassment and rescinded an honor bestowed on a scientist facing allegations of misbehavior. Universities have suspended or fired researchers under investigation for harassment, or found to be harassers.

Until last week, however, the academies had remained mostly silent on how they might address misconduct among their 7000 members, despite mounting criticism. As of 29 May, more than 2700 people had signed the petition launched by McLaughlin, which asked NAS to kick out members "who have been sanctioned for sexual harassment, retaliation and assault."

The conundrum presented by lifetime memberships in the academies has been apparent for some time. NAM member Arthur Kellermann, dean of the Uniformed Services University of the Health Sciences (USUHS) in Bethesda, Maryland, last year filed a complaint urging his academy to eject physician Eric Noji. A 2016 investigation by the university found that Noji, who had been an adjunct professor at USUHS, had plagiarized several research papers and misrepresented his credentials prior to his election to NAM, according to *The New York Times*. The university fired Noji, but he remains a member of NAM. In late 2016, the case prompted NAM to adopt a new rule allowing it to "rescind" a membership if "it is later determined by an authorized body that the information relied on for election is false."

Other current academies members could be vulnerable to expulsion under new bylaws covering harassment. In 2015, astronomer Geoffrey Marcy resigned from the University of California, Berkeley, after Buzzfeed published the results of a university investigation that concluded he had violated its policies on sexual harassment. In March, Thomas Jessell, a Columbia University neuroscientist, was fired by the school and the Howard Hughes Medical Institute after a university investigation concluded he had violated Columbia's policies on consensual sexual relationships between faculty and students, according to the *Columbia Daily Spectator*.

Exactly how the academies would carry out an expulsion and what evidence they might require before acting are just two questions facing their leadership councils. Some argue that findings of misconduct by an institution should be enough to hit the eject button. But NAS member Robert Weinberg, a cancer scientist at the Massachusetts Institute of Technology in Cambridge, disagrees. "I have little faith that findings of sexual harassment by the host institutions of accused parties will be adjudicated in a fashion that applies uniform standards of evidence and fairness," Weinberg wrote in an email to *Science*.

"It's important to make sure there was due process. … Allegations should not be sufficient to eject a member," says Robert Cook-Deegan, a longtime observer of the academies and a science policy specialist with Arizona State University who is based in Washington, D.C. He adds: "The academies would do well not to get into the policing and prosecution, but rather identify the findings of courts or systematic and credible administrative processes."

Unlike the U.S. academies, several foreign honorary societies do have procedures for ejecting members for misconduct. But the German academy (called the Leopoldina) and the Royal Netherlands Academy of Arts and Sciences have not in living memory ejected members, according to their spokespeople. At the Royal Society in the United Kingdom, "the list of expulsions is largely historical and the top reason cited is nonpayment of subscriptions," a spokesperson wrote in an email.

AAAS (publisher of *Science*) in Washington, D.C., also has no mechanism for ejecting fellows, who are elected for life. But spokesperson Tiffany Lohwater says AAAS leaders are drafting a policy for revoking fellows who don't live up to "the commonly held standards of professional ethics and scientific integrity." ■

PHOTO: STEPHEN VOSS

HUMAN EVOLUTION

New copies of old gene drove brain expansion

Research shows how genes supercharge neuron formation during human development

By **Elizabeth Pennisi**

Three nearly identical genes could help explain how 0.5 liters of gray matter in early human ancestors became the 1.4-liter organ that has made our species so successful and distinctive. The newly identified genes could also help explain how brain development sometimes goes wrong, leading to neurological disorders.

The genes, descendants of an ancient developmental gene that multiplied and changed in the course of evolution, add to a growing list of DNA implicated in human brain expansion (*Science*, 3 July 2015, p. 21). But they stand out because so much has been learned about how they work their magic, says James Noonan, an evolutionary genomicist at Yale University. Researchers have shown that this trio boosts the number of potential nerve cells in brain tissue, and one team even pinned down the protein interactions likely responsible. "These are new proteins that are potentially modifying a very important pathway in brain development in a very powerful way," Noonan adds.

Until now, the four genes were thought to be one, *NOTCH2NL*, itself a spinoff of the NOTCH gene family, which controls the timing of development in everything from fruit flies to whales. But two studies in the 31 May issue of *Cell* trace a series of genetic accidents in recent evolutionary history that have yielded four very closely related *NOTCH2NL* genes in humans (see graphic, right).

David Haussler, a bioinformatician at the University of California, Santa Cruz, and his colleagues got on the trail of the genes after they discovered that the NOTCH pathway works differently in human and macaque brain organoids—test tube models of the developing brain. *NOTCH2NL* was missing in the macaque organoid and, later analyses showed, in other nonhuman apes as well. That suggested *NOTCH2NL* might have played a unique role in human evolution.

By comparing *NOTCH2NL*-related DNA in the genomes of humans and other primates, Haussler's team reconstructed the genes' evolutionary history. They concluded that during DNA replication perhaps 14 million years ago, part of an ancestral *NOTCH2* gene was copied by mistake. The new "gene" was incomplete and nonfunctional, but about 11 million years later—shortly before human ancestors' brains began to expand—an additional piece of *NOTCH2* got inserted into this copy, making the gene functional. "This event marks the birth of the *NOTCH2NL* genes we now have in our brains," says Frank Jacobs, a co–senior author on the paper and an evolutionary genomicist at the University of Amsterdam.

Subsequently, that active *NOTCH2NL* gene was duplicated twice more, yielding three active *NOTCH2NL* genes in a row at one end of human chromosome 1 and one inactive copy on the other end. Gene copies can be potent evolutionary forces because one copy continues its necessary job, leaving the others free to do something new.

A boost for the brain

In an ape ancestor, duplication of *NOTCH2* yielded a nonfunctional *NOTCH2NL* (gray). Repair and later gene duplications produced multiple working copies.

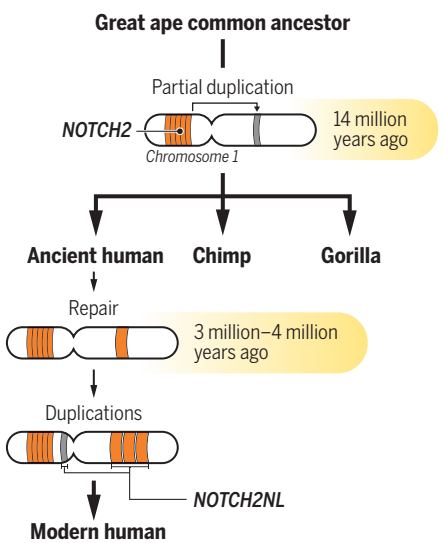

Pierre Vanderhaeghen, a developmental neurobiologist at the Free University of Brussels, uncovered the same set of genes when he found a way to screen human fetal brain tissue for duplicated genes. To find out what they do, his team ramped up *NOTCH2NL* activity in cultured brain tissue. The tissue made more stem cells, they report in the second *Cell* paper.

The finding complements one reported earlier this spring by Wieland Huttner, a neurobiologist at the Max Planck Institute of Molecular Cell Biology and Genetics in Dresden, Germany. He and his team had decided to focus on *NOTCH2NL* (which they thought was a single gene) after finding it was highly active in fetal brain cells. When they put a human *NOTCH2NL* gene into incipient brain tissue from mice embryos, more stem cells developed. That suggests the human gene delays the specialization of those cells so they have a chance to produce many more copies of themselves, the researchers reported in *eLife* on 21 March.

Now, in their *Cell* paper, Vanderhaeghen and his colleagues describe molecular details of how *NOTCH2NL* works to boost neuron formation. They found that a *NOTCH2NL* protein blocks a key step in a signaling pathway that causes stem cells to differentiate and stop dividing. As a result, the cells persist and keep producing progeny, ultimately yielding a larger crop of neurons. "That's really compelling biological data," Noonan says. "In other studies of genes involved in human evolution, it's been very difficult to draw a line from the genetic difference to the phenotype to a biochemical mechanism that's responsible."

The location of the three active *NOTCH2NL* genes is also telling, Haussler says. They are smack in the middle of DNA implicated in autism, schizophrenia, and a developmental delay syndrome. Such duplicated DNA is prone to getting copied extra times or losing DNA during replication, and instability is a hallmark of these disorders. To Greg Wray, an evolutionary developmental biologist at Duke University in Durham, North Carolina, this clue to brain diseases is the most compelling new result. "These genes likely play an important role in cortical development, and misregulation leads to disease," he says.

Wray is less convinced that the genes had a unique role in human evolution because the chromosomal region in which they reside is complex and difficult to sequence, and because the evidence for an evolutionary difference in gene function between humans and other species is indirect.

But Haussler thinks these genes will prove key players in human brain expansion. "One change didn't do it alone, but some will be found to be more fundamental than others," he points out. "*NOTCH2NL* has a shot at this." ■

CREDITS: (GRAPHIC) V. ALTOUNIAN/*SCIENCE*; (DATA) FIDDES *ET AL.*, *CELL* 173, 1 (2018)

The company that developed HELIOtube, an inflatable solar heat collector, received funding under Horizon 2020. The European Commission plans to give innovation a bigger boost in Horizon Europe.

RESEARCH FUNDING

Europe's science spending set for another big boost

Commission seeks €97.6 billion for "Horizon Europe"

By **Tania Rabesandratana**

On 7 June, the European Commission will lay out detailed plans for one of the biggest single research programs on the planet. Called Horizon Europe, the program could be worth €97.6 billion between 2021 and 2027, up from about €77 billion for the current 7-year program, Horizon 2020. Its influence, however, will go beyond size.

Europe's research programs provide stable funding for 7 years, some of it up for grabs for researchers around the world. And although they represent less than 10% of the total research money available in the European Union, the continuous growth of the EU science budget in the past decades (see graph, right), at the expense of agriculture and regional development, is a clear signal that it sees research and innovation as the future drivers of its economy.

Next week's proposals are unlikely to contain major surprises, because the commission has unveiled its main ideas over the past months, in particular its overall 7-year budget plan, issued on 2 May. Although Horizon Europe will keep Horizon 2020's main features, the commission has laid the groundwork for several novelties, including a new agency to tackle the continent's perennial innovation problem and a big, separate push on collaborative defense research. But contentious negotiations lie ahead. The United Kingdom is negotiating the terms of its impending exit from the European Union, and some member states want to tighten budgets. Meanwhile, research advocates want more generous spending, noting the low application success rates in Horizon 2020—a frustrating 11.9% so far.

Like previous programs, Horizon Europe will have three main "pillars"; next week's plan will detail how much money could go to each. The first component, called Open Science, will provide funding for projects "driven by researchers themselves," as the commission puts it, through the well-liked basic research grants of the European Research Council (ERC) in Brussels and the Marie Skłodowska-Curie fellowships for doctoral programs, postdocs, and staff exchanges. This part of the program is largely unchanged from Horizon 2020.

The second pillar, Global Challenges, will set so-called missions addressing issues "that worry us daily such as the fight against cancer, clean mobility, and plastic-free oceans," says a commission fact sheet. The "missions" are meant to be flexible, as priorities change, and they appear to have a sharper focus than the "societal challenges" named in a comparable pillar of Horizon 2020, including energy and food security.

The third part of Horizon Europe, called Open Innovation, addresses an old problem: Europe's shortage of successful innovative businesses, despite its world-class science. At the moment, EU science funding for businesses largely goes through sizable public-private partnerships involving big firms, for example in the fields of aeronautics and pharmaceuticals. Now, EU research commissioner Carlos Moedas is launching a new project, the European Innovation Council (EIC), to encourage startup companies and "breakthrough technologies."

The commission says EIC will differ from the European Institute of Innovation and Technology (EIT) in Budapest, set up in 2008. EIT—the pet project of former commission President José Manuel Barroso—brings together businesses, research centers, and universities in six pan-European "Innovation Communities." Some observers say EIC's creation signals that EIT didn't quite deliver and is being marginalized.

EIC will use the ingredients that made ERC successful: focusing on individual entrepreneurs rather than big cross-border teams, letting ideas emerge from the bottom up, and keeping grants and procedures simple. Its success "will depend on putting the right evaluation system into place," says Austrian sociologist and former ERC President Helga Nowotny. "It takes excellence to recognize excellence." But many universities are upset that the current pilot program for EIC, worth €2.7 billion for 3 years, didn't include them in its group of advisers. "Next to CEOs and entrepreneurs, there is also room for researchers," says Kurt Deketelaere, secretary-general of the League of European Research Universities in Leuven, Belgium. He adds that there are more pressing barriers to innovation than a lack of funding, noting that the European Union's 28 member states "have 28 different schemes for taxation, intellectual property, bankruptcy."

Science on the rise

The European Union's average annual research spending would continue to grow under the commission's proposal for Horizon Europe.

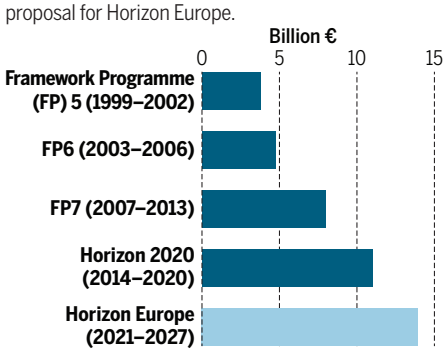

CREDITS: (PHOTO) HELIOVIS AG; (GRAPH) J. YOU/*SCIENCE*; (DATA) EUROPEAN COMMISSION

In addition to Horizon Europe, the commission has proposed another bold move for research: setting aside €4.1 billion over 7 years as a separate budget line for defense research, up from just €90 million under an ongoing 3-year pilot program. Member states have long been lukewarm about cooperation in this secretive area, where national interests prevail. But in times of growing "geopolitical instability," as the commission puts it, some member states seem more willing to pool resources.

Yet some 700 scientists have signed a petition against any EU funding of military research; others worry the plan could come at the expense of nonmilitary science. "We will oppose anything that could take funding away from Horizon Europe's civilian research," says Maud Evrard, head of policy at Science Europe in Brussels, a group of national science funding agencies and research organizations.

The commission's €97.6 billion opening bid represents a 27% increase from the previous 7-year period—or even a 46% rise if compared to Horizon 2020 without the share of the United Kingdom, which is leaving the European Union in March 2019. But with some member states keen to tighten the European Union's purse strings, Horizon Europe's budget is likely to go down in coming negotiations with the European Parliament and EU member states. As a result, both Evrard and Deketelaere say they are disappointed that the commission didn't aim higher.

Negotiations for such programs can easily stretch to at least 18 months, but the commission wants to make as much progress as possible before elections to renew the European Parliament—which usually is very supportive of research—in May 2019. That will give the United Kingdom a chance to help shape the 7-year plan before it loses its seats in Parliament and the European Council. "We need to make the most of these channels whilst we can," Jessica Cole, head of policy at the Russell Group, a London-based group of 24 leading U.K. universities, wrote in a blog post on 4 May.

The United Kingdom has made clear that it wants to keep taking part in EU research programs after it leaves the bloc. This will require buying its way in through a bilateral association agreement, as other, smaller, non-EU countries such as Norway and Israel do. Other non-EU countries will be following the negotiations closely. Under Moedas's mantra of "Open Science, Open Innovation, Open to the World," the commission is likely to lift restrictions and make it easier for countries outside Europe and its immediate neighborhood to buy a stake in the research flagship—a sign that Europe's horizons are widening further. ■

AIR POLLUTION

United Kingdom unveils ambitious air pollution plan

Bid to slash particulate pollution draws praise and doubts

By **Matthew Warren**

The United Kingdom wants to become a global leader in cleaning up polluted air—but the island nation may not be able to meet some of its ambitious new goals by itself. Last week, the U.K. government released a draft strategy for reducing air pollution that would impose the industrialized world's strictest emission targets for tiny particles of soot and other compounds that can lodge in peoples' lungs and shorten their lives. The plan would also tackle a source of particulate smog that is especially hard to rein in: ammonia from farm fields and manure piles.

Air quality researchers are applauding the goals of the 104-page Clean Air Strategy, which Prime Minister Theresa May's government released on 22 May for public comment. But achieving those goals will be a challenge, they caution, in part because much of the United Kingdom's particulate pollution drifts in from other nations. Even at home, cleaning up multiple, widespread pollution sources will require money and political will.

> ***"They're fighting on an awful lot of fronts here ..."***
>
> **Alastair Lewis**, University of York

The boldest goal is to halve, by 2025, the number of people breathing air with concentrations of fine particulates—particles less than 2.5 microns wide—that exceed levels set by the World Health Organization (WHO). WHO's particulate standard of 10 micrograms per cubic meter (μg/m^3), averaged over a year, is much tighter than the European Union's limit, which is set to drop to 20 μg/m^3 in 2020. (The U.S. standard is 12 μg/m^3.)

That commitment is welcome, says Alastair Lewis, an atmospheric chemist at the University of York in the United Kingdom and deputy director of the National Centre for Atmospheric Science in Leeds, U.K. Although it stops short of requiring the United Kingdom to meet the stringent WHO limit in every community in the nation, it will likely "become the de facto standard that people will hold [the government] to. You can't put the genie back in the bottle and pretend you never said it."

To achieve the goal, the government proposes tackling emissions produced by domestic stoves and fireplaces, which account for 38% of the United Kingdom's particulate pollution. New rules could limit the use of polluting fuels such as wet wood, for example, and raise emission standards for new stoves. The plan also envisions phasing out diesel-fueled trains by 2040 and tightening standards on vehicle tires and brakes, which throw off tiny particles during use. (The plan does not address other vehicle emissions, which a second document will cover.)

Another key strategy is to reduce emissions of ammonia, which fuels chemical reactions in the atmosphere that produce an array of problematic particulates. Farm use of fertilizers and manure from livestock and poultry produce about 88% of the United Kingdom's ammonia emissions, so proposed plans would curb fertilizer use and require covering manure heaps to trap ammonia gas. Such steps could mark "a key turning point" for controlling ammonia emissions, says environmental physicist Mark Sutton of the Centre for Ecology & Hydrology in Edinburgh. If current trends continue, Sutton notes, the United Kingdom will fall short of meeting ammonia goals set for 2020.

But enforcing ammonia limits on thousands of farms will be complicated and could meet with resistance from agriculture interests. And although the government says it is demonstrating a commitment to go "further and faster than the EU" in combatting particulates, the United Kingdom will likely need help from other European nations to realize cuts, given that up to one-third of the nation's smog—especially in the southeastern part of the country—drifts in from the continent in the form of precursor gases.

The sweeping plan isn't scheduled to be finalized until early 2019, and many of the details have yet to be hashed out. "They're fighting on an awful lot of fronts here ... a huge, wide range of sectors and industries," Lewis says. "The question is: Have they really set out a case that they will have the resources and the capacity to do that?" ■

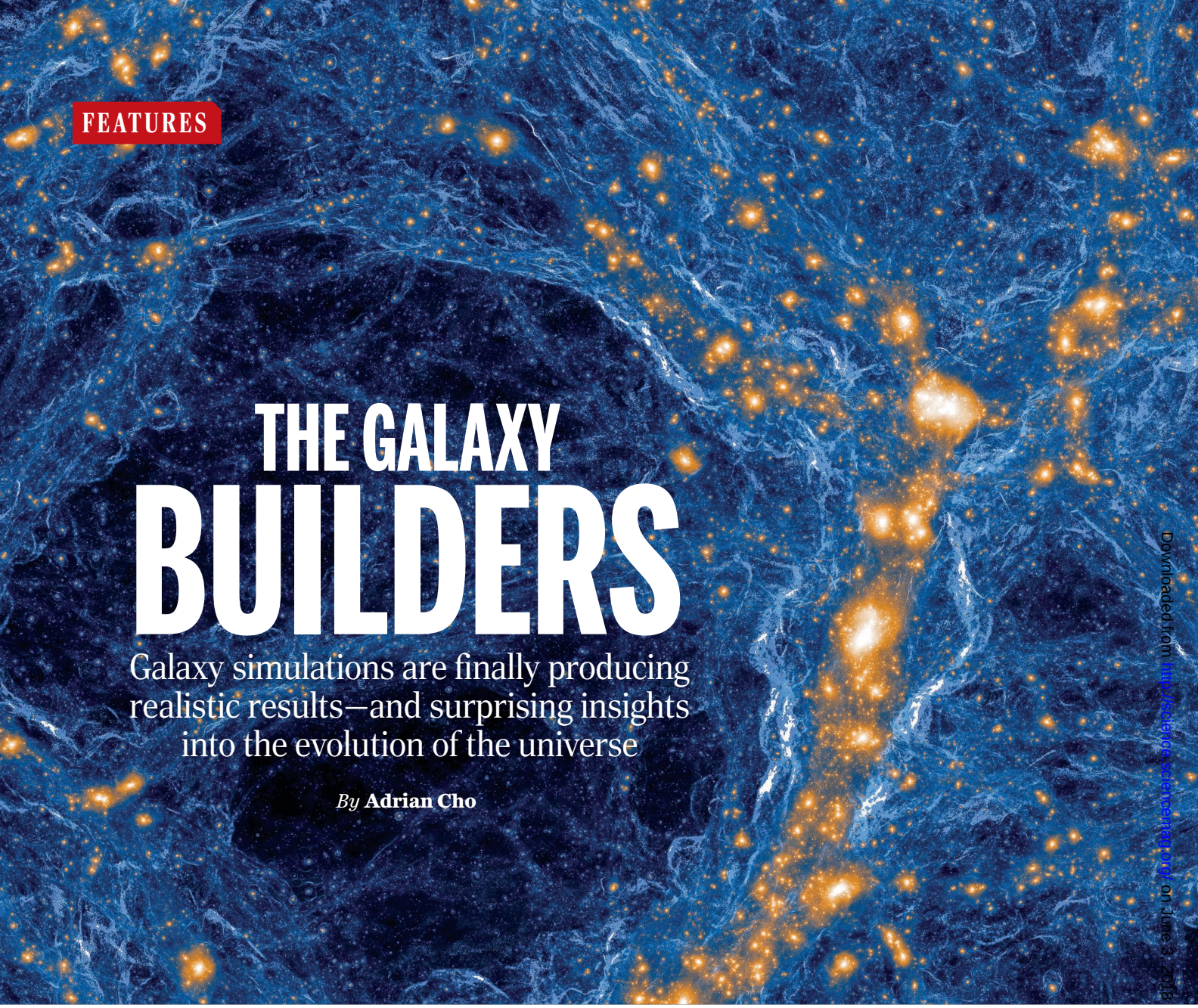

THE GALAXY BUILDERS

Galaxy simulations are finally producing realistic results—and surprising insights into the evolution of the universe

By **Adrian Cho**

Philip Hopkins, a theoretical astrophysicist at the California Institute of Technology in Pasadena, likes to prank his colleagues. An expert in simulating the formation of galaxies, Hopkins sometimes begins his talks by projecting images of his creations next to photos of real galaxies and defying his audience to tell them apart. "We can even trick astronomers," says Hopkins, a leader of FIRE, the Feedback in Realistic Environments simulation. "Of course, it's not a guarantee that the models are accurate, but it's sort of a gut check that you're on the right track."

For decades, scientists have tried to simulate how the trillions of galaxies in the observable universe arose from clouds of gas after the big bang. But in the past few years, thanks to faster computers and better algorithms, the simulations have begun to produce results that accurately capture both the details of individual galaxies and their overall distribution of masses and shapes. "The whole thing has reached this little golden age where progress is coming faster and faster," says Tiziana Di Matteo, a numerical cosmologist at Carnegie Mellon University in Pittsburgh, Pennsylvania, and a leader of the BlueTides simulation.

As the fake universes improve, their role also is changing. For decades, information flowed one way: from the astronomers studying real galaxies to the modelers trying to simulate them. Now, insight is flowing the other way, too, with the models helping guide astronomers, says Stephen Wilkins, an extragalactic astronomer at the University of Sussex in Brighton, U.K., who works on BlueTides. "In the past the simulations were always trying to keep up with the observations," says Wilkins, who is using BlueTides to predict what NASA's James Webb Space Telescope will see when it launches in 2020 and peers deep into space and far back in time. "Now we can predict things that we haven't observed."

For example, the models suggest that the earliest galaxies were oddly pickle-shaped, that wafer-thin spiral galaxies are surprisingly rugged in the face of collisions, and that to explain the evolution of the universe, galaxies must form stars far more slowly than astrophysicists expected.

The simulations also sound a cautionary note. Some cosmologists hope galaxy formation will ultimately turn out to be a relatively simple process, governed by a few basic rules. However, modelers say their

IMAGE: TNG COLLABORATION

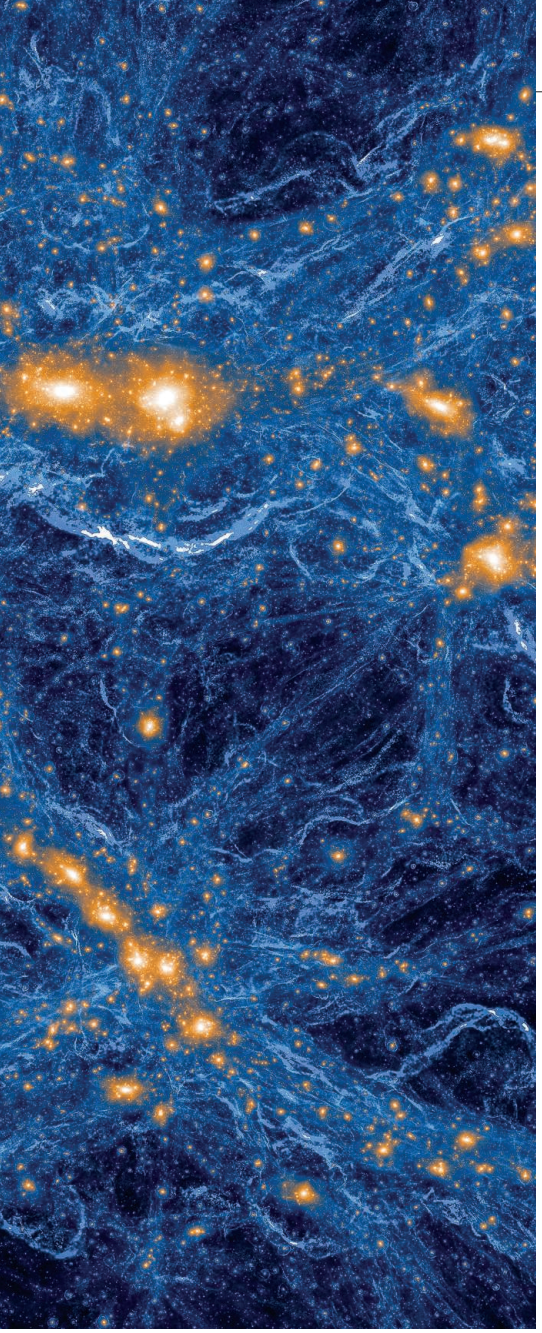

A view of the present-day cosmic web 300 million light-years across, as modeled by IllustrisTNG. Galaxies (gold) have blown off shocked gas (white).

faux universes suggest that, like maturing teenagers, galaxies are unpredictable. It's hard, for example, to tell why one turns into a graceful spiral but another evolves into a blob. "It's clear from everything that we've done that the physics of galaxy formation is incredibly messy," Wilkins says.

BEFORE YOU CAN cook up a universe, you need to know the ingredients. From various measurements, cosmologists have deduced that just 5% of the mass and energy of the cosmos is ordinary matter like that in stars and planets. Another 26% consists of mysterious dark matter that, so far, appears to interact only through gravity—and presumably consists of some undiscovered particle. The remaining 69% is a form of energy that stretches space and is speeding up the expansion of the universe. That "dark energy" may be a property of the vacuum of space itself, so physicists call it the cosmological constant, denoted lambda (Λ).

Cosmologists also know the recipe's basic steps. The universe sprang into existence in the big bang as a hot, dense soup of subatomic particles. Within a sliver of a second, it underwent an exponential growth spurt called inflation, which stretched infinitesimal quantum fluctuations in the particle soup into gargantuan ripples. Slowly, dense regions of dark matter coalesced under their own gravity into a vast tangle of clumps and filaments known as the cosmic web. Attracted by the dark matter's gravity, gas settled into the clumps, also called haloes, and condensed into the fusing balls of hydrogen called stars. By 500 million years after the big bang, the first galaxies had formed. Over the next 13 billion years, they would drift on cosmic gravitational tides and grow by merging with one another.

Computer simulations helped develop that theory. In the 1980s they showed that to form clumps large enough to bind the observed clusters of galaxies, dark matter particles had to be slow moving and cold. The basic theory, which assumes a cosmological constant, became known as Λ cold dark matter (ΛCDM). As the theory grew more refined, so did the simulations. By 2005 the Millennium simulation, led by researchers at the Max Planck Institute for Astrophysics in Garching, Germany, produced a rendering of the cosmic web whose structure closely matched how the galaxies are strewn through space in clusters, threads, and sheets.

Millennium and similar simulations suffered from a fundamental shortcoming, however. They modeled the gravitational interactions of dark matter alone, which are easy to simulate because, as far as scientists know, dark matter flows through itself without friction or resistance. Only once the haloes formed did the programs insert galaxies of various sizes and shapes, following certain ad hoc rules. In such simulations, "The fundamental assumption is that the galaxies occupy the haloes and don't do anything to them," says Yu Feng, a cosmologist at the University of California (UC), Berkeley. "The interaction is all one way."

Now, modelers include the interactions of ordinary matter with itself and with dark matter—processes that are far harder to capture. Unlike dark matter, ordinary matter heats up when squeezed, generating light and other electromagnetic radiation that then pushes the matter around. That complex feedback reaches an extreme when gas clouds collapse into glowing stars, stars blow up in supernova explosions, and black holes swallow gas and spew radiation. Critical to the behavior of galaxies, such physics must be modeled by using the equations of hydrodynamics, which are notoriously difficult to solve, even with supercomputers.

In general, modelers attack the problem by breaking it into billions of bits, either by dividing space into a 3D grid of subvolumes or by parceling the mass of dark and ordinary matter into swarms of particles. The simulation then tracks the interactions among those elements while ticking through cosmic time in, say, million-year steps. The computations strain even the most powerful supercomputers. BlueTides, for example, runs on Blue Waters—a supercomputer at the University of Illinois in Urbana that can perform 13 quadrillion calculations per second. Merely loading the model consumes 90% of the computer's available memory, Feng says.

For years such simulations produced galaxies that were too gassy, massive, and blobby. But computer power has increased, and, more important, models of the radiation-matter feedback have improved. Now, hydrodynamic simulations have begun to produce the right number of galaxies of the right masses and shapes—spiral disks, squat ellipticals, spherical dwarfs, and oddball irregulars—says Volker Springel, a cosmologist at the Heidelberg Institute for Theoretical Studies in Germany who worked on Millennium and leads the Illustris simulation. "Until recently, the simulation field struggled to make spiral galaxies," he says. "It's only in the last 5 years that we've shown that you can make them."

The models now show that, like people, galaxies tend to go through distinct life stages, Hopkins says. When young, a galaxy roils with activity, as one merger after another stretches and contorts it, inducing spurts of star formation. After a few billion years, the galaxy tends to settle into a relatively placid and stable middle age. Later, it can even slip into senescence as it loses its gas and the ability make stars—a transition our Milky Way appears to be making now, Hopkins says. But the wild and violent turns of adolescence make the particular path of any galaxy hard to predict, he says.

The simulations are far from perfect. They cannot come close to modeling individual stars—even though the simulations point to the importance of feedback effects on that scale, such as the winds and radiation from supernovae and from galaxies' central black holes. Instead, each grid element or particle stands for hundreds to

millions of solar masses of stars and gas, depending on the resolution of the simulation. Researchers then employ ad hoc "subgrid" rules to describe how all that material behaves on average. "It's like you're looking through foggy glasses and trying to describe this shape that you cannot see perfectly," says Avishai Dekel, a cosmologist at the Hebrew University of Jerusalem and a leader of the VELA simulation.

Those ad hoc rules include dozens of parameters that researchers tune to reproduce known features of the universe, such as the tallies of galaxies of different masses. That tuning raises the question of whether the models explain reality or merely mimic it, like a painting. But researchers say the models should be reliable as long as they avoid predictions that depend strongly on the tuning. "We're not going to get away from subgrid prescriptions, there's no way," Di Matteo says. "But this is not some kind of magic. It's still physics."

show no such connection, she adds. "We're now at a loss," Faber says. "What makes a big galaxy big and a small galaxy small?"

The shapes of newborn galaxies yield another surprise. Most galaxies today are spherical or oblate, like flattened spheres. Ellipticals are thick, like round cakes of soap; disks are much flatter. But the models predict that early in the universe, emerging galaxies were prolate—longer than they were wide, Faber says. "They're pickles," she says. "You try to make a pickle out of gas. It's not easy." NASA's Hubble Space Telescope has begun to spot examples of these pickle-shaped galaxies, she says.

The models predict other subtle phenomena that observers can try to spot. For example, astrophysicists had assumed that gas flows into a growing galaxy equally from all directions. However, the simulations show that gas pours into a galaxy in cold streams that flow along the dark matter filaments connecting its halo to the cosmic web, been spotted. That deficit was dubbed the missing-satellites problem.

But mix in the ordinary matter, and the predictions change. The gravitational push and pull between dark and ordinary matter smooths things out, reducing the number of small haloes. In those that do emerge, winds kicked up by supernovae tend to overwhelm the halo's relatively weak gravitational pull and blow out the gas, starving the halo of the raw material to make more stars and snuffing out the nascent galaxy. Couple that process with the fact that observers have now found 59 dwarf galaxies surrounding the Milky Way, and the disconnect between observations and simulations largely disappears, Springel says. "I don't see the missing-satellites problem as a problem anymore," he says.

Similarly, the older simulations suggested the concentration of dark matter should peak sharply at the very center of a halo. Yet the speeds of stars in nearby dwarf galax-

Simulations great and small

Some models operate at cosmic scales, whereas others generate individual, realistic-looking galaxies (left). They divide space into volume elements or model matter as swarms of particles, then trace their interactions.

NAME	SIMULATION SIZE (LIGHT-YEARS)	NUMBER OF VOLUME ELEMENTS/PARTICLES	MINIMUM ELEMENT MASS (SOLAR MASSES)	FOCUS	FIRST PAPERS
Millennium	2.2 billion	10 billion	1 billion	Dark matter only	2005
VELA	45 million	500 million	1000	Individual galaxies	2009
◀ **FIRE**	3 million–10 million	Few hundred million–1 billion	200–2000	Individual galaxies	2014
EAGLE	80 million–325 million	100 million–7 billion	1.8 million	Cosmic evolution	2014
BlueTides	1.9 billion	700 billion	2 million	First galaxies	2015
IllustrisTNG	110 million–1 billion	270 million–30 billion	1 million–10 million	Cosmic evolution	2018

THE MODELS HAVE already overturned some long-held assumptions. For example, astrophysicists believed that when two delicate disk galaxies like our Milky Way collide and merge, the process would wad them up into a single blobby elliptical galaxy. However, the models show that spiral galaxies are tougher than expected, if they hold enough gas. "You have disks partially surviving and recovering so quickly," Springel says. That finding was a big surprise, Hopkins says.

The usual explanation of what determines galactic size has also been knocked down, says Sandra Faber, an astronomer at UC Santa Cruz who works with VELA. Astrophysicists had assumed that a galaxy's size is determined by the spin of the dark matter halo enveloping it, with faster-spinning haloes producing larger, more diffuse galaxies, she says. But simulations Dekel says. Observers with the Atacama Large Millimeter/submillimeter Array, a battery of 66 radio dishes in Chile, have begun to peer into space for evidence of the streams.

The simulations also aim to test the basic theory of ΛCDM. By comparing real and simulated galaxies, researchers can test the assumption that dark matter interacts only through gravity. Any discrepancy might point to new interactions and help particle theorists figure out what dark matter is.

None has been seen so far, but the newer simulations have patched up mismatches between observations and earlier dark matter–only simulations. For example, 20 years ago, those simulations spawned swarms of small dark matter haloes around the bigger ones, which suggested that a galaxy like our Milky Way should be surrounded by hundreds of dwarf satellite galaxies. But only a few had ies indicate that in their cores dark matter is spread out smoothly over a larger volume. The new simulations get that detail right because they capture how the gravitational effects of stars stir up the dark matter and spread it out. "Even if the stars are a small fraction of the mass, they really shake up the halo," Hopkins says.

Perhaps the simulations' single biggest lesson so far is not that scientists need to revise their overarching theory of cosmology, but rather that problems lurk in their understanding of astrophysics at smaller scales. In particular, their theory of star formation comes up wanting, Springel says. To produce realistic galaxies, modelers must drastically reduce the rate at which clouds of gas form stars from what astrophysicists expect, he says. "Basically, the molecular clouds form stars 100 times slower than you'd think," he says.

IMAGE: A. WETZEL, P. HOPKINS, AND THE FIRE COLLABORATION

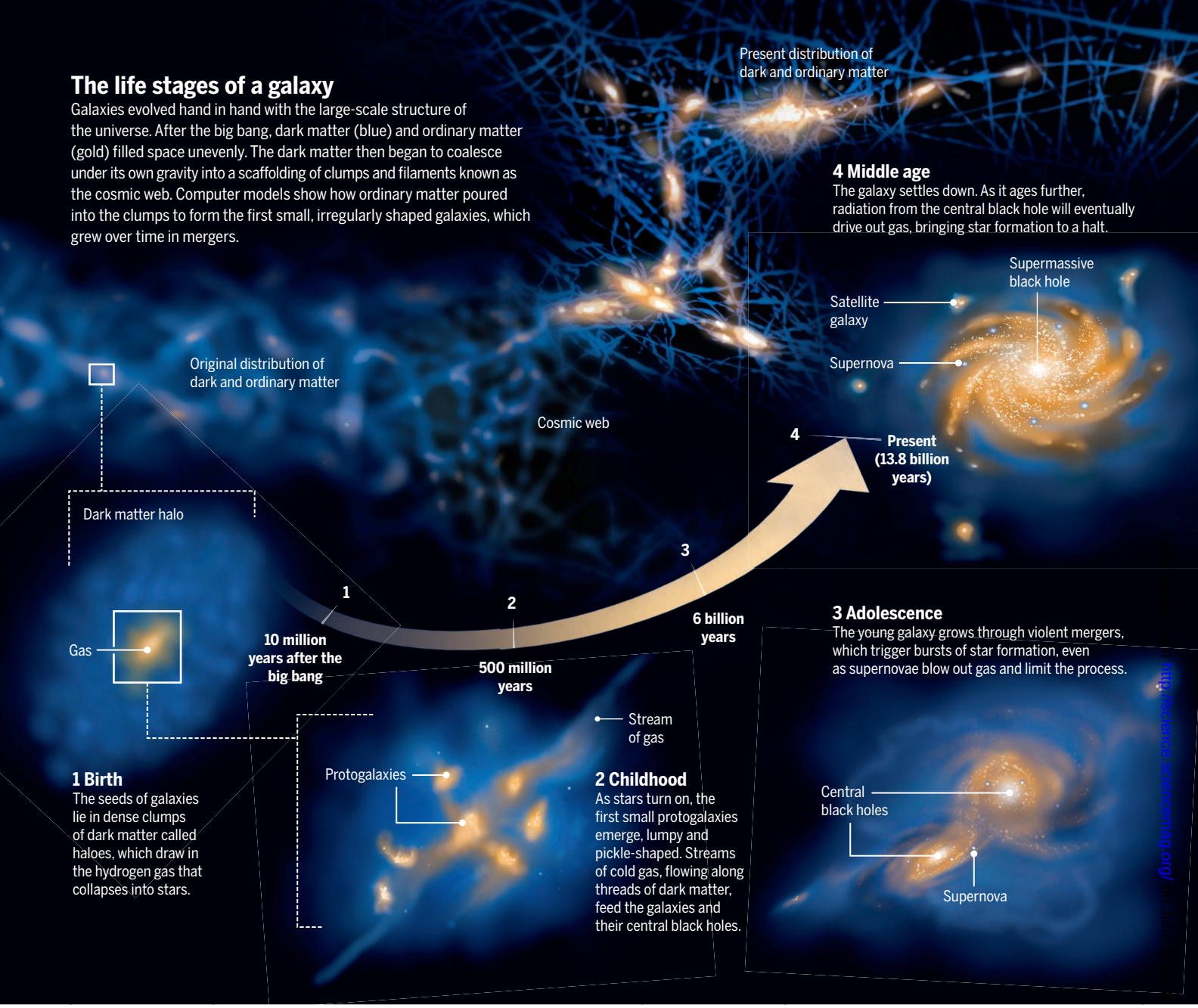

GRAPHIC: C. BICKEL/*SCIENCE*

Most likely, star formation flags because feedbacks from supernovae and supermassive black holes drive gas out of a galaxy. Unfortunately, those processes are far too small to resolve in the simulations. When modelers deposit the energy of a supernova in a larger grid element, not much happens: Instead of generating wind, the energy just radiates away. Similarly, researchers cannot simulate the fitful way that black holes feed on gas and radiate x-rays. To capture these key bits of astrophysics, modelers must rely on the ad hoc subgrid prescriptions that they tune by hand.

Simulators hope to replace such crude assumptions with models based more solidly on physics. To do that, they're hoping to enlist the help of astrophysicists working on much more finely resolved models that simulate the birth of stars from molecular clouds just a few light-years wide and even the evolution of individual stars. Those smaller-scale models are themselves works in progress. For example, astrophysicists modeling supernova explosions still struggle to make their virtual stellar time bombs go off.

Nevertheless, Eve Ostriker, an astrophysicist at Princeton University who models interstellar gas, says she's eager to help put galaxy simulations on a sounder footing. "My interest in this is to replace the tuning with some physics and say, 'OK, this is what it is, no tuning allowed,'" she says. The hope is to string together results from different size scales in a way that minimizes the need for fudge factors, researchers say. "What you want is a picture that's coherently stitching together across the entire range of scales," Hopkins says.

Ultimately, through observations and simulations, some researchers still hope to develop a unified narrative that can explain how any galaxy gets its shape and properties. Taking an extreme position, Faber predicts all galaxies will ultimately be sorted and explained by just two parameters: mass and radius. "There's a galaxy law that we're only now discovering that makes it simple."

But many galaxy modelers believe the recipes will always be complicated and uncertain. Galaxy formation may be like the weather, which keeps precise predictions forever out of reach because of its chaotic nature, Springel says. "I'm a little bit concerned that we'll understand the big picture but never understand the details," he says. In that case, the increasing realism of galaxy simulations may serve only to underscore a fundamental complexity in the universe. ■

BRIDGE: PESTICIDES AND SOCIETY

Decision-making in a storm of discontent

Regulation of pesticides such as glyphosate needs to include societal assessment

By **Nico M. van Straalen**[1]
and **Juliette Legler**[2,3]

On 12 December 2017, the European Commission reapproved the use of glyphosate, the world's most widely used active ingredient in herbicides and possibly the most heavily debated plant protection product since DDT (dichlorodiphenyltrichloroethane), for another 5-year period (*1*). Less than a week later, the U.S. Environmental Protection Agency (EPA) released its draft risk assessment for glyphosate, which concluded that human health risk levels associated with glyphosate exposure from food, drinking water, and residential sources are below the agency's levels of concern (*2*). Both in Europe and the United States, these decisions faced a storm of public discontent owing to concerns about the possible risks of chemical exposures and the role of large multinational companies. We argue that a broader societal assessment should be included in the decision-making process on pesticide registration.

IS GLYPHOSATE SAFE OR NOT?

The European Commission's decision to reapprove glyphosate was taken after lengthy and recurrent reviews by the European Chemicals Agency (ECHA), the European Food Safety Authority (EFSA), and the responsible ministries in member states of the European Union (EU). It was in line with conclusions reached by the Food and Agriculture Organization of the United Nations (FAO)–World Health Organization (WHO) Joint Meeting on Pesticide Residues on the carcinogenic risk to humans from dietary exposure (*3*). It was not, however, in line with the International Agency for Research on Cancer (IARC) of the WHO, which classified glyphosate as a probable human carcinogen in 2015 and again in an updated review in 2017 (*4*). The discrepancy between IARC's conclusions and the EU, FAO-WHO, and EPA assessments has been attributed to the use of different datasets and methods to evaluate the data (*5*), which points to a lack of international standardization of risk assessment procedures.

Prior to the European Commission's decision and that of the EPA, nongovernmental organizations (NGOs) had fought hard for years to curb the use of glyphosate-based herbicides. This ongoing plea has found support in an increasing number of scientific peer-reviewed articles, which have argued that glyphosate may have more profound ecotoxicological effects than concluded by regulatory authorities (*6*, *7*).

In the EU, the campaign to end the license of glyphosate culminated in a European

[1]*Department of Ecological Science, Vrije Universiteit Amsterdam, Amsterdam, Netherlands.* [2]*Institute for Risk Assessment Sciences, Utrecht University, Utrecht, Netherlands.* [3]*Utrecht Institute for Pharmaceutical Sciences, Utrecht University, Utrecht, Netherlands.*
Email: n.m.van.straalen@vu.nl

PHOTO: JOERG BOETHLING/ALAMY STOCK PHOTO

Glyphosate-based herbicide is sprayed to control weeds in an asparagus field in Brandenburg, Germany.

PHOTO: B CHRISTOPHER/ALAMY STOCK PHOTO

Citizens' Initiative that received over 1 million verified statements of support from 22 EU member states and was submitted to the European Commission on 6 October 2017 (*8*). The European Commission defended its position, arguing that "there are neither scientific nor legal grounds to justify a ban of glyphosate" (*9*). However, its decision to renew the license of glyphosate for 5 years, rather than the more common 10 or 15 years, can be viewed as a compromise, requiring the European Commission to revisit the approval of glyphosate on a shorter-than-usual time scale.

EXPLAINING THE DIVERGENT VIEWS

There are several reasons for the large discrepancy of views between regulatory authorities (except the IARC) on the one hand and some academic groups, several NGOs, and a substantial part of the general public on the other.

The glyphosate case is inherently complicated. Glyphosate inhibits a pathway of aromatic amino acid synthesis that is only present in plants, fungi, and bacteria and was therefore not expected to cause toxicity to animals (*7*). However, glyphosate is an active ingredient in many different herbicide formulations. In addition to the active ingredient, formulated herbicides such as Roundup contain additional chemicals, called adjuvants, that improve herbicidal activity or application characteristics. The toxicity of several Roundup formulations to human cell lines has been mainly attributed to such adjuvants rather than to glyphosate itself (*10*). The same is true for effects on ecological targets, although a smaller but separate effect of glyphosate cannot not be excluded in these studies (*11*).

Thus, many of the claims for glyphosate toxicity in the literature may be due to effects of one or more adjuvants, acting either directly or through interaction with glyphosate (*7*). Adjuvants are authorized under European legislation by including them on the "Official List of Adjuvants," but in the past these substances did not undergo a risk assessment comparable to the active ingredient. In its act on glyphosate (*1*), the European Commission has now forbidden the use of polyoxyethylene tallow amines as adjuvants in plant protection products.

Another issue complicating decision-making on glyphosate-based herbicides is that their use is interwoven with the planting of genetically modified (GM) glyphosate-resistant crop varieties. The global use of glyphosate has increased 15-fold since the introduction of GM crops in 1996 (*12*). Glyphosate-resistant GM crops are presently not grown in Europe, but their widespread culture in the United States and South American countries has resulted in appreciable residues of glyphosate on plant products, such as soybeans, that are imported into Europe and used for food and feed production. This is aggravated by the use of glyphosate as a desiccant to kill foliage before harvest (*6*). The glyphosate residues are generally in compliance with maximum residue levels (MRLs) set by the EFSA; however, when the EFSA raised the MRL for glyphosate in lentils from 0.1 to 10 mg/kg in 2012, suspicion arose that thresholds principally set to protect consumers and husbandry animals were adjusted to accommodate agricultural use of pesticides (*6*).

The widespread and rising use of glyphosate worldwide is also in itself a concern. Estimated global use was ~826 million kg in 2014, up from ~56 million kg in 1994 (*12*). A recent study found residues of glyphosate and/or its main metabolite, aminomethylphosphonic acid (AMPA), in 45% of European topsoils (*13*). The migration of herbicide residues into groundwater and their possible spread to drinking water extraction facilities is a serious concern. In addition, the effects of glyphosate on soil microbial communities and invertebrates in soils remain largely undocumented and constitute a substantial knowledge gap.

SOCIOECONOMIC ANALYSIS

Apart from the inherent scientific complexity, the glyphosate case illustrates a fundamental societal issue. The mere fact that the European Citizens' Initiative attracted so many adherents is indicative of a wide societal aversion to the massive increase in the production of chemicals and their use in pesticide-based agricultural mass production. Public concern is not only limited to glyphosate but also covers other chemicals such as neonicotinoids, endocrine-disrupting compounds, and food additives.

Activists demand the stop of glyphosate use in the European Union as they protest in Madrid, Spain on 8 February 2017.

The European Registration, Evaluation, Authorisation, and Restriction of Chemicals (REACH) regulation was adopted in 2007 to improve the protection of human health and the environment from possible risks posed by chemicals other than pesticides, food additives, and drugs. The scheme requires a socioeconomic impact analysis as part of the authorization and restriction process (*14*). In this analysis, conducted by the ECHA's Committee for Socio-Economic Analysis (SEAC), the socioeconomic benefits of authorization or restriction are weighed against the associated risks to human health or the environment. A recent evaluation of the SEAC's work showed that the ECHA's experts struggle with estimating the societal benefits and determining what costs involved in restricting the use of a chemical are proportional to the risks that are avoided through such restriction (*15*). However, the scientific basis and the methodologies for performing socioeconomic analysis are improving (*14*).

Presently there is no societal assessment in pesticide registration. Recently, a promising framework for the combination of cost-benefit analyses with factors such as risk perception, uncertainty, and trust in regulatory decision-making on toxic substances in food, including pesticides, has been proposed (*16*). We argue that including such a framework in pesticide authorization would be an appropriate way to take factors such as citizens' initiatives, societal attitudes toward agricultural chemicals, and economic benefits of chemical pest and weed control into account.

In a recent commentary, EFSA's executive director, Bernhard Url, called for a broader societal discussion about the role of modern agricultural practices to be "framed ahead of and outside scientific work" (*17*). We believe, however, that integration rather than a separate assessment is the way forward to move the discussion away from the present binomial decision of whether an individual pesticide is safe or unsafe. It is time for a new scheme for pesticide evaluation in which regulatory decision-making takes into account not only the technical evidence on safety but also the societal context in which decisions are made. ■

REFERENCES AND NOTES

1. https://ec.europa.eu/food/plant/pesticides/glyphosate_en
2. EPA, "Glyphosate. Draft human health risk assessment in support of registration review" (EPA, Office of Chemical Safety and Pollution Prevention, 2017).
3. Joint Meeting on Pesticide Residues, "Joint FAO/WHO meeting on pesticide residues, Summary report" (FAO, WHO, Geneva, 2016).
4. IARC, "Some organophosphate insecticides and herbicides. Glyphosate (updated 11 August 2016)" (IARC Monographs on the Evaluation of Carcinogenic Risk to Humans, vol. 112, IARC, WHO, Lyon, France, 2017).
5. J. V. Tarazona *et al.*, *Arch. Toxicol.* **91**, 2723 (2017).
6. M. Cuhra *et al.*, *Front. Environ. Sci.* **4**, 28 (2016).
7. A. H. C. Van Bruggen *et al.*, *Sci. Total Environ.* **616–617**, 255 (2018).
8. http://ec.europa.eu/citizens-initiative/public/initiatives/successful/details/2017/000002
9. Communication from the Commission on the European Citizens' Initiative, C(2017) 8414, European Commission, Strasbourg, 2017; http://ec.europa.eu/food/sites/food/files/plant/docs/pesticides_glyphosate_eci_final.pdf.
10. R. Mesnage *et al.*, *Toxicology* **313**, 122 (2013).
11. L. Janssens, R. Stoks, *Aquat. Toxicol.* **193**, 210 (2017).
12. C. M. Benbrook, *Environ. Sci. Eur.* **28**, 3 (2016).
13. V. Silva *et al.*, *Sci. Total Environ.* **621**, 1352 (2018).
14. https://echa.europa.eu/support/socio-economic-analysis-in-reach
15. R. Brouwer *et al.*, *Regul. Toxicol. Pharmacol.* **68**, 438 (2014).
16. C. Graven *et al.*, "Estimation of the socio-economic consequences of regulatory measures on toxic substances in food. A proposed framework: SEATS" (RIVM Letter Report 2017-0079, National Institute for Public Health and the Environment, Bilthoven, Netherlands, 2018).
17. B. Url, *Nature* **553**, 381 (2018).

ACKNOWLEDGMENTS

The authors were not involved in glyphosate risk assessment nor have they any relations with parties in the debate described in this paper. N.M.v.S. is a member of the Netherlands Commission on Genetic Modification.

10.1126/science.aat0567

PLANETARY SCIENCE

Dunes across the Solar System

Despite a very thin atmosphere, dunes may form on Pluto

By **Alexander G. Hayes**

Before NASA's New Horizons mission, the surface of Pluto was shrouded in mystery. No one knew what to expect from its surface and most scientists shied away from detailed speculation, except to say that the one thing we should expect is to be surprised (*1*). On page 992 of this issue, Telfer *et al.* (*2*) present such a surprise by describing features interpreted as dunes on Pluto's surface.

An eloquent, although perhaps dour, summary of the pre–New Horizons view of Pluto was given by the amateur astronomer Sir Patrick Moore in his 1955 book, *Guide to the Planets*: "Beyond all doubt, Pluto is the loneliest and most isolated world in the Solar System—cut off from its fellows, plunged in everlasting dusk, silent, barren, and touched with the chill of death. Nature seems to have passed it by, and it can never have known the breath of life. It marks the frontier of the Sun's kingdom" (*3*).

Spacecraft Planetary Imaging Facility, Cornell University, 412 Space Science Building, Ithaca, NY 14853-6801, USA. Email: hayes@astro.cornell.edu

If Sir Patrick was with us today, New Horizons might have changed his opinion. Although Pluto is indeed isolated, nature has in no way passed it by. Images from New Horizons have revealed a geologically diverse and dynamic world driven by internal heat, extreme seasons, and sublimating ices (*4*). Rather than representing the end of the Sun's kingdom, Pluto perhaps represents the gateway to an unexplored realm where volatile ices (consisting, for example, of nitrogen, methane, ammonia, and carbon dioxide) dominate the landscapes of the dwarf planets and irregular bodies that make up the Kuiper Belt. New Horizons will provide a close-up view of this realm on New Year's Day 2019, when it passes within 3500 km of Kuiper Belt object 2014 MU69.

In the latest discovery from New Horizons, Telfer *et al.* describe a collection of regularly spaced, linear ridges on Pluto's surface. They interpret these ridges as transverse dunes of granular methane ice. The features are oriented orthogonal to dark wind streaks on Sputnik Planitia, a vast plain of nitrogen ice near Al-Idrisi Montes, a collection of large water-ice blocks with up to 5 km of relief. With this discov-

PHOTO: NASA/JOHNS HOPKINS UNIVERSITY APPLIED PHYSICS LABORATORY/SOUTHWEST RESEARCH INSTITUTE/ZL DOYLE

In this image of Pluto's surface, the red luminance corresponds to the infrared data acquired by the Ralph/MVIC instrument carried by New Horizons.

ery, Pluto joins Earth, Mars, Venus, Titan (a moon of Saturn), and perhaps even the comet 67P/Churyumov-Gerasimenko (*5*), demonstrating that the mobilization and self-organization of granular material into dunes occur throughout the Solar System (see the figure). What makes this discovery surprising is that the sediment can be mobilized despite Pluto's tenuous atmosphere, with a surface pressure (1 Pa) that is a factor of 100,000 times lower than that on Earth.

The processes by which grains are mobilized in a fluid medium have long been studied in both planetary science and terrestrial sedimentology. One of the earliest papers addressing this problem in a tenuous atmosphere was written in 1975 by Carl Sagan and Ralph Alger Bagnold, who investigated sediment transport on Mars (*6*). Despite the tremendous progress that has been made on the subject (*7*), many puzzles remain. Typical surface winds on Pluto are expected to be sufficient to transport particles once lofted, but even the strongest winds driven by interactions with the nearby Al-Idrisi Montes are not expected to be sufficient to begin lofting grains from rest.

To overcome this problem, Telfer *et al.* suggest that motion is initiated by the sublimation of nitrogen ice from Sputnik Planitia itself. The idea of sublimation-induced lofting has previously been proposed to explain the erosional CO_2 troughs that form spiderlike structures at the south pole of Mars (*8*) and the dark streaks on Neptune's moon Triton (*9*). In contrast to these previous studies, Telfer *et al.* intimately tie sublimation to dune formation in a tenuous atmosphere. If an extremely tenuous atmosphere like that of Pluto can support the generation of bedforms from wind-driven sediment, what kind of eolian activity might we see on places like Io (a moon of Jupiter) or Triton?

Despite vast differences in gravity, atmospheric pressure, and sediment type, windblown sand dunes on Earth, Mars, Venus (*10*), and Titan self-organize into remarkably similar landscape patterns (see the figure) (*11*). This property of dune pattern formation aided Telfer *et al.* and Jia *et al.* (*5*) in identifying candidate dunefields on Pluto and comet 67P, respectively. However, interpreting formative mechanisms and environmental conditions from well-organized patterns alone can be hazardous. Nature tends to converge toward a set of relatively few forms and generic patterns using a variety of processes (*12*). Accordingly, much work is left to do to understand dunes on Pluto. Most notably, it remains to be shown how high the dunes are, when they are most active, whether they change, and whether entrainment can occur without lofting (*5*).

Regardless, Telfer *et al.* convincingly argue that lofted granular material entrained in a flow will self-organize into patterns and—given the right flow regime, determined by the particle Reynolds number and Shields stress (*13*)—those patterns will be recognizable as dunes. With the requirements of a thicker atmosphere for dune formation relaxed, it is perhaps not that surprising that dunes appear throughout the Solar System, so long as there is sediment and a mechanism to mobilize it. ■

REFERENCES AND NOTES

1. J. M. Moore *et al.*, *Icarus* **246**, 65 (2015).
2. M. W. Telfer *et al.*, *Science* **360**, 992 (2018).
3. P. Moore, *Guide to the Planets* (Eyre & Spottiswoode, 1955), pp. 174–175.
4. S. A. Stern *et al.*, *Science* **350**, aad1815 (2015).
5. P. Jia, B. Andreotti, P. Claudin, *Proc. Natl. Acad. Sci. U.S.A.* **114**, 2509 (2017).
6. C. Sagan, R. A. Bagnold, *Icarus* **26**, 209 (1975).
7. R. D. Lorenz, J. R. Zimbelman, *Dune Worlds: How Windblown Sand Shapes Planetary Landscapes* (Springer, Berlin/Heidelberg, 2016).
8. S. Piqueux, S. Byrne, M. I. Richardson, *J. Geophys. Res. Planets* **108**, 5084 (2003).
9. C. Sagan, C. Chyba, *Nature* **346**, 546 (1990).
10. R. Greeley *et al.*, *J. Geophys. Res. Planets* **97**, 13319 (1992).
11. R. C. Ewing, A. G. Hayes, A. Lucas, *Nat. Geosci.* **8**, 15 (2015).
12. G. Nicolis, I. Prigogine, *Exploring Complexity: An Introduction* (Freeman, 1989).
13. M. P. Lamb, J. P. Grotzinger, J. B. Southard, N. J. Tosca, in *Sedimentary Geology of Mars*, J. P. Grotzinger, R. E. Milken, Eds. (SEPM special publication no. 102, Society for Sedimentary Geology, 2012), pp. 139–150.

ACKNOWLEDGMENTS

I am grateful to J. Moore, R. Lorenz, R. Ewing, and S. Birch for helpful discussions and insights during the preparation of this manuscript.

10.1126/science.aat7488

Dunes everywhere

Similar dune-like patterns have been found on Solar System bodies including planets, moons, and a comet that all have very different gravity, atmospheric pressures, and sediment types.

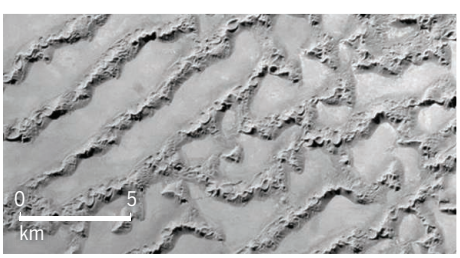

Linear star dunes formed by changing winds in the Rub' al Khali sand desert on the Arabian Peninsula.

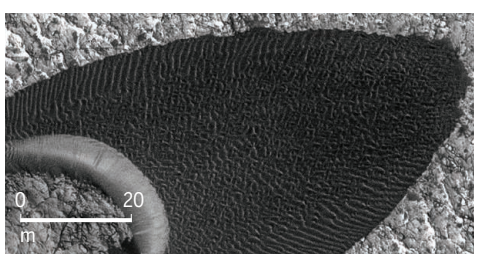

A crescent-shaped dune with wind ripples in Nili Patera, one of the most active dunefields on Mars.

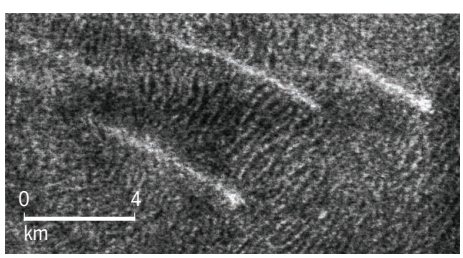

Slowly changing dunes formed by gentle surface winds in the Fortuna-Meshkenet dunefield on Venus.

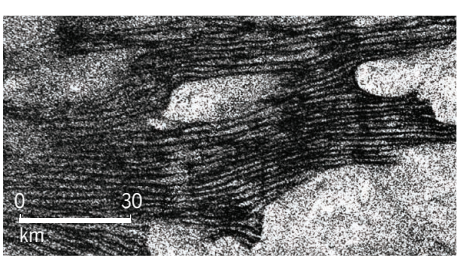

Linear dunes diverted around topographic features in the Belet dunefield on Titan, Saturn's largest moon.

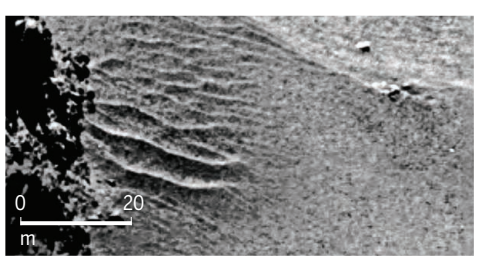

Dune-like patterns in the Hapi region of comet 67P/Churyumov-Gerasimenko created by thermal winds.

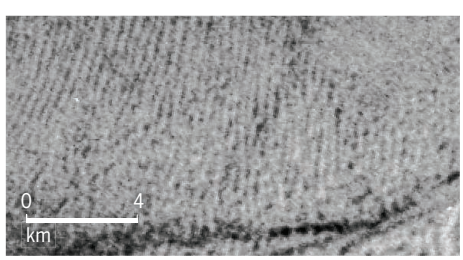

Surface features interpreted as dunes in Sputnik Planitia, a vast plain of nitrogen ice on Pluto.

PHOTOS: (CLOCKWISE FROM TOP LEFT) NASA; NASA/JPL/UNIVERSITY OF ARIZONA; GREELEY *ET AL.* (9); TELFER *ET AL.* (2); JIA *ET AL.* (4); NASA/JPL-CALTECH/ASI

CANCER METABOLISM

The nutrient environment affects therapy

Nutrient availability affects cancer cell metabolism and therapeutic responses

By **Alexander Muir**[1] *and* **Matthew G. Vander Heiden**[1,2]

Understanding the molecular basis of cancer has led to a revolution in how cancers are classified and treated. Subsets of patients benefit from precision-medicine drugs that target growth-promoting signaling networks, but not all cancer patients respond to these approaches (*1*). Precision medicine is largely built on the assumption that cancer cell–intrinsic factors, such as genetic mutations or epigenetic identity, determine which pathways and processes are required in cells and thus response to therapies. However, in many cases, the presence of particular genetic lesions is insufficient to identify patients that will respond to a drug (*1*). For instance, standard cell culture models have not identified the subsets of cancer patients that respond to most conventional chemotherapies (*1*). Nevertheless, these chemotherapy drugs remain standard of care for many cancers and, in some cases, contribute to curative regimens. Emerging data suggest that beyond cell-intrinsic factors, nutrient availability in the tumor microenvironment can also influence drug response. This highlights the importance of understanding the microenvironmental factors that dictate which cellular processes are essential for disease progression and ultimately how tumors respond to treatments that target these processes.

The success of conventional chemotherapy to treat patients with cancer argues that drugs that target cell metabolism and proliferative machinery, such as antimetabolite chemotherapy, can be effective. Recent efforts to target cancer metabolism have focused on how different cell-intrinsic factors such as oncogenic mutations rewire metabolism to require cells to use specific metabolic pathways and nutrients for growth and survival (*2*). There have been clinical successes from this approach, such as targeting mutant isocitrate dehydrogenases. However, the development of drugs that target enzymes in core metabolic pathways, such as those that metabolize glucose, has been challenging. Even though profound metabolic alterations are observed broadly in cancer, an inability to match the right patients with specific drugs has limited therapeutic development of new molecules that target metabolism.

Experiments in microorganisms have demonstrated that gene function and essentiality for proliferation and survival is largely environment dependent (*3*). That is, the availability of nutrients in the environment can affect whether microorganisms require certain genes to thrive. By extension, the tumor microenvironment may alter the essentiality of pathways in cancer cells and influence sensitivity to drugs ranging from classic chemotherapies to new, targeted agents (see the figure). Recent studies have demonstrated that microenvironmental factors have a profound influence on cancer cell metabolism and sensitivity to drugs that target metabolism. For example, biochemical analysis of both mouse and human tumors revealed different nutrient preferences for lung and brain tumors in vivo compared with cancer cells cultured from these tumors. In cultured lung and brain cancer cells, glutamine is used as a primary carbon source for metabolic pathways needed to synthesize macromolecules for growth, whereas glutamine catabolism can be less important in tumors formed from the same cells in mice (*2*). Furthermore, genetic screens of human cells in culture and in xenograft tumors have yielded discordant results with respect to metabolic gene essentiality (*4*), lending further support to the idea that cancer cells require different metabolic processes, depending on their microenvironment. The microenvironment can also affect drug response. For example, inhibitors of the enzyme glutaminase slow the proliferation of most cancer cells in culture, but this has not been predictive of tumor response to glutaminase inhibitors in either patients or mouse cancer models (*2*). Similarly, drugs targeting mammalian target of rapamycin (mTOR), a protein involved in nutrient sensing and metabolic regulation, are much more successful at limiting cell growth and proliferation in cultured cells than they are at slowing tumor growth in mouse cancer models and in patients (*5*). These observations argue that the tumor microenvironment affects cancer cell metabolism and can alter drug sensitivity.

> ***"...defining physiological levels of nutrients and how physiology constrains cell metabolic processes could lead to a better understanding of drug responses..."***

Standard cell culture models of cancer do not mimic the tumor microenvironment. One major difference between classical cell culture conditions, where most drugs are initially tested, and tumors is the level of available nutrients. Indeed, most culture media formulations were not intended to mimic tumor physiology but were instead derived from experiments to identify the minimal nutrients required to grow mammalian cells in culture dishes (*6*). Levels of oxygen, which affect cancer cell metabolism and therapy response, have long been appreciated to be nonphysiologically elevated in standard culture conditions (*7*). Concentrations of other nutrients are different in tumors in vivo than in standard culture media, which alters cell metabolism and affects therapy response. For example, glioblastoma cells cultured in media that contains nutrients at physiological levels found in blood rely, to a lesser extent, on glutamine consumption for proliferation than the same cells in standard culture media (*8*). Importantly, glioblastoma tumors in mouse models in vivo produce rather than catabolize glutamine, and this difference has been attributed to artificial nutrient levels in standard culture media creating a nonphysiological state with respect to glutamine metabolism. Similarly, culturing lung cancer cells in medium containing nutrients at physiological levels also reduces the dependence on glutamine catabolism and reproduces the lack of glutaminase inhibitor sensitivity observed in vivo (*9*). Many cell culture formulations contain high levels of the amino acid cystine, which drives glutamine catabolism and sensitivity to glutaminase inhibitors. Cancer cells in tumors are exposed to lower cystine levels, which explains at least in part why glutaminase inhibitors are less effective at slowing the growth of tumors in

[1]Koch Institute for Integrative Cancer Research and the Department of Biology, Massachusetts Institute of Technology, Cambridge, MA, USA. [2]Dana-Farber Cancer Institute, Boston, MA, USA. Email: mvh@mit.edu

mice derived from cells that are sensitive to these drugs in culture. Thus, nutrient levels are an important component of the tumor microenvironment that alters metabolism and drug responses.

Environmental nutrient levels can also alter the requirement for "recycling metabolism." In culture, intracellular protein recycling to obtain amino acids (*10*) and recapture of acetate from histone modifications (*11*) is dispensable for cancer cell proliferation, but both become required for tumor growth in vivo, where many nutrients are more limiting. Catabolism of extracellular protein can also be used by cells as a source of amino acids (*10*). Most media formulations are protein deficient, but otherwise amino acid rich, which may limit protein catabolism. However, cells grown with limiting amino acids but physiological levels of the protein albumin, the most abundant protein in blood and tissues, rely on albumin to obtain amino acids for growth (*5*). Interestingly, this switch in nutrient acquisition affects drug response. mTOR signaling promotes growth under amino acid replete conditions but constrains protein catabolism. Therefore, cells relying on extracellular protein catabolism for growth are resistant to mTOR inhibition (*5*). Thus, differences in amino acid acquisition between tumor cells and cells in culture may contribute to the limited efficacy of mTOR inhibitors in the clinic.

Cancer cells in tumors have access to nutrients that are not always added to standard cell culture media. For instance, the presence of uric acid, a nucleotide breakdown product found in vivo but absent from cell culture media, renders cells resistant to the pyrimidine analog and chemotherapeutic drug 5-fluorouracil, which is a standard treatment for many cancers (*12*). Furthermore, the addition of pyruvate to cell culture media alters the cellular redox state, which limits the ability of the antidiabetic drug metformin (which may also benefit some patients with cancer) to slow cancer cell proliferation (*13*). The altered sensitivity to these widely used drugs illustrates that microenvironmental nutrient levels can affect metabolic pathway use and response to metabolism-targeted therapy.

The tumor microenvironment also contains numerous cell types that can interact metabolically with cancer cells. Noncancer cells within a tumor can share metabolites with cancer cells, compete with cancer cells for nutrients, and provide signals that alter cancer cell metabolic pathway utilization. For example, competition between cancer cells and infiltrating lymphocytes for limited nutrients, and secretion of metabolic byproducts by cancer cells, can create an immunosuppressive microenvironment that limits antitumor immune responses (*14*). Thus, understanding the tumor microenvironment may even lead to improved therapies that control cancer via noncell autonomous mechanisms such as immunotherapy.

Relying on in vivo models to identify cancer targets is impractical, but current scalable ex vivo models are inaccurate with respect to microenvironment. Microenvironmental factors clearly alter drug responses, and differences in nutrient levels between tumors and normal tissues could even drive targetable liabilities of cancer cells. Different nutrient levels across tissues might also influence where specific cancers can thrive as metastases. Therefore, identifying how nutrients vary in tissue and tumor microenvironments and efforts to model this in tractable culture systems will be crucial to identify patients likely to respond to both existing and new drugs that target cancer processes, such as metabolism. Tumor nutrient levels also fluctuate both spatially and temporally within an individual tumor and could be affected by additional factors such as diet. This metabolic heterogeneity could be an important component of tumor heterogeneity that limits therapeutic effectiveness. Thus, defining physiological levels of nutrients and how physiology constrains cell metabolic processes could lead to a better understanding of drug responses and uncover new therapeutic opportunities. By combining knowledge of the nutritional microenvironment with models that consider other features of the tumor microenvironment, such as organoid culture, ex vivo models could be generated that might have better predictive power for drug response in patients with cancer, as well as with other diseases (*15*). Ultimately, redefining culture conditions to incorporate knowledge of the tumor microenvironment could transform our understanding of cell physiology and eliminate a bottleneck in identifying new cancer therapeutics. ■

The microenvironment influences phenotype

Cell-intrinsic factors, such as cell lineage and genetic mutations, define a metabolic network that the cell is capable of using. However, the way this network operates is constrained by available nutrients and stromal interactions in the microenvironment. Thus, identical cells in different metabolic microenvironments exhibit distinct metabolic programs and variation in phenotypes, such as drug response.

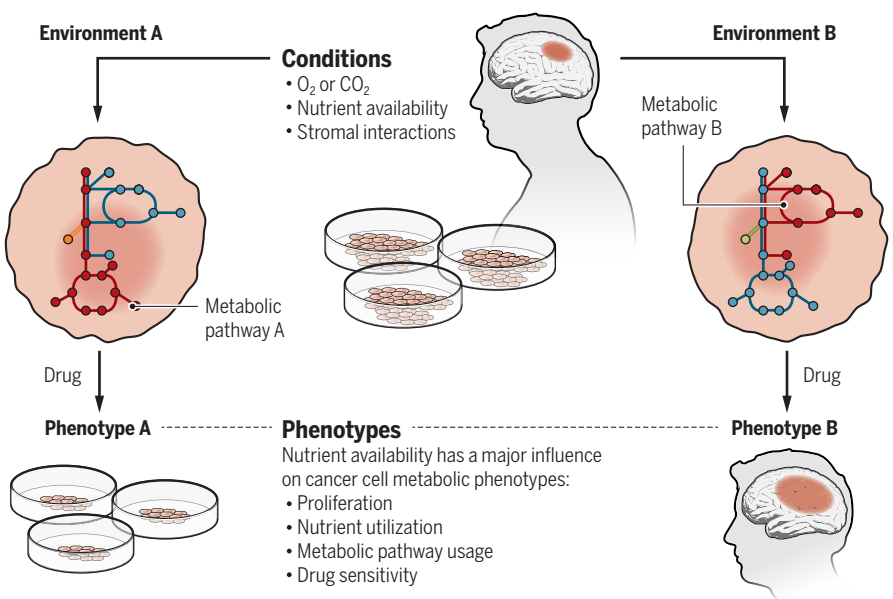

GRAPHIC: C. BICKEL/*SCIENCE*

REFERENCES AND NOTES

1. A. Letai, *Nat. Med.* **23**, 1028 (2017).
2. A. J. Wolpaw *et al.*, *Trends Cell Biol.* **28**, 201 (2018).
3. G. Rancati *et al.*, *Nat. Rev. Genet.* **19**, 34 (2018).
4. E. H. Yau *et al.*, *Cancer Res.* **77**, 6330 (2017).
5. W. Palm *et al.*, *Cell* **162**, 259 (2015).
6. H. Eagle, *Science* **122**, 501 (1955).
7. J. A. Bertout *et al.*, *Nat. Rev. Cancer* **8**, 967 (2008).
8. S. Tardito *et al.*, *Nat. Cell Biol.* **17**, 1556 (2015).
9. A. Muir *et al.*, *eLife* **6**, e27713 (2017).
10. R. Amaravadi *et al.*, *Genes Dev.* **30**, 1913 (2016).
11. Z. T. Schug *et al.*, *Nat. Rev. Cancer* **16**, 708 (2016).
12. J. R. Cantor *et al.*, *Cell* **169**, 258 (2017).
13. D. Y. Gui *et al.*, *Cell Metab.* **24**, 716 (2016).
14. M. D. Buck *et al.*, *Cell* **169**, 570 (2017).
15. P. Horvath *et al.*, *Nat. Rev. Drug Discov.* **15**, 751 (2016).

ACKNOWLEDGMENTS

The authors thank B. Bevis for assistance with the figure and acknowledge support from the Massachusetts Institute of Technology (MIT) Center for Precision Cancer Medicine, the Lustgarten Foundation, the Ludwig Center at MIT, SU2C, Howard Hughes Medical Institute, and the National Cancer Institute (F32CA213810 to A.M. and R01CA168653 to M.G.V.H.). M.G.V.H. is a consultant and scientific advisory board member for Agios Pharmaceuticals and Aeglea Biotherapeutics.

10.1126/science.aar5986

GENETICS

Ancient human genomes—keys to understanding our past

Ancient genomes from different times and continents are helping to understand past human migrations

By **Alessandro Achilli, Anna Olivieri, Ornella Semino, Antonio Torroni**

In 2000, when the term "archaeogenetics" (*1*) was initially proposed to describe the study of the human past by using the techniques of molecular genetics, ancient DNA studies were in their infancy. At that time, DNA data samples provided by geneticists to archaeologists, anthropologists, and linguists for archaeogenetic studies were almost entirely derived from living populations, with a few ancient DNA samples mainly restricted to mitochondrial DNA (mtDNA, or mitogenome). However, it was already clear that ancient DNA could play a much greater role once a number of major technical problems were resolved. Two studies in this issue exemplify the rapid progress that has been made since then. On page 1028, Ebenesersdóttir *et al.* (*2*) report the genomes of the first Icelanders, and on page 1024, Scheib *et al.* (*3*) use ancient Native American genomes to reconstruct the first phases of the human spread in the Americas.

In the early years of this century, no one anticipated the extent and speed at which ancient genomes and new inferences concerning prehistoric demographic events and historical accounts would be published. Moreover, ancient genomes are no longer retrieved solely from geographic regions with climate conditions that allow DNA to be well preserved, but are now recovered from sites all over the world. Today, we are in a second phase of the discipline initially baptized by Renfrew and Boyle (*1*), a phase that could be more accurately defined as the era of archaeogenomics, as exemplified by the two papers in this issue (*2*, *3*) and by other very recent studies (see the figure) (*4*, *5*).

The skeletal remains of a male (SSG-A3) with grave goods. This individual was a first-generation Icelandic settler estimated to have an equal mix of Norse and Gaelic ancestry.

THE POWER OF GENETIC DRIFT

Ebenesersdóttir *et al.* analyzed 27 genomes from skeletal remains excavated at multiple sites in Iceland. This European island was peopled in the second half of the 9th century by Vikings and their slaves who were mostly from Norway and the British-Irish Isles. The skeletal remains were selected for DNA studies because archaeological and radiocarbon dates indicated that they were from the earliest settlers of Iceland. The genomes show that first-generation settlers were mainly unmixed, coming from either Norse or Gaelic sources (see the photo). This finding was supported by the study of strontium 87 and 86 isotope ratios in the settlers' tooth enamel; these ratios reflect the place of childhood residence through diet.

Comparison with modern genomes yielded an unexpected finding. The ancient settlers' genomes are more similar to those of the modern populations of Scandinavia and the British-Irish Isles than those of modern Icelanders. This observation highlights the power of genetic drift on a population that, for almost the entire first millennium after its foundation, rarely counted more than 50,000 people.

ANCIENT GENOMES FROM AFRICA

In a recent study, van de Loosdrecht *et al.* (*4*) reported genomic data from seven individuals from Grotte des Pigeons near Taforalt in eastern Morocco. These individuals are associated with the Later Stone Age Iberomaurusian culture and lived between 15,100 and 13,900 years ago. Their genomes are the most ancient analyzed so far from Africa, a technical success that overcomes previous limitations in obtaining ancient DNA from tropical or subtropical regions. The most likely reason is that all Taforalt DNAs were extracted from petrous bones, where endogenous DNA is best preserved.

Comparison with genomes from other ancient samples and modern populations reveal three major ancestry components that best characterize the Taforalt genomes: early-Holocene Levantines (Natufians), West Africans, and East African hunter-gatherers (Hadza). The first component indicates an important pre-Neolithic genetic input from the Near East, whereas the other two indicate a substantial input from sub-Saharan Africa, a contribution that is much less evident in modern North Africans. No gene flow signals from Paleolithic Europeans were detected, directly and definitively refuting a previously proposed European origin for the Iberomaurusian culture.

As a single, maternally inherited locus, mtDNA often does not reflect the whole complexity of demographic events and is also particularly prone to genetic drift. However, after refinements in its evolution rate (*6*, *7*) and the nesting relationships within its phylogeny, mtDNA can now provide rather narrow time boundaries for dating specific demographic events. All seven Taforalt specimens belong to two North African branches (haplogroups) of the mtDNA tree: Six belong to mitochondrial haplogroup U6, and one belongs to M1. These two haplogroups are those proposed 12 years ago, on the basis of modern DNA data, as markers of an Upper Paleolithic migration from the Levant to North Africa (*8*). At least for U6, this is a scenario that the ancient mitogenomes from Taforalt (and elsewhere) now confirm.

MIGRATIONS OF THE FIRST AMERICANS

The first ancient human genome sequence was from a ~4000-year-old Paleo-Eskimo from Greenland (*9*). In 2015, Raghavan *et al.* reported 23 ancient genomes from North and South American individuals, dated to between 6000 and 200 years ago (*10*). Comparison with modern and other ancient genomes led to the conclusion that modern Amerindian and Athabaskan groups derive from a single source population that began to diversify ~13,000 years ago, when it split into two branches: a northern one now restricted to North America (Athapaskans and northern Amerindians) and a southern one that is now dispersed across North and South America. The latter also includes the

Dipartimento di Biologia e Biotecnologie, Università di Pavia, 27100 Pavia, Italy. Email: antonio.torroni@unipv.it

genome of Anzick-1, a Clovis-culture male infant from Montana dated at ~12,600 years ago. The split was considered to have most likely happened in lower-latitude North America (south of the Cordilleran and Laurentide ice sheets) rather than in eastern Beringia (Alaska).

Recently, the same group reported the genome from another infant, in this case a female from Upward Sun River, Alaska, dated at 11,500 years ago (*5*). Her genome belonged to a Beringian-specific ancient population that had diverged from the ancestors of Amerindians and Athapaskans between 22,000 and 18,100 years ago, showing that the ancestors of Native Americans were already differentiating during their stay in Beringia ("Beringian standstill"). More importantly, this infant Alaskan genome suggests that the split between the southern and northern branches occurred 17,500 to 14,600 years ago, rather than ~13,000 years ago as previously proposed. This date range is much more realistic in light of the age (≥14,500 years) of Monte Verde in southern Chile, the oldest known archaeological site in South America.

Scheib *et al.* have now sequenced an even larger number of genomes—91, including mitogenomes—from ancient Native American remains; only 27 of these remains were radiocarbon-dated, with ages ranging between 4800 and 200 years ago (*3*). They were mainly selected from the Channel Islands of California and from Southwestern Ontario. Both regions show signs of human occupation as early as 13,000 years ago, were never reached by the much more recent ancient Neo- and Paleo-Eskimo migrations, and were expected to provide a good representation of the southern and northern Native American branches.

Scheib *et al.* identified two distinct basal ancestries, ANC-A and ANC-B, which differentiated before the split between the northern and southern Native American branches. ANC-A is largely associated with the southern branch (and Anzick-1), whereas ANC-B reaches its maximum in the northern ancient Ontarians and modern Algonquians. However, both components are present and admixed in the ancient Californian populations as well as in present-day populations from Central and South America, including the Chilote and Huilliche, who show a very high ANC-B frequency despite living in Chile, not far from the Monte Verde site.

To explain these findings, the authors propose different models, which all assume an initial split between ANC-A and ANC-B south of the Cordilleran and Laurentide ice sheets (see the figure) and different possible merging points between the two derived groups either in North America (once or multiple times) or along the way to South America. However, they could not have begun to merge until a few thousand years after the split, taking into account that the differentiation of ANC-A and ANC-B was not a sudden process. Alternatively, the split may have occurred north of the ice sheets in Beringia, but in this case, ANC-A and ANC-B would have theoretically been susceptible to differential gene flow from other human groups in Beringia. Scheib *et al.* reject this possibility because the two ancestries do not differ significantly in their affinity to modern non-American populations, including Asians.

In their models, Scheib *et al.* do not exploit the mitogenome information that they obtained. For instance, the ancient Ontarians harbored mtDNA haplogroups X2a and C4c, which are currently found at high frequency among the Algonquian-speaking populations; they could thus be distinctive mitochondrial markers of ANC-B. In this view, the detection of an early offshoot of C4c in modern Colombians (*11*) is in full agreement with the scenario that ANC-B contributed to the shaping of South American genomes.

Given an upper boundary of 17,500 years ago for the split time between the southern and northern branches (*5*) and the requirement of a few thousand years of differentiation after the split (*3*), it may be time to reconsider an initial differentiation in Beringia. A reconsideration of the time and the place of the population split (see the figure) would also be compatible with the most recent archaeological findings in South America (*12*). However, a split in Beringia brings back the scenario of a dual entry into the American continent and thus the possibility that the two ancestries entered the Americas either at the same time or at different times, following the same or different routes (*13*–*15*).

Considering the rapid progression in the production of ancient genomes, their densities on geographical maps are expected to increase very rapidly. There is no doubt that these data will allow many long-lasting questions to be addressed, but it is likely that many others will arise. ■

Genome clues to ancient migrations

Three studies (*2*–*4*) illustrate the power of archaeogenomics to elucidate how modern humans moved and mixed as they populated the globe.

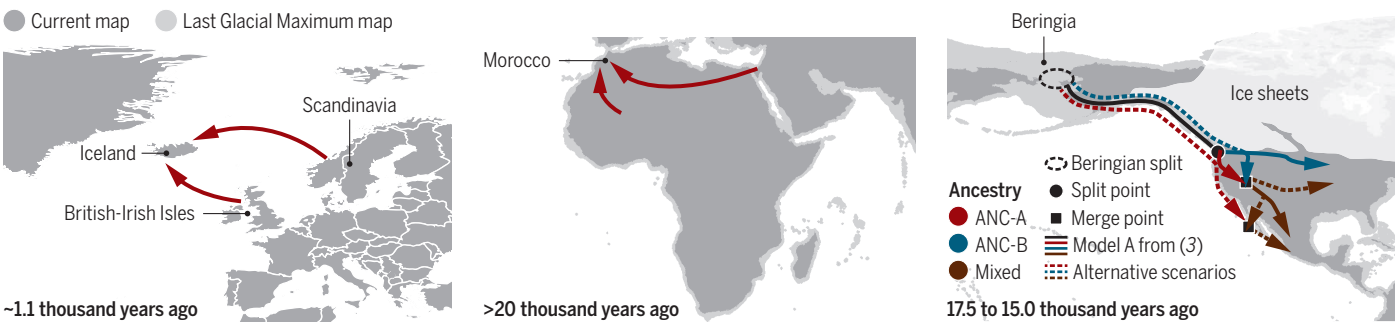

Iceland: The genomes of the earliest settlers more closely resemble those of modern inhabitants of Scandinavia and the British-Irish Isles than those of modern Icelanders.

North Africa: The ancestors of Late Stone Age people in Morocco came from the Near East and from sub-Saharan Africa, but not from Europe.

Americas: Ancient Native American genomes suggest different models of how populations may have split and merged during the initial settlement of the Americas.

GRAPHIC: J. YOU/*SCIENCE*

REFERENCES

1. A. C. Renfrew, K. V. Boyle, Eds., *Archaeogenetics: DNA and the population prehistory of Europe* (McDonald Institute for Archaeological Research, 2000).
2. S. S. Ebenesersdóttir *et al.*, *Science* **360**, 1028 (2018).
3. C. L. Scheib *et al.*, *Science* **360**, 1024 (2018).
4. M. van de Loosdrecht *et al.*, *Science* **360**, 548 (2018).
5. J. V. Moreno-Mayar *et al.*, *Nature* **553**, 203 (2018).
6. P. Soares *et al.*, *Am. J. Hum. Genet.* **84**, 740 (2009).
7. C. Posth *et al.*, *Curr. Biol.* **26**, 827 (2016).
8. A. Olivieri *et al.*, *Science* **314**, 1767 (2006).
9. M. Rasmussen *et al.*, *Nature* **463**, 757 (2010).
10. M. Raghavan *et al.*, *Science* **349**, eaab3884 (2015).
11. B. H. Kashani *et al.*, *Am. J. Phys. Anthropol.* **147**, 35 (2012).
12. T. J. Braje *et al.*, *Science* **358**, 592 (2017).
13. U. A. Perego *et al.*, *Curr. Biol.* **19**, 1 (2009).
14. A. Achilli *et al.*, *Proc. Natl. Acad. Sci. U.S.A.* **110**, 14308 (2013).
15. B. A. Potter *et al.*, *Science* **359**, 1224 (2018).

10.1126/science.aat7257

BIOMATERIALS

Neuromorphic circuits impart a sense of touch

Flexible organic transistors transmit force signals encoded for direct input to human neurons

By **Chiara Bartolozzi**

The sense of touch is the ability to perceive consistency, texture, and shape of objects that we manipulate, and the forces we exchange with them. Touch is a source of information that we effortlessly decode to smoothly and naturally grasp and manipulate objects, maintain our posture while walking, or avoid stumbling into obstacles, allowing us to plan, adapt, and correct actions in an ever-changing external world. As such, artificial devices, such as robots or prostheses, that aim to accomplish similar tasks must possess artificial tactile-sensing systems. On page 998 of this issue, Kim *et al.* (*1*) report on a "neuromorphic" tactile sensory system based on organic, flexible, electronic circuits that can measure the force applied on the sensing regions. The encoding of the signal is similar to that used by human nerves that are sensitive to tactile stimuli (mechanoreceptors), so the device outputs can substitute for them and communicate with other nerves (e.g., residual nerve fibers of amputees or motor neurons). The proposed system exploits organic electronics that allow for three-dimensional printing of flexible structures that conform to large curved surfaces, as required for placing sensors on robots (*2*) and prostheses.

The use of neuromorphic circuits—electronic circuits that work under principles similar to those of our nervous system—leads to better efficiency, compactness, and fault tolerance. The resulting devices can interpret the often-ambiguous and noisy sensory signals to gather information about their surroundings that is useful for providing sensory feedback to humans or robots. From those data, relevant information can be extracted to plan appropriate actions at an affordable computational cost and power budget (*3*).

The system devised by Kim *et al.* is based on the encoding of tactile stimuli with trains of digital pulses (spikes or action potentials) like those exchanged in neural systems. In the brain, diverse features of the spike train, including the spike rate and the precise temporal pattern of the spikes (*4*), encode stimulus properties and also the behavioral choices (*5*) associated with the stimulus itself. The neural code is at the same time rich and efficient, being an optimal choice to design artificial systems for sensing and perception. In this respect, Kim *et al.* add to the current state of the art by using a neural representation that efficiently encodes relevant stimulus characteristics, such as direction of motion, shape, texture, slip, and softness (*6*–*8*).

This contribution confirms the idea that a neuromorphic approach to the implementation of artificial tactile systems can be relevant in robotics (*9*), where tactile information can improve the interaction of the robot with objects. In this scenario, objects can be better recognized because touch complements the information gathered from vision about the shape of occluded or badly illuminated regions of the object, such as its texture or hardness (*10*). Tactile information also allows objects to be better manipulated—for example, by exploiting contact and slip detection to maintain a stable but gentle grasp of fragile or soft objects (see the photo).

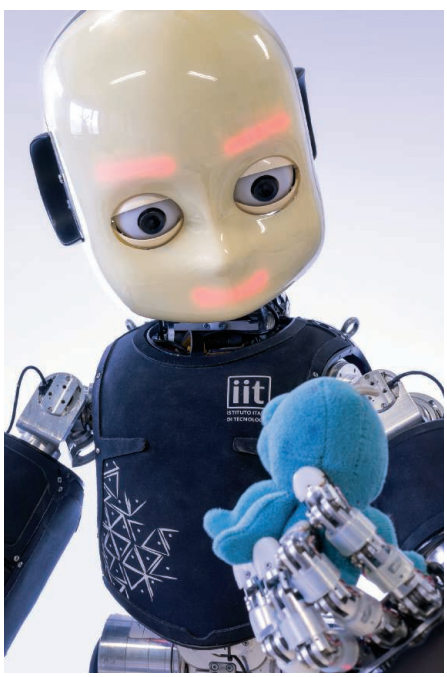

The iCub robot gently holds a soft toy. Tactile information is used for grasping, in-hand manipulation, shape exploration for object classification, safety, learning a body schema, obstacle avoidance, and for perceiving and counteracting perturbations for balancing.

This approach applies not only to autonomous robots, such as industrial manipulators and robot companions, that cooperate with humans in unstructured environments, but also to remotely operated robots. A notable example is surgical robots, where the surgeon must finely calibrate the force applied to the tip of the surgical robot. In this context, haptic feedback about tissue softness or hardness and texture can greatly help the surgeon improve the precision of the intervention and ease of use of the instrument.

Most important, natural haptic feedback can minimize the continuous visual attention required to successfully perform manipulation in upper-limb prosthetics. Patients wearing functional prosthetics that can be actuated to perform daily living activities need to constantly visually monitor the execution of their actions to successfully accomplish a task. An intuition of the required effort can be gathered when putting one's hands in an ice bucket for some minutes; the low temperature impairs our tactile sensors, and we have difficulty even just maintaining a stable grasp.

Information about shape, softness, slip, and contact forces also greatly improves the usability of upper-limb prosthetics in fine manipulation (*11*). The few devices equipped with tactile sensing focus on this aspect by adding sensors at the fingertips. The advantage of the technology devised by Kim *et al.* is the possibility of covering at a reasonable cost larger surfaces, such as fingers, palms, and the rest of the prosthetic device. Safety is enhanced when sensing contacts inform the wearer that the limb is encountering obstacles. The acceptability of the artificial hand by the wearer is also improved because the limb is perceived as part of the body, rather than as an external device. Lower-limb prostheses can take advantage of the same technology, which can also provide feedback about the distribution of the forces at the foot while walking.

The contribution of Kim *et al.* fits in the general effort of deploying neuromorphic technology in neuroprosthetics (*12*–*14*). The spikes emitted by the proposed artificial tactile sensor (neural afferent) were directly used to stimulate a biological neuron that elicits muscle contraction. This hybrid bio-

iCub Facility, Istituto Italiano di Tecnologia, Genova, Italy. Email: chiara.bartolozzi@iit.it

electronic proof of concept paves the way to the use of this technology to restore muscular activation, such as in foot drop (abnormal gait caused by nerve damage) or bladder dysfunction.

Important challenges lie ahead to translate this result to a breakthrough in the prosthetic (and robotic) domain. So far, each application has focused on a single dimension of the tactile stimulus, such as slip detection, texture, or shape, or direction-of-motion classification. The next generation of tactile sensory systems must integrate all of these to offer richer sensory information. The contribution of computational neuroscientists will be essential to this field in order to understand which feature of the neural code is related to each stimulus property and which neural architecture can support the encoding and decoding of such information.

In the proposed implementations, only one of the four types of mechanoreceptors of human glabrous skin has been emulated, and a single type of transduction is available in each system. These single types of transduction relate to both the physical transduction properties (capacitive, resistive, piezoelectric, optical, etc.) and the spiking behavior (e.g., fast with respect to slow-adapting receptors). The challenge will be to develop a hybrid system with transduction sites of different bandwidth, dynamic range, resolution, sensitivity, and mechanical characteristics, with the help of materials science, and to implement neural models that can take into account the different adaptation characteristics of skin receptors. The ultimate system will include temperature sensors and proprioception. ■

REFERENCES

1. Y. Kim *et al.*, *Science* **360**, 998 (2018).
2. C. Bartolozzi, L. Natale, F. Nori, G. Metta, *Nat. Mater.* **15**, 921 (2016).
3. C. Mead, *Proc. IEEE* **78**, 1629 (1990).
4. H. P. Saal, X. Wang, S. J. Bensmaia, *Curr. Opin. Neurobiol.* **40**, 142 (2016).
5. S. Panzeri, C. D. Harvey, E. Piasini, P. E. Latham, T. Fellin, *Neuron* **93**, 491 (2017).
6. K. E. Friedl, A. R. Voelker, A. Peer, C. Eliasmith, *IEEE Robot. Autom. Lett.* **1**, 516 (2016).
7. T.-S. Chou, L. D. Bucci, J. L. Krichmar, *Front. Neurorobot.* **9**, 6 (2015).
8. Z. Yi, Y. Zhang, J. Peters, *Sens. Actuators A Phys.* **255**, 46 (2017).
9. C. Bartolozzi *et al.*, in *IEEE/RSJ International Conference on Intelligent Robots and Systems (IROS)*, Vancouver, 2017, pp. 166–173.
10. M. Regoli, N. Jamali, G. Metta, L. Natale, in *2017 18th International Conference on Advanced Robotics (ICAR)*, Hong Kong, 2017, pp. 47–54.
11. D. W. Tan *et al.*, *Sci. Transl. Med.* **6**, 257ra138 (2014).
12. C. M. Oddo *et al.*, *eLife* **5**, e09148 (2016).
13. L. Osborn, R. R. Kaliki, A. B. Soares, N. V. Thakor, *IEEE Trans. Haptics* **9**, 196 (2016).
14. D. M. Rager *et al.*, in *35th Annual International Conference of the IEEE Engineering in Medicine and Biology Society (EMBS)*, 2013, pp. 5922–5925.

10.1126/science.aat3125

DEVELOPMENT

A new view of embryo development and regeneration

Transcriptome atlases of vertebrate embryos and regeneration enrich our understanding of development

By **Richard M. Harland**

Among the major milestones in developmental biology are those that authoritatively describe how cells differentiate during development. Conklin (*1*) described the mosaic development of marine invertebrates (sea squirt), in which specific and recognizable cells of the dividing embryo consistently produce specific tissues of the larva and naturally pigmented myoplasm segregates to the muscle lineage of the larva, supporting the idea of localized cytoplasmic determinants that influence cell fate. Later, lineage tracer dyes were used to track the fates of different regions in amphibian embryos (*2*). More recently, careful observation produced the triumph of a complete cell lineage map of the nematode worm (*Caenorhabditis elegans*) embryo (*3*). On pages 980, 979, and 981 of this issue, Briggs *et al.* (*4*), Farrell *et al.* (*5*), and Wagner *et al.* (*6*), respectively, as well as Fincher *et al.* (*7*) and Plass *et al.* (*8*), mark another innovation: a description of gene expression in all of the cells of fish and frog embryos (*4*–*6*) and in the adult regenerating planarian (flatworm) (*7*, *8*). These papers describe the transcriptional information that forms the blueprints of development and regeneration in these organisms.

Although we now understand many mechanisms underlying developmental decisions, such as the inheritance of localized RNAs or stereotypical arrangement of signaling and responding cells, there is still a great deal that we do not know; for example, experiments have sampled many important regulators of cell fate, but the complete set of transcripts that regulate cell fate decisions has been unattainable.

These studies demonstrate the power of single-cell RNA sequencing (scRNA-seq) in producing detailed and comprehensive plots of gene expression correlations with emerging cell fates. This technology has adapted previous single-cell microfluidics; the embryo is dissociated into single cells, each of which merges with a drop containing barcoded primers on a bead so that mRNA can be amplified for high-throughput sequencing of cDNA. For embryos, the dissociation and gentle handling of the large and delicate cells were a crucial advance in permitting the sequencing of enough cells to reconstruct gene expression in all cells, even in rare cells such as germ cells. The barcodes identify transcripts from the single cells they were extracted from, and similarities and differences in transcript composition sort the cells into clusters, representing states of differentiation.

Technically, it is a challenge to capture all the different transcripts from a single cell, so inevitably, some important transcripts can be missed. This technical limitation is further complicated by biological variation in gene expression between similar cells. Although the recovered population of transcripts is not comprehensive, it is good enough to recognize cells that are similar, or different, and cluster them accordingly. By analyzing cells from different embryonic stages, trajectories of differentiation can be reconstructed over time, because cells follow a progressive pathway of transcriptional changes as they differentiate. As cells become different, these paths branch to provide a molecular picture of emerging differentiation, and the transcripts that define the differences can be identified. Satisfyingly, the differences include ones that have been identified and characterized by previous methods. Reassuringly, the various computational approaches to clustering cell types provide consistent outcomes. Adding human annotation of the branches of differentiation, on the basis of known markers, superimposes them onto devel-

> ***"These papers describe the transcriptional information that forms the blueprints of development..."***

Department of Molecular and Cell Biology, University of California, Berkeley, Berkeley, CA 94720-3200, USA. Email: harland@berkeley.edu

opmental anatomy, providing a reconstruction of transcription in early embryos at the cellular level. This manual annotation can account for the loss of spatial information when the organism was dissociated and is complemented by a semiautomated approach (*5*).

The studies have developed impressive visualization tools that allow us to see how cells start to differentiate, and, after embarking on specific lineages, how cell fate is reinforced and specialized over time. Overall, the developing animals show an initial trunk of unresolved cell types, from which large branches and eventually "fine twigs" of specialization emerge. As the branches spread, the expression of known mRNAs confirms that cells are becoming restricted to specific fates. From these datasets, we can infer the progress of individual cells over time and some of the variation in routes that cells take toward the differentiated state. Although most branches become progressively divided, an exception occurs where two divergent branches from neural crest and pharyngeal arches coalesce again, consistent with the idea that neural crest cells adopt a fate appropriate to their local environment (*9*).

Importantly, the scRNA-seq data capture cells at branch points, a previously inaccessible cell state in which fate choices are made. Resolution of the decision shows which transcription factors are enriched and may determine cell fate. In most cases, it appears that decisions are binary, although there are examples where there is a choice between multiple fates. Specific cases document a mixed cell state, for example, in the choice between prechordal plate and notochord where a substantial fraction of cells appear bipotential, even after territories have been defined. Such cells must resolve their expression quickly to adopt the fate of their local community, or presumably be eliminated.

Apart from the amount of information to be digested from these transcriptome atlases, what other nuggets have emerged? The information enriches what we already know and additionally identifies transcripts that had not previously been associated with pathways of differentiation. The simultaneous expression of determinants for multiple lineages in individual cells has been documented for a few cell types (*10*) but is now documented for dozens of cell fate decisions. Examination of the transcription factors that are coexpressed at decision points will suggest new experiments on the cooperation between transcriptional regulators. Cells that appear to be superficially similar, coming from the same region of the embryo, may express nonoverlapping transcripts, indicating a fundamental heterogeneity in cell identity, something that has been difficult to establish by whole-tissue analysis.

The fish and frog have been extensively studied, so a lot of the information in these studies provides fine detail, but in an animal like the regenerating planarian, which has only recently become a standard model of regeneration and development, there are new cell types and developmental trajectories to be discovered. The analyses of the regenerating planarian highlights how scRNA-seq provides a fast start to establishing the molecular anatomy of the organism, including rare cell types, which will accelerate research in this and other new models.

The studies of Fincher *et al.* and Plass *et al.* on the regenerating planarian also illustrate, for a whole organism, what had been achieved in previous work on tissue renewal during homeostasis, where cells asynchronously differentiate from a variety of stem cell precursors. The clustering of progressive changes in transcripts allows the trajectories of differentiation from stem cells to be reconstructed in "pseudotime." In these cases, they describe trajectories from neoblasts (stem cells) that describe the development of the entire organism.

Where is this scRNA-seq technique leading? The studies of zebrafish embryogenesis by Farrell *et al.* and Wagner *et al.* show that, in principle, scRNA-seq is a rapid assay to understand the phenotypes of mutants, with loss of Chordin, a bone morphogenetic protein antagonist, or loss of Nodal signaling. Previous work is confirmed, and the additional observation that the alteration of signaling does not cause formation of any new cell types, but instead alters the proportions of cell types that would develop in the wild-type animal, is provided. This technique is currently prohibitively expensive for routine use, but, just as genotyping by DNA sequencing has largely replaced laborious genetic mapping, so too might scRNA-seq provide a more cost-effective approach to understanding complex phenotypes than multiple rounds of hypotheses and experiments. The comparison of transcriptomes also highlights similarities and differences in distantly related species such as bony fish (zebrafish) and frogs that will lead to analysis of how different cell types may have evolved from common ancestors.

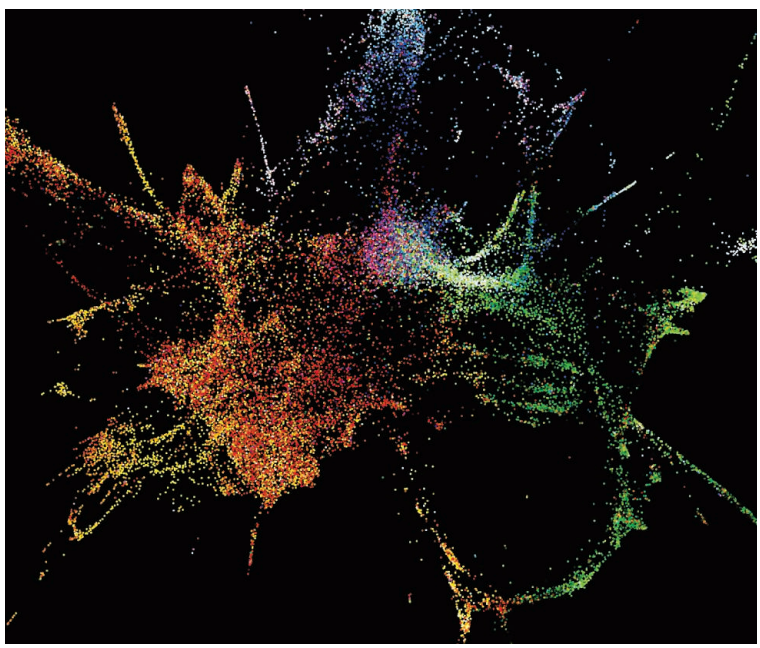

The gene expression landscape of a developing zebrafish embryo is visualized. Dots represent snapshots of individual cell states measured by scRNA-seq during the first day of development. Cells of the early embryo are at the center, with differentiating cells radiating along branches to form neural (red), epidermal (blue), and mesendodermal (green) tissues.

Just as the emergence of genomic information forced communities to join together to annotate genomes, there is tremendous benefit to annotating developmental processes and search for new insights and discoveries as a community. Now that these data are available, the door to imagining new uses is wide open. ■

REFERENCES

1. E. G. Conklin, *The Organization and Cell-Lineage of the Ascidian Egg* (Academy of Natural Sciences of Philadelphia, 1905).
2. W. Vogt, *Wilhelm Roux Arch. Entwickl. Mech. Org.* **120**, 384 (1929).
3. J. E. Sulston *et al.*, *Dev. Biol.* **56**, 110 (1977).
4. J. A. Briggs *et al.*, *Science* **360**, eaar5780 (2018).
5. J. A. Farrell *et al.*, *Science* **360**, eaar3131 (2018).
6. D. E. Wagner *et al.*, *Science* **360**, 981 (2018).
7. C. T. Fincher *et al.*, *Science* **360**, eaaq1736 (2018).
8. M. Plass *et al.*, *Science* **360**, eaaq1723 (2018).
9. P. A. Trainor *et al.*, *Nat. Rev. Neurosci.* **1**, 116 (2000).
10. R. A. Nimmo *et al.*, *Trends Cell Biol.* **25**, 459 (2015).

10.1126/science.aat8413

POLICY FORUM

GRADUATE EDUCATION

Student-centered, modernized graduate STEM education

Rebalance incentives to promote culture change

By **Alan I. Leshner**

The U.S. graduate education system for science technology, engineering, and mathematics (STEM) is widely regarded as among the best in the world. However, evolution in the structure and functioning of the U.S. graduate education system is lagging ongoing changes in the broader scientific enterprise, in the requirements of employers, in the demographics of the student population, and, particularly, in their career ambitions. In response to these disconnects, the U.S. National Academies of Sciences, Engineering, and Medicine (NASEM) recently released a report (*1*) that lays out a vision of an ideal modern graduate education in any STEM field and a comprehensive plan to achieve that vision. The report emphasizes core competencies that all students should acquire, a rebalancing of incentives to better reward faculty teaching and mentoring of students, increased empowerment of graduate students, and the need for the system to better monitor and adapt to changing conditions over time. Although these issues have been raised in the past, and some institutions have taken positive steps, graduate students are still too often seen as being primarily sources of inexpensive skilled labor for teaching undergraduates and for performing research. Graduate students should demand the kind of education outlined in the report.

There have been many other reports on graduate education produced by various groups since the National Academies' last comprehensive report on this subject in 1995 (*2*), and some of their recommendations have been similar to those in the new report. Yet the system still lags modern trends and needs. For example, most students now pursue nonacademic careers, yet many institutions train them, basically, in the same way that they have for 100 years, to become academic researchers (*3*). Numerous surveys of employers and students suggest that many graduate programs are not preparing students adequately to succeed in a variety of careers; employers are finding many recent graduates overly naïve about research and development activities in government and industry.

What is special about this latest report that makes one expect anything different will happen? First, the report lays out a systems approach to modernizing graduate education, emphasizing the need for coordinated action on the part of every stakeholder (including students, faculty, universities, government agencies and other funders, and employers). Second, the report lays out a vision of an ideal 21st-century graduate STEM education, emphasizing the need for the system to become much more student-centered. Importantly, the report recognizes that achieving its goals will entail substantial cultural change throughout the system and identifies key leverage points, particularly the incentive system that drives much of academic culture.

High-quality advising and mentoring are essential for student success in graduate school.

A 21ST-CENTURY IDEAL

The model proposed in this report builds on the strengths of the current approach that have made U.S. graduate education so effective and attractive to students throughout the world but offers ways to make it more relevant to the needs of a very diverse student population, to prospective employers, and to broader society. Central to the ideal is for every student to achieve a set of core competencies that are the essence of being a master's or doctoral level STEM professional. Achieving those competencies would ensure that students have acquired broad technical literacy as well as deep specialization in an area of interest. Students would acquire both an understanding of and ability to apply the ethics and norms of the scientific enterprise and to communicate findings to colleagues and the public.

In the ideal, all prospective graduate students would be provided fully transparent, easily accessible data about career pathways and successes of previous students, so they can make more informed choices about whether and where to go to graduate school. Moreover, students from all backgrounds would be encouraged and better enabled to participate fully and achieve their greatest potential in STEM fields in diverse, equitable, and inclusive environments. Students would be encouraged and given time and resources to explore a broad range of career options, through courses, seminars, internships, or other real-life experiences. Institutions would provide faculty with training and resources to improve their skills as advisers and mentors. Departments and programs would help students identify advisers and mentors who can best support their academic and career development, and students would be encouraged to sample multiple research groups and faculty styles before settling on a group in which to focus. They would have experiences working across disciplines and in teams. And students would be provided opportunities to communicate their work to both professional and public audiences and to understand the broader impacts of their research.

Some universities now offer some or all of these kinds of experiences, and some disciplines have moved further in this direction

Chief Executive Officer Emeritus, American Association for the Advancement of Science, Washington, DC, USA. Former Executive Publisher, Science, Washington, DC, USA. Email: alan.i.leshner@gmail.com

than others. But this modern approach is far from universal. It should become the norm. If we do not make needed changes, we risk weakening the ability of our programs to attract the best and brightest students both domestically and internationally.

EFFECTING CHANGE

The proposed changes are not trivial and will require substantial attitudinal, behavioral, and cultural adjustments throughout the graduate education system. The entire system must become more student-centric. It must increase the value it places on high-quality teaching, mentoring, and advising students. The mindset that often stigmatizes students with nonacademic research career goals needs to adjust to the reality of the 21st century, where most students do not pursue academic careers but will still contribute importantly in other sectors. The report lays out an action plan that includes steps to be taken by every stakeholder; success in modernizing the system requires that everyone does his or her part.

Central to the success of this plan will be a readjustment of the incentives that drive so many attitudes and behaviors throughout the graduate education system. Those incentives currently are heavily weighted toward rewarding research productivity in the form of numbers of grants received, papers published, and future academic researchers produced. Although those metrics should remain important for some purposes, more weight needs to be given to providing quality graduate education and mentoring if the other recommended changes are to happen.

An essential step in rebalancing the academic incentive system and, in turn, faculty behavior will be changes in federal, state, and private granting-agency funding policies, at a minimum in those cases where graduate education is being supported either directly or indirectly. As currently structured, funding criteria for training grants or for supporting graduate assistants on research grants typically emphasize traditional measures of research productivity and the numbers of academic researchers being produced, but place much less emphasis on the quality of teaching and mentorship that students receive. Those criteria need to be rebalanced to give more weight to quality educational experiences that will benefit students no matter their career aspirations.

The fact that some government agencies are already using funding policies to help shape graduate education is cause for optimism that this approach can be effective. For example, funding of training by all seven of the United Kingdom's research councils (*4*) includes policies to stimulate changes in the graduate education paradigm, many in directions consistent with the NASEM report's recommendations. For example, the new U.K. funding criteria include quality of both mentoring and career advising. Similar requirements are in place for institutional graduate training grants issued by the U.S. National Institutes of Health's National Institute of General Medical Sciences (*5*). Both are relatively new policy initiatives and are somewhat controversial, because their implementation will inevitably incur some financial and human resource costs. It will take some time before it is clear whether they are effective in leading cultural change. Other examples include certain grants from the U.S. National Science Foundation (NSF) that require mentoring plans for postdoctoral researchers (*6*), which might provide models for similar policies at the graduate student level.

The U.S. Congress can play an important role by advocating for these kinds of funding policy changes in both its authorizing and appropriation processes for federal research and development agencies. Those kinds of congressional actions (*7*) helped seed cultural change concerning the adoption and use of NSF's "broader impacts" project review criterion. Adding that criterion was influential in ensuring that NSF grantees more seriously considered the consequences of their projects beyond the narrow limits of their work (*8*).

Once funding criteria are rebalanced, it will be much more likely that there is a similar rebalancing of incentives in other components of the system, such as academic promotion and tenure policies. And when those incentives are adjusted to give greater weight to quality graduate education and mentoring, it will be much easier to make many of the other changes recommended in the report.

But funding policy changes alone cannot produce all the changes needed in the graduate education paradigm. To achieve its vision, the NASEM report specifies a detailed action plan, with explicit steps to be taken by each stakeholder. For example, although the details of implementation will vary according to local contexts, higher education institutions, their graduate schools, departments, and faculty will have to ensure that they provide a truly inclusive and equitable environment to attract students from diverse backgrounds and enable them to achieve their full potentials. They will have to develop and provide training opportunities for new faculty and refresher courses for established faculty in mentoring. They will have to work actively to reduce the stigma that students frequently report they experience if they are not interested in pursuing academic careers.

Prospective industry, nonprofit, government, and other employers should provide internships and course offerings to enable graduate students to become familiar with and facilitate their transition into nonacademic careers.

COSTS, BENEFITS, AND CONCLUSIONS

The changes recommended in the NASEM report span the entire U.S. graduate education system. The recommendations will not be universally popular nor necessarily easy to implement. They will require courage, leadership, commitment, and persistence. In addition to considerable policy changes on the part of the institutions that fund academia, success in modernizing the system will require changes in the way faculty and academic administrators view their roles and will alter to some degree the way they spend their time. Fortunately, many universities are already moving in these directions, and some academic leadership organizations have been working to tackle many of the same issues with the same goals and similar recommendations in mind. Their initiatives, one hopes, will help lead the way toward the needed system changes.

Modernizing graduate STEM education will inevitably incur some additional costs, in both financial and human resource terms. Those costs have at times been used as an excuse not to make the needed changes, many of which were recommended in earlier studies of graduate education but not implemented across the system. But such investments will likely pay off in the long term in more satisfied students and in a better-educated, modern workforce in the expanding array of sectors of society where STEM professionals work. ■

REFERENCES AND NOTES

1. National Academies of Sciences, Engineering, and Medicine, *Graduate STEM education for the 21st century* (NASEM, Washington, DC, 2018).
2. Institute of Medicine, National Academy of Sciences, and National Academy of Engineering, *Reshaping the graduate education of scientists and engineers* (IOM, Washington, DC, 1995).
3. National Science Foundation (2018); https://nsf.gov/statistics/2018/nsb20181/assets/968/tables/tt05-12.pdf.
4. Research Councils UK (2016); https://www.ukri.org/files/legacy/skills/statementofexpectation-revisedseptember2016v2-pdf.
5. National Institute of General Medical Sciences (2017); www.nigms.nih.gov/training/instpredoc/documents/ABRCMS.pdf.
6. National Science Foundation (2018); https://www.nsf.gov/pubs/policydocs/pappg18_1/nsf18_1.pdf.
7. U.S. Congress, Public Law 111-358 (2011); https://www.gpo.gov/fdsys/pkg/PLAW-111publ358/pdf/PLAW-111publ358.pdf.
8. National Science Foundation (2011); https://nsf.gov/nsb/publications/2011/nsb1211.pdf.

ACKNOWLEDGMENTS

The author, who chaired the committee responsible for (*1*), thanks its members: S. Black, M. S. Coleman, J. Curtis-Fisk, K. Gibbs Jr., M. Grasso, S. Mason, M. Maxon, S. Ortega, C. Ortiz, M. Roberts, H. Sauermann, B. Schaal, S. Singhal, K. Stoll, J. Tien, K. Yamamoto, and NASEM study director L. Scherer. The opinions expressed here are solely those of the author and do not necessarily reflect views of the committee members or NASEM.

10.1126/science.aau0590

BOOKS *et al.*

MARINE BIOLOGY

The accessible predator

Bloodthirsty murderers no more, captive killer whales helped to transform the species's reputation

By **Robin W. Baird**

Killer whales, also known as orcas, are idolized, loved, and even revered. Such sentiments, however, have not always been held toward this species, as historian Jason Colby reveals in his new book, *Orca*.

From the 1940s into the 1960s, killer whales were often depicted as a menace to the rest of the ocean's inhabitants, as well as to humans. The belief that they were a competitor for fish, for example, led local fishermen and U.S. soldiers with machine guns to kill hundreds of killer whales off the coast of Iceland in a single expedition in 1954.

As recently as 1983, fishermen in British Columbia were shooting killer whales. By that time, however, researchers and whale-watching operators in the area were horrified by such incidents, as the whales under attack were well known to both communities. This change in attitudes, Colby convincingly argues, largely came about because killer whales were brought into captivity starting in the mid-1960s.

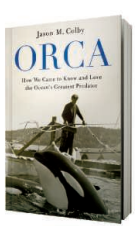

Orca
How We Came to Know and Love the Ocean's Greatest Predator
Jason M. Colby
Oxford University Press, 2018. 404 pp.

Ted Griffin, an entrepreneur who established the Seattle Marine Aquarium, would become the first person to swim and perform with a captive killer whale. Griffin purchased the killer whale Namu, named after his capture location in British Columbia, and displayed the whale on the Seattle waterfront beginning in 1965. Griffin's account of "making friends" with Namu, published in *National Geographic* in 1966, helped rapidly change human attitudes toward killer whales.

Colby notes that over a 5-year period, about 20 million people viewed killer whales captured by Griffin. "To be sure, many visitors came away from such exhibits with misgivings about captivity, but most left more likely to view cetaceans as individuals and to care about the fate of whales in the wild."

Colby does an excellent job of framing these events within the larger environmental movement of the time, as well as placing them within the context of the nationalism that was spreading on both sides of the U.S.-Canadian border at the time. (Frustrated by the sale of a Canadian-caught killer whale to an American marine park in 1965, the manager of Victoria's Pacific Undersea Gardens lamented, "It seems that every time we get something good … it gets funneled off to the U.S.")

We aren't inclined to protect that with which we have no experience, observed David Attenborough.

Perhaps more than any other individual, Griffin's early efforts to capture and display killer whales led to the burgeoning of live-capture fisheries. But the methods employed to capture live killer whales, which often occurred in plain sight of local residents, could be violent and disturbing. The use of explosive "seal bombs" (loud noisemakers normally used to drive seals away from fishing grounds), the practice of chasing whales into narrow inlets, and the inevitable deaths (and subsequent cover-ups) of some of the whales involved resulted in a tremendous backlash. Within a span of 7 years, Griffin went from being "fêted by politicians, courted by Hollywood, and consulted by the Pentagon" to being "villainized by journalists, harassed by activists, and alienated from the region he had helped change."

This backlash, along with growing concern that this poorly understood whale population was not being well managed in captivity, led to public pressure to enact legislation to restrict whale capture and killing. "'Only the Vietnam War generated more protest letters to the White House in the early 1970s than did whaling,'" notes historian Kurkpatrick Dorsey.

In 1971, the Canadian marine biologist Michael Bigg began tracking wild killer whale populations (individual whales were identified from photographs that revealed distinctive features—e.g., notches in the dorsal fin or color patterns on the skin) and studying their social organization and life history. Before Bigg's efforts—with the exception of Clifford Carl's attempt to follow the movements of a single white killer whale in the 1940s and 1950s—killer whales were assumed to be indistinguishable from one another, and the population in the Pacific Northwest was thought to number in the thousands.

It was soon revealed, however, that most of the whales captured or killed during live capture's heyday came from what we now know as the fish-eating southern "resident" population, a community numbering just over a hundred individuals at the time of the start of the capture operations. Live captures reduced the population to about 70 individuals, and the captures of young females and juveniles would limit its recovery for many years.

Today the population is endangered, jeopardized not by removal of individuals for captivity but by degradation of their environment and reduction of their prey base. With only ourselves to blame, do we still "care enough to save them?" asks Colby in the book's closing pages. ■

10.1126/science.aat7051

The reviewer is at the Cascadia Research Collective, Olympia, WA 98501, USA, and is the author of Killer Whales of the World: Natural History and Conservation *(Voyageur Press, Minneapolis, MN, 2002). Email: rwbaird@cascadiaresearch.org*

MICROBIOLOGY

Probing the microbial

A wide-ranging text synthesizes what we know (and don't know) about the microbiome

Fundamentals of Microbiome Science
How Microbes Shape Animal Biology
Angela E. Douglas
Princeton University Press, 2018. 246 pp.

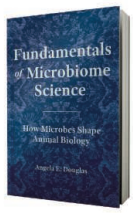

By **Fernando E. Vega**

Angela Douglas is an internationally recognized expert on symbiosis, with a number of foundational texts to her name (*1*, *2*). In her new book, *Fundamentals of Microbiome Science*, Douglas synthetizes data from the burgeoning field of microbiome science in eight highly informative chapters. Topics include the origins of the animal microbiome, what we know about the microbiome's interactions with the immune system, hints at how microbes drive animal behavior, and how the gut microbiota are involved in gut-brain communication. The book also clearly delineates the influence of the microbiome in determining human health and disease.

The microbiome revolution is expanding at breakneck speed and moving from "the study of correlation to causation and mechanism." For example, mice lacking the leptin gene, which regulates satiety, consume more food and become obese. When the microbiota of obese mice are transferred to lean mice, the mice eventually become obese.

The reciprocal mechanisms involved in the interactions between the immune system and the microbiota are just beginning to be understood. In mammals, for example, the production of immunoglobulin A prevents contact of the microbiota with the epithelial cells of the gut, thus impeding microbe access to internal organs. Other innate immune effectors, including antimicrobial peptides, lectins, and certain enzymes, complement this effect, but many other factors (e.g., age of host, sex, and genotype) could also influence the outcome. The immune system can thus promote, tolerate, or inhibit the composition of the microbiota. In contrast, the microbiota can "promote or dampen immune system function," and the effects of microbial products on the regulation of immune effectors have been implicated in this process.

The book includes interesting studies on how the microbiome might influence complex processes, including circadian rhythms (e.g., the sleep-wake cycle), and mental health. One particularly interesting example is the possible involvement of *Bifidobacterium infantis* in mental health and, specifically, in the reduction of anxiety. When germ-free mice were subjected to restraint stress, their plasma titers of corticosterone and adrenocorticotropic hormone (stress hormones) increased, compared with conventional mice. The significantly higher titers were reversed when the germ-free mice were given *B. infantis*.

Grooming partners influence the gut microbiome of Amboseli baboons.

The microbiota have also been shown to influence animal communication and feeding behavior. Volatile carboxylic acids, for example, are known to emanate from the anal glands of many carnivorous mammals. These volatiles are the fermentation products of the microbiota that inhabit the glands and "play important roles in the social interactions of these mammals, including individual and group identity, territory marking, and recognition of mate and offspring."

Douglas discusses how signaling molecules produced by microbes may represent a possible mechanism in the regulation of feeding behavior but cautions that the current data are "far from conclusive." Similarly, she reveals that, although possible, "there is no definitive evidence" showing that the microbiota regulate the production of feeding regulatory molecules in the host. This kind of tempered analysis is one of the many strengths of this book.

In the final chapter, Douglas delves into some interesting and provocative topics and brings to the forefront the need to reframe our understanding of animals. Here, she includes a discussion of climate change and its potential effects on microbiota. A widely reported consequence of climate change is an increased range for animals into higher elevations and higher latitudes. How, Douglas wonders, will microbiota acquired in these new environments influence animals? This is an area in which "data are almost entirely lacking."

For many years, I have studied the microbiota of coffee plants and of the coffee berry borer, a small bark beetle considered the most important insect pest of coffee worldwide. Reading Douglas's book resulted in a cavalcade of new research ideas, an effect I have only very rarely experienced while reading scientific literature. How did the coffee berry borer and its microbiota coevolve? How does the insect acquire these bacteria and pass them on to its progeny? How do the microbiota differ between insects in cooler versus warmer coffee-growing areas?

Douglas has an encyclopedic knowledge of microbial systems, their ecology, and their metabolic functions with which she explains complex physiological mechanisms and identifies important research gaps. A summary at the end of each chapter succinctly recaps the preceding material, and 440 highly useful (but unobtrusive) references direct readers to the primary literature on which Douglas has based her claims. Dozens of figures elaborate on the complex concepts discussed in the text.

Overall, reading this book is a most satisfying intellectual feast. ■

The reviewer is at the Sustainable Perennial Crops Laboratory, U.S. Department of Agriculture, Agricultural Research Service, Beltsville, MD 20705, USA. Email: fernando.vega@ars.usda.gov

REFERENCES

1. A. Douglas. *Symbiotic Interactions* (Oxford University Press, Oxford, 1994).
2. A. Douglas. *The Symbiotic Habit* (Princeton University Press, Princeton, NJ, 2010).

10.1126/science.aat8572

Neonicotinoids threaten aquatic insects, such as this mayfly, as well as species that rely on them for food.

PHOTO: ISTOCKPHOTO.COM/HEKAKOSKINEN

Edited by **Jennifer Sills**

Call to restrict neonicotinoids

Neonicotinoids are the most widely used insecticides in the world (*1*). They are applied to a broad range of food, energy, and ornamental crops, and used in domestic pest control (*2*). Because they are neurotoxins, they are highly toxic to insects (*2*), a group of organisms that contains the majority of the described life on Earth, and which includes numerous species of vital importance to humans such as pollinators and predators of pests (*3*). Neonicotinoids have proved to be highly persistent in the environment, such that substantial residues are commonly found in soils, wildflowers, streams, and lakes (*4*). One recent study found neonicotinoids in 75% of honey samples collected from around the world (*5*). Hundreds of independent scientific studies have been performed to assess their impacts on beneficial organisms such as bees, aquatic insects, butterflies, and predatory beetles (*4*, *6*).

It is the view of the undersigned scientists that the balance of evidence strongly suggests that these chemicals are harming beneficial insects and contributing to the current massive loss of global biodiversity. As such, there is an immediate need for national and international agreements to greatly restrict their use, and to prevent registration of similarly harmful agrochemicals in the future. On 28 April, the European Parliament voted for a complete and permanent ban on all outdoor uses of the three most commonly used neonicotinoid pesticides (*7*). With the partial exception of the province of Ontario, Canada (*8*), governments elsewhere have failed to take action.

Failure to respond urgently to this issue risks not only the continued decline in abundance and diversity of many beneficial insects, but also the loss of the services they provide and a substantial fraction of the biodiversity heritage of future generations.

Dave Goulson and 232 signatories*
School of Life Sciences, University of Sussex, Falmer, Brighton, BN1 9QH, UK. Email: d.goulson@sussex.ac.uk
*The full list of signatories is available online.

REFERENCES

1. P. Jeschke *et al.*, *J. Ag. Food Chem.* **59**, 2897 (2011).
2. N. Simon-Delso *et al.*, *Environ. Sci. Pollut. Res.* **22**, 5 (2015).
3. J. A. Noriega *et al.*, *Basic Appl. Ecol.* **26**, 8 (2018).
4. T. Wood, D. Goulson, *Environ. Sci. Poll. Res.* **24**, 17285 (2017).
5. E. A. D. Mitchell *et al.*, *Science* **358**, 109 (2017).
6. L. Pisa *et al.*, *Environ. Sci. Poll. Res.* **22**, 68 (2015).
7. D. Butler, *Nature*, 10.1038/d41586-018-04987-4 (2018).
8. Government of Ontario, "Neonicotinoid regulations: What you need to know about the new regulations that govern selling neonicotinoid-treated corn and soybean seed" (2017); www.ontario.ca/page/neonicotinoid-regulations.

SUPPLEMENTARY MATERIAL

Full list of signatories
www.sciencemag.org/content/360/6392/973.1/suppl/DC1

10.1126/science.aau0432

U.S. budget targets fish and wildlife work

In 1935, embracing the principle that science should serve as the basis of federal wildlife policy, the U.S. Geological Survey (USGS) established the Cooperative Fish and Wildlife Research Unit Program (*1*). The Cooperative Research Units (CRUs) facilitate research among natural resource agencies and universities to inform decisions on how to manage millions of acres of land nationwide. The work of CRU scientists has helped guide hundreds of natural resource management decisions. Most recently, it has informed energy exploration on the Colorado Plateau and offshore areas of Alaska, a decision not to list the Sonoran desert tortoise as endangered, strategies to manage the Klamath River Basin to sustain its Chinook salmon, and surveillance of deer to prevent the spread of chronic wasting disease (*2*). Despite the CRUs' measurable successes, the Trump Administration's proposed FY 2019 federal budget—the starting point for the budget that will take effect on 1 October—calls for the program's elimination, closing 40 units in 38 states and terminating more than 700 projects (*3*). If implemented, the proposed budget cut would have a dire effect on research and academic jobs, the U.S. economy, and the preservation of the country's flora and fauna.

University and state agency support, facilitated by CRUs, multiply the return on the USGS's modest investment in this wildlife science. Federal withdrawal of CRU funding would dissolve partnerships that provide office space, courtesy faculty appointments for unit leaders, access to graduate students, and state funding for CRU research that informs management of public lands. Because the faculty who lead the CRU research are USGS employees, withdrawal of federal funding support would result in the termination of faculty members scattered across 38 states and essentially shut down all the research projects they lead or oversee.

Hunting, fishing, and other outdoor recreation generate annual sales of $887 billion, support 7.6 million American jobs, and contribute $65.3 billion in federal tax revenue (*4*). This economic engine is fueled in large part by the science that CRUs provide to state and federal agencies. Such research allows these agencies to manage the conservation and protection of the wondrous natural settings on which current and future generations of hunters, fishers, hikers, and campers depend. With the closure of the CRU program, we discard one of the most powerful tools we have for the long-term sustainability of the industries that rely on the responsible management of our natural resources.

The loss of the CRU program would put U.S. ecosystems and species at risk. These cuts would halt research on some of the nation's most iconic species: elk, moose, mountain lion, turkey, and largemouth bass (*5*). Science provided by CRUs also underpins decisions to classify species' status (*2*), allowing for appropriate protection measures to be taken.

The American Fisheries Society and The Wildlife Society have sent a joint letter of concern to the U.S. Senate, explaining that the demise of CRUs would substantially reduce the ability to manage the nation's fish and wildlife resources (*6*). I urge legislators and policy-makers to reject the administration's proposal and instead to fully fund the CRUs.

Jack M. Payne
University of Florida Institute of Food and Agricultural Sciences, Gainesville, FL 32611, USA.
Email: jackpayne@ufl.edu

REFERENCES

1. W. R. Goforth, "The Cooperative Fish and Wildlife Research Units Program—Serving the nation since 1935 (U.S. Geological Survey, Reston, VA, 2006), p. 5.
2. National Cooperators' Coalition, "Funding crisis for USGS Cooperative Research Units affects state, federal, and university fish and wildlife conservation partners" (2018); https://fisheries.org/wp-content/uploads/2018/03/NCC-Talking-Points-USGS-Coop-Research-Units-8Feb2018-Final.pdf.
3. American Fisheries Society, "President's budget eliminates funding for Cooperative Units" (2018); https://fisheries.org/2018/03/presidents-budget-eliminates-funding-for-cooperative-units/.
4. Outdoor Industry Association, "The Outdoor Recreation Economy" (Outdoor Industry Association, Boulder, CO, 2017), p. 2.
5. J. F. Organ, J. D. Thompson, E. D. Dennerline, D. E. Childs, "Cooperative Fish and Wildlife Research Units Program, 2017 year in review" (U.S. Department of the Interior, U.S. Geological Service, Reston, VA, 2018), pp. 13, 15, 16, 27, 38, 46.
6. American Fisheries Society, "Senate letter requesting full funding for USGS Cooperative Research Units (2017); https://fisheries.org/2017/09/senate-letter-requesting-full-funding-for-usgs-cooperative-research-units/.

10.1126/science.aat9562

A Taiwanese student explores the properties of tough gels.

PHOTO: DR DAVE WARREN, UNIVERSITY OF OTAGO

OUTSIDE THE TOWER

Science transcends cultures in Taiwan

As my co-instructor, Sam, waxes lyrical about tough gels, I survey the hall: The timid faces of 144 of the brightest students in Taiwan look back at us, uncertain of what to expect. It's very different from the lively atmosphere we are accustomed to in New Zealand classrooms.

Our team has traveled 10,000 km to participate in the Madame Curie Senior High School Chemistry Camp (*1*). I have longed to bring the science-through-play ideals of our outreach program to the students of my home country. Many Taiwanese students grow up under immense academic pressure and rarely get to experience hands-on or carefree childhood activities. Today we intend to change that.

"It's just for fun, so don't worry about getting everything right. Prepare to get messy!" I repeat Sam's words and sentiment in Mandarin, and then the students begin experimenting with PVA/borax slime, modified using cornstarch to simulate a tough gel. Reserved smiles turn into joyous laughter as the slime stretches and dribbles off their fingers. The ice is broken! We move on to some "real" chemistry: measuring stretch in nano-clay composite tough gel samples. In this make-shift venue, the perceived formality of science in laboratories has been stripped away as we showcase Sam's research.

Play first; measurements later. We elected to reverse the usual order of experiments because, even more so than Kiwi kids, these students needed a fun and relaxed environment to facilitate engagement. Working with an understanding of their culture and language, we were able to show them that science is everywhere, and that anyone can do it and have fun along the way.

Jacqueline Kao[1]* and Sam P. H. Sutherland[2]
[1]Science Knowledge Ltd., Taipei 11444, Taiwan. [2]Department of Chemistry, University of Otago, Dunedin, 9010, New Zealand.
*Corresponding author. Email: scienceknowledgeltd@gmail.com

REFERENCE

1. Science Knowledge Ltd, "Otago Chemistry Outreach at Madame Curie Senior High School Chemistry Camp!" (2018); www.youtube.com/watch?v=V2c5w4o48_w&feature=youtu.be.

10.1126/science.aat6407

RESEARCH

Building an artificial sensory nerve

Kim et al., *p. 998*

IN *SCIENCE* JOURNALS

Edited by **Caroline Ash**

Seeds of the small mustard plant *Arabidopsis thaliana* in their pod

PLANT SCIENCE

Controls on seed dormancy

Herbivores and an inopportune cold snap can destroy fragile plant seedlings. Plants control the dormancy of their seeds in anticipation of more favorable growth conditions. Chen and Penfield analyzed the molecular controls on seed dormancy in the model plant *Arabidopsis thaliana*. Two genes and an antisense RNA, known from the process of vernalization, integrate ambient temperature to control seed dormancy via their opposing configurations. —PJH

Science, this issue p. 1014

SUSTAINABILITY

The global impacts of food production

Food is produced and processed by millions of farmers and intermediaries globally, with substantial associated environmental costs. Given the heterogeneity of producers, what is the best way to reduce food's environmental impacts? Poore and Nemecek consolidated data on the multiple environmental impacts of ~38,000 farms producing 40 different agricultural goods around the world in a meta-analysis comparing various types of food production systems. The environmental cost of producing the same goods can be highly variable. However, this heterogeneity creates opportunities to target the small numbers of producers that have the most impact. —AMS

Science, this issue p. 987

EVOLUTION

Predation favors the unadventurous

Selection is likely to shape behavior by acting on behavioral differences between individuals. Testing this idea has been challenging. Lapiedra *et al.* took advantage of a chain of small islands in the Caribbean colonized by anole lizards. A series of repeated behavioral selection experiments were set up in which brown anole populations were established with and without predators. On predator-free islands, animals that were more exploratory were favored, whereas when predators were present, less adventurous animals survived better. Selection for behavior occurred simultaneously with morphological selection but was predominant when predators were present. —SNV

Science, this issue p. 1017

The Caribbean brown anole lizard, *Anolis sagrei*

INDUCED SEISMICITY

Triggering quakes in a geothermal space

Enhanced geothermal systems (EGSs) provide a potentially clean and abundant energy source. However, two magnitude-5 earthquakes recently occurred in South Korea during EGS site development. Grigoli *et al*. and Kim *et al*. present seismic and geophysical evidence that may implicate the second of these earthquakes, which occurred in Pohang, as an induced event. The combination of data from a local

Published by AAAS

seismometer network, well logs, satellite observations, teleseismic waveform analysis, and stress modeling leads to the assessment that the earthquake was probably or almost certainly anthropogenically induced. The possibility remains that the earthquake occurred coincidentally at the EGS site location, but the aftershock distribution and other lines of evidence are concerning for future development of this geothermal resource. —BG

Science, this issue p. 1003, p. 1007

POLITICAL SCIENCE

Curtailed conversations

Most articles written about U.S. politics in the past few years have mentioned the increasing polarization of the electorate. But is this real, or does it merely reflect the increasing polarization of the media? Chen and Rohla estimate that in 2016, Thanksgiving dinners in which the hosts and guests lived in oppositely voting precincts were up to 50 minutes shorter than same-party-precinct dinners. That is, family members, adjured to avoid talking about contentious subjects, may have simply talked less. —AMS and GJC

Science, this issue p. 1020

ORGANIC CHEMISTRY

Arenes get a light boost onto copper

Insertion of palladium into an aryl halide bond is the first step in numerous variants of cross-coupling chemistry used to make carbon-carbon bonds. Copper is an appealing alternative catalyst for such reactions because of its abundance and downstream reactivity profile. However, this preliminary step, termed oxidative addition, is often prohibitively slow for the cheaper metal. Le *et al*. report a photocatalytic way around this problem. A photoredox catalyst paired with a silane can activate aryl bromides to react with copper, likely via aryl radicals. The copper in this case then catalyzes trifluoromethylation of the arenes. —JSY

Science, this issue p. 1010

NEUROPROSTHETICS

A leg up for neuroprosthetics

Amputation severs bone, nerves, and muscles needed for limb movement, limiting an amputee's ability to sense and control a prosthesis. Clites *et al.* tested autologous muscle-nerve interfaces made at the time of below-knee amputation in a human subject. In comparison with traditional amputations, the subject who received myoneural interfaces in his residuum (which were connected via synthetic electrodes to his powered prosthesis) had better control during stair walking. This person noted little delay between intention and movement of his prosthesis and expressed a strong sense that the prosthesis was part of him. —CC

Sci. Transl. Med. **10**, eaap8373 (2018).

IMMUNE REGULATION

Unexpected basophil activation

Basophils are granulocytes that exist at a relatively rare frequency in the blood but are critical mediators of allergic and inflammatory responses. Regulatory T cells (T_{regs}) suppress the functions of different immune cells. Sharma *et al*. examined how T_{regs} regulate basophil functions. Unexpectedly, resting human basophils were activated and not suppressed in the presence of T_{regs}. The activated basophils expressed activation markers—CD69, CD203c, and CD13—and released interleukin-4 (IL-4), IL-8, and IL-13. T_{reg}-induced activation of basophils involved IL-3 and STAT5 but was not contact-dependent. These counterintuitive results showing activation mediated by T_{regs} provide insight into how basophils are regulated. —CNF

Sci. Immunol. **3**, eaan0829 (2018).

IN OTHER JOURNALS

Edited by **Sacha Vignieri** *and* **Jesse Smith**

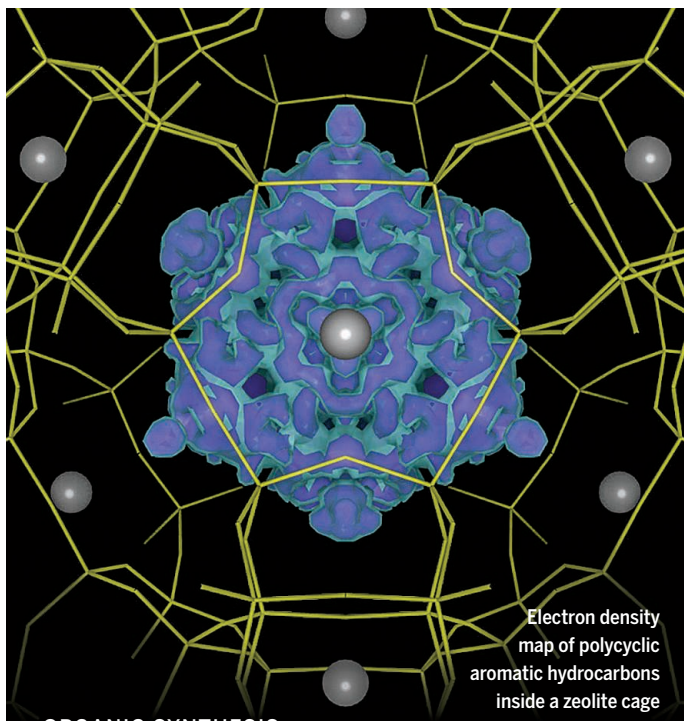

Electron density map of polycyclic aromatic hydrocarbons inside a zeolite cage

ORGANIC SYNTHESIS

Acetylene in, PAHs out

Polyaromatic hydrocarbons (PAHs) are attractive for optoelectronics applications, but their synthesis can be challenging. Solution routes tend to have low yields, and high-temperature vacuum pyrolysis (~1000°C) generates numerous carbonaceous side products. Ko *et al.* synthesized PAHs by polymerizing acetylene in Ca^{2+} ion–exchanged Linde type-A zeolites at ~400°C. The Ca^{2+} ions appear to lower the barrier for carbon-carbon bond formation. The PAHs remained trapped in the α-cages of the zeolite but were recovered after dissolving the zeolite with acid. The product mixture exhibited white fluorescence in N-methylpyrrolidone solution. Column chromatography separation isolated violet, blue, green, and orange emitters, with coronene being the main component of the blue emitter.—PDS

J. Am. Chem. Soc. 10.1021/jacs.8b00900 (2018).

NEURODEGENERATION

Keeping stress granules in check

Stress granules are membraneless organelles composed of RNAs and proteins that can accumulate in the presence of potentially pathogenic proteins. These include proteins linked to neurodegenerative disorders such as C9-ALS/FTD (amyotrophic lateral sclerosis and frontotemporal dementia linked to C9ORF72). The pathomechanisms of these same disorders can involve disruption of nucleocytoplasmic transport. Zhang *et al*. found that a variety of components of the nuclear import machinery were sequestered in stress granules, which reduced nucleocytoplasmic transport. Inhibiting stress granule assembly suppressed these transport defects in cells,

CREDIT: S. H. KO *ET AL*., *J. AM. CHEM. SOC.* 10.1021/JACS.8B00900 (2018)

A Cretaceous mammal shows signs of island-related adaptation.

VERTEBRATE PALEONTOLOGY

Island life

Among modern faunas, a well-established phenomenon occurs as species evolve to live on islands. Specifically, many species undergo dwarfism and other related changes after island colonization, likely owing to resource limitation and restriction of landscapes. Csiki-Sava *et al.* describe a multituberculate mammal from a Cretaceous island in Romania that displays several unusual traits, notably a reduced brain size and domed skull. The authors argue that these changes reflect adaptation to the island habitat of this group and, further, that a small brain (relative to body size) may be a previously undescribed adaptation to insular living. —SNV

Proc. Natl. Acad. Sci. U.S.A. 10.1073/pnas.1801143115 (2018).

and it also interfered with the neurodegeneration process in patient-derived iPS (induced pluripotent stem cell–derived) motor neurons and in a fly C9-ALS disease model system. —SMH

Cell **173**, 958 (2018).

HOST DEFENSE

Bacteria restricted via C3-mediated autophagy

The complement system has several important host-defense functions. Complement component C3, for example, can enhance phagocytosis, contribute to the bactericidal membrane attack complex, and initiate adaptive immune responses against invading microorganisms. Sorbara *et al*. uncovered another mechanism by which C3 can control pathogens. They observed interactions between the autophagy protein ATG16L1 and C3. In opsonized intracellular bacteria such as *Listeria*, this resulted in increased targeting to the autophagy system (xenophagy) and, in turn, greater autophagy-dependent growth restriction. Certain intracellular bacteria, such as *Shigella* and *Salmonella*, were able to escape C3-mediated targeting via the omptin proteases IcsP and PgtE, which cleave complement components including C3. Mouse models reveal that C3-mediated autophagy-dependent restriction may be important in protecting host mucosal tissues during the early stages of *Listeria* infection. —STS

Cell Host Microbe **23**, 644 (2018).

POLYMER COLLOIDS

Structured in a flash

Block copolymers will assemble into a range of complex structures driven both by thermodynamics, as defined by the chemical makeup of the blocks, and by the kinetics of the chain motion. When formed into sheets, these structures can range from those with regular periodicity to those with complex, tortuous, random interconnected phases. Grundy *et al.* developed a scalable process in which a feed stream containing polymers in a solvent contacts a counterstream based on a poor solvent for the polymers, which causes the polymers to precipitate out. Depending on the choice of polymers, one can get anything from simple Janus particles or layered ones to far more complicated, internally structured particles made by kinetic trapping of nonequilibrium phases. —MSL

ACS Nano 10.1021/acsnano.8b01260 (2018).

EDUCATION

A (dis)course in postdoc identities

Adapting postdoctoral training to include the development of skills that are translatable to careers outside of the laboratory is critical for diversifying the STEM (science, technology, engineering, and mathematics) workforce. We do not know much about the scientific identities of postdoctoral researchers (postdocs), which could ultimately limit their understanding of additional STEM career opportunities. Price *et al.* interviewed 30 postdocs to better understand how their scientific identities influenced their career goals. Using discourse analysis, the research team categorized two primary scientific identities among the postdocs: (i) bench scientists, who implement the scientific visions of others, and (ii) principal investigators, who formulate their own scientific visions. A further understanding of how these identities develop is essential for implementing better professional development programs for postdocs as they embark on scientific careers. —MMc

CBE Life Sci. Educ. 10.1187/cbe.17-08-0177 (2018).

NEUROSCIENCE

Overcoming working memory limitations

The capacity of our working memory is limited. We normally do not notice these limitations because we use a repertoire of behavioral strategies to overcome them. To investigate how these high-level strategies interact with working memory, Chiang and Wallis trained rhesus macaques to perform a search task and recorded from neurons in their lateral prefrontal cortex. Individual neurons encoded the location of the current search target, as well as the location of other targets several steps earlier or later in the search sequence. Both upcoming targets and previously visited targets were encoded well above chance. However, lateral prefrontal cortical neurons were more likely to encode upcoming targets. Macaques spontaneously used behavioral strategies that helped them solve the task; this improved their performance while simultaneously reducing the neuronal load required. —PRS

Proc. Natl. Acad. Sci. U.S.A. **115**, 5010 (2018).

PHOTO: ROB CRANDALL/A LAMY STOCK PHOTO

ALSO IN *SCIENCE* JOURNALS

Edited by **Caroline Ash**

SINGLE-CELL ANALYSIS

Mapping the vertebrate developmental landscape

As embryos develop, numerous cell types with distinct functions and morphologies arise from pluripotent cells. Three research groups have used single-cell RNA sequencing to analyze the transcriptional changes accompanying development of vertebrate embryos (see the Perspective by Harland). Wagner *et al*. sequenced the transcriptomes of more than 90,000 cells throughout zebrafish development to reveal how cells differentiate during axis patterning, germ layer formation, and early organogenesis. Farrell *et al*. profiled the transcriptomes of tens of thousands of embryonic cells and applied a computational approach to construct a branching tree describing the transcriptional trajectories that lead to 25 distinct zebrafish cell types. The branching tree revealed how cells change their gene expression as they become more and more specialized. Briggs *et al*. examined whole frog embryos, spanning zygotic genome activation through early organogenesis, to map cell states and differentiation across all cell lineages over time. These data and approaches pave the way for the comprehensive reconstruction of transcriptional trajectories during development. —BAP

Science, this issue p. 981, p. 979, p. 980; see also p. 967

PLANETARY SCIENCE

Methane ice dunes on Pluto

Wind-blown sand or ice dunes are known on Earth, Mars, Venus, Titan, and comet 67P/Churyumov-Gerasimenko. Telfer *et al*. used images taken by the New Horizons spacecraft to identify dunes in the Sputnik Planitia region on Pluto (see the Perspective by Hayes). Modeling shows that these dunes could be formed by sand-sized grains of solid methane ice transported in typical Pluto winds. The methane grains could have been lofted into the atmosphere by the melting of surrounding nitrogen ice or blown down from nearby mountains. Understanding how dunes form under Pluto conditions will help with interpreting similar features found elsewhere in the solar system. —KTS

Science, this issue p. 992; see also p. 960

BIOMATERIALS

I've got a feeling

Sensory (or afferent) nerves bring sensations of touch, pain, or temperature variation to the central nervous system and brain. Using the tools and materials of organic electronics, Kim *et al*. combined a pressure sensor, a ring oscillator, and an ion gel–gated transistor to form an artificial mechanoreceptor (see the Perspective by Bartolozzi). The combination allows for the sensing of multiple pressure inputs, which can be converted into a sensor signal and used to drive the motion of a cockroach leg in an oscillatory pattern. —MSL

Science, this issue p. 998; see also p. 966

HUMAN EVOLUTION

Founder effects in modern populations

The genomes of ancient humans can reveal patterns of early human migration (see the Perspective by Achilli *et al*.). Iceland has a genetically distinct population, despite relatively recent settlement (~1100 years ago). Ebenesersdóttir *et al*. examined the genomes of ancient Icelandic people, dating to near the colonization of Iceland, and compared them with modern-day Icelandic populations. The ancient DNA revealed that the founders had Gaelic and Norse origins. Genetic drift since the initial settlement has left modern Icelanders with allele frequencies that are distinctive, although still skewed toward those of their Norse founders. Scheib *et al*. sequenced ancient genomes from the Channel Islands of California, USA, and Ontario, Canada. The ancient Ontario population was similar to other ancient North Americans, as well as to modern Algonquian-speaking Native Americans. In contrast, the California individuals were more like groups that now live in Mexico and South America. It appears that a genetic split and population isolation likely occurred during the Ice Age, but the peoples remixed at a later date. —LMZ

Science, this issue p. 1028, p. 1024; see also p. 964

PESTICIDES AND SOCIETY

Glyphosate: Menace or savior?

The herbicide glyphosate is used in numerous products, including Roundup, to kill weeds that compete with crops and to dry out crops, making them easier to harvest. In a Perspective, van Straalen and Legler highlight the recent decision by the European Union to reapprove glyphosate for another 5 years. Although several assessments have concluded that glyphosate does not pose a danger to humans at the concentrations typically encountered, these assessments do not account for the combinatorial effects of other chemicals in the herbicide products. Because little is known about how glyphosate affects ecosystems, increasing its use is worrisome. Societal concerns about reliance on pesticides need to be considered through socioeconomic impact analysis as part of the decision-making process. —JFU

Science, this issue p. 958

CANCER METABOLISM

Metabolic plasticity foils drug development

The metabolism of cancer cells is increasingly being targeted in drug development, but the results in patients are not always consistent with preclinical models. In a Perspective, Muir and Vander Heiden discuss the importance of nutrient availability in the microenvironment as a determinant of responses to drugs that target metabolism and how metabolic targets in cancer cells might be identified more effectively. —GKA

Science, this issue p. 962

ECOLOGY

Reducing bycatch while sustaining harvests

Reducing bycatch—the capture of nontarget marine species—remains challenging for global fisheries, which provide essential sources of protein for billions of people. Even in well-managed fisheries, the ensnaring of species such as turtles, seabirds, and sharks is a problem. For many species, the solutions used to mitigate bycatch have not been successful. Focusing on the California drift gillnet fishery, Hazen *et al*. developed a multispecies ocean management approach that combines several types of historical data on multiple species' movement to predict daily catch. With this tool, they discovered that operating the California drift gillnet fishery on the basis of daily oceanographic conditions, instead of more static approaches based on rigid boundaries, could greatly reduce bycatch while maintaining fish harvests. —PJB

Sci. Adv. 10.1126/sciadv.aar3001 (2018).

ACTUATORS

Strength and stability through opposition

Biohybrid robots that combine living muscles with synthetic skeletons can be limited in their utility by the muscles spontaneously shrinking over time. Morimoto *et al.* used antagonistic pairs of skeletal muscle tissues to prevent this shrinkage and extend the robot's life span. They attached myoblast-laden hydrogel sheets to both sides of a jointed resin skeleton; the sheets formed into antagonistic muscles after 10 days of culture. The resulting robot achieved large actuation over a long lifetime and used finger-like movements to pick and place a ring onto a pillar. —RLK

Sci. Robot. **3**, eaat4440 (2018).

RESEARCH ARTICLE SUMMARY

SINGLE-CELL ANALYSIS

Single-cell reconstruction of developmental trajectories during zebrafish embryogenesis

Jeffrey A. Farrell,* Yiqun Wang,* Samantha J. Riesenfeld, Karthik Shekhar, Aviv Regev,† Alexander F. Schier†

INTRODUCTION: During embryogenesis, pluripotent cells gradually become specialized and acquire distinct functions and morphologies. Because much of the specification process is controlled through changes in gene expression, the identification of the transcriptional trajectories underlying cell fate acquisition is paramount to understanding and manipulating development.

RATIONALE: Traditional approaches have studied specific fate decisions by analyzing the transcription of a few selected marker genes or by profiling isolated, predefined cell populations. The advent of large-scale single-cell RNA sequencing (scRNA-seq) provides the means to comprehensively define the gene expression states of all embryonic cells as they acquire their fates. This technology raises the possibility of identifying the molecular trajectories that describe cell fate specification by sampling densely during embryogenesis and connecting the transcriptomes of cells that have similar gene expression profiles. However, the numerous transcriptional states and branch points, as well as the asynchrony in developmental processes, pose major challenges to the computational reconstruction of developmental trajectories from scRNA-seq data.

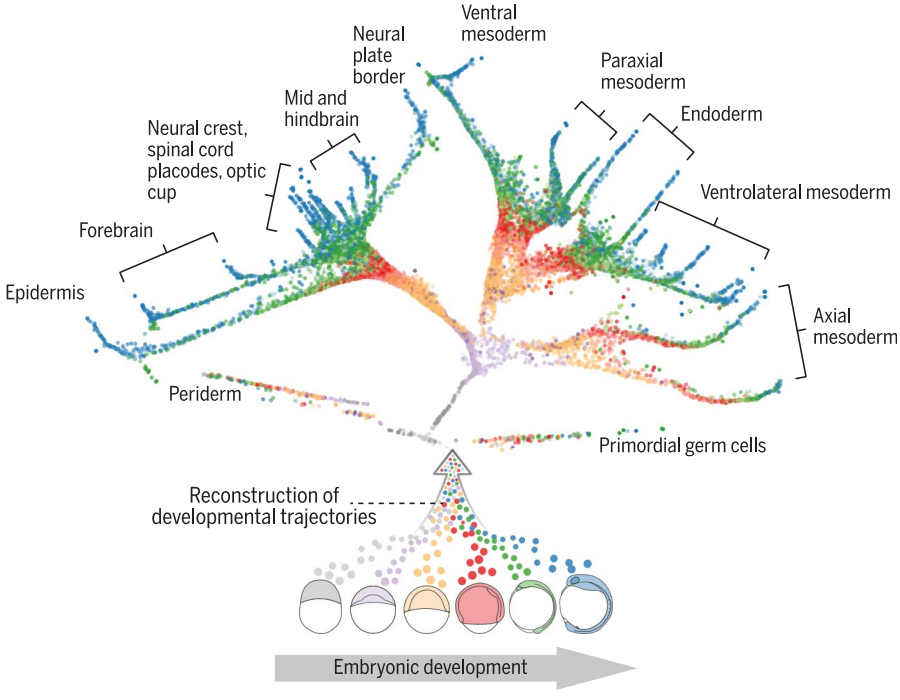

Developmental tree of early zebrafish embryogenesis. Single-cell transcriptomes were generated from zebrafish embryos at 12 developmental stages (six of which are shown). The transcriptional trajectories that describe the fate specification of 25 cell types were reconstructed from the data. Molecular specification is visualized with a force-directed layout, in which each cell is represented by a point (colored by developmental stage), proceeding from pluripotent cells (at the bottom center) outward to 25 distinct cell types. A subset of the identified trajectories are labeled in groups.

RESULTS: We generated single-cell transcriptomes from 38,731 cells during early zebrafish embryogenesis at high temporal resolution, spanning 12 stages from the onset of zygotic transcription through early somitogenesis. We took two complementary approaches to identify the transcriptional trajectories in the data. First, we developed a simulated diffusion-based computational approach, URD, which identified the trajectories describing the specification of 25 cell types in the form of a branching tree. Second, we identified modules of coexpressed genes and connected them across developmental time. Combining the reconstructed developmental trajectories with differential gene expression analysis uncovered gene expression cascades leading to each cell type, including previously unidentified markers and candidate regulators. Combining these trajectories with Seurat, which infers the spatial positions of cells on the basis of their transcriptomes, connected the earlier spatial position of progenitors to the later fate of their descendants.

ON OUR WEBSITE

Read the full article at http://dx.doi.org/10.1126/science.aar3131

Inspection of the developmental tree led to new insights about molecular specification in zebrafish. For example, the first branch point in the tree indicated that the first molecular specification event may not only separate the germ layers but also define the axial versus nonaxial mesendoderm. Additionally, some developmental branch points contained intermediate cells that expressed genes characteristic of multiple downstream cell fates. Gene expression analysis at one such branch point (the axial mesoderm) suggested that the intermediate cells switch their specification from one fate (notochord) to another (prechordal plate). Last, analysis of single-cell transcriptomes from a Nodal-signaling mutant revealed that even at the whole-transcriptome level, mutant cells were canalized into a subset of wild-type states and did not adopt any transcriptional states not observed in wild type, despite abnormal developmental signaling.

CONCLUSION: These findings reconstruct the gene expression trajectories during the embryogenesis of a vertebrate and highlight the concurrent canalization and plasticity of cell type specification. The scRNA-seq data and developmental tree provide a rich resource for future studies in zebrafish: The raw and processed data and the URD software are available for download, and the data can be browsed interactively online. Last, this approach provides a broadly applicable framework with which to reconstruct complex developmental trajectories from single-cell transcriptomes. ■

The list of author affiliations is available in the full article online.
*These authors contributed equally to this work.
†Corresponding author. Email: aregev@broadinstitute.org (A.R.); schier@fas.harvard.edu (A.F.S.)
Cite this article as J. A. Farrell *et al.*, *Science* **360**, eaar3131 (2018). DOI: 10.1126/science.aar3131

RESEARCH ARTICLE

SINGLE-CELL ANALYSIS

Single-cell reconstruction of developmental trajectories during zebrafish embryogenesis

Jeffrey A. Farrell,[1]* Yiqun Wang,[1]* Samantha J. Riesenfeld,[2] Karthik Shekhar,[2] Aviv Regev,[2,3]† Alexander F. Schier[1,2,4,5,6,7]†

During embryogenesis, cells acquire distinct fates by transitioning through transcriptional states. To uncover these transcriptional trajectories during zebrafish embryogenesis, we sequenced 38,731 cells and developed URD, a simulated diffusion-based computational reconstruction method. URD identified the trajectories of 25 cell types through early somitogenesis, gene expression along them, and their spatial origin in the blastula. Analysis of Nodal signaling mutants revealed that their transcriptomes were canalized into a subset of wild-type transcriptional trajectories. Some wild-type developmental branch points contained cells that express genes characteristic of multiple fates. These cells appeared to trans-specify from one fate to another. These findings reconstruct the transcriptional trajectories of a vertebrate embryo, highlight the concurrent canalization and plasticity of embryonic specification, and provide a framework with which to reconstruct complex developmental trees from single-cell transcriptomes.

During embryogenesis, a single totipotent cell gives rise to numerous cell types with distinct functions, morphologies, and spatial positions. Because this process is primarily controlled through transcriptional regulation, the identification of the transcriptional states underlying cell fate acquisition is paramount to understanding and manipulating development. Previous studies have presented different views of cell fate specification. For example, artificially altering transcription factor expression (such as in reprogramming) has revealed remarkable plasticity of cellular fates (*1*–*3*). Conversely, classic embryological studies have indicated that cells are canalized to adopt perduring fates separated by epigenetic barriers. Technological limitations necessitated that traditional embryological studies focus on specific fate decisions with selected marker genes, but the advent of single-cell RNA sequencing (scRNA-seq) raises the possibility of fully defining the transcriptomic states of embryonic cells as they acquire their fates (*4*–*8*). However, the large number of transcriptional states and branch points, as well as the asynchrony in developmental processes, pose major challenges to the comprehensive identification of cell types and the computational reconstruction of their developmental trajectories. Pioneering computational approaches to uncover developmental trajectories (*5*–*7*, *9*–*11*) were either designed to address stationary or steady-state processes or accommodate only small numbers of branch points and thus are insufficient for addressing the complex branching structure of time-series developmental data. We addressed these challenges by combining large-scale single-cell transcriptomics during zebrafish embryogenesis with the development of a new simulated diffusion-based computational approach to reconstruct developmental trajectories, called URD (named after the Norse mythological figure who nurtures the world tree and decides all fates).

[1]Department of Molecular and Cellular Biology, Harvard University, Cambridge, MA 02138, USA. [2]Klarman Cell Observatory, Broad Institute of MIT and Harvard, Cambridge, MA 02142, USA. [3]Howard Hughes Medical Institute, Koch Institute for Integrative Cancer Research, Department of Biology, Massachusetts Institute of Technology, Cambridge, MA 02140, USA. [4]Center for Brain Science, Harvard University, Cambridge, MA 02138, USA. [5]FAS Center for Systems Biology, Harvard University, Cambridge, MA 02138, USA. [6]Biozentrum, University of Basel, Switzerland. [7]Allen Discovery Center for Cell Lineage Tracing, University of Washington, Seattle, WA 98195, USA.
*These authors contributed equally to this work.
†Corresponding author. Email: aregev@broadinstitute.org (A.R.); schier@fas.harvard.edu (A.F.S.)

High-throughput scRNA-seq from zebrafish embryos

We profiled 38,731 cells from 694 embryos across 12 closely spaced stages of early zebrafish development using Drop-seq, a massively parallel scRNA-seq method (*12*). Samples spanned from high blastula stage (3.3 hours postfertilization, just after transcription from the zygotic genome begins), when most cells are pluripotent, to six-somite stage (12 hours postfertilization, shortly after the completion of gastrulation), when many cells have differentiated into specific cell types (Fig. 1A and table S1). In a *t*-distributed stochastic neighbor embedding (tSNE) plot (*13*) of the entire data set based on transcriptional similarity, it is evident that developmental time was a strong source of variation in the data, but the underlying developmental trajectories were not readily apparent (Fig. 1B). Consistent with the understanding that cell types become more transcriptionally divergent over time, cells from early stages formed large continuums in the tSNE plot, whereas more discrete clusters emerged at later stages (Fig. 1C).

URD reconstructs complex branching developmental trajectories

Acquisition of many single-cell embryonic transcriptomes with high temporal resolution created the possibility of reconstructing developmental trajectories through similarity in gene expression profiles. Such an approach would allow the investigation of the gene expression dynamics and the timing of molecular specification—when progenitor populations become transcriptionally distinct from each other and begin to express the regulators that will drive their future fates. Therefore, we developed URD, an approach to uncover complex developmental trajectories as a branching tree. URD extends diffusion maps [originally presented for single-cell differentiation analysis in pioneering work by Haghverdi *et al.* and their R package, *destiny* (*9*, *10*)] through several advances: It introduces a new way to order cells in pseudotime, finds developmental trajectories, discovers an underlying branching tree that abstracts specification, and visualizes the data (Fig. 1D and supplementary materials, materials and methods).

In general, URD operates by means of "simulating diffusion," using discrete random walks and graph searches to approximate the continuous process of diffusion (supplementary materials, materials and methods). Briefly, URD constructs a *k*-nearest-neighbor graph between transcriptomes in gene expression space; graph edges are assigned transition probabilities that are used as weights in later simulations and describe the chance a random walk would move along each edge (Fig. 1D, 1) (*9*, *10*). The user identifies the root(s) (starting points) and tips (end points) of the developmental process. Cells are next assigned a pseudotime—an ordering that should reflect their developmental progress rather than absolute time—in order to compensate for developmental asynchrony. URD calculates pseudotime by simulating diffusion from the root to determine each cell's distance from the root (as the average number of diffusive transitions needed to reach it across several simulations) (Fig. 1D, 2). Next, the developmental trajectory (the path in gene expression) between each tip and the root is determined by identifying which cells are visited by simulated biased random walks initiated in that tip; the walks are biased to only transition to cells of equal or earlier pseudotime so that when they reach developmental branch points, they proceed toward the root and do not explore other cell types (Fig. 1D, 3). Then, URD reconstructs a branching tree structure by joining pairs of trajectories where they pass through the same cells (Fig. 1D, 4; black and purple edges, for example). Last, the data are visualized with a force-directed layout based on cells' visitation

frequency by the random walks from each tip (Fig. 1D, 5) (*14*). The developmental trajectories identified with URD are akin to cell lineages but differ from classical definitions of cell lineage because they are reconstructed from observed gene expression and do not measure mother-daughter relationships between cells. URD does not require any prior knowledge of the developmental trajectories it seeks to find (such as the number of branch points or definition of intermediate states).

Reconstructed developmental tree recapitulates molecular specification during zebrafish embryogenesis

Application of URD to the early zebrafish embryogenesis scRNA-seq data generated a tree whose branches reflected embryonic specification trajectories. To define the final cell populations (the tips of the tree), we clustered cells from the final stage of our time course and determined cluster identity through the expression of known marker genes (fig. S1). The recovered tree followed the specification of 25 final cell populations across 16 branch points (Fig. 1E, fig. S2, and movie S1). The reconstructed tree substantially recapitulated the developmental trajectories expected from classical embryological studies (*15*–*17*). For example, the primordial germ cells, the enveloping layer cells (EVLs), and the deep-layer blastomeres already formed separate trajectories by high stage (Fig. 1F). Unexpectedly, the first branch point within the blastoderm not only separated the ectoderm from the mesendoderm but also divided the axial mesoderm from the remainder of the mesendoderm (Fig. 1G). Later branching events were also recovered, such as the separation of paraxial, lateral, and intermediate mesoderm (Fig. 1H); the separation of the non-neural and neural ectoderm (Fig. 1I); and the eventual branching of the non-neural ectoderm into epidermis, neural plate border, and multiple preplacodal ectoderm trajectories (Figs. 1E and 2, trajectory, and fig. S3). Displaying the expression of classic marker genes on the developmental tree highlighted expected trajectories and confirmed their annotation (Fig. 2, gene expression, and fig. S3). For example, consistent with its known expression, the notochord marker gene *noto* was restricted primarily to two trajectories (the entire notochord trajectory and the later stages of the tailbud trajectory) and confirmed that the branch point between the notochord and prechordal plate was correctly placed (*18*). These results show that URD can reconstruct the highly complex branching trajectories of early zebrafish embryogenesis solely on the basis of large-scale scRNA-seq data.

Connected gene modules support reconstructed developmental trajectories

To complement the specification tree, and in order to find groups of genes that are coexpressed within cell populations, we applied non-negative matrix factorization (NMF) to the single-cell transcriptomes (*19*). This approach produced modules of covarying genes and described cells in terms of module expression (which is more robust than individual gene expression measurements) (*4*, *20*). Modules were annotated post hoc according to their highly ranked classic marker genes, and similar modules from adjacent stages were linked to each other according to the overlap of their most highly ranked genes. This approach

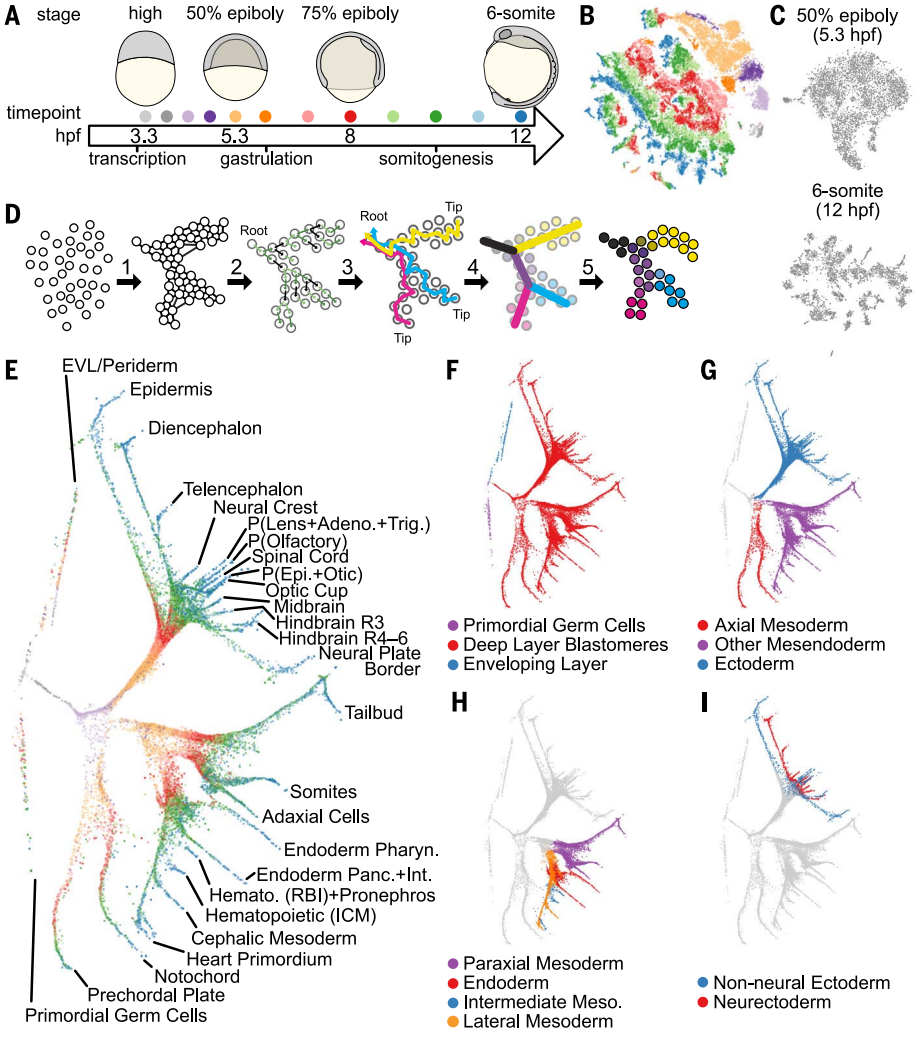

Fig. 1. Generation of a developmental specification tree for early zebrafish embryogenesis using URD. (**A**) Single-cell transcriptomes were collected from zebrafish embryos at 12 developmental stages (colored dots) spanning 3.3 to 12 hours postfertilization (hpf). (**B**) tSNE plot of the entire data, colored by stage [as in (A)]. Developmental time is a strong source of variation, and the underlying developmental trajectories are not immediately apparent. (**C**) tSNE plot of data from two stages (top, 50% epiboly; bottom, six-somite). Clusters are more discrete at the later stage. (**D**) URD's approach for finding developmental trajectories. 1: Transition probabilities are computed from the distances between transcriptomes and used to connect cells with similar gene expression. 2: From a user-defined "root" (such as cells of the earliest time point), pseudotime is calculated as the average number of transitions required to reach each cell from the root. 3: Trajectories from user-defined "tips" (such as cell clusters in the final time point) back to the root are identified by simulated random walks that are biased toward transitioning to cells younger or equal in pseudotime. 4: To recover an underlying branching tree structure, trajectories are joined agglomeratively at the point where they contain cells that are reached from multiple tips. 5: The data are visualized with a force-directed layout based on cells' visitation frequency by the random walks from each tip. (**E**) Force-directed layout of early zebrafish embryogenesis, optimized for 2D visualization (supplementary materials, materials and methods, fig. S2, and movie S1), colored by stage [as in (A)] with terminal populations labeled. EVL, enveloping layer; P, placode; Adeno., adenohypophyseal; Trig., trigeminal; Epi., epibranchial; Panc.+Int., pancreatic + intestinal; RBI, rostral blood island; ICM, intermediate cell mass. (**F** to **I**) Cell populations downstream of early and intermediate branch points recovered by URD.

created chains of connected gene modules that provided an alternative way to track developmental trajectories (fig. S4 and table S2). For example, the prechordal plate chain of connected gene modules extended from 50% epiboly to six-somite stage, during which the top ranking genes gradually changed from early to late markers for the prechordal plate (table S3).

The URD-generated developmental tree and the chains of connected gene modules provided two different ways to analyze the scRNA-seq data and define developmental trajectories. To determine how congruent these approaches are, we highlighted cells in the developmental tree according to their expression of connected gene modules. Cells that express connected gene modules occupied specific URD-recovered developmental trajectories, further supporting the structure of the developmental tree reconstructed by URD (Fig. 2, module expression, and fig. S3).

Gene cascades reveal expression dynamics along developmental trajectories

Gene expression and gene module analysis were combined in order to find candidate regulators and markers along each trajectory uncovered with URD. Genes and connected gene modules were associated with developmental trajectories by testing for their differential expression downstream of each branch point of URD's recovered branching structure (Fig. 3, A and B; and supplementary materials, materials and methods). Gene expression dynamics were then fit with an impulse model (*21*) so as to determine the onset and offset time of their expression, which was then used to order genes. As an example, sequential expression was observed for 197 genes enriched in the prechordal plate during its specification, including several well-known transcription factors or signaling molecules that confirm the validity of our approach (such as *gsc*, *foxa3*, *klf17*, and *frzb*) (Fig. 3C and figs. S5 to S7) (*22*–*25*). This cascade contained several regulatory factors (such as *fzd8a*, *fzd8b*, *mllt1b*, and *inhbaa*) without described roles in the prechordal plate that would be candidates for reverse genetic screens. This cascade also contained more than 40 genes that were not previously annotated as associated with the prechordal plate (fig. S6), and those tested by means of in situ hybridization were indeed expressed in the prechordal plate (fig. S7). Thus, combining URD and gene module analysis uncovered the transcriptional cascades that accompanied the development of progenitors into differentiated cells and highlighted both previously characterized and newly identified trajectory-enriched genes.

Combining developmental trajectories with spatial analysis infers progenitor locations

The URD-generated tree is a powerful way to visualize developmental trajectories but lacks spatial information. We therefore asked whether the trajectories could be traced to their spatial origin at the late blastula stage (*16*, *17*). First, a spatial map of the Drop-seq 50% epiboly transcriptomes was generated by using Seurat, a method we previously developed to infer the spatial locations of single-cell transcriptomes by comparing the genes expressed in each transcriptome with the spatial expression patterns of a few landmark genes obtained from RNA in situ hybridization (*20*). Second, Seurat's spatial map was combined with either URD or connected gene module analysis (as parallel, independent approaches) in order to associate cell populations at six-somite stage with the location of their "pseudoprogenitors" at 50% epiboly. In one approach, we used URD's simulated random walks from cell populations at six-somite (Fig. 3A, pink bars) to infer their pseudoprogenitor cells and then plotted the spatial location of the 50% epiboly pseudoprogenitors using Seurat (Fig. 4A). In the other approach, we plotted the spatial expression of each 50% epiboly gene module and identified its connected gene modules at later stages (Fig. 3B, blue bars on right); the cells that express these connected gene modules are highlighted on the developmental tree (Fig. 4B) and are the "pseudodescendents" that arise from the spatial domain identified by the 50% epiboly gene module.

The results from the two approaches were highly concordant and agreed with classic fate-mapping experiments (*16*, *17*). For example, both approaches associated the dorsal margin of the 50% epiboly embryo with axial mesodermal fates (prechordal plate and notochord). Likewise, in both cases the animal pole was associated with ectodermal fates, with the ventral animal side biased to non-neural fate and the dorsal animal side to neural fate. Overall, these results show that scRNA-seq data can be used not only to reconstruct specification trajectories and their associated gene cascades but also to connect the earlier spatial position of progenitors to the later fate of their descendants.

Nodal signaling mutant cells are canalized into a subset of wild-type transcriptional states

Previous studies of mutant embryos have provided important insights into embryonic fate specification, but scRNA-seq raises the possibility of rapidly phenotyping mutants both genome-wide and at single-cell resolution. To test this idea, we profiled maternal-zygotic *one-eyed pinhead* mutants (MZ*oep*), which lack the coreceptor for the mesendoderm inducer Nodal (*26*, *27*). We first asked whether previous MZ*oep* embryological results could be reconstructed simply from scRNA-seq data. Transcriptomes were generated with Smart-seq2 (*28*), with deeper mRNA coverage than that of Drop-seq (fig. S8); 325 MZ*oep* and 1047 wild-type transcriptomes were collected at 50% epiboly, when Nodal signaling is normally active at the blastoderm margin. Using Seurat, we inferred the spatial origin of both wild-type and MZ*oep* transcriptomes based on a wild-type landmark map (Fig. 5A). As predicted, no MZ*oep* cells

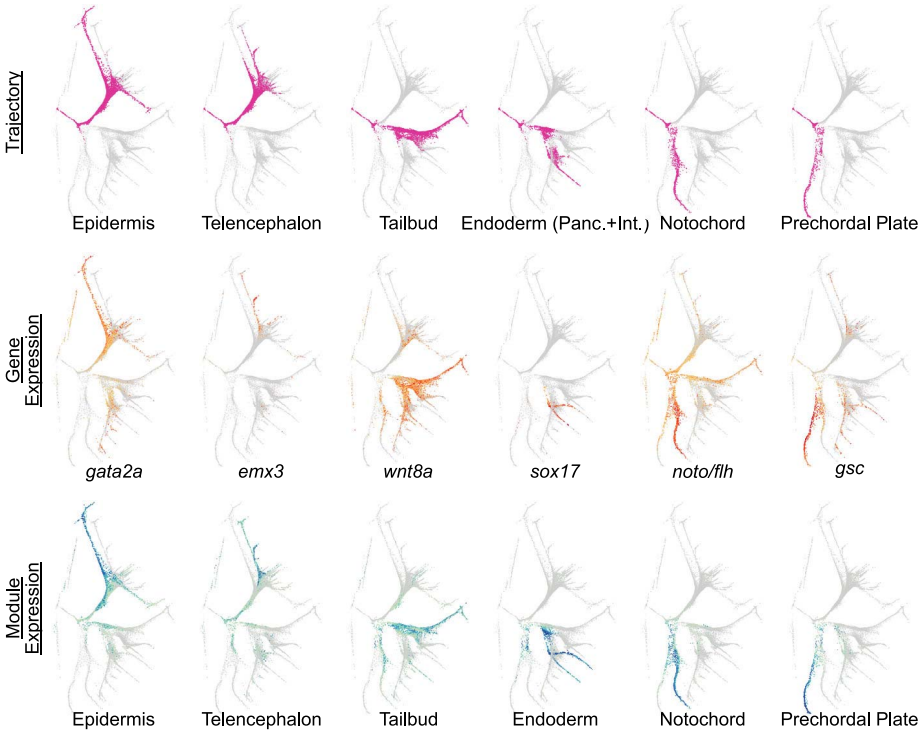

Fig. 2. Developmental trajectories, genes, and connected gene modules overlaid on the force-directed layout. From top to bottom, (i) the trajectories identified by URD from the root to a given population (or group of populations), (ii) gene expression of a classical marker of that population, and (iii) expression of a six-somite gene module active in the population and its connected modules from earlier stages. The remainder are presented in fig. S3.

mapped to the margin of a wild-type embryo, where mesendodermal progenitors arise. Applying NMF revealed that in MZ*oep* mutants, expression of the marginal dorsal, dorsal, and marginal gene modules is greatly reduced or absent, but no mutant-specific modules were found (Fig. 5B). NMF recovered the same 50% epiboly gene modules from Smart-seq and Drop-seq data (Fig. 5B and table S4), which allowed us to use the chains of connected Drop-seq gene modules to predict the MZ*oep* mutant phenotype at later stages. Namely, our approach successfully predicted the loss of paraxial mesoderm, ventrolateral mesoderm, axial mesoderm, and endoderm (Fig. 5C), as well as the continued presence of the tailbud, as found in previous embryological studies (*26*). Analysis of additional single-cell transcriptomes from wild-type and MZ*oep* mutants at six-somite stage largely verified our predictions (fig. S9 and table S5). Together, these results show that combining modest-scale scRNA-seq in mutants with the large-scale developmental reference tree constructed for wild type can rapidly provide phenotypic insights: In the absence of Nodal signaling, marginal blastomeres that would normally become mesendodermal progenitors instead become ectodermal and tail progenitors, resulting in the absence of mesendodermal cell types and an altered fate map, as shown in previous cell-tracing experiments (*27*).

We next asked whether the mutant scRNA-seq dataset could provide novel insights into cell identity in the absence of Nodal signaling. Morphological analysis and fate mapping of MZ*oep* mutants has found that all cells appear to adopt wild-type fates (*26*, *27*). However, intricate interactions exist between the several signaling pathways active during early development, and the elimination of Nodal signaling changes levels and domains of other developmental signals in the embryo. Thus, MZ*oep* mutant cells could potentially perceive signaling input combinations that do not occur in wild-type embryos, which may result in gene expression states not observed in wild type. We therefore wondered whether mutant cells expressed previously unknown combinations of gene modules under this altered signaling landscape or were transcriptionally equivalent to a subset of wild-type states. Co-clustering of wild-type and MZ*oep* transcriptomes according to their gene module expression revealed that while some mesendodermal cell types were absent in MZ*oep* at 50% epiboly, the remaining cells clustered with wild-type states (Fig. 5D and fig. S10). This result indicates that even on the whole-transcriptomic and single-cell level, mutant cells are canalized into a subset of wild-type fates after the loss of an essential signaling pathway.

Hybrid gene expression states reveal developmental plasticity

Inspection of the developmental tree revealed that most cells fell along tight trajectories, but some cells were located in intermediate zones between branches. This observation seemed at odds with the view that embryonic cells traverse a developmental trajectory until a branch point

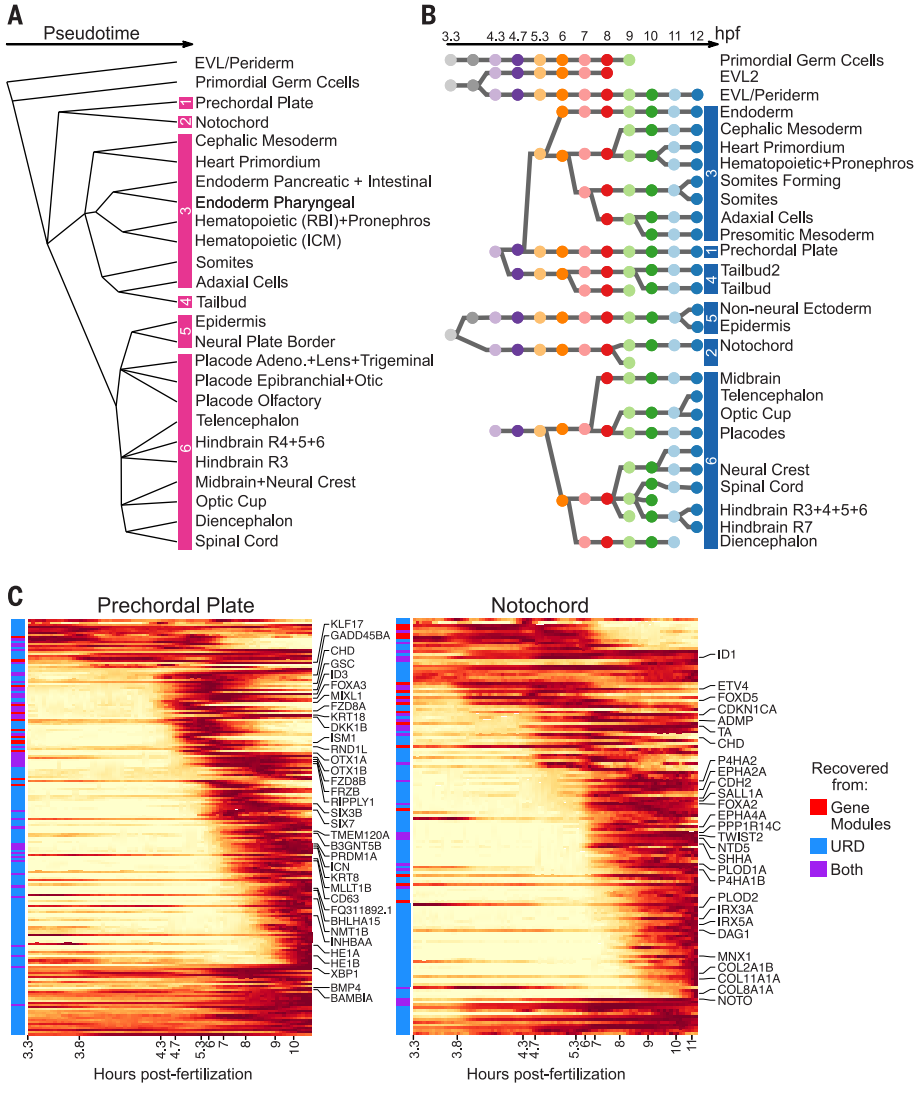

Fig. 3. Association of developmental trajectories with temporal gene expression patterns. (**A**) The underlying branching structure found by URD. Pink bars demarcate collections of cell types used in Fig. 4A. (**B**) The structure of connected gene modules. Each circular node represents a module and is colored by the developmental stage from which the module was computed (as in Fig. 1A). Blue bars demarcate collection of modules downstream of each 50% epiboly (5.3 hpf) gene module used in Fig. 4B. (**C**) Gene expression cascades during specification of the prechordal plate and notochord. Expression is displayed as a moving-window average in pseudotime (along the *x* axis), scaled to the maximum observed expression. Selected genes are labeled along the *y* axis. Genes are annotated with whether they were identified as a differentially expressed gene, as a top ranking member of a differentially expressed connected gene module, or both. Cascades for all trajectories (with all genes labeled) are presented in fig. S5.

funnels them cleanly and irreversibly into one of multiple downstream branches. For example, at the axial mesoderm branch point, most cells fell along the classic bifurcation from progenitor into notochord or prechordal plate fates (*15*, *29*), with waves of gene expression corresponding to their specification and differentiation status (Fig. 6A, highlighted). However, ~5.4% were intermediate cells that expressed both notochord and prechordal plate markers (Fig. 6, A and B). The intermediate cells and the completely bifurcated axial mesoderm cells with similar pseudotimes came from embryos at the same developmental stage (Fig. 6C); moreover, they no longer expressed genes characteristic of the progenitors (such as *nanog* and *mex3b*). These observations eliminated models in which intermediate cells retained their progenitor state and delayed specification. Instead, we noticed that these cells expressed early markers of both programs (*gsc*, *frzb*, *ta*, and *noto*) but later markers of only the notochord program (*ntd5* and *shha*). This observation raised two possible models: (i) Cells initially express both programs, then shut off the prechordal plate program, and produce only notochord markers later ("dual-specification" model);

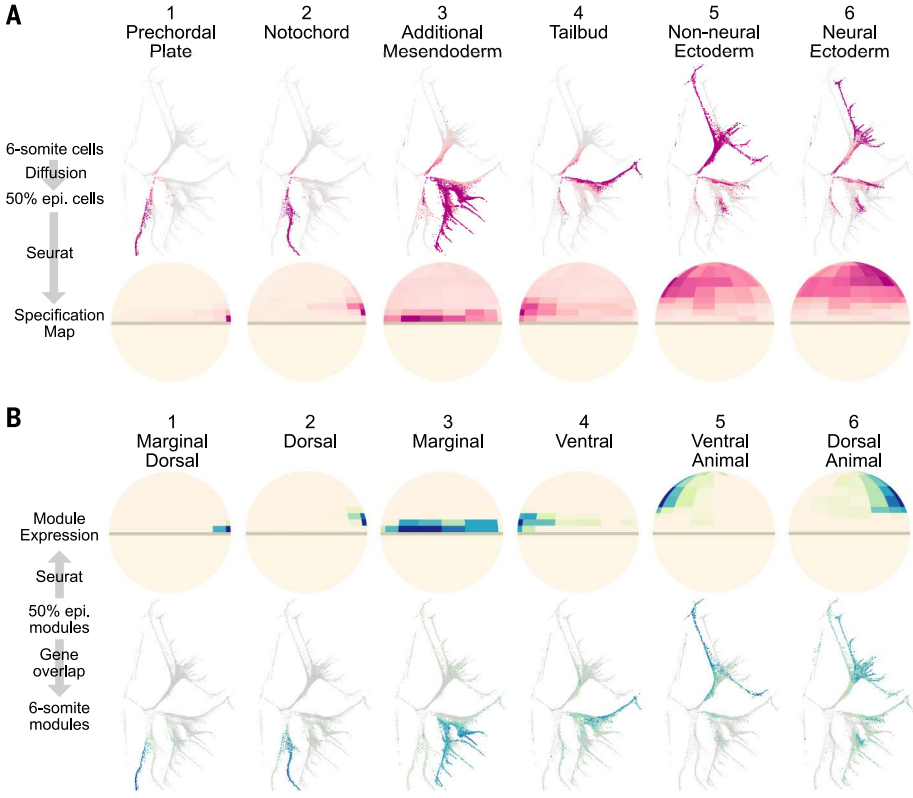

Fig. 4. Molecular specification maps relate cell position at 50% epiboly to cell fate at six-somite. (**A**) Visitation by random walks from given tip(s) (as proportion of visitation from all tips) and the spatial location of visited 50% epiboly cells (ventral side to the left). The six tip groups are marked in Fig. 3A. (**B**) Spatial expression of 50% epiboly gene modules. Expression of connected gene modules is plotted on the force-directed layout to highlight populations that will emerge from the 50% epiboly module's expression domain. The six groups of connected gene modules are marked in Fig. 3B.

or (ii) cells specified as notochord first express early and late notochord markers and then change their specification by shutting off notochord expression and initiating early prechordal plate marker expression ("trans-specification" model).

To distinguish between these two models, we investigated their properties and location using fluorescent RNA in situ hybridization. At 75% epiboly, some cells located in the border region between the two tissues coexpressed an early prechordal plate marker (*gsc*) with either an early (*ta/ntl*) or late (*ntd5*) notochord marker (Fig. 6, D to F, and fig. S11). The existence of these intermediate cells in situ confirms that they are not an artifact of scRNA-seq (such as cell doublets), and their defined spatial localization near the border of the two tissues suggests that they are not merely biological or technical noise. Instead, the location of coexpressing cells raises the possibility that the boundary between the notochord and prechordal plate territories is refined during gastrulation, after the two populations become transcriptionally distinct. Many of the coexpressing cells exhibited bright nuclear foci that denoted sites of active transcription of the probed genes. Most of the cells with nuclear transcription foci for a single gene exhibited transcription of the early prechordal plate marker, *gsc*. By contrast, cells with active transcription of the notochord markers *ta/ntl* or *ntd5* were rare (Fig. 6, E and F). The active transcription of the prechordal plate program supports the trans-specification model—the intriguing possibility that some axial mesoderm cells move down the notochord specification path but then trans-specify into prechordal plate cells.

Discussion

We describe a molecular specification tree of an early vertebrate embryo by exploring large-scale single-cell transcriptomic data with URD, a computational approach to reveal developmental trajectories in transcriptional space. Our study lays the foundation for multiple areas of future exploration.

First, URD is a powerful tool to reveal the transcriptional trajectories of complex developmental processes such as zebrafish embryogenesis. Combining URD with connected gene module analysis uncovered the transcriptional cascades underlying fate specification. Moreover, combining URD with Seurat enabled the anchoring of developmental trajectories to their spatial origins. We anticipate that similar augmentation of URD with information about lineage relationships (*30*, *31*), chromatin dynamics (*32*), and signaling will further deepen insights into developmental processes. Additionally, some of URD's limitations could be addressed by future enhancements. For instance, branching events driven by single genes (such as *sox32* in the endoderm) (*33*, *34*) are not captured with URD until additional transcriptional differences arise, which could potentially be improved with more aggressive, iterative branch calling. Also, improvements to the throughput and quality of scRNA-seq may drive improved performance from URD: More closely spaced time points could enable detection of rapidly changing fate decisions and could reveal sequential bifurcations at branch points currently thought to enter multiple trajectories; larger numbers of cells could enable reconstruction of rare, transcriptionally indistinct populations (such as the floor plate and hypochord); and improved sequencing depth could enable detection of important but lowly expressed regulators that are not found in the current data (such as *npas4l/cloche*). In the future, URD could be used to analyze additional systems, such as in vitro differentiation, tissue regeneration, cancer, and disease progression.

Second, the scRNA-seq data and developmental tree provide a rich resource for future studies of zebrafish embryogenesis. The presented data describe embryonic gene expression with unparalleled temporal and cellular resolution, and the reconstructed tree thus provides an atlas of the expression pattern and dynamics for nearly all genes. This allows inspection of gene coexpression with much greater ease than with multicolor in situ hybridization, reveals markers for cell types of interest, and associates uncharacterized genes with particular cell types. Moreover, the data reveal the progressive nature of cell fate specification and suggest potentially redundant regulators of developmental decisions with overlapping spatial and temporal expression, which would be missed in forward genetic screens.

Third, this work begins to illustrate the trajectories, canalization, and potential plasticity of fate specification. With respect to trajectories, our analysis suggests that not all cell fate decisions are binary; multiple trajectories can arise simultaneously from a pool of equipotent progenitors. For example, at the molecular level, the earliest specification of blastomeres separates the axial mesoderm, nonaxial mesendoderm, and ectoderm, rather than just separating the germ layers. This conclusion is compatible with the observation that the axial mesoderm progenitors reside at the dorsal blastula margin, where maternal factors that specify the Mangold-Spemann organizer simultaneously affect the fate of those progenitors (*15*). Concerning canalization, the analysis of a Nodal signaling mutant reveals that even on the whole-transcriptomic level, mutant cells adopt a subset of wild-type transcriptomic states, but not new ones, demonstrating the extensive canalization during embryogenesis even after abnormal developmental signaling. With respect to plasticity, the identification of intermediate cells at the axial mesoderm branch point demonstrates hybrid developmental states. In situ hybridization experiments

suggest that these cells trans-specify from one cell type (notochord) to another (prechordal plate), and their border zone spatial localization suggests refinement of the boundary between these two regions. These results support an alternative view of developmental fate choice to the common interpretation of Waddington's model: Downstream of some branch points, some cells still transition across the "ridges" between different lineages even after they are canalized into well-defined transcriptional states. This suggests a developmental plasticity that has been observed after perturbation (*1*–*3*, *35*) but has not been well established in normal developmental processes. We propose that in a continuous morphogen

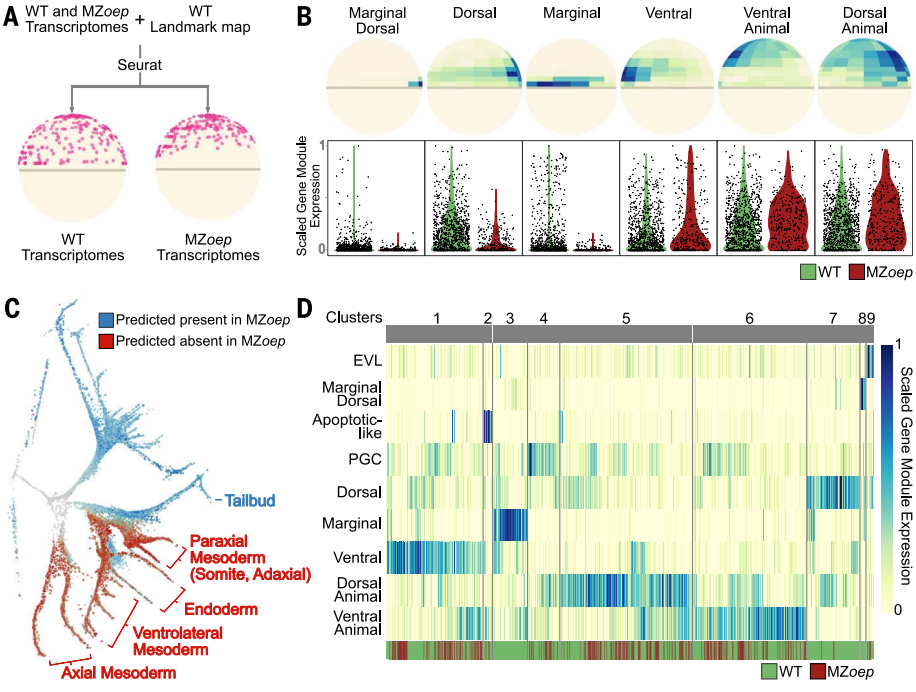

Fig. 5. Characterization of Nodal signaling mutant with scRNA-seq and the developmental specification tree. (**A**) Spatial assignment of wild-type and MZ*oep* transcriptomes according to a wild-type landmark map indicates an absence of wild-type marginal fates in MZ*oep* (ventral, left). Shown at random are 311 wild-type transcriptomes (to match MZ*oep* cell number). (**B**) (Top) wild-type expression domain of spatially restricted gene modules identified in Smart-seq data (ventral to left). (Bottom) Violin plot of the maximum-scaled gene module levels in wild-type and MZ*oep* mutant cells. The marginal dorsal, dorsal, and marginal gene modules are absent or strongly reduced in MZ*oep*. (**C**) Expression of gene modules connected to those missing in MZ*oep* (marginal dorsal, dorsal, and marginal; red) and connected to those remaining in MZ*oep* (blue). (**D**) Hierarchical clustering of wild-type and MZ*oep* mutant transcriptomes, based on the scaled expression of gene modules. Number of clusters is determined by the Davies-Bouldin index. Genotype is indicated beneath the heatmap (wild type, green; MZ*oep*, red). Clusters 3 and 8 contain only wild-type cells. All other clusters contain a mixture of wild-type and MZ*oep* cells. This clustering analysis was sufficiently sensitive to detect computationally simulated altered states (fig. S10).

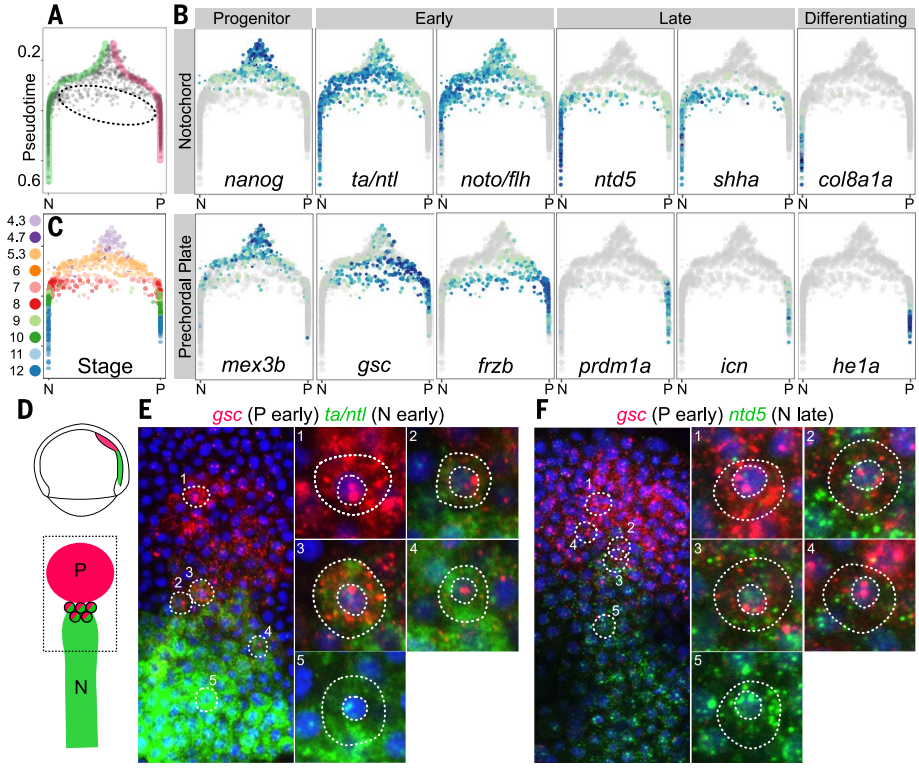

Fig. 6. Hybrid state of cells in the axial mesoderm. (**A**) Branch point plot, showing pseudotime (*y* axis) and random walk visitation preference from the notochord (N, left) and prechordal plate (P, right) tips (*x* axis), defined as the difference in visitation from the two tips divided by the sum of visitation from the two tips. Direct trajectories to notochord (green) and prechordal plate (pink) are highlighted, and intermediate cells are circled. (**B**) Gene expression of notochord markers (top row) and prechordal plate markers (bottom row) at the axial mesoderm branch point. Intermediate cells express early (*ta/ntl* and *noto*) and late (*ntd5* and *shha*) notochord markers but only early prechordal plate markers (*gsc* and *frzb*). (**C**) Cells at the branch point, colored by developmental stage. Intermediate cells have the same developmental stage as that of fully bifurcated cells with similar pseudotimes. (**D**) Illustration of the prechordal plate (P) and notochord (N) in the 75% epiboly embryo. (**E** and **F**) Double fluorescent in situ expression of the early prechordal plate marker *gsc* (red) and either the early notochord marker *ta/ntl* [(E), green] or the late notochord marker *ntd5* [(F), green] at 75% epiboly (8 hpf). Most cells contain only prechordal plate marker mRNA (for example, "1") or notochord marker mRNA (for example, "5"). Cells with both prechordal plate and notochord marker mRNA are observed at the boundary of the two tissues, with red nuclear transcription foci, indicating active transcription of *gsc* (for example, "2" to "4") (fig. S11). Cells that contained both *ntd5* and *gsc* mRNA were identified and scored for their nuclear transcription foci, which indicate active transcription (supplementary materials, materials and methods); 56% had one or more observable nuclear transcription dots, of which 80% showed only active *gsc* transcription, 7% showed both active *gsc* and active *ntd5* transcription, and 13% showed active *ntd5* transcription alone.

gradient that resolves into discrete states, some cells will receive an amount of signal that is on the cusp between the two states; these cells would end up at the boundary between the two tissues. It is conceivable that continued signaling could provide a "push" over a shallow ridge, such as continued Nodal signaling in the axial mesoderm (*22*) or continued retinoic acid signaling in the hindbrain (*36*, *37*). Future studies combining lineage tracing and in vivo imaging of gene expression will be needed to directly observe such transitions.

Collectively, our approach provides a framework with which to reconstruct the specification trajectories of many developmental systems without the need for prior knowledge of gene expression patterns, fate maps, or lineage trajectories. The generation of developmental trees for different species will enable comparative studies, and developmental statistics generated from such comparisons will help reveal conserved pathways and species-specific idiosyncracies.

REFERENCES AND NOTES

1. R. L. Davis, H. Weintraub, A. B. Lassar, Expression of a single transfected cDNA converts fibroblasts to myoblasts. *Cell* **51**, 987–1000 (1987). doi: 10.1016/0092-8674(87)90585-X; pmid: 3690668
2. S. J. Tapscott *et al*., MyoD1: A nuclear phosphoprotein requiring a Myc homology region to convert fibroblasts to myoblasts. *Science* **242**, 405–411 (1988). doi: 10.1126/science.3175662; pmid: 3175662
3. K. Takahashi, S. Yamanaka, Induction of pluripotent stem cells from mouse embryonic and adult fibroblast cultures by defined factors. *Cell* **126**, 663–676 (2006). doi: 10.1016/j.cell.2006.07.024; pmid: 16904174
4. A. Wagner, A. Regev, N. Yosef, Revealing the vectors of cellular identity with single-cell genomics. *Nat. Biotechnol.* **34**, 1145–1160 (2016). doi: 10.1038/nbt.3711; pmid: 27824854
5. R. Cannoodt, W. Saelens, Y. Saeys, Computational methods for trajectory inference from single-cell transcriptomics. *Eur. J. Immunol.* **46**, 2496–2506 (2016). doi: 10.1002/eji.201646347; pmid: 27682842
6. S. C. Bendall *et al*., Single-cell trajectory detection uncovers progression and regulatory coordination in human B cell development. *Cell* **157**, 714–725 (2014). doi: 10.1016/j.cell.2014.04.005; pmid: 24766814
7. C. Trapnell *et al*., The dynamics and regulators of cell fate decisions are revealed by pseudotemporal ordering of single cells. *Nat. Biotechnol.* **32**, 381–386 (2014). doi: 10.1038/nbt.2859; pmid: 24658644
8. S. Jang *et al*., Dynamics of embryonic stem cell differentiation inferred from single-cell transcriptomics show a series of transitions through discrete cell states. *eLife* **6**, e20487 (2017). doi: 10.7554/eLife.20487; pmid: 28296635
9. L. Haghverdi, F. Buettner, F. J. Theis, Diffusion maps for high-dimensional single-cell analysis of differentiation data. *Bioinformatics* **31**, 2989–2998 (2015). doi: 10.1093/bioinformatics/btv325; pmid: 26002886
10. L. Haghverdi, M. Büttner, F. A. Wolf, F. Buettner, F. J. Theis, Diffusion pseudotime robustly reconstructs lineage branching. *Nat. Methods* **13**, 845–848 (2016). doi: 10.1038/nmeth.3971; pmid: 27571553
11. M. Setty *et al*., Wishbone identifies bifurcating developmental trajectories from single-cell data. *Nat. Biotechnol.* **34**, 637–645 (2016). doi: 10.1038/nbt.3569; pmid: 27136076
12. E. Z. Macosko *et al*., Highly parallel genome-wide expression profiling of individual cells using nanoliter droplets. *Cell* **161**, 1202–1214 (2015). doi: 10.1016/j.cell.2015.05.002; pmid: 26000488
13. L. van der Maaten, G. Hinton, Visualizing data using t-SNE. *J. Mach. Learn. Res.* **9**, 2579–2605 (2008).
14. T. M. J. Fruchterman, E. M. Reingold, Graph drawing by force-directed placement. *Softw. Pract. Exper.* **21**, 1129–1164 (1991). doi: 10.1002/spe.4380211102
15. A. F. Schier, W. S. Talbot, Molecular genetics of axis formation in zebrafish. *Annu. Rev. Genet.* **39**, 561–613 (2005). doi: 10.1146/annurev.genet.37.110801.143752; pmid: 16285872
16. C. B. Kimmel, R. M. Warga, T. F. Schilling, Origin and organization of the zebrafish fate map. *Development* **108**, 581–594 (1990). pmid: 2387237
17. K. Woo, J. Shih, S. E. Fraser, Fate maps of the zebrafish embryo. *Curr. Opin. Genet. Dev.* **5**, 439–443 (1995). doi: 10.1016/0959-437X(95)90046-J; pmid: 7580134
18. W. S. Talbot *et al*., A homeobox gene essential for zebrafish notochord development. *Nature* **378**, 150–157 (1995). doi: 10.1038/378150a0; pmid: 7477317
19. J.-P. Brunet, P. Tamayo, T. R. Golub, J. P. Mesirov, Metagenes and molecular pattern discovery using matrix factorization. *Proc. Natl. Acad. Sci. U.S.A.* **101**, 4164–4169 (2004). doi: 10.1073/pnas.0308531101; pmid: 15016911
20. R. Satija, J. A. Farrell, D. Gennert, A. F. Schier, A. Regev, Spatial reconstruction of single-cell gene expression data. *Nat. Biotechnol.* **33**, 495–502 (2015). doi: 10.1038/nbt.3192; pmid: 25867923
21. G. Chechik *et al*., Activity motifs reveal principles of timing in transcriptional control of the yeast metabolic network. *Nat. Biotechnol.* **26**, 1251–1259 (2008). doi: 10.1038/nbt.1499; pmid: 18953355
22. C. Thisse, B. Thisse, M. E. Halpern, J. H. Postlethwait, *Goosecoid* expression in neurectoderm and mesendoderm is disrupted in zebrafish cyclops gastrulas. *Dev. Biol.* **164**, 420–429 (1994). doi: 10.1006/dbio.1994.1212; pmid: 8045345
23. I. Seiliez, B. Thisse, C. Thisse, *FoxA3* and *goosecoid* promote anterior neural fate through inhibition of Wnt8a activity before the onset of gastrulation. *Dev. Biol.* **290**, 152–163 (2006). doi: 10.1016/j.ydbio.2005.11.021; pmid: 16364286
24. M. R. Gardiner, M. M. Gongora, S. M. Grimmond, A. C. Perkins, A global role for zebrafish *klf4* in embryonic erythropoiesis. *Mech. Dev.* **124**, 762–774 (2007). doi: 10.1016/j.mod.2007.06.005; pmid: 17709232
25. E. C. Swindell *et al*., Regulation and function of *foxe3* during early zebrafish development. *Genesis* **46**, 177–183 (2008). doi: 10.1002/dvg.20380; pmid: 18327772
26. K. Gritsman *et al*., The EGF-CFC protein one-eyed pinhead is essential for nodal signaling. *Cell* **97**, 121–132 (1999). doi: 10.1016/S0092-8674(00)80720-5; pmid: 10199408
27. A. Carmany-Rampey, A. F. Schier, Single-cell internalization during zebrafish gastrulation. *Curr. Biol.* **11**, 1261–1265 (2001). doi: 10.1016/S0960-9822(01)00353-0; pmid: 11525740
28. S. Picelli *et al*., Smart-seq2 for sensitive full-length transcriptome profiling in single cells. *Nat. Methods* **10**, 1096–1098 (2013). doi: 10.1038/nmeth.2639; pmid: 24056875
29. K. Gritsman, W. S. Talbot, A. F. Schier, Nodal signaling patterns the organizer. *Development* **127**, 921–932 (2000). pmid: 10662632
30. A. McKenna *et al*., Whole-organism lineage tracing by combinatorial and cumulative genome editing. *Science* **353**, aaf7907 (2016). doi: 10.1126/science.aaf7907; pmid: 27229144
31. B. Raj *et al*., Simultaneous single-cell profiling of lineages and cell types in the vertebrate brain. *Nat. Biotechnol.* **40**, 181 (2018). pmid: 29608178
32. D. A. Cusanovich *et al*., The *cis*-regulatory dynamics of embryonic development at single-cell resolution. *Nature* **555**, 538–542 (2018). doi: 10.1038/nature25981; pmid: 29539636
33. T. Dickmeis *et al*., A crucial component of the endoderm formation pathway, CASANOVA, is encoded by a novel sox-related gene. *Genes Dev.* **15**, 1487–1492 (2001). doi: 10.1101/gad.196901; pmid: 11410529
34. Y. Kikuchi *et al*., *casanova* encodes a novel Sox-related protein necessary and sufficient for early endoderm formation in zebrafish. *Genes Dev.* **15**, 1493–1505 (2001). doi: 10.1101/gad.892301; pmid: 11410530
35. M. E. Halpern *et al*., Cell-autonomous shift from axial to paraxial mesodermal development in zebrafish *floating head* mutants. *Development* **121**, 4257–4264 (1995). pmid: 8575325
36. C. B. Moens, V. E. Prince, Constructing the hindbrain: Insights from the zebrafish. *Dev. Dyn.* **224**, 1–17 (2002). doi: 10.1002/dvdy.10086; pmid: 11984869
37. L. Zhang *et al*., Noise drives sharpening of gene expression boundaries in the zebrafish hindbrain. *Mol. Syst. Biol.* **8**, 613 (2012). doi: 10.1038/msb.2012.45; pmid: 23010996

ACKNOWLEDGMENTS

We thank B. Raj and J. Gagnon for assistance collecting samples when two hands were insufficient, M. Rabani for assistance with the impulse model, M. Haesemeyer for the critical suggestions of directly simulating diffusion and of using visitation frequency as a method of dimensionality reduction, the Harvard Center for Biological Imaging and Bauer Core Facility for support, and members of the Schier and Regev laboratories for helpful discussions. We thank B. Raj, J. Gagnon, S. Pandey, N. Lord, M. Rabani, A. Carte, M. Haesemeyer, I. Whitney, and T. Montague for comments on the manuscript. **Funding:** This research was supported by the NIH (A.F.S., J.A.F., and A.R.), Allen Discovery Center for Cell Lineage Tracing (A.F.S.), Jane Coffin Childs Memorial Fund (J.A.F.), Charles A. King Trust (J.A.F.), Howard Hughes Medical Institute (A.R.), and Klarman Cell Observatory (A.R.). **Author contributions:** J.A.F., Y.W., A.R., and A.F.S, conceived the study; J.A.F., Y.W., and A.F.S. wrote the paper with revisions by A.R. and S.J.R.; J.A.F. and Y.W. collected the data; S.J.R. performed preliminary analyses; J.A.F., Y.W., and A.F.S. performed the data analysis presented in the manuscript; J.A.F. developed URD with input from A.R, S.J.R., and Y.W.; K.S. developed the variable gene identification method. S.J.R. and J.F. developed the 5′ UMI Smart-seq2 mapping pipeline; Y.W. performed the connected gene modules and spatial analyses. **Competing interests:** A.R. is a SAB member of ThermoFisher Scientific, Syros Pharmaceuticals, and Driver Group. **Data and materials availability:** The raw data reported in this paper are archived at NCBI GEO (accession no. GSE106587) and in processed and interactively browseable forms in the Broad Single-Cell Portal (https://portals.broadinstitute.org/single_cell/study/single-cell-reconstruction-of-developmental-trajectories-during-zebrafish-embryogenesis). URD is available from GitHub (https://github.com/farrellja/URD).

SUPPLEMENTARY MATERIALS

www.sciencemag.org/content/360/6392/eaar3131/suppl/DC1
Materials and Methods
Figs. S1 to S11
Tables S1 to S5
References (*38*–*51*)
Movie S1
Supplementary Analysis

26 October 2017; accepted 5 April 2018
Published online 26 April 2018
10.1126/science.aar3131

RESEARCH ARTICLE SUMMARY

SINGLE-CELL ANALYSIS

The dynamics of gene expression in vertebrate embryogenesis at single-cell resolution

James A. Briggs, Caleb Weinreb, Daniel E. Wagner, Sean Megason, Leonid Peshkin, Marc W. Kirschner,* Allon M. Klein*

INTRODUCTION: Metazoan development represents a big jump in complexity compared with unicellular life in two aspects: cell-type differentiation and cell spatial organization. In vertebrate embryos, many distinct cell types appear within just a single day of life after fertilization. Studying the developmental dynamics of all embryonic cell types is complicated by factors such as the speed of early development, complex cellular spatial organization, and scarcity of raw material for conventional analysis. Genetics and experimental embryology have clarified major transcription factors and secreted signaling molecules involved in the specification of early lineages. However, development involves parallel alterations in many cellular circuits, not just a few well-described factors.

RATIONALE: We recently developed a microfluidics-based single-cell RNA sequencing method capable of efficiently profiling tens of thousands of individual transcriptomes. Building on earlier studies that showed how single-cell transcriptomics can reveal cell states within complex tissues, we reasoned that a series of such measurements from embryos, if collected with sufficient time resolution, could allow reconstruction of developmental cell-state hierarchies. We focused on the western claw-toed frog, *Xenopus tropicalis*, which serves as one of the best-studied model systems of early vertebrate development. We profiled these embryos from just before the onset of zygotic transcription up to a point at which dozens of distinct cell types have formed encompassing progenitors of most major organs. To establish aspects of development general to vertebrates, we additionally incorporated data from the copublished paper by Wagner *et al.* on zebrafish embryos, which separated from frogs about 400 million years ago.

RESULTS: We profiled 136,966 single-cell transcriptomes over the first day of life of *Xenopus tropicalis*. Our analysis classifies 259 gene expression clusters across 10 time points, which belong to 69 annotated embryonic cell types and capture further substructure. Using a computational approach to link cell states between time points, a resulting cell-state graph agrees well with previous lineage-tracing studies and shows that developmental fate choices can be well approximated by a treelike model. Many cell states are detected considerably earlier than previously understood, thus revealing the earliest events in their differentiation. The data lends clarity to numerous specific developmental processes, such as the developmental origin of the vertebrate neural crest. Through an evolutionary comparison with zebrafish, we identified diverging features of developmental dynamics, including many genes showing cell-type specificity in one organism but not in another. Yet, we also identified conserved patterns in the reuse of transcription factors across lineages and in multilineage priming at fate branch points. The resulting resource is available in an interactive online browser that allows in silico exploration of any gene in any cell state (tinyurl.com/scXen2018).

ON OUR WEBSITE

Read the full article at http://dx.doi.org/10.1126/science.aar5780

CONCLUSION: The approaches and results presented here, along with the copublished paper by Wagner *et al.*, establish the first steps toward a data-driven dissection of developmental dynamics at the scale of entire organisms. They provide a useful, annotated resource for developmental biologists, comprehensively tracking differentiation programs as they unfold on a high-dimensional gene expression landscape. Although demonstrated on model organisms, the same approaches could be transformative to the study of nonmodel organisms by allowing rapid and quantitative description of differentiation processes across the tree of life, opening up a new front in evolutionary biology. ■

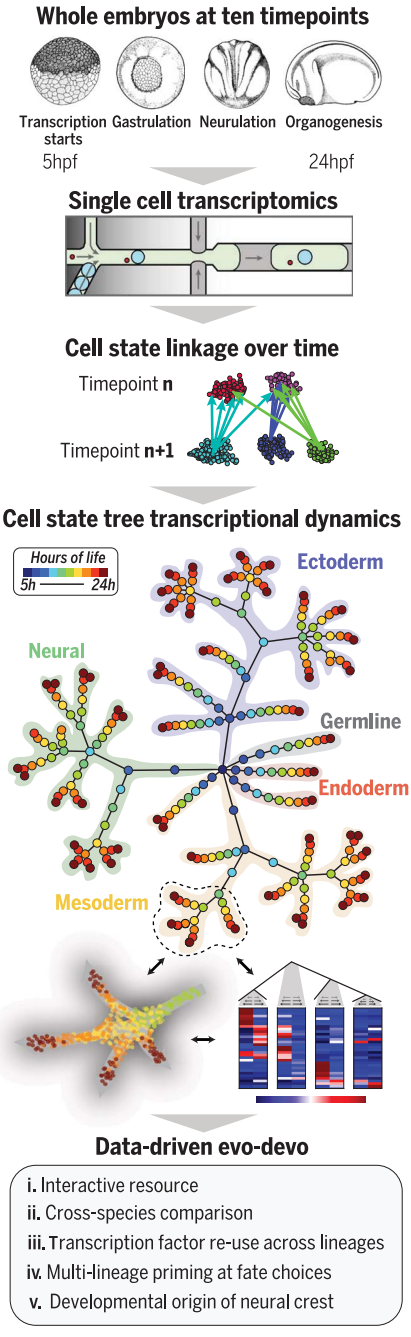

Single-cell analysis of whole developing vertebrate embryos. *Xenopus* embryos at 10 time points over the first day of life were dissociated, barcoded, and sequenced, yielding 136,966 single-cell transcriptomes. These data were clustered and connected over time to reveal a complete view of transcriptional changes in each embryonic lineage and clarify numerous features of early development. hpf, hours postfertilization.

The list of author affiliations is available in the full article online.
*Corresponding author. Email: marc@hms.harvard.edu (M.W.K.); allon_klein@hms.harvard.edu (A.M.K.)
Cite this article as J. A. Briggs *et al.*, *Science* **360**, eaar5780 (2018). DOI: 10.1126/science.aar5780

RESEARCH ARTICLE

SINGLE-CELL ANALYSIS

The dynamics of gene expression in vertebrate embryogenesis at single-cell resolution

James A. Briggs, Caleb Weinreb, Daniel E. Wagner, Sean Megason, Leonid Peshkin, Marc W. Kirschner,* Allon M. Klein*

Time series of single-cell transcriptome measurements can reveal dynamic features of cell differentiation pathways. From measurements of whole frog embryos spanning zygotic genome activation through early organogenesis, we derived a detailed catalog of cell states in vertebrate development and a map of differentiation across all lineages over time. The inferred map recapitulates most if not all developmental relationships and associates new regulators and marker genes with each cell state. We find that many embryonic cell states appear earlier than previously appreciated. We also assess conflicting models of neural crest development. Incorporating a matched time series of zebrafish development from a companion paper, we reveal conserved and divergent features of vertebrate early developmental gene expression programs.

Metazoan development represents a big jump in complexity compared with unicellular life in two aspects: cell type differentiation and cell spatial organization. The fertilized egg was once itself thought to be very complex, concealing the spatial and compositional differentiation of the adult. However, it is now clear that the egg is a rather simple cell, and the complexity of the embryo and adult arises by bootstrapping: repeatedly exploiting spatial asymmetries to build the complex embryo by stages. In vertebrate embryos, as well as in other phyla, a provisional body plan organization arises before overt cell-type–specific differentiation, and this provides a scaffold for the emerging complexity.

The process of increasing spatial and cell-type heterogeneity has been difficult to follow comprehensively at the molecular level. Many insights have emerged from genetic studies and experimental embryology, but those analyses generally focus on a few transcription factors and/or secreted signaling molecules. Instead, development involves alterations in many different intracellular and intercellular circuits. Recent technology advances have enabled the mapping of mRNA content in single cells over time, which could in principle systematically reveal differentiation pathways across entire developing embryos (Fig. 1A).

Two years ago, we developed a versatile single-cell transcriptomic method based on droplet microfluidics that accurately measures genome-wide RNA levels in individual cells at high throughput (*1*). We applied this method to analyze all of the cells in the embryos of the Western clawed frog, *Xenopus tropicalis*, over the first day of life after fertilization. Along with its larger relative *X. laevis*, the frog embryo serves as one of the best-studied model systems of early vertebrate development. The egg undergoes 12 rapid cleavage divisions, during which time zygotic transcription is suppressed. The resulting 4000 cells are initially pluripotent. However, within 4 hours of activating zygotic transcription at the midblastula transition (*2*, *3*), embryos go through gastrulation to establish the major germ layers, followed by fate commitment and progressive differentiation (*4*). We profiled embryos before the onset of zygotic transcription, through fate commitment, and into the early tailbud stage—a point at which dozens of distinct cell types have formed encompassing the early progenitors of most major organs. In the course of this work, we developed general computational tools that can relate cell states over time, providing a global view of gene expression diversification in the early embryo. Finally, we compared the results of this analysis to our recently completed time series of the developing zebrafish, *Danio rerio*. Through systematic analyses across lineages, time, and species, we note generalities and differences in embryonic cell differentiation in the two vertebrate clades, which separated about 400 million years ago.

Department of Systems Biology, Harvard Medical School, Boston, MA 02115, USA.
*Corresponding author. Email: marc@hms.harvard.edu (M.W.K.); allon_klein@hms.harvard.edu (A.M.K.)

Single-cell RNA sequencing of whole developing embryos

Xenopus blastomeres are large and fragile, with cell diameters up to 50 μm (for *X. tropicalis*, compared with 100 μm for *X. laevis*) at the onset of zygotic transcription (stage 8.5). To preserve the integrity of cells through tissue dissociation and microfluidic handling, we optimized the inDrop platform to accommodate large cells. We also formulated a dissociation buffer that uses alkaline pH to promote dissociation and handling procedures that minimize shear stresses placed on cells. The new protocol enables rapid and complete dissociation of whole embryos to single cells within 25 min, with minimal mechanical agitation and cell handling, preservation of >95% cell viability, and background single-cell RNA sequencing (scRNA-seq) signal (indicative of cell lysis) of <1 to 4% of total cellular RNA from stage 10 onward (fig. S1).

The samples for scRNA-seq were taken at 10 time points from zygotic genome activation [stage 8, 5 hours postfertilization (hpf)] through early organogenesis (stage 22, 22 hpf), profiling a total of 136,966 single cells in two replicate experiments (table S1 and movies S1 to S3). The first replicate consisted of 42 k cells sequenced to a depth of 5.4 k unique molecular identifiers (UMIs) per cell on average (99% of genes from bulk RNA-seq observed in pools of >100 cells), whereas the second replicate of 95 k cells was sequenced to an average depth of 1.4 k UMIs per cell. The number of measured cells allows detection of rare subpopulations such as germ cells. Overall, we expect to observe transcriptional states as rare as 0.1% of the embryo represented by at least 10 cells with 95% confidence (fig. S2). There may be rare or transient subpopulations that are missed given the total number of cells, time sampling, and the depth of sequencing we used.

Low-dimensional visualization of the scRNA-seq time series shows a pattern of increasing complexity over time, with cells fragmenting from a continuum of gene expression states in the early gastrula into distinct clusters at later time points (Fig. 1B and figs. S3 and S4). To relate the scRNA-seq data to known embryonic cell types, we first classified gene expression states at each time point by a hierarchical clustering approach (Figs 1B and fig. S3). These cluster assignments were robust to different clustering algorithms (figs. S5 and S6). We then annotated each cluster by matching cluster-specific genes to >2000 in situ measurements of marker genes for embryonic cell types documented on the *Xenopus* Bioinformatics database (Xenbase) (*5*) (see Data S1). We additionally shared our annotations with experts in the *Xenopus* research community, convened in part for that purpose at a recent Jamboree meeting, who helped to standardize our cell-state nomenclature and choice of annotations. In total, we identified 87 distinct cell-type annotations, many of which persisted in clusters across multiple time points (average of 2.9 time points each) (Fig. 2C). Of these 87 states, 69 corresponded unambiguously to a specific Xenbase anatomical term, whereas the remaining 18 states correspond to finer structure (i.e., cell subtypes) or unidentified cell states within these anatomically defined tissues. Further substructure

may be resolved by manual inspection of marker genes employing previous expert knowledge.

Reconstructing developmental cell-state transitions

Fate mapping studies have previously established a set of spatial lineage relationships in the *Xenopus* embryo; these generally support the notion of a hierarchical pattern of differentiation, albeit with some exceptions (*6*). We investigated the extent to which these known hierarchical lineage relationships are reflected in our map of expression states. A close match was not assured because there are several reasons that cell lineage hierarchies might not be reflected in molecular expression. First, gene expression states are defined not only by tissue but by spatial position and cell cycle state, which cross lineage boundaries. Second, asymmetric cell divisions could lead to discontinuities in cell state as a mother cell partitions into daughter cells with distinct molecular compositions. Third, although the lineage history of individual cells consists entirely of discrete bifurcation (mitosis) events, cell states could be continuous or show complex branching structures or even loops. Yet, counteracting this, in the lineage data of the early embryo, new gene expression generally arises in single contiguous domains.

To ask whether the single-cell gene expression states conform to a branching pattern and, if so, whether the pattern overlaps with the previously deduced lineage patterns, we devised a simple algorithm that connects each cell to its most likely ancestors (i.e., nearest neighbors) in the previous time point and uses the consensus of these connections to assign an ancestor to each cell state (Fig. 2A). By applying this algorithm to all 259 cell states, composed of 136,966 *Xenopus* cells spread over 10 time points (Fig. 2B), we generated a detailed map of putative cell-state transitions during early development (Fig. 2C and fig. S7). The map recapitulates known expression domains of master regulators within each germ layer over time (fig. S8). Notably, only 17% of all votes fell outside of consensus ancestor clusters, showing that cell states over development can generally be approximated by a treelike structure (Fig. 2D and fig. S7). The majority of votes cast outside of consensus ancestor states occurred at early time points, due to their continuum structure. The branching nature of cell states can also be appreciated by inspecting individual lineages at single-cell resolution (Fig. 2, E and F). The inferred cell-state tree structure was consistent with ancestor assignments generated using an alternative-state graph coarse-graining algorithm reported in our companion paper (*7*) (fig. S9).

The ancestor assignments largely agree with the known lineage relationships. Of all cross–time point edges inferred by the algorithm (Fig. 2C), we could confirm 234 (91%) by comparison to Xenbase anatomy ontology (XAO) (*8*, *9*) and the literature (see Data S2). Of the remainder, 22 could not be ruled in or out, and only 2 (1%) were identifiably incorrect. The two errors, which occurred in somites and erythroid lineages, reflected a specific limitation of the tree-building approach: In both lineages, mature states initially arise from progenitors but then form a parallel branch rather than continuously arising from progenitors anew at each time point. Visualization of the raw scRNA-seq data reveals the underlying asynchronous differentiation process (fig. S10). In addition to these errors, the cell-state tree does not consistently resolve spatial localizations—e.g., we do not resolve individual somites. The tree-building approach could additionally generate errors when applied to other data sets lacking the dense time-sampling carried out here. When inferring cell-state transitions from scRNA-seq snapshots separated by large gaps in time, intermediate progenitor states may be overlooked. Overall, these results support a growing body of single-cell bioinformatics methods that seek to infer developmental cell trajectories on the basis of continuity (*10*, *11*) and distance minimization (*12*) in gene expression space, but also illuminate where this principle can be misleading.

Among the developmental relationships inferred on the tree, there is also a question about the timing at which known cell types first appear. Of the 69 cell types with an unambiguous match to Xenbase, 60 appeared in our data at the developmental stage indicated in XAO (*8*, *9*) or earlier. Several appeared much earlier than previously recognized (Fig. 3A), including an endothelial/hemangioblast progenitor, which appeared from the dorsal lateral plate region at stage 18, as compared with stages 26 and 31, respectively, as previously thought (*13*, *14*) (Fig. 3B). This afforded an opportunity to explore the earliest transcriptional events associated with the specification of these fates (Fig. 3C). The tail bud and multiple epidermal cell types also appeared much earlier than indicated by XAO (Fig. 3A and Data S2) and revealed previously unknown early transcriptional dynamics.

Overall, the cell-state tree provides a resource for probing gene expression in the early *Xenopus* embryo, incorporating annotations of cell states, linking related states across time, and discovering the earliest transcriptional record of the specification of each cell type. It is now possible to identify genes that are differentially expressed

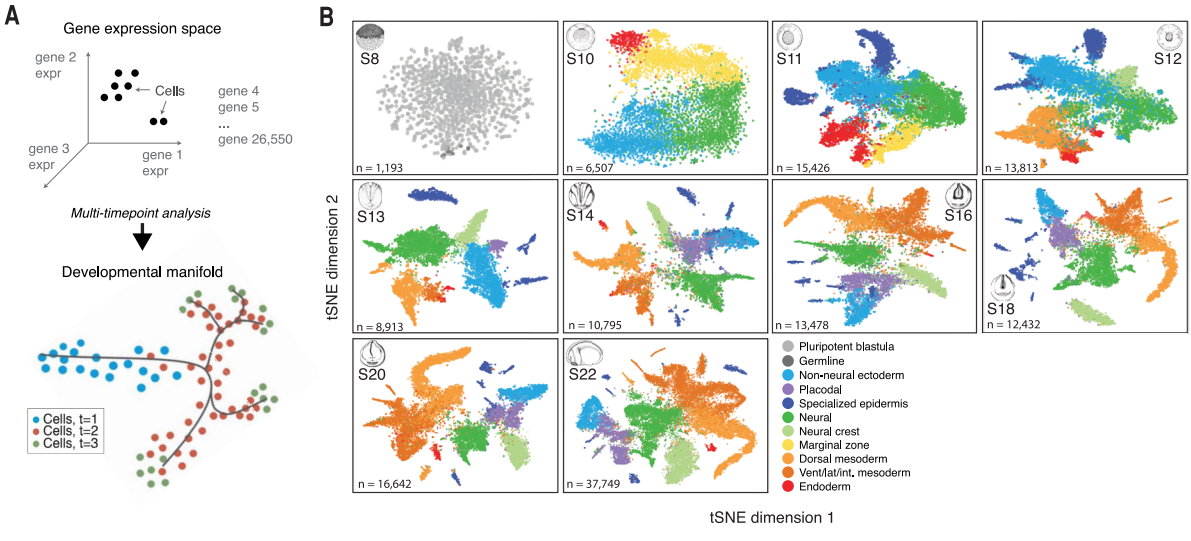

Fig. 1. Dissection of early *Xenopus tropicalis* development by scRNA-seq. (**A**) Single-cell transcriptomes represent points in a high-dimensional gene expression space. By collecting single-cell transcriptomes over time of embryo development, it is possible to infer a continuum gene expression manifold connecting cell states across all lineages. (**B**) Summary of scRNA-seq developmental time course, including 136,966 single-cell transcriptomes sampled over 10 embryonic stages (S8, S10 to S14, S16, S18, S20, and S22). T-Distributed stochastic neighbor embedding (tSNE) plots show increasing cell population structure over time. Colors indicate major tissues grouped by germ layer. Further details on subclustering shown in figs. S3, S5, and S6 and at tinyurl.com/scXen2018.

between bifurcating cell states, to assess gene expression changes along the developmental history of each lineage, and to automatically identify specific marker genes for each cell state (fig. S11). We have tabulated genes differentially expressed at every embryonic cell-fate choice (see Data S3), indicating potential fate regulators, as well as marker genes for every cell state (see Data S4). The complete data set is available through an interactive online browser (tinyurl.com/scXen2018), which supports visualization of gene expression across the cell-state tree, identification of enriched genes in specific states, differential expression analysis between cell states, coexpression analysis of gene pairs, and visualization of the dynamics of gene expression along particular cell-state tree branches. Interactive plots of single cells from each stage are also available through this browser.

Divergence of developmental gene expression between frog (amphibians-anurans) and fish (teleosts)

There are numerous cladograms of gene sequence that confirm the basic paleontological record of vertebrates, reflected in clear differences as well as similarities between *Xenopus* and zebrafish in their sequenced genomes. But whenever there is a change in anatomy, cell type, and physiology there must be an underlying alteration in the developmental program. Time-series single-cell gene expression measurements offer an opportunity to look deeply into these developmental gene expression programs and give us clues about the most consequential evolutionary changes across species. We first asked whether the same (i.e., orthologous) genes are conserved in developing tissues in frog and fish using data from our companion paper on zebrafish development (*7*), which spans a developmental period similar to that of the frog dataset. We processed the zebrafish time series through the same tree-building algorithm over annotated cell states. We manually aligned cell states between species (Fig. 4A, red shading) on the basis of tissue name, marker gene expression, developmental stage, and lineage relationships. In some cases, nomenclature of homologous tissues differed slightly between species. Thirty tissues could be matched with high confidence, jointly covering 66 of 87 *Xenopus* states (79% of cells) and 83 of 122 zebrafish states (83% of cells). The cell-state tree alignment indicated broad conservation of lineage topologies between species, although the observed abundances of cell types differed markedly between species, and the proportion of matched states and cells decreased over time as species-specific features accumulated—such as specialized epidermal cell types in both species (fig. S12). Notably, the zebrafish neural ectoderm grew to 60% of sequenced cells in the embryo at 24 hpf, compared with 31% in the stage 22 frog (fig. S13). Differences in cell survival rates during InDrops processing in either species could affect estimates of cell-state abundances.

The alignment of the cell-state trees also highlighted significant changes in developmental patterning between the two species, which could further be understood by deeper inspection of the underlying single-cell data. In the epidermis, for example, the two species show a radiation of common and distinct cell types from gata2-expressing non-neural ectoderm (Fig. 4B and fig. S14). Trajectories of differentiating ionocytes can be seen in both species, whereas ciliated cells expressing foxj1, goblet cells expressing itln1, and small secretory cells expressing met (fig. S14), each of which is an important component of the *Xenopus* epidermis, are absent in zebrafish. These different epidermal cell types likely reflect the demands of development in different environments, potentially requiring an early immune barrier in the frog but not the fish. Rearrangements of lineage topology can also be understood: *Xenopus* and zebrafish both produce specialized hatching glands (HG) that secrete shared hatching enzymes and that are specified by the conserved transcription factor klf17, seen by scRNA-seq (fig. S15). Single-cell trajectories link the HG to non-neural ectoderm in *Xenopus* but to the organizer mesoderm in zebrafish (Fig. 4A and fig. S15), reflecting a known difference in HG germ layer origin between amphibians and teleosts (*15*).

Other more subtle changes in lineage topology involved the addition or loss of specialized progenitor cell states within a partially shared developmental history. For example, xanthoblasts appear at 18 hpf in zebrafish from an early neural crest population but do not appear until stage 46 in *Xenopus* (*16*), after the shared ancestral neural crest population has progressed through multiple

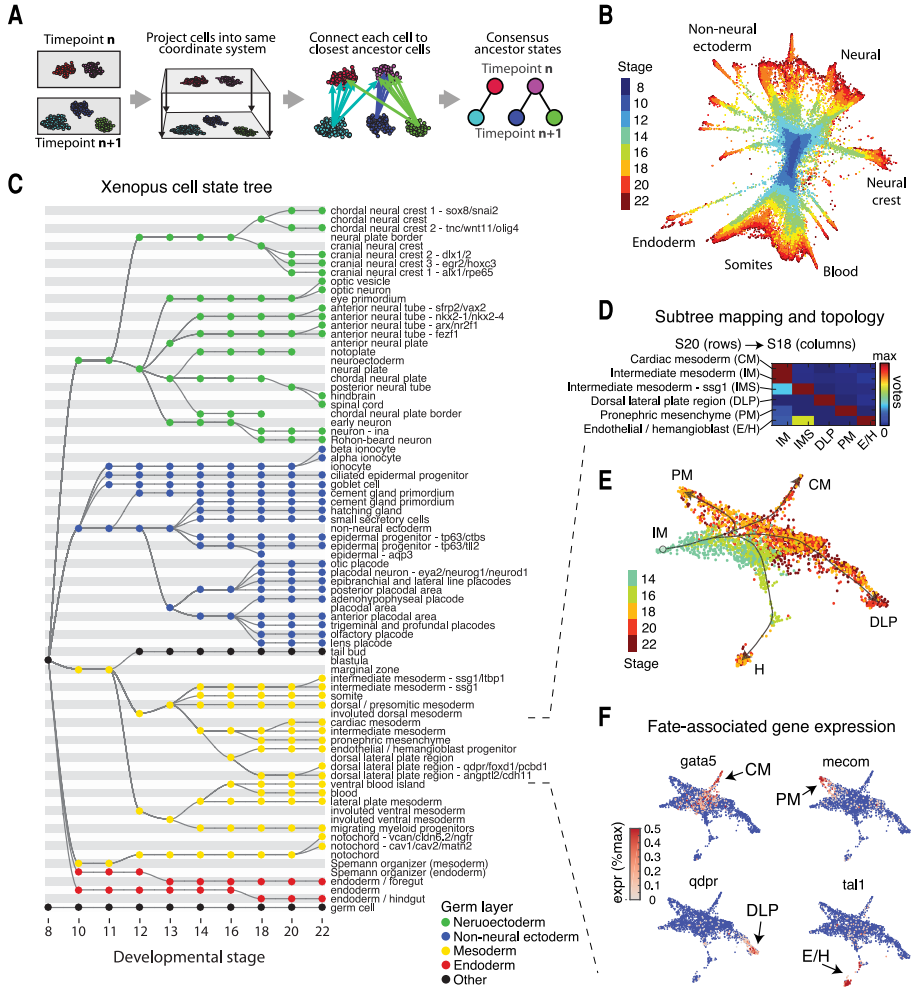

Fig. 2. Inference of developmental cell-state transitions from gene expression similarity. (**A**) Schematic of the mapping algorithm used to make similarity connections between clusters across time. (**B**) Global visualization of single cells profiled in the *Xenopus* developmental time course using a *k*-nearest neighbor graph (*7*). (**C**) Cell-state tree showing all inferred developmental transitions. Generated by applying the mapping algorithm in (A). (**D**) Representative cell voting outcomes between time points, generated during state tree construction. (**E**) Single-cell visualization of a representative subtree, showing lateral and intermediate mesoderm fates. Lines indicate corresponding topology of the cell-state tree. (**F**) Marker gene expression associated with the formation of each intermediate mesoderm cell state.

additional specialized neural crest intermediate states. Similarly, myeloid cells appear in *Xenopus* at stage 14 from early involuted ventral mesoderm, whereas they (macrophages and leukocytes) appear only at 18 to 24 hpf in zebrafish, after the ventral mesoderm has differentiated through specialized cardiovasculature and lateral plate intermediate states. Terminal differentiation of myeloid cells in both cases involves activation of several conserved master regulators, including cybb, cyba, spib, and cebpa. These observations support a degree of independence between the differentiation path characterizing a lineage and the activation of particular conserved terminal cell phenotypes (*17*). Variation in differentiation paths can reflect not only drift or flexibility in developmental programs but also selected features of embryonic cells, including roles in interacting with and instructing other differentiation and morphogenetic mechanisms.

To obtain a systematic view of similarities and differences in developmental gene expression across species, we used the aligned cell-state trees to investigate whether orthologous genes show correlation in expression values across matched embryonic tissues (Fig. 4C). Focusing on the subset of genes that were robustly expressed and dynamically varying in both species, we observed that orthologous genes correlated in their expression between species (Fig. 4C), seemingly supporting the notion that cell-state gene expression is largely conserved. However, only a minority (30%) of orthologous pairs were correlated with high confidence [5% false discovery rate (FDR)] compared with random pairs. For example, in contrast to the well-conserved (r = 0.9) neuroectodermal marker sox2, we identified many examples of poorly correlated genes such as the transcription factor gata5 (r = 0.1) (Fig. 4C). Despite being a conserved endoderm and cardiac master regulator, gata5 is also expressed in the erythropoietic tissue only of *Xenopus* (*18*) and in the marginal zone only of zebrafish (*19*) at a distinct spatiotemporal location of endoderm specification compared with the vegetal expression seen in *Xenopus*. Accordingly, we were surprised to find that the genes best marking cell states within one species did not generally perform well at marking the same cell states within the other (fig. S16).

We tried to understand what properties predict whether a gene shows conserved expression patterns across tissues across species—i.e., whether specific functional categories of genes are more likely to be conserved in expression dynamics. Analysis of gene ontology annotations spanning diverse cellular processes revealed a striking enrichment of gene expression conservation among transcription factors, identifying three statistically significant (P < 0.05; binomial-test, Bonferroni corrected) functional annotations that include "nucleus," "regulation of transcription," and "transcription factor activity" (Fig. 4D). By contrast, protein sequence conservation was uncorrelated to gene expression conservation (r = 0.01; P = 0.6). Orthologous genes with 20 to 40% sequence identity had the same expression conservation as those with 95 to 100% sequence identity (average expression conservation of 0.41 versus 0.38, P = 0.5; t test). A gene's function is therefore more strongly predictive of its conservation in developmental gene expression programs across species than conservation of its protein sequence, decoupling two fundamental processes underlying evolutionary changes in embryonic development.

Reuse of developmental transcription factors

Given the close association and conservation of transcription factors with differentiation, and hence cell type, we asked two questions: (i) How are transcription factors deployed across cell types and across time during development? (ii) How, at the level of genes, do new cell identities emerge at branch points in development? These questions can be examined here in dozens of cell states and in the unperturbed setting of the embryo, rather than in cell culture.

Classical experiments have described differentiation in terms of the activation of single transcription factors, called master regulators, which established cell identity and after which other transcription factors progressively refined the phenotype (*20*) (Fig. 5A). Alternative views, however, ascribe the initial specification of cell identity to interactions among multiple transcription factors (TFs), a "combinatorial code," capable of defining a larger number of identities with different combinations from a small set of TFs (*21*, *22*) (Fig. 5B). We asked which of these views best describes early development. This is not just of theoretical interest, because knowing which transcription factor(s) could specify a given cell type could aid in the formulation of combinations that could be used therapeutically (*23*). Our experiments identify some cases where candidate TFs are activated just once in early development and after which they persist and may define a lineage, suggesting a master regulator model. But we also see TFs that are expressed more than once de novo in distinct and unrelated cell states, which may support a model of combinatorial deployment.

To understand the prevalence of these modes of TF use, we scored the number of times a TF was expressed independently—i.e., in states that share a nonexpressing common ancestor. From this analysis, we found that the expression of half of developmentally variable TFs is initiated only once during early development (52% in frog, 54% in zebrafish) (Fig. 5C). The detected single-use TF induction events occurred in just 35% of annotated cell states, seemingly inconsistent with the view that distinct master TFs define each fate. Reused TFs, by contrast, cover 58% of tissue annotations in a complex combinatorial code

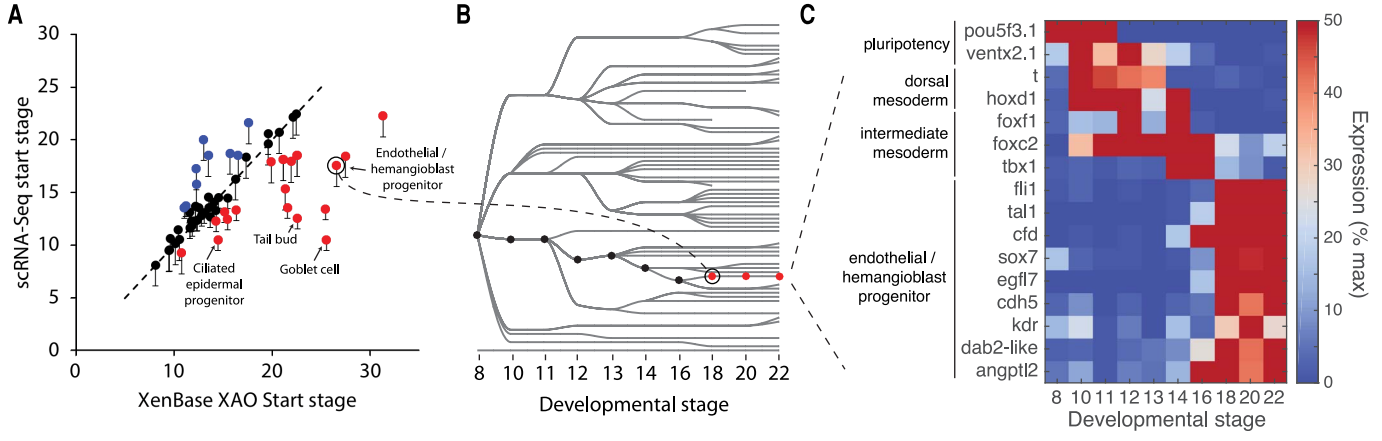

Fig. 3. scRNA-seq detects early transcriptional events during specification of embryonic cell states. (**A**) Time of first appearance for each cell state in the cell-state tree as compared with documented appearance times in the *Xenopus* anatomy ontology (XAO). Red/blue points are detected early/late in scRNA-seq as compared with XAO. Sixty of 69 states appear as early or earlier than documented. Error bars represent time interval of scRNA-seq experiment. (**B** and **C**) scRNA-seq reveals an early endothelial/hemangioblast progenitor that appears at stage 18 (red lineage), as compared with stage 26 for hemangioblasts and stage 31 for endothelial cells [XAO (*12*, *13*)], with recognizable activation of the endothelial/hemangioblast gene expression program (C).

(see Data S5). In the remaining 7% of cell states, a specific TF induction was not detected. Over time, the average fraction of transcription factors being reused in a second circumstance climbs, reaching ~90% of new TF expression initiation events by stage 20 (18.5 hpf) in *Xenopus* and by 20 hpf in zebrafish (Fig. 5D). Together these results underscore the importance of combinatorial TF reuse in developmental gene expression programs.

Consistent with the notion that combinatorial interactions could lead to complex gene expression responses, the expression of the same TF in different tissues did not generally correlate with the same gene sets, as seen in the example of Pax8, which is independently expressed in the otic placode and pronephric mesenchyme (Fig. 5E). Some putative downstream targets of reused TFs could, however, be identified in more than one tissue, as in the case of foxj1, which is expressed in both the ciliated epidermis and the floor plate and orchestrates motile cilia formation. Many of the genes correlating with foxj1 transcript abundance within the floor plate also correlated with foxj1 in the epidermis and were highly enriched for ciliogenesis gene ontology (GO) terms (Fig. 5F). Interestingly, we found that TFs deployed just once over the observed time series were more conserved in their expression pattern across the two species compared with reused TFs (median

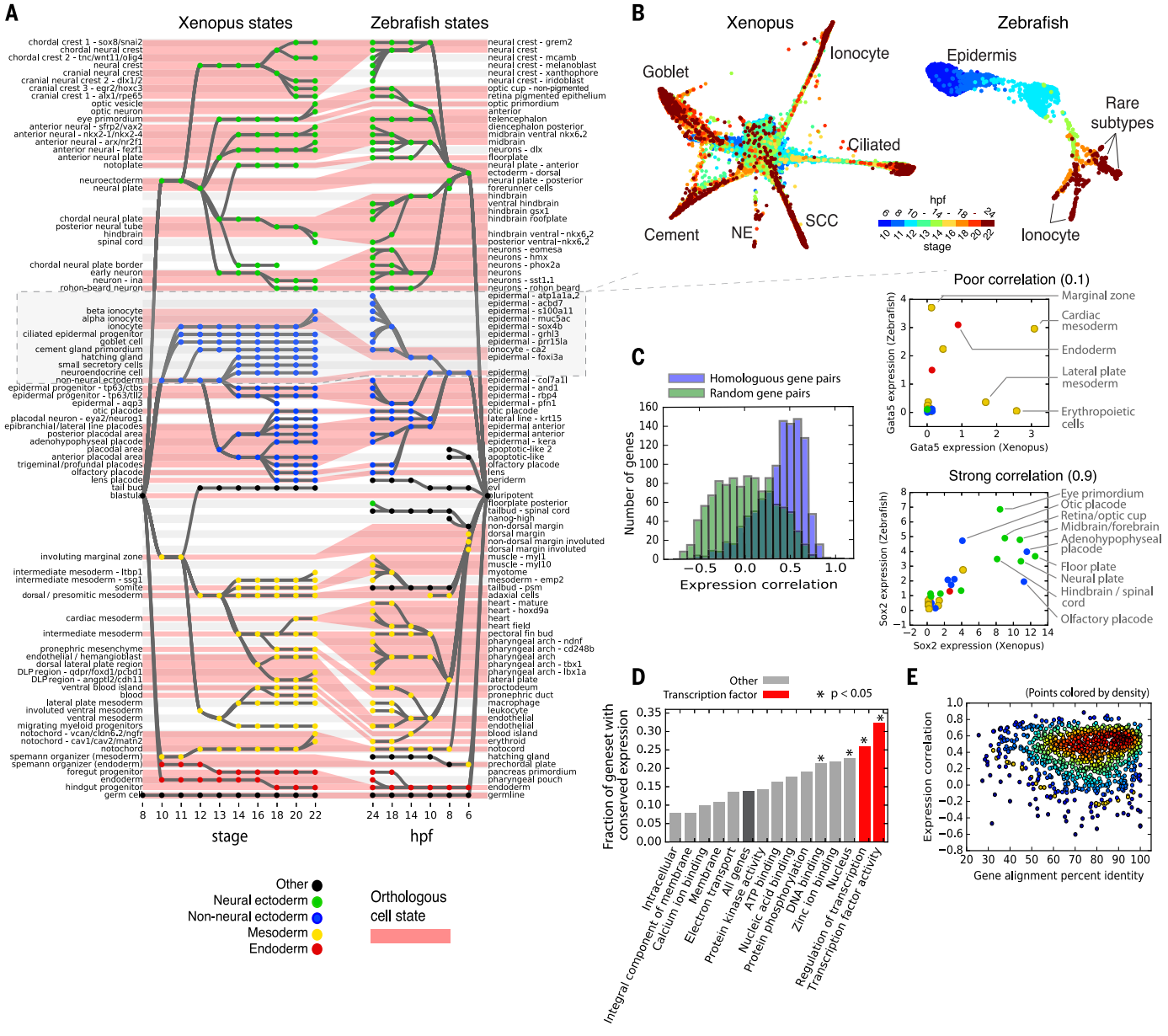

Fig. 4. Similarities and differences in developmental cell-state hierarchies and gene expression between frog and fish. (**A**) *Xenopus* and zebrafish cell-state trees aligned by orthologous cell states (red shading). Gray/white stripes provide a visual guide. (**B**) Single-cell visualization of matched epidermal subtrees in frog and fish showcase similarities and differences in developmental hierarchy. SCC, small secretory cell; NE, neuroendocrine cell. Unidentified zebrafish cell types are labeled by marker genes. (**C**) (Left) Ortholog genes across species have variable conservation of cell-state–specific expression. Just 30% of self-similar orthologs are conserved at a 95% FDR compared with random gene pairs. (Right) Examples of highly (Sox2) and poorly (Gata5) correlated TFs across species. (**D** and **E**) Function, not sequence, predicts gene expression conservation. (D) Orthologs with highly conserved expression patterns across species are enriched in TF-associated GO terms. *P* values show Bonferroni-corrected binomial test results. (E) Protein sequence conservation is not correlated with gene expression conservation (r = 0.01; P = 0.6).

correlation 0.72 versus 0.48 in frog; 0.64 versus 0.36 in fish). This may indicate that reused TFs are more commonly rearranged across tissues during evolution to generate novelties, whereas TFs whose field of expression is established just once might have more conserved regulatory functions.

Multilineage gene expression priming during fate choices

It has been shown in several specific cell types—including hematopoietic stem cells (*24*) and mouse embryonic stem cells (*25*)—that uncommitted cells may coexpress competing fate regulators associated with more than one terminal cell fate. Such gene expression overlap, followed by refinement as cells differentiate, is known as multilineage priming (MLP) (Fig. 6A). MLP has been argued to be a part of the process of cell-type decision-making, through competition between fate regulators, and also to play a role in specifying an undifferentiated state by blocking lineage commitment (*25*–*28*).

The importance of MLP for cell-fate decisions is clearly supported by these specific examples, but its importance would be further strengthened if it were generally associated with branch points in differentiation. Our scRNA-seq data offered an opportunity to assess this over entire embryos. Wardle and Smith had previously (*29*) noted transient overlap and then refinement between the ectoderm-specific TF Sox2 and the mesoderm-specific TF Brachyury (T) during gastrula stages in *Xenopus*. This was recapitulated in our data, which shows coexpression of these markers in 26% of cells expressing either gene at stage 10, but refinement to just 3% overlap by stage 14 (Fig. 6, B and C). Our data also show numerous other examples, including similar MLP between early ectodermal TF Zic1, and the mesodermal TF Foxc1, which overlap in expression at stage 10 (7% coexpression) before refinement by stage 12 (<3% coexpression) (Fig. 6B). Across all fate choices in the embryo, we identify 412 MLP genes in *Xenopus* (see Data S6). We find that MLP is initially widespread, encompassing a considerable fraction of highly cell-state specific genes at each branch point (>4-fold differentially expressed), but reduces over time (Fig. 6, D and E). For fate choices that occur before or up until the end of gastrulation, over 70% of highly cell-state specific genes overlapped in their progenitor state in fish and ~50% in frog. By contrast, for subsequent fate choices, MLP ultimately drops to <10% in both species (Fig. 6D). All differentiation branch points showed multilineage overlap before gastrulation, whereas only selected branch points showed frequent MLP after gastrulation (Fig. 6E).

Where MLP did occur, we wondered if it reflected generally noisy gene expression or, more specifically, coexpression of regulators of cell fate. Suggestive of the latter possibility, MLP genes were significantly enriched for TF-associated GO terms, including "transcription factor activity," "regulation of transcription," "nucleus," and "DNA binding," as compared to all differentially expressed (DE) genes (fig. S17) (two-fold enriched; $P < 0.001$ binomial test, Bonferroni corrected).

Assessing the retention of pluripotency during neural crest development

The utility of single-cell gene expression maps extends from studying general features of development to clarifying specific developmental relationships. Among embryonic lineages, the neural crest is unique in its broad fate potential, contributing to multiple tissues spanning germ layer boundaries. It remains an open question how this unique fate potential arises. As the neural crest forms (stages 13 and 14), it expresses at least eight pluripotency genes—*foxd3*, *c-myc*, *id3*, *tfap2*, *ventx2*, *ets1*, *snai1*, and *oct25*—which are also expressed in the early blastula (stages 8 and 9) (*30*). Functional assays showed that several of these genes are required for multipotency of both blastula and neural crest cells (*30*). This raised the intriguing possibility that the neural crest may retain multipotency from the blastula stage (a "retention model"), in contrast to the classical view that a field of ectodermal tissue

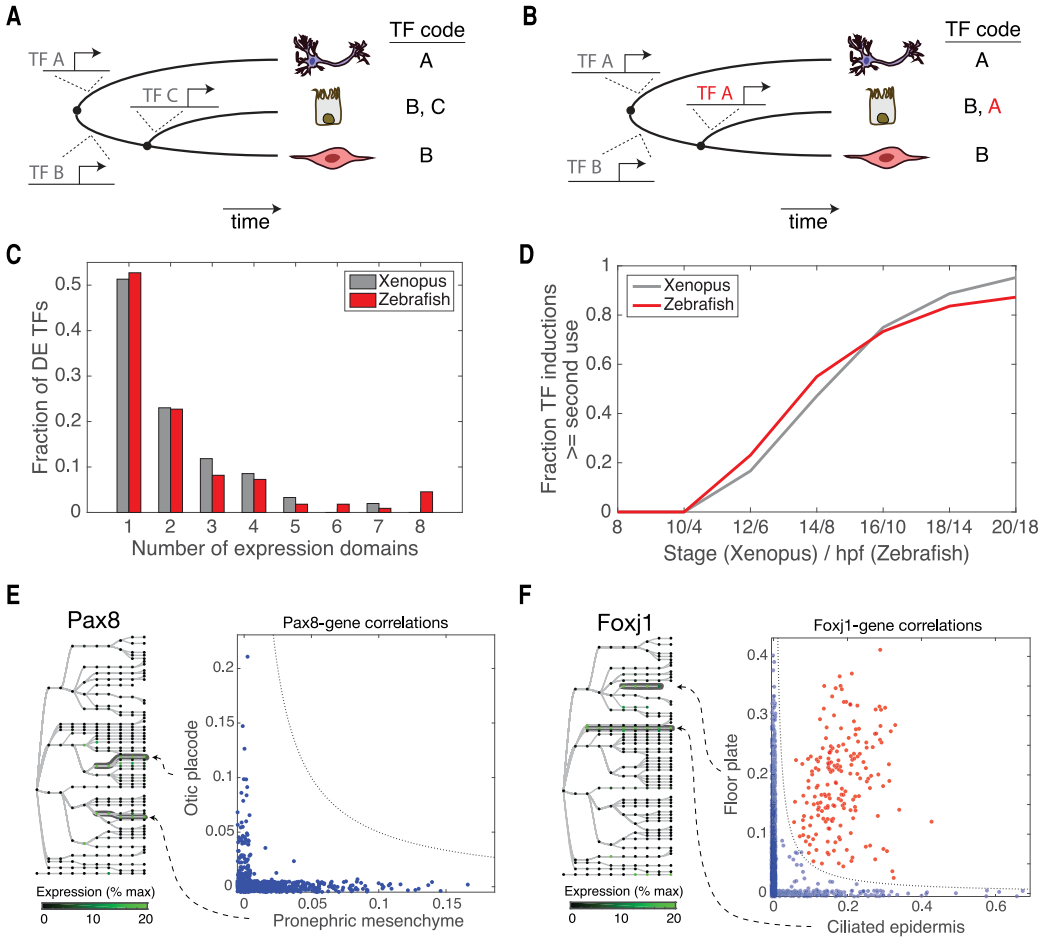

Fig. 5. TF reuse is pervasive in vertebrate development. (**A**) Progressive programming of cell identity through sequential TF activation. (**B**) Programming of cell identity through combinatorial reuse of TFs. TF A is reused (red) in combination with TF B to generate a new fate. (**C**) Half of DE TFs are induced more than once in early frog and fish development. (**D**) Reused TFs increasingly dominate new TF expression during fate choices over time. (**E** and **F**) Reused TFs correlate with context-dependent (blue; off-diagonal) or conserved (red; on-diagonal) gene expression modules. (E) Pax8 correlates with different genes in the otic placode and the pronephric mesenchyme. (F) Foxj1 correlates with ciliogenesis genes both in the floor plate and in ciliated epidermal cells.

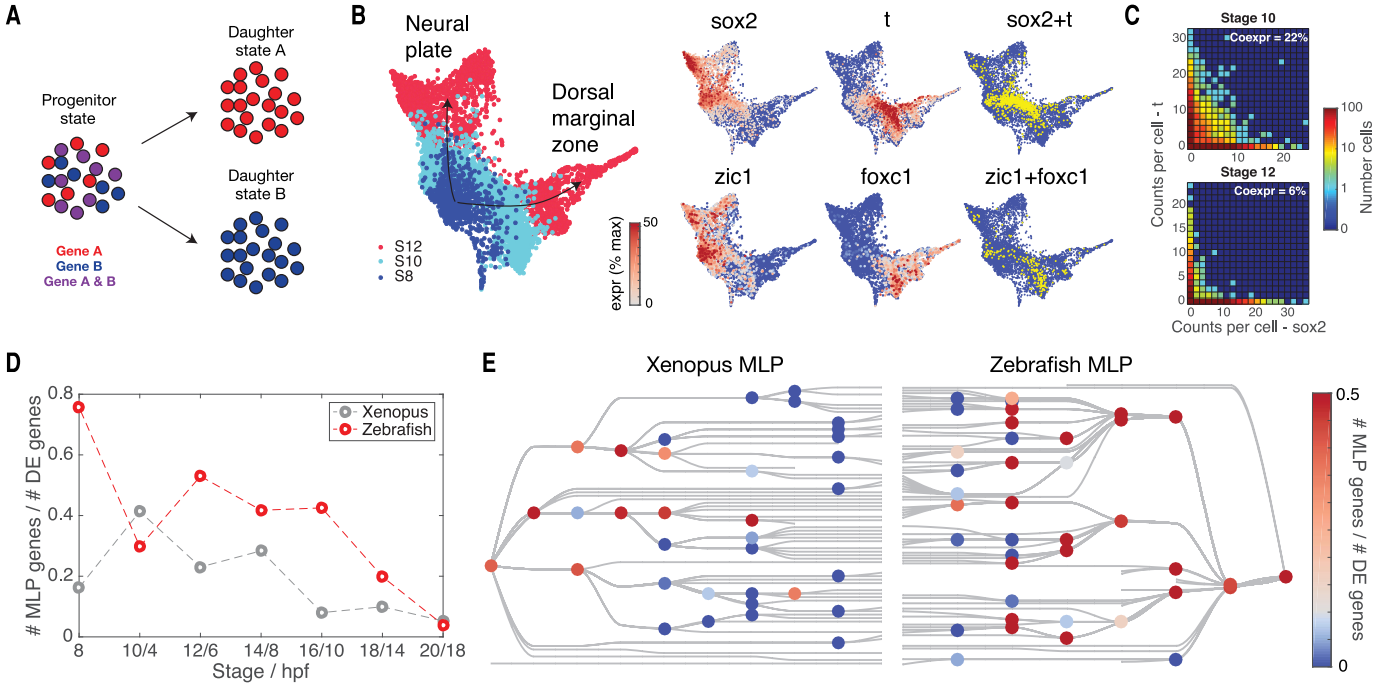

Fig. 6. Refinement of promiscuous multilineage gene expression during early embryonic fate choices. (**A**) Illustration of multilineage priming (MLP). Two genes, specific to daughter states A and B, respectively, transiently overlap in the ancestor progenitor state as a fate decision is being made. (**B** and **C**) MLP during the fate choice between neural plate and dorsal marginal zone in *Xenopus*. Sox2 and T, as well as Zic1 and Foxc1, overlap in progenitor cells before becoming specific. (**D** and **E**) Global patterns of MLP in early development. (D) Multilineage primed genes are initially pervasive among DE genes at fate branch points but become progressively rarer. (E) MLP frequency shown for each cell-fate choice on the cell-state trees indicates sporadic MLP at later time points.

reacquires multipotency during early neurulation (Fig. 7A). However, this model remains a hypothesis because a multipotent intermediate state between blastula and neural crest stages has not been directly identified.

Our single-cell data offers an opportunity to reexamine these alternative hypotheses with a high-resolution view of the intermediate states between blastula and neurula stages in neural crest development. To support the "retention model," we specifically searched for a subset of cells that maintain a blastula gene expression program, distinct from the remaining early ectoderm. To further increase the likelihood of finding such cells, we supplemented our whole embryo time series with additional scRNA-seq data (9308 cells) collected from tissue that we dissected from the neural plate border region, which is fated to become neural crest, of stage 11 embryos, immediately before the expression of neural crest genes (total of 15,426 stage 11 cells). These data in frog, and matching data in fish, failed to reveal a distinct cluster of cells defined by expression of the proposed pluripotency genes, nor a cluster defined by any other set of genes enriched in the blastula. Instead, the data supported a more conventional differentiation pathway through clearly identifiable neuroectodermal intermediates (Figs. 7B and 4A). The same results held when examining differentiation progression not at the cell cluster level but at single-cell resolution (Fig. 7C). Far from showing a gene expression program that persists from the blastula stage, we found that the inferred precursors of the neural crest showed large changes in gene expression with hundreds of dynamically varying genes (Fig. 7D). The proposed suite of eight pluripotency genes, in particular, were not limited to a single cluster of cells but were broadly expressed across most of the ectoderm, as well as in nonpluripotent states such as the endoderm and mesoderm at stage 11 (Fig. 7E) (see fig. S18 for individual genes). This broad expression pattern would have been more difficult to detect without single-cell data. The original experiments (*30*) could not weigh equally the expression across all tissues because the whole-mount in situ staining used emphasizes superficial tissues.

We conclude that, at least at the level of transcription, there is no evidence of a distinct expression program that persists from the blastula to give rise to the neural crest. We fail to see such cells both using unsupervised approaches (clustering) and by examining the set of eight shared genes previously proposed to maintain pluripotency. It is not possible to completely rule out the retention of a blastula-like pluripotency program in neural crest precursors from our data: If functional pluripotency was maintained by chromatin state or posttranslational modification, it may be undetectable by scRNA-seq. Nevertheless, these new studies argue against a persistent transcriptional program preserved from an earlier stage uniquely in the neural crest. Rather, we argue in favor of a more conventional view of neural crest development proceeding from a well-defined ectodermal lineage.

Discussion

Embryonic development involves a carefully timed set of changes in cell behavior that drives the egg to a complex spatial and compositional pattern of cell types. A biochemical dissection of the underlying processes in development is complicated by limited material in the embryo and the heterogeneity of its composition, both of which must be considered together. Methods such as in situ hybridization have bridged these difficulties and can now be performed quantitatively and simultaneously over many genes (*31*, *32*). However, registering such spatial information at single-cell resolution can be challenging, particularly in three-dimensional tissues. In an alternative approach, we and others have developed single-cell transcriptomic methods, which sacrifice spatial information and in return provide a universal modality of measurement that is easily adapted to diverse situations (*1*, *33*). In a short time, these methods have been widely deployed and excelled in revealing cell population structures and dynamics (*17*, *34*, *35*). The resulting cell atlases can be computationally related to spatial structure

using extensive in situ expression databases such as Xenbase (*36*, *37*). For embryos, applying scRNA-seq involves important considerations. The method should not preferentially select a single cell type. It should be highly efficient in yield of cells. The dissociation procedure adopted should be quick and complete. Background RNA released by lysed cells in the sample should be minimized. These problems are acute for *Xenopus* embryos because it has large yolk-filled blastomeres that are sensitive to shear forces and handling. Yet these problems have been overcome with a method of efficient capture and very little cell lysis.

We also developed analytical methods for interpreting the time-course measurements of single-cell gene expression in the embryo. Large temporal differences obscured temporal mappings between cell states using established tools. This challenge was solved in our analysis by using shared latent spaces to measure similarities between states across adjacent time points. Upon linking cell states over time based on their gene expression, we found a strong match to known lineages. There were some differences that could be explained by the heterochronic formation of the same cell type, such as in the differentiation of the somite tissue, and in some cases the transcriptional cell states did not cluster along spatial boundaries. Yet in other aspects the data showed high sensitivity and could detect the first appearance of numerous cell states far earlier than previously known. As shown for the neural crest, the sensitivity and single-cell resolution of our gene expression resource can be used to test specific hypotheses about fundamental developmental processes.

In this study, we looked for general features of development that might be difficult to appreciate from examination of individual lineages. In both *Xenopus* and zebrafish, we observed a transition from pervasive multilineage gene expression during gastrulation to more specific and combinatorial deployment of differentiation programs later. In particular, newly induced transcription factors increasingly demarcated multiple independent cell fates in the embryo after gastrulation, as transcriptional states within each germ layer are further specialized. The drop in the frequency of multilineage priming, and the increase in combinatorial TF deployment, co-occur with the formation of the first discrete embryonic cell states. In *Xenopus*, this transition appears to be particularly switchlike, occurring between stages 12 and 14, just 2.5 hours apart in time. Curiously, the timing of appearance of distinct cells states correlates precisely with that of cell-fate commitment in *Xenopus* (*38*, *39*). The global nature of this transition is reminiscent of the midblastula transition, which occurs in stage 8 *Xenopus* embryos, when the gradual titration of DNA-to-histone ratios during blastula-stage cleavage cycles abruptly drives transcriptional activation, a longer cell cycle, onset of asynchronous cell divisions, and the start of cell motility across the embryo (*2*, *3*). We do not know whether any single mechanism coordinates the rapid appearance of multiple cell types in the postgastrula embryo, however. A candidate process could be the formation of heterochromatin domains, which occurs on the appropriate time scale (*40*, *41*), and could facilitate both the refinement of lineage program conflicts (*42*) and the combinatorial reuse of transcription factors by restricting their targets in a tissue-specific manner (*43*, *44*).

In contrast to these seemingly conserved global features of transcriptional dynamics in embryos, we found that the tissue-specific expression of individual genes was relatively variable across species. Rather than preserving global transcriptional profiles, orthologous cell states maintained expression of just a subset of genes, which were most notably enriched for TFs, and among TFs, those that are used in a single tissue rather than those that are combinatorially reused across lineages. Developmental programs thus appear to preserve an underlying core set of transcriptional programs that define cellular hierarchies while exploring significant variation in the way most genes are deployed across tissues to define cellular phenotypes. This finding supports previous arguments that cell identities and phenotypes may be decoupled across evolution (*45*). Indeed, new cell states and changes in cellular hierarchies across species could be associated with the deployment of TFs in novel locations or combinations and concomitant acquisition of batteries of effector genes. We found that this expression plasticity is independent of variation in protein sequence itself, surprisingly decoupling a gene's structure from its expression pattern in the embryo across evolution. Taken together, the approaches and analyses presented here establish first steps toward a data-driven dissection of developmental programs and how they change across species.

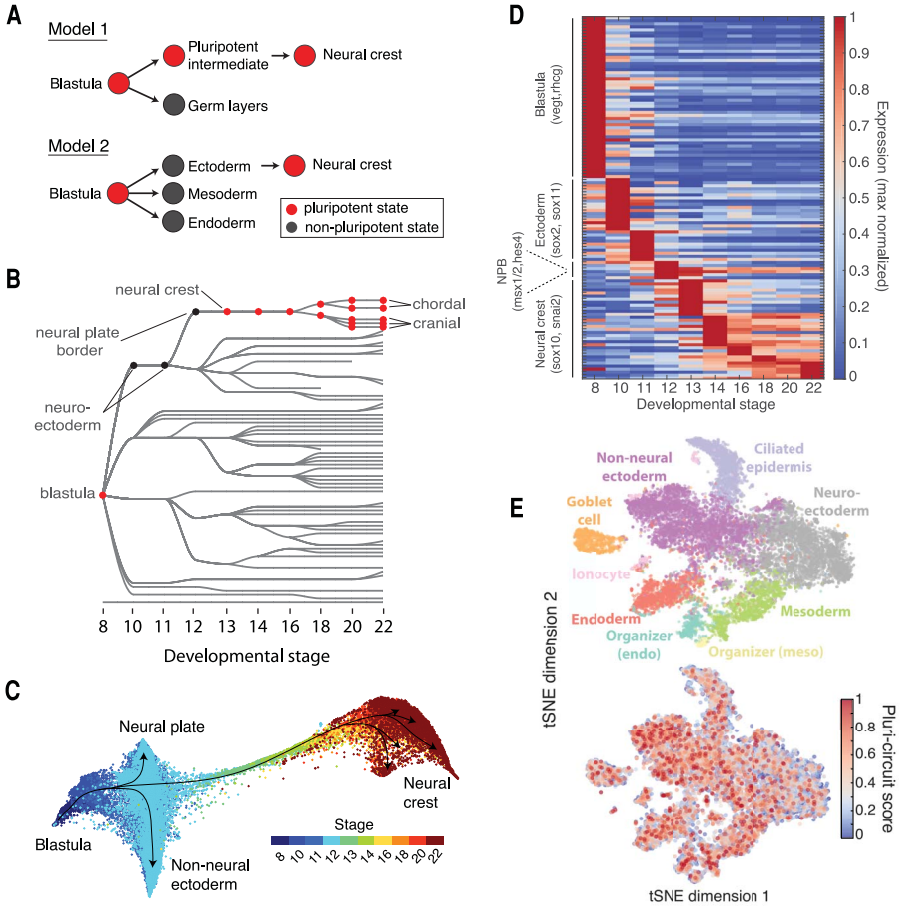

Fig. 7. Assessing the retention of pluripotency during neural crest development. (**A**) Contrasting models of neural crest development. (Model 1) Neural crest emerges from an intermediate population that retains blastula pluripotency (*29*). (Model 2) Neural crest emerges from ectoderm and reactivates pluripotency. (**B**) Ancestors inferred from scRNA-seq support model 2, where neural crest derives from neural cells at the neural plate border. (**C**) Single-cell visualization (using SPRING) of neuroectoderm, non-neural ectoderm, and neural crest also indicates that neural crest derives from the neural plate border. (**D**) Neural crest differentiation involves hundreds of >3-fold dynamic marker genes. (**E**) At stage 11, the shared pluripotency circuit proposed by Buitrago-Delgado *et al*. (*30*)—foxd3, c-myc (myca), id3, tfap2a, ventx2.1, ets1, snai1, and pou3f5.2—is expressed broadly in nonpluripotent cells. Score shows normalized aggregate expression; see fig. S18 for individual genes.

REFERENCES AND NOTES

1. A. M. Klein *et al*., Droplet barcoding for single-cell transcriptomics applied to embryonic stem cells. *Cell* **161**, 1187–1201 (2015). doi: 10.1016/j.cell.2015.04.044; pmid: 26000487
2. J. Newport, M. Kirschner, A major developmental transition in early Xenopus embryos: I. characterization and timing of cellular changes at the midblastula stage. *Cell* **30**, 675–686 (1982). doi: 10.1016/0092-8674(82)90272-0; pmid: 6183003
3. J. Newport, M. Kirschner, A major developmental transition in early Xenopus embryos: II. Control of the onset of transcription. *Cell* **30**, 687–696 (1982). doi: 10.1016/0092-8674(82)90273-2; pmid: 7139712
4. J. Heasman, Patterning the early Xenopus embryo. *Development* **133**, 1205–1217 (2006). doi: 10.1242/dev.02304; pmid: 16527985
5. K. Karimi *et al*., Xenbase: A genomic, epigenomic and transcriptomic model organism database. *Nucleic Acids Res.* **46**, D861–D868 (2018). pmid: 29059324
6. R. L. Davis, M. W. Kirschner, The fate of cells in the tailbud of Xenopus laevis. *Development* **127**, 255–267 (2000). pmid: 10603344
7. D. E. Wagner *et al*., Single-cell mapping of gene expression landscapes and lineage in the zebrafish embryo. *Science* **360**, aar4362 (2018).
8. E. Segerdell *et al*., Enhanced XAO: The ontology of Xenopus anatomy and development underpins more accurate annotation of gene expression and queries on Xenbase. *J. Biomed. Semantics* **4**, 31 (2013). doi: 10.1186/2041-1480-4-31; pmid: 24139024
9. E. Segerdell, J. B. Bowes, N. Pollet, P. D. Vize, An ontology for Xenopus anatomy and development. *BMC Dev. Biol.* **8**, 92 (2008). doi: 10.1186/1471-213X-8-92; pmid: 18817563
10. C. Trapnell *et al*., The dynamics and regulators of cell fate decisions are revealed by pseudotemporal ordering of single cells. *Nat. Biotechnol.* **32**, 381–386 (2014). doi: 10.1038/nbt.2859; pmid: 24658644
11. C. Weinreb, S. Wolock, B. K. Tusi, M. Socolovsky, A. M. Klein, Fundamental limits on dynamic inference from single-cell snapshots. *Proc. Natl. Acad. Sci. U.S.A.* **115**, E2467–E2476 (2018). doi: 10.1073/pnas.1714723115; pmid: 29463712
12. G. Schiebinger *et al*., Reconstruction of developmental landscapes by optimal-transport analysis of single-cell gene expression sheds light on cellular reprogramming. *bioRxiv* 191056 [preprint]. 27 September 2017. doi: 10.1101/191056
13. M. Walmsley, A. Ciau-Uitz, R. Patient, Adult and embryonic blood and endothelium derive from distinct precursor populations which are differentially programmed by BMP in Xenopus. *Development* **129**, 5683–5695 (2002). doi: 10.1242/dev.00169; pmid: 12421708
14. F. Liu, M. Walmsley, A. Rodaway, R. Patient, Fli1 acts at the top of the transcriptional network driving blood and endothelial development. *Curr. Biol.* **18**, 1234–1240 (2008). doi: 10.1016/j.cub.2008.07.048; pmid: 18718762
15. T. Nagasawa *et al*., Evolutionary Changes in the Developmental Origin of Hatching Gland Cells in Basal Ray-Finned Fishes. *Zool. Sci.* **33**, 272–281 (2016). doi: 10.2108/zs150183; pmid: 27268981
16. M. Yasutomi, T. Hama, Electron microscopic study on the xanthophore differentiation in Xenopus laevis, with special reference to their pterinosomes. *J. Ultrastruct. Res.* **38**, 421–432 (1972). doi: 10.1016/0022-5320(72)90080-9; pmid: 4335114
17. J. A. Briggs *et al*., Mouse embryonic stem cells can differentiate via multiple paths to the same state. *eLife* **6**, e26945 (2017). doi: 10.7554/eLife.26945; pmid: 28990928
18. H. Weber, C. E. Symes, M. E. Walmsley, A. R. Rodaway, R. K. Patient, A role for GATA5 in Xenopus endoderm specification. *Development* **127**, 4345–4360 (2000). pmid: 11003835
19. J. F. Reiter *et al*., Gata5 is required for the development of the heart and endoderm in zebrafish. *Genes Dev.* **13**, 2983–2995 (1999). doi: 10.1101/gad.13.22.2983; pmid: 10580005
20. H. Weintraub, The MyoD family and myogenesis: Redundancy, networks, and thresholds. *Cell* **75**, 1241–1244 (1993). doi: 10.1016/0092-8674(93)90610-3; pmid: 8269506
21. T. Ravasi *et al*., An atlas of combinatorial transcriptional regulation in mouse and man. *Cell* **140**, 744–752 (2010). doi: 10.1016/j.cell.2010.01.044; pmid: 20211142
22. J. Monod, F. Jacob, Teleonomic mechanisms in cellular metabolism, growth, and differentiation. *Cold Spring Harb. Symp. Quant. Biol.* **26**, 389–401 (1961). doi: 10.1101/SQB.1961.026.01.048; pmid: 14475415
23. D. E. Cohen, D. Melton, Turning straw into gold: Directing cell fate for regenerative medicine. *Nat. Rev. Genet.* **12**, 243–252 (2011). doi: 10.1038/nrg2938; pmid: 21386864
24. M. Hu *et al*., Multilineage gene expression precedes commitment in the hemopoietic system. *Genes Dev.* **11**, 774–785 (1997). doi: 10.1101/gad.11.6.774; pmid: 9087431
25. M. Thomson *et al*., Pluripotency factors in embryonic stem cells regulate differentiation into germ layers. *Cell* **145**, 875–889 (2011). doi: 10.1016/j.cell.2011.05.017; pmid: 21663792
26. L. Velten *et al*., Human haematopoietic stem cell lineage commitment is a continuous process. *Nat. Cell Biol.* **19**, 271–281 (2017). doi: 10.1038/ncb3493; pmid: 28319093
27. J. Shu *et al*., Induction of pluripotency in mouse somatic cells with lineage specifiers. *Cell* **153**, 963–975 (2013). doi: 10.1016/j.cell.2013.05.001; pmid: 23706735
28. P. Laslo *et al*., Multilineage transcriptional priming and determination of alternate hematopoietic cell fates. *Cell* **126**, 755–766 (2006). doi: 10.1016/j.cell.2006.06.052; pmid: 16923394
29. F. C. Wardle, J. C. Smith, Refinement of gene expression patterns in the early Xenopus embryo. *Development* **131**, 4687–4696 (2004). doi: 10.1242/dev.01340; pmid: 15329341
30. E. Buitrago-Delgado, K. Nordin, A. Rao, L. Geary, C. LaBonne, Shared regulatory programs suggest retention of blastula-stage potential in neural crest cells. *Science* **348**, 1332–1335 (2015). doi: 10.1126/science.aaa3655; pmid: 25931449
31. E. Lubeck, A. F. Coskun, T. Zhiyentayev, M. Ahmad, L. Cai, Single-cell in situ RNA profiling by sequential hybridization. *Nat. Methods* **11**, 360–361 (2014). doi: 10.1038/nmeth.2892; pmid: 24681720
32. K. H. Chen, A. N. Boettiger, J. R. Moffitt, S. Wang, X. Zhuang, Spatially resolved, highly multiplexed RNA profiling in single cells. *Science* **348**, aaa6090 (2015). doi: 10.1126/science.aaa6090; pmid: 25858977
33. E. Z. Macosko *et al*., Highly Parallel Genome-wide Expression Profiling of Individual Cells Using Nanoliter Droplets. *Cell* **161**, 1202–1214 (2015). doi: 10.1016/j.cell.2015.05.002; pmid: 26000488
34. N. Karaiskos *et al*., The *Drosophila* embryo at single-cell transcriptome resolution. *Science* **358**, 194–199 (2017). doi: 10.1126/science.aan3235; pmid: 28860209
35. J. Cao *et al*., Comprehensive single-cell transcriptional profiling of a multicellular organism. *Science* **357**, 661–667 (2017). doi: 10.1126/science.aam8940; pmid: 28818938
36. K. Achim *et al*., High-throughput spatial mapping of single-cell RNA-seq data to tissue of origin. *Nat. Biotechnol.* **33**, 503–509 (2015). doi: 10.1038/nbt.3209; pmid: 25867922
37. R. Satija, J. A. Farrell, D. Gennert, A. F. Schier, A. Regev, Spatial reconstruction of single-cell gene expression data. *Nat. Biotechnol.* **33**, 495–502 (2015). doi: 10.1038/nbt.3192; pmid: 25867923
38. D. Forman, J. M. Slack, Determination and cellular commitment in the embryonic amphibian mesoderm. *Nature* **286**, 492–494 (1980). doi: 10.1038/286492a0; pmid: 7402328
39. J. Heasman, C. C. Wylie, P. Hausen, J. C. Smith, Fates and states of determination of single vegetal pole blastomeres of X. laevis. *Cell* **37**, 185–194 (1984). doi: 10.1016/0092-8674(84)90314-3; pmid: 6722871
40. S. Hontelez *et al*., Embryonic transcription is controlled by maternally defined chromatin state. *Nat. Commun.* **6**, 10148 (2015). doi: 10.1038/ncomms10148; pmid: 26679111
41. R. C. Akkers *et al*., A hierarchy of H3K4me3 and H3K27me3 acquisition in spatial gene regulation in Xenopus embryos. *Dev. Cell* **17**, 425–434 (2009). doi: 10.1016/j.devcel.2009.08.005; pmid: 19758566
42. M. Hemberger, W. Dean, W. Reik, Epigenetic dynamics of stem cells and cell lineage commitment: Digging Waddington's canal. *Nat. Rev. Mol. Cell Biol.* **10**, 526–537 (2009). doi: 10.1038/nrm2727; pmid: 19603040
43. S. John *et al*., Chromatin accessibility pre-determines glucocorticoid receptor binding patterns. *Nat. Genet.* **43**, 264–268 (2011). doi: 10.1038/ng.759; pmid: 21258342
44. L. Ho, G. R. Crabtree, Chromatin remodelling during development. *Nature* **463**, 474–484 (2010). doi: 10.1038/nature08911; pmid: 20110991
45. D. Arendt *et al*., The origin and evolution of cell types. *Nat. Rev. Genet.* **17**, 744–757 (2016). doi: 10.1038/nrg.2016.127; pmid: 27818507

ACKNOWLEDGMENTS

We thank A. Ratner for technical support, S. Wolock for assistance with data analysis, and the Bauer Core Facility at Harvard University for sequencing support. **Funding:** A.M.K was supported by an Edward J. Mallinckrodt Foundation Grant, a Burroughs Wellcome Fund CASI Award, and NIH award 5R33CA212697-02. J.A.B., L.P. and M.W.K were supported by NIH award 2R01HD073104-06. M.W.K was also supported by R21 HD087723. **Author contributions:** J.A.B. designed and performed all single-cell experiments, processed and analyzed data, and generated figures. J.A.B., M.W.K, and A.M.K. conceived the study and wrote the manuscript. M.W.K., A.M.K., and L.P. assisted with experiments and data analysis. C.W. developed the web browser for viewing single-cell data and assisted with data analysis, generating figures, and writing the manuscript. D.E.W. and S.M. provided clustering analysis and annotations of zebrafish data. **Competing interests:** A.M.K. and M.W.K are founders of 1Cell-Bio, Inc. All other authors declare no competing interests. **Data and materials availability:** All data are available for interactive exploration at tinyurl.com/scXen2018. The underlying scRNA-seq counts data can be downloaded from the same browser. Raw FASTQ files and scRNA-seq counts data have been deposited in the National Center for Biotechnology Information's Gene Expression Omnibus (GEO), accession GSE113074.

SUPPLEMENTARY MATERIALS

www.sciencemag.org/content/360/6392/eaar5780/suppl/DC1
Materials and Methods
Figs. S1 to S18
Table S1
References (*46*–*51*)
Movies S1 to S3
Data S1 to S7

23 November 2017; accepted 16 April 2018
Published online 26 April 2018
10.1126/science.aar5780

RESEARCH ARTICLE

SINGLE-CELL ANALYSIS

Single-cell mapping of gene expression landscapes and lineage in the zebrafish embryo

Daniel E. Wagner, Caleb Weinreb, Zach M. Collins, James A. Briggs, Sean G. Megason,* Allon M. Klein*

High-throughput mapping of cellular differentiation hierarchies from single-cell data promises to empower systematic interrogations of vertebrate development and disease. Here we applied single-cell RNA sequencing to >92,000 cells from zebrafish embryos during the first day of development. Using a graph-based approach, we mapped a cell-state landscape that describes axis patterning, germ layer formation, and organogenesis. We tested how clonally related cells traverse this landscape by developing a transposon-based barcoding approach (TracerSeq) for reconstructing single-cell lineage histories. Clonally related cells were often restricted by the state landscape, including a case in which two independent lineages converge on similar fates. Cell fates remained restricted to this landscape in embryos lacking the *chordin* gene. We provide web-based resources for further analysis of the single-cell data.

A major goal of developmental biology is to understand the progression of embryonic cell lineages from pluripotency to adulthood (*1*). Fate mapping and analysis of mutant phenotypes have explained much of what we know of development, yet we still lack a systematic atlas of all cell states in a developing embryo. Owing to technical advances in single-cell RNA sequencing (scRNA-seq) (*2*–*6*), it is now possible to assemble comprehensive single-cell atlases describing complex and dynamic in vivo biological processes. Here we utilized inDrops scRNA-seq (*4*, *7*) to collect more than 92,000 single-cell transcriptomes from dissociated wild-type and mutant zebrafish embryos during the first 24 hours of embryonic development (Fig. 1 and fig. S1). For different developmental stages, we sampled 17 to 97% of the total cells per embryo, sufficient to detect cell states as rare as 0.1 to 0.5% of all cells (fig. S1C), including germ cells, which were detected in all time points (Fig. 1B and table S2). From this dataset, clustering of the wild-type transcriptomes revealed an expanding set of epidermal, neural, mesodermal, and endodermal cell states over developmental time, many of which could be specifically annotated on the basis of expression of marker genes (Fig. 1B, fig. S2A, and table S2) (*8*). We collected seven biological replicates for the final time point [24 hours postfertilization (hpf)], which demonstrated consistency of both transcriptional signatures and cell-state proportions across independent specimens (fig. S2, B and C).

Department of Systems Biology, Harvard Medical School, Boston, MA 02115, USA.
***Corresponding author. Email: sean_megason@hms.harvard.edu (S.G.M.); allon_klein@hms.harvard.edu (A.M.K.)**

A single-cell graph of cell-state progression in the developing zebrafish embryo

We sought to map trajectories of cell state during development by linking cell states across time. Several computational approaches exist to infer orderings of asynchronous processes from scRNA-seq data (*9*–*11*), typically by projecting all cells into a single low-dimensional latent space. Such strategies may be ill-suited to map gene expression in developing embryos, which exhibit dramatically increasing cell-state dimensionality and continuous changes in the sets and numbers of cell state–defining genes (fig. S2, D and E). To overcome these obstacles, we developed a graph-based strategy for locally embedding consecutive time points on the basis of the biological variation that they share, rather than using a global coordinate system for all time points. This approach first constructs a single-cell k-nearest neighbor graph for each time point t_i, with nodes representing cells and edges that link neighbors in a low-dimensional subspace; it then joins the graphs by identifying neighboring cells in pairs of adjacent time points, by using a coordinate system learned from the future (t_{i+1}) time point (see methods). The resulting graph spans all time points and allows application of formal graph-based methods for data analysis. When applied to our zebrafish data, the full graph forms a branching network (Fig. 2A). Inspection of numerous domain and cell type–specific transcriptional markers shows that major initial branches represent neural, epidermal, and mesendodermal states undergoing progressive and spatially restricted differentiation (Fig. 2, B and C, and fig. S3). We also noted distinct and early branching events for germline, notochord, enveloping layer epidermis, and the prechordal plate.

To test whether this graph recapitulates known lineage relationships, we used a measure of graph distance (diffusion pseudotime, or DPT) (*12*) to

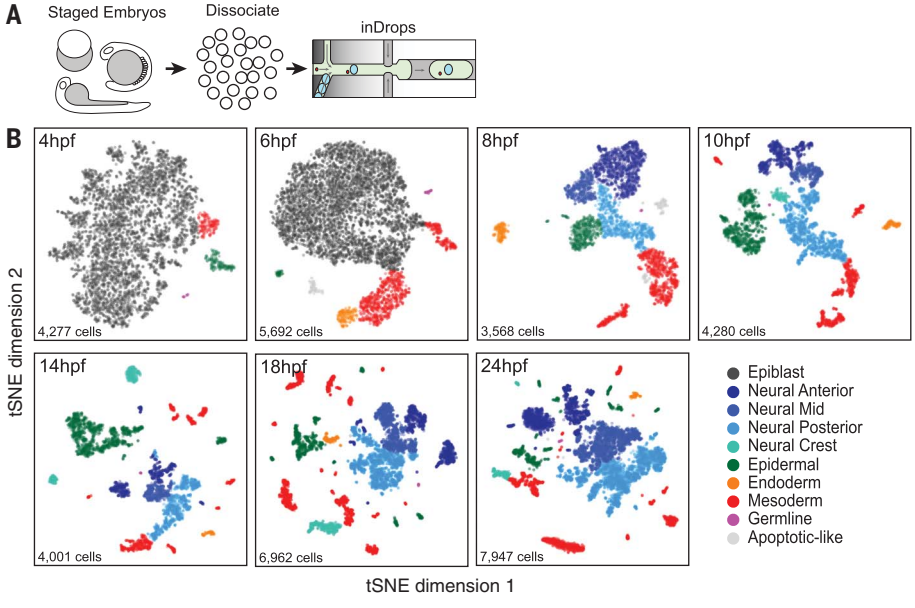

Fig. 1. A single-cell transcriptional atlas of the zebrafish embryo. (**A**) Experimental workflow. Single-cell suspensions were dissociated from staged zebrafish embryos and introduced into the inDrops microfluidic device. Single-cell transcriptome libraries were prepared and sequenced by RNA-seq. (**B**) tSNE maps for each time point, constructed in dimensionality-reduced principal component analysis subspace defined by highly covariable genes (see methods). Cells are colored by germ layer identities inferred from expressed marker genes (see also fig. S2A and table S2).

explore long-range temporal connections between cell states. Cell states of the early gastrula (shield stage, 6 hpf) are defined largely by positional marker genes (Fig. 3A), yet these cells are connected, through the single-cell graph, to tissue-specific states that emerge later (for example, pharyngula stage, 24 hpf). We found that the shield-stage cells with the shortest mean graph distance to each particular 24-hpf tissue were clustered and expressed spatial marker genes predicted from previous in vivo fate-mapping studies (*13*–*16*); for example, 24-hpf neural tissues mapped to the 6-hpf dorsal anterior epiblast (Fig. 3B and fig. S4). Conversely, direct comparison of 6- and 24-hpf gene expression states failed to capture lineage relationships (Fig. 3B and fig. S4, blue points).

We next tested the extent to which the single-cell graph represents a simple treelike hierarchy of discrete states. For this, we "coarse-grained" the graph by collapsing groups of similar cells into state nodes; edges between state nodes were weighted by the number of original single-cell connecting edges. A spanning tree was then traced through the most densely weighted edges to a 4-hpf root state (Fig. 3C and fig. S5A). This spanning tree (the "state tree") reflects many specific aspects of early development. In the neural plate, we observe notable branch points for the optic cup, diencephalon, telencephalon, mesencephalon, and rhombencephalon, with associated states for region-specific postmitotic neurons (for example, *eomes*$^+$ and *dlx1*$^+$ neurons in distinct forebrain branches). The neural plate also includes neural crest, which branches to include cell states for melanoblasts, iridoblasts, and xanthoblasts. In the lateral plate and ventral mesoderm, the state tree encodes extensive branching into hematopoietic cells, endothelial cells, heart, pharyngeal arches, the pronephritic duct, and fin buds. In the endoderm, two branch points give rise to cell states for pancreatic primordium (which includes *insulin*$^+$

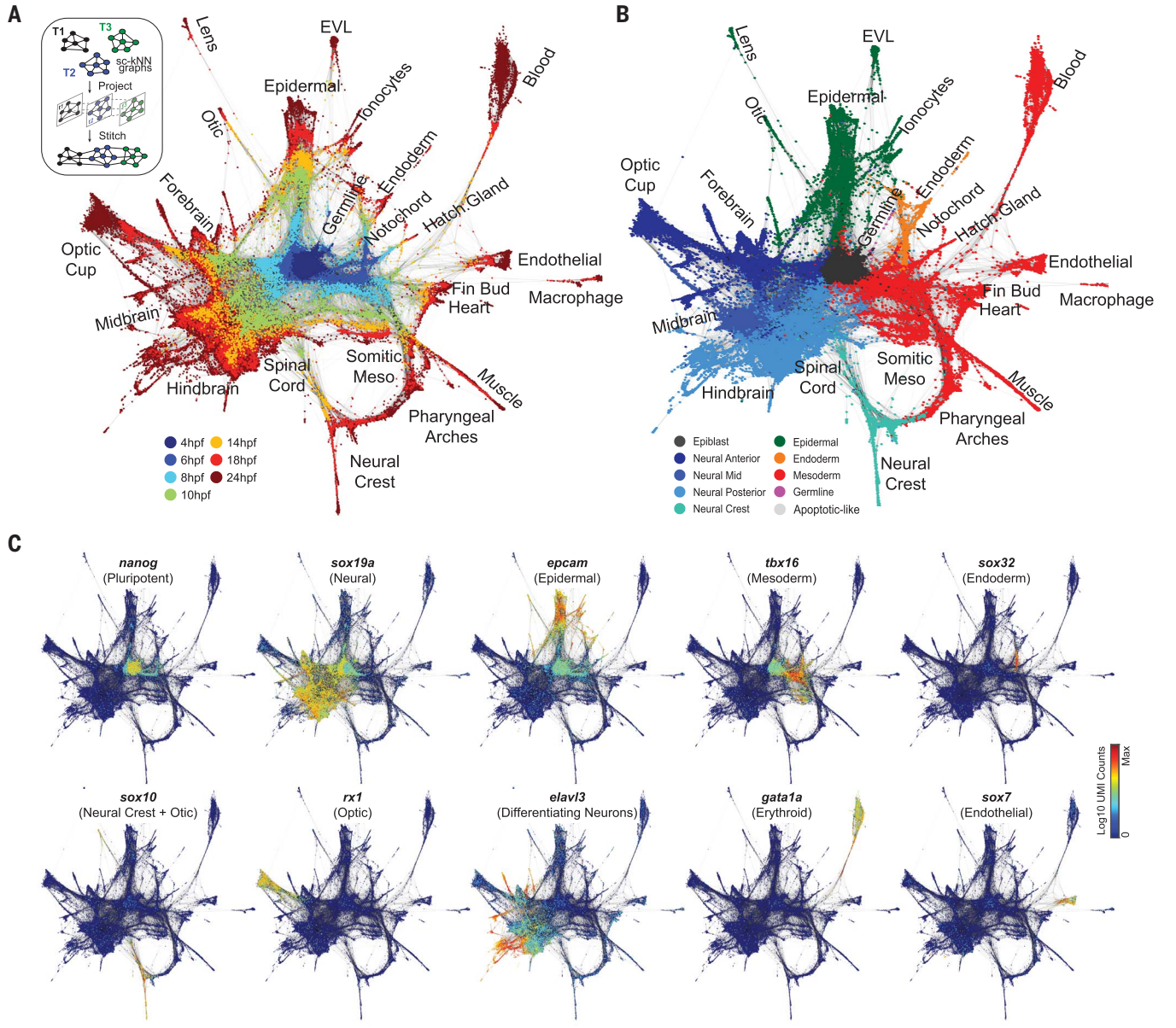

Fig. 2. Single-cell graph reveals a continuous developmental landscape of cell states. (**A**) Overview of graph construction strategy and a force-directed layout of the resulting single-cell graph (nodes colored by collection time point). For each cell, up to 20 within– or between–time point mutual nearest neighbor edges are retained. sc-kNN, single cell–*k*-nearest neighbor; EVL, enveloping layer epidermis. (**B**) Single-cell graph colored by germ layer identities inferred from differentially expressed marker genes (see table S2). (**C**) Single-cell graphs, colored by $\log_{10}$ expression counts for indicated cell type–specific marker genes. UMI, unique molecular identifier.

cells) and the pharyngeal pouch. In the epidermal lineage, branch points differentiate the otic placode, lateral line, ionocytes, and several states expressing markers for annotated mucous-secreting cells (*8*). To facilitate data exploration, we developed web-based interfaces for the state tree and the full single-cell graph (www.tinyurl.com/scZfish2018). These tools permit interactive examination of the inferred state hierarchy, expression for any gene of interest, and differential expression analysis between states, state combinations, or single cells.

Although many major cell-state transitions are captured in the state tree, more complex features are evident in the coarse-grained and single-cell graphs. Off-tree interconnections between states, for example, were evident for the neural crest and pharyngeal arches, spinal cord and somitic mesoderm, the neural plate, and others (Fig. 3C and fig. S5A). To formalize the degree to which the developmental landscape can be approximated as a hierarchy with discrete, non-looping branches, we defined a "canalization score" (Fig. 3D, see legend for definition), which reflects the off-tree connectivity of each coarse-grained state node. This analysis revealed widespread regions of low canalization, particularly in the neural plate and somitic mesoderm. These observations suggest that, in contrast to the classic notion of a cell lineage, the zebrafish cell-state landscape cannot be fully represented as a tree.

Cell-lineage history does not invariantly reflect cell-state graph topology

Although the single-cell and coarse-grained graphs represent an inferred landscape of developmental cell states, they do not reveal how individual cells traverse these states. A simple prediction would be that individual cell histories mirror graph topology. We tested this prediction by developing an inDrops-compatible strategy for recording in vivo lineage histories at the single-cell level: sequencing of transcribed clonally encoded random barcodes (TracerSeq). TracerSeq utilizes the Tol2 transposase system (*17*) to randomly integrate green fluorescent protein (GFP) reporter cassettes driven by the β-actin promoter (*actb2*) into the zebrafish genome. To render each integration event unique and detectable by RNA-seq, we utilized Gibson assembly (*18*) without subsequent amplification to introduce a random 20-nucleotide oligomer sequence barcode into the GFP 3′ untranslated region (Fig. 4A and fig. S6). Because transgenic insertions can occur asynchronously over successive cell divisions, TracerSeq barcodes can facilitate the construction of lineage trees (Fig. 4A). TracerSeq offers an advantage over related Cas9-based approaches (*19*, *20*), which can generate identical edits and/or large barcode deletions in independent lineages at nontrivial frequencies. By contrast, TracerSeq barcodes are uniformly distributed over a large sequence space (for example, 4^{20} nucleotide combinations = 10^{12} unique barcode sequences), facilitating straightforward calling of genetic clones (fig. S7). The small (20–base pair) locus size also greatly simplifies the construction, sequencing, and analysis of TracerSeq inDrops libraries.

The use of TracerSeq to analyze potentially small clones of cells (each restricted to a single embryo) requires high-efficiency tissue dissociation and transcriptomic barcoding methods. We therefore optimized a high-yield cell dissociation and recovery protocol for individual 24-hpf zebrafish embryos (fig. S1D and methods) and leveraged the high cell barcoding efficiency (>80%) of the inDrops platform (*7*). We then sequenced individual embryos (n = 5) at 24 hpf (fig. S7) that were injected at the one-cell stage with the TracerSeq library, generating combined lineage and transcriptome datasets for 1269 clonal barcodes distributed over 4342 single cells (fig. S8). Of these cells, 2361 (54%) were each marked by ≥2 distinct barcode integrations; 624 cells (14%) were marked by ≥5 integrations (fig. S8). Hierarchical clustering of TracerSeq barcodes organized these cells into more than a hundred distinct founder clones with internal nested clone structures (Fig. 4B and fig. S9, A to D). We then compared the lineage history and inferred transcriptional history of each founder clone by embedding its constituent cells onto the single-cell graph (Fig. 4C). We found that the largest clones often marked a wide diversity of cell states. In multiple cases, however, additional barcode integrations in the same founder clone marked cells that were state restricted. For example, one such clone (34F1) marked cells of the neural plate, epidermal tissues, and muscle but contained a subclone restricted to ectoderm. Similar lineage restriction events could be described for other founder clones (Fig. 4C). These observations suggest that the current timing of TracerSeq integrations encompasses the transition from unrestricted pluripotency to the first fate-restriction events appearing in the zebrafish embryo.

To investigate lineage relationships more systematically, we assessed the likelihood of recovering shared TracerSeq barcodes from all pairs of transcriptional states in the 24-hpf zebrafish embryo. We first calculated a lineage coupling score (fig. S9E and methods), defined as the number of shared barcodes relative to randomized data (z-score standardized), with values ranging from positive (coupled fates) to negative (anti-coupled fates). Hierarchical clustering of the pairwise correlation between coupling scores revealed structured groups of cell states (Fig. 5A), which comprised related tissues and/or inferred

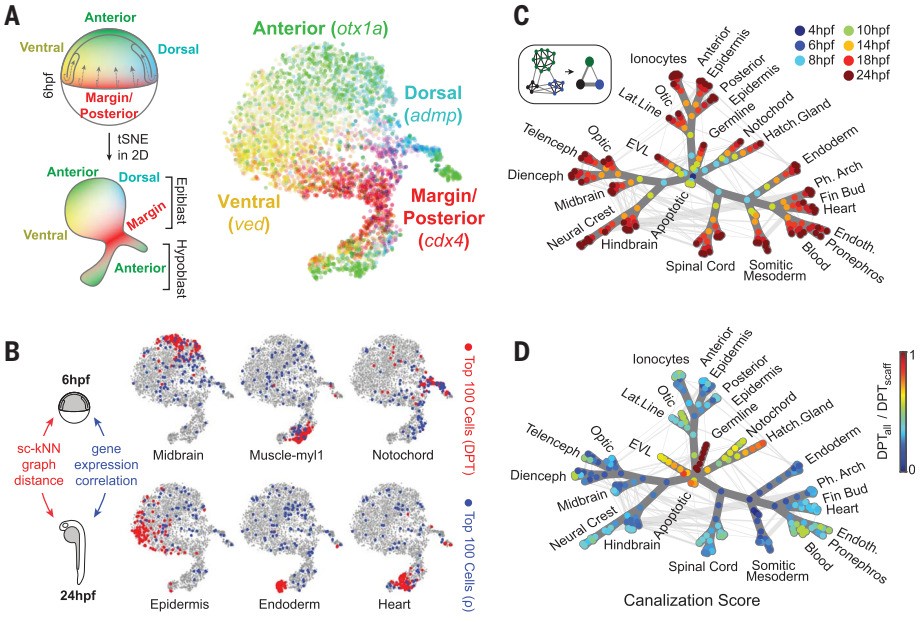

Fig. 3. Single-cell and coarse-grained graphs encode progenitor-fate relationships. (**A**) tSNE map of 6-hpf epiblast and hypoblast states, colored by normalized transcript counts for select positional marker genes. Overlapping color gradients demonstrate continuous expression domains defined by position. Diagram relates positions of cells in the tSNE map to theoretical positions in the embryo. 2D, two dimensions. (**B**) In silico fate predictions for 6-hpf embryo cells. The top 100 cells with predicted 24-hpf fate outcomes are indicated for shortest graph diffusion distances (red) or direct single-cell gene expression correlation distances (blue) between 6-hpf cells and 24-hpf cluster centroids. ρ, Pearson correlation. (**C**) Construction and overview of the coarse-grained graph (see also fig. S5). Nodes indicate states (groups of transcriptionally similar cells), colored by time point. Weighted edges connect similar states within or between time points. Spanning tree edges connecting each node to the 4-hpf root state through the top weighted edges are highlighted in dark gray. (**D**) Coarse-grained graph nodes are colored by a canalization score, defined as the ratio of diffusion distances between each node (DPT_{all}) and the 4-hpf root node through state tree edges only (DPT_{scaff}) versus through all graph edges. Highly canalized regions of the graph correspond to branches with the fewest off-tree edges.

germ layer derivatives. These included one distinct group that contained both mesodermal and endodermal derivatives, four groups containing ectodermal derivatives, and two groups containing mixtures of ectoderm and mesoderm. Several of these lineage groups are corroborated by prior fate-mapping studies. We discuss here three examples. The first major lineage group (MesEndo) includes derivatives of both lateral plate mesoderm and endoderm. These tissues originate from the marginal blastomeres of the early zebrafish gastrula, which involute first during gastrulation to form the hypoblast and then rapidly migrate toward the animal pole (*13*, *15*, *21*). The observed lineage isolation of these tissues is thus consistent with an early spatial partitioning of this region, further reflected in Fig. 5A by negative lineage correlations to most other states. A second group (Fig. 5A, Ecto III) captures strong lineage couplings both between anterior neural tissues—including the optic cup, midbrain, and telencephalon (*16*)—and to anterior epidermal derivatives such as the olfactory placode (*22*). These tissues are coupled to a lower degree with another group (Ecto II), which includes couplings between the hindbrain, spinal cord, and neural crest (*grem2*$^{+}$). The third example we note is a group coupling ectoderm and mesoderm (Fig. 5A, MesEcto II), including muscle (*myl1*$^{+}$), myotome, spinal cord, posterior neural crest, and epidermal states. These correlations mirror the development of posterior body regions, which trace their origins to blastomeres proximal to the medial and ventral margin (*13*). These mesodermal–spinal cord couplings might also be explained by the presence of a later population of transient, multipotent neuromesodermal progenitor cells in the embryonic tailbud, which give rise to both of these populations (*23*–*25*). Interestingly, these lineage groups tend to be organized by position (for example, along the anterior-posterior axis) rather than strictly by germ layer or tissue origin (for example, neural, epidermal, and mesodermal).

We next questioned how clonal relationships compared with cell-state relationships. A simplistic model of development is that cells progressively diverge in state as they diverge in lineage. Developing embryos, however, could violate this prediction in at least two ways: First, clonally distinct embryonic fields can give rise to similar cell types ("convergent clones"); second, major transcriptional changes might drive related cells into qualitatively dissimilar states, possibly even late in development ("divergent clones"). Overlaying TracerSeq lineage correlation scores on the cell-state graph and comparing these scores to graph-derived state distances (Fig. 5B and fig. S10) revealed that some nearby states on the state graph were indeed clonally correlated, as expected by the simplistic model. However, nearby cell states also frequently displayed weak clonal correlations, suggesting convergent differentiation. These patterns were evident among state relationships for endothelial, optic cup, and muscle tissues (Fig. 5B and fig. S10, A to F) and systematically when examining all states (fig. S10G).

We observed considerably fewer cases of divergent clonal behavior (fig. S10G). However, one notable example manifested as apparent looping of the neural crest into the pharyngeal arches, which originate in the graph from both neural plate and lateral plate mesoderm and merge at 18 to 24 hpf (Fig. 2, A and B, and fig. S11A). Although the contribution of neural crest to various mesenchymal tissues is well established (*26*–*28*), the transcriptional information reflected by the graph loop alone does not reveal which annotated pharyngeal arch states arise from neural crest. TracerSeq data, however, provide a clear signature of distinct clonal patterns between pharyngeal arch states: One pharyngeal arch state (ph.arch-tbx1) is a member of the MesEndo lineage group with mesodermal clonal associations, whereas

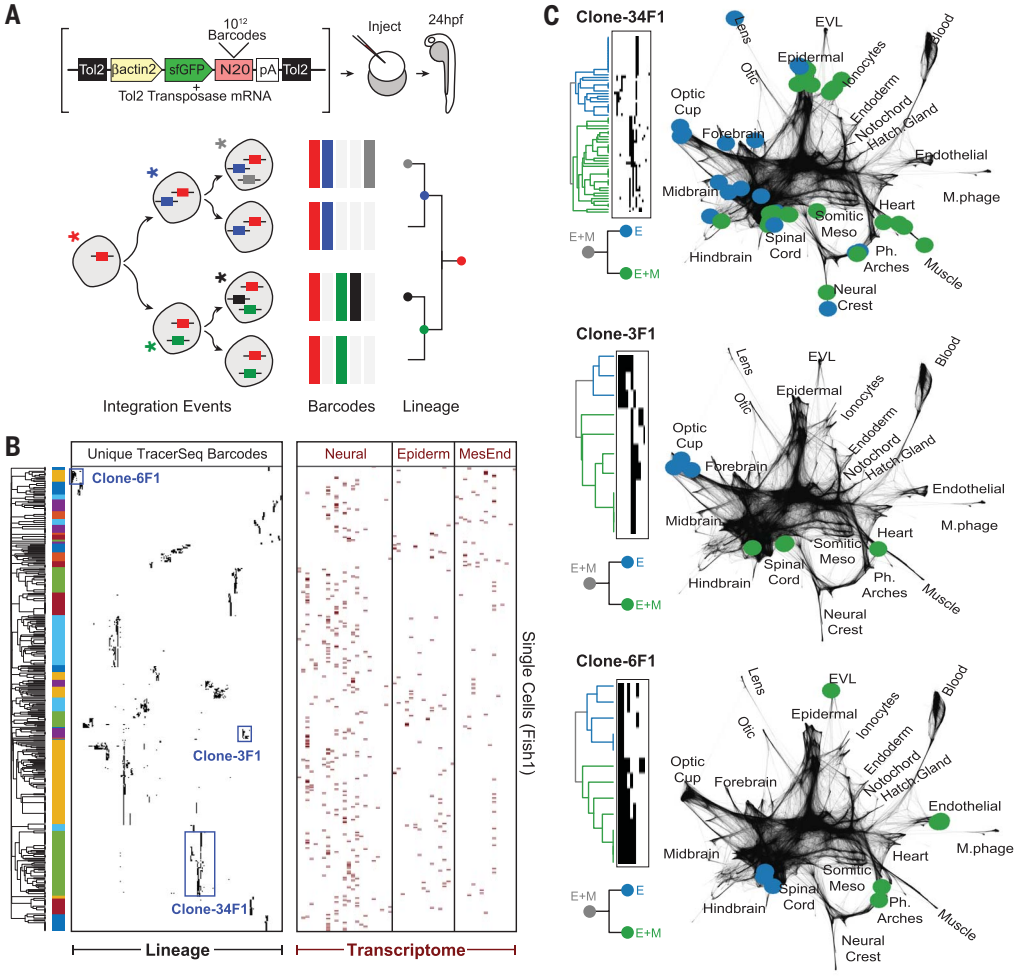

Fig. 4. Single-cell transcriptomic barcoding of cell lineages using TracerSeq. (**A**) Method overview. Tol2 transposase system integrates barcode-containing GFP reporter cassettes into zebrafish genome. Asterisks denote integration events. Colors (red, blue, black, and green) indicate unique barcode sequences. (**B**) Clustered heatmap for one of five TracerSeq embryos (see also fig. S9, A to D), displaying lineage and transcriptome information for each cell. Heatmap rows are single cells for which both transcriptome and >1 TracerSeq barcodes were recovered. Columns denote unique TracerSeq barcodes (left: black squares, ≥1 UMI) and tissue identities (right: red squares) inferred from cluster annotations (table S2). Heatmaps were clustered using Jaccard similarity and average linkage. (**C**) Examples of TracerSeq founder clones with positions of constituent cells (colored nodes) overlaid on the single-cell graph. Graph edges are shown in dark gray. Colors indicate the first lineage bifurcation within each founder clone. In the three cases shown, the founder clone included cells that differentiated into both ectodermal (E) and mesodermal (M) states, whereas one of the two first subclones was restricted to ectoderm.

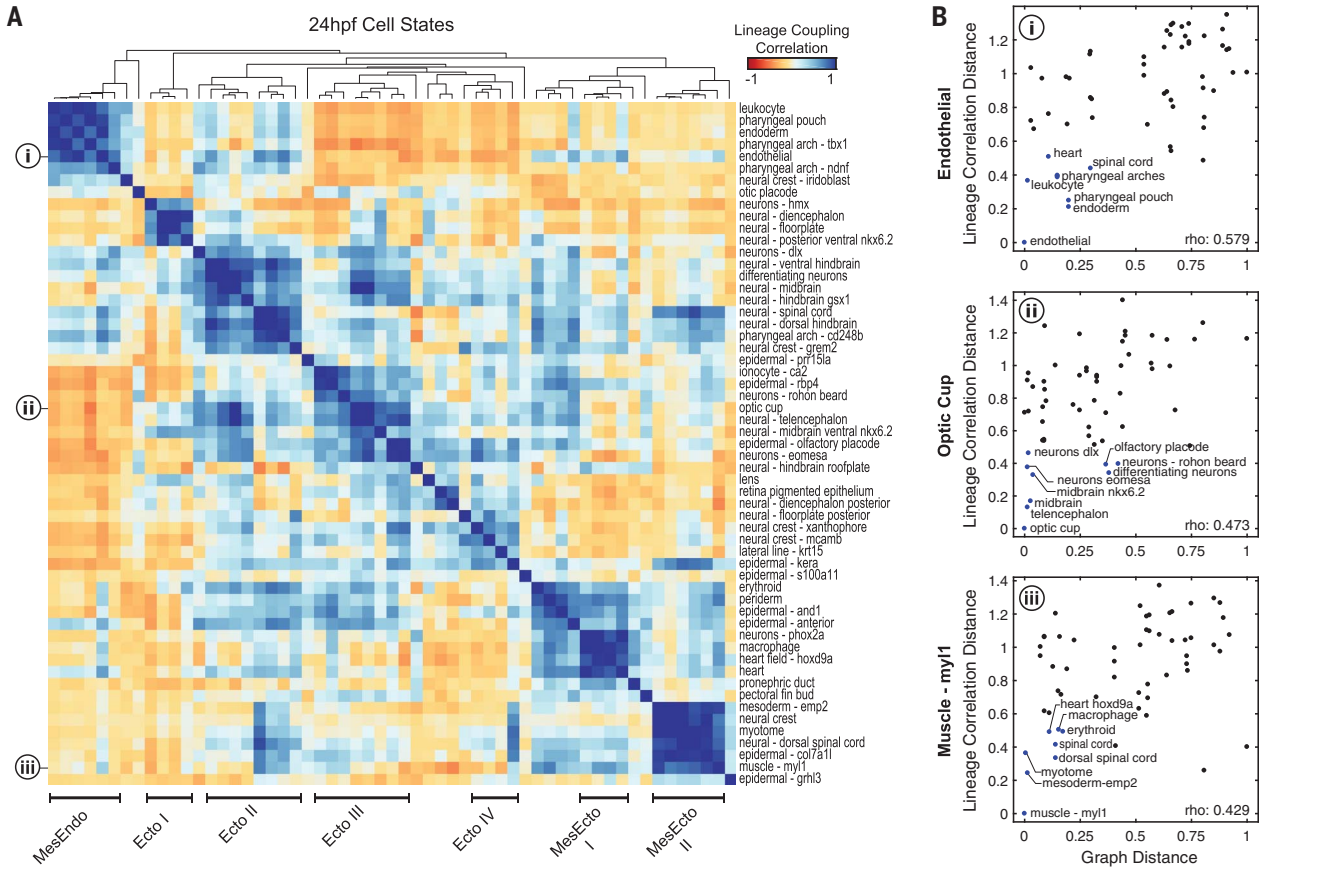

Fig. 5. TracerSeq reveals systematic relationships between cell lineage and cell state. (**A**) Heatmap of TracerSeq lineage coupling scores (see methods) between pairs of 24-hpf states, clustered by correlation distance and average linkage. Groups of states with similar lineage coupling signatures are annotated. (**B**) Quantitative relationships between lineage coupling correlation distances and scaled state tree diffusion distances for (i) endothelial, (ii) optic cup, and (iii) *myl*$^{+}$ muscle states (see also fig. S10, A to F).

the second pharyngeal arch state (ph.arch-cd248b) is clonally related to neural crest and posterior neural states (Fig. 5A and fig. S11, B to F). These data indicate that cells in the ph.arch-cd248b state diverged from a neural plate lineage and subsequently converged with other lateral plate–derived states. The ability of embryonic clones to undergo dramatic converging and diverging behaviors thus underscores a continued need for independent measurements of both cell state and lineage in the mapping of cell-fate hierarchies.

Robustness of cell-type transcriptional programs after a signaling perturbation

Single-cell maps of vertebrate development can, in principle, facilitate unbiased, systematic analyses of mutant phenotypes and disease states. We used scRNA-seq to analyze the mutant phenotype for *chordin*, a well-studied developmental gene that encodes a secreted bone morphogenetic protein (BMP) inhibitor expressed in the organizer and required for patterning the early dorsal-ventral axis (*29*–*33*). Disruption of *chordin* leads to changes in gross embryo morphology, with an expansion of ventral tissues and a reduction of dorsal tissues (*30*). The scRNA-seq method is well suited to address how all cell types in the embryo change in frequency, and in gene expression, while also allowing detection of qualitatively new states, or combinations of states, if they occur.

We used CRISPR-Cas9 (*34*) to disrupt the *chordin* locus, resulting in highly penetrant clutches of mutant zebrafish embryos (fig. S12). We performed inDrops profiling on *chordin*-targeted and control embryos (*tyrosinase*-targeted, see methods) in a narrow time series corresponding to ~14 to 16 hpf (Fig. 6A). After sequencing, we classified each of the *chordin*- and control-targeted cells to reference cell clusters of the 14-hpf wild-type embryo (fig. S13 and methods) and tested for altered gene expression. We reasoned that a qualitatively new cell state, if formed as a result of the aberrant patterning, would manifest as widespread changes in gene expression after mutation, with a magnitude comparable to the differences between wild-type embryonic states. Applying this criterion, we found no evidence of a qualitatively new cell state after *chordin* depletion. Rather, the number of genes differentially expressed within states was modest compared to the differences defining the wild-type states of the 14-hpf embryo (Fig. 6B and fig. S14A). Moreover, a t-distributed stochastic neighbor embedding (tSNE) mapping of CRISPR-targeted cells (fig. S13, A to C) identified only a single cluster solely occupied by *chordin*-mutant cells (fig. S13D), distinguished primarily by a heat shock–like transcriptional signature. This same stress signature was increased in multiple states in *chordin*-targeted embryos (fig. S14A).

We next tested whether *chordin* disruption led to changes in abundance of particular classified cell types. As expected, expansion of states corresponding to ventral tissues (for example, somitic mesoderm, epidermis, hatching gland, blood, and endothelial tissues) at the expense of dorsal tissues (for example, the neural plate and notochord) was observed (fig. S14, A and B) (*30*, *35*). Additional features could be appreciated by projecting the CRISPR datasets directly onto the wild-type single-cell graph (Fig. 6, C and D). For example, a sharp boundary bisected the lateral plate mesoderm into two compartments of opposing *chordin* sensitivity, separating the heart and fin bud progenitor fields. Similar juxtaposed domains of opposing *chordin* sensitivity were evident in the axial mesoderm, partitioning notochord from hatching gland, and in the tailbud separating spinal cord from somitic mesoderm (Fig. 6D). Notably, each of these pairs of phenotypic domains appeared to beorganized downstream of an inferred branchpoint in the cell-state landscape. These domain

pairs, therefore, likely reflect binary fate choices that are tuned by BMP signaling in wild-type embryos.

In a final analysis, we searched for the putative identity of the cells responding to *chordin* in the tailbud, as this is the site showing the largest expansion (somitic mesoderm) and loss (spinal cord) after perturbation. In zebrafish, *chordin* is expressed in the embryonic shield, adaxial cells, posterior tailbud region, and also transiently in the neural plate (*36*). All of these expression patterns were confirmed in our single-cell graphs (fig. S15A). Furthermore, in contrast to its earlier expression in the shield, continued expression of *chordin* in the tailbud was distinct among a large panel of known BMP inhibitor genes (fig. S15A) and was tightly apposed by expression domains for multiple *bmp* transcripts (fig. S15B). These expression characteristics might explain the increased *chordin* sensitivity of posterior body regions. To examine this region in greater detail, we isolated a subgraph of tailbud and descendent cells. Consistent with previous studies, two cell-state trajectories branching from a common neuromesodermal-like *brachyury*$^{+}$;*sox2*$^{+}$ progenitor state were identified, each expressing markers of neural fates (*sox3*, *sox19a*, *pax6a*, and *neurog1*) or somitic fates (*tbx16*, *tbx6*, *tbx24*, *msgn1*, and *myod1*) (fig. S16, A to C) (*25*, *37*–*39*). Notably, the neural-mesodermal branchpoint coincided with the boundaries of both *chordin* expression and sensitivity (fig. S16, D and E). The *chordin*-expressing cells in this region of the single-cell graph exhibited a distinct expression profile (fig. S17), including a cadherin (*cdh11*), early neurogenic markers (*her3*, *her8a*, and *sox19a*), and several relatively uncharacterized genes (*gig2g*, *foxb1b*, and *foxb1a*). We hypothesize that these cells represent a key transition state, at which point tailbud cells initiate a posterior neurogenic program in a *chordin*-dependent manner.

Discussion

Our study demonstrates a graph-based approach for mapping whole-embryo developmental landscapes, over time, from scRNA-seq data. The graph was constructed with minimal assumptions about development and describes individual cell states transitioning from pluripotent blastomeres to a large array of cell types and tissues during the first day of zebrafish embryogenesis. This dataset can now be mined to identify temporal and tissue associations for any gene, cell type, or biological process of interest. As with genome annotation efforts over the years, we expect that the annotation of identified cell states may undergo refinement with community input.

As single-cell atlases and landscapes of embryo development become routinely available, one is challenged to reconsider the relationship between a cell lineage (by definition, a tree) and the considerably more topologically complex gene expression landscape through which these cells traverse. Using TracerSeq, we confirmed that differentiating cells of the zebrafish embryo do not invariantly follow treelike hierarchies. Instead, we observed both widespread convergence in cell states for clonally distant cells and instances in which clonally related cells diverged into distant states. Non-treelike convergence of cell states could be explained by the differentiation of well-separated spatial domains of the embryo into the same basic cell types (for example, along the anterior-posterior axis), whereas divergence could involve mechanisms such as asymmetric cell division or exposure to spatially varying signals (*40*). We anticipate that the synthesis of single-cell lineage and transcriptome information will continue to be crucial for deciphering how cells traverse state trajectories with complex topologies (for example, loops or continua).

Single-cell mapping of genetic perturbation data presents a powerful framework for identifying regulatory features of a developmental landscape. After disruption of *chordin*, which encodes a BMP inhibitor, we showed that the defining transcriptional features of the landscape remained mostly unchanged, yet cell-state abundances could be dramatically and reciprocally altered, as if the landscape were "tilted" but cell fates remain canalized. Future systematic mapping of signaling perturbations could be

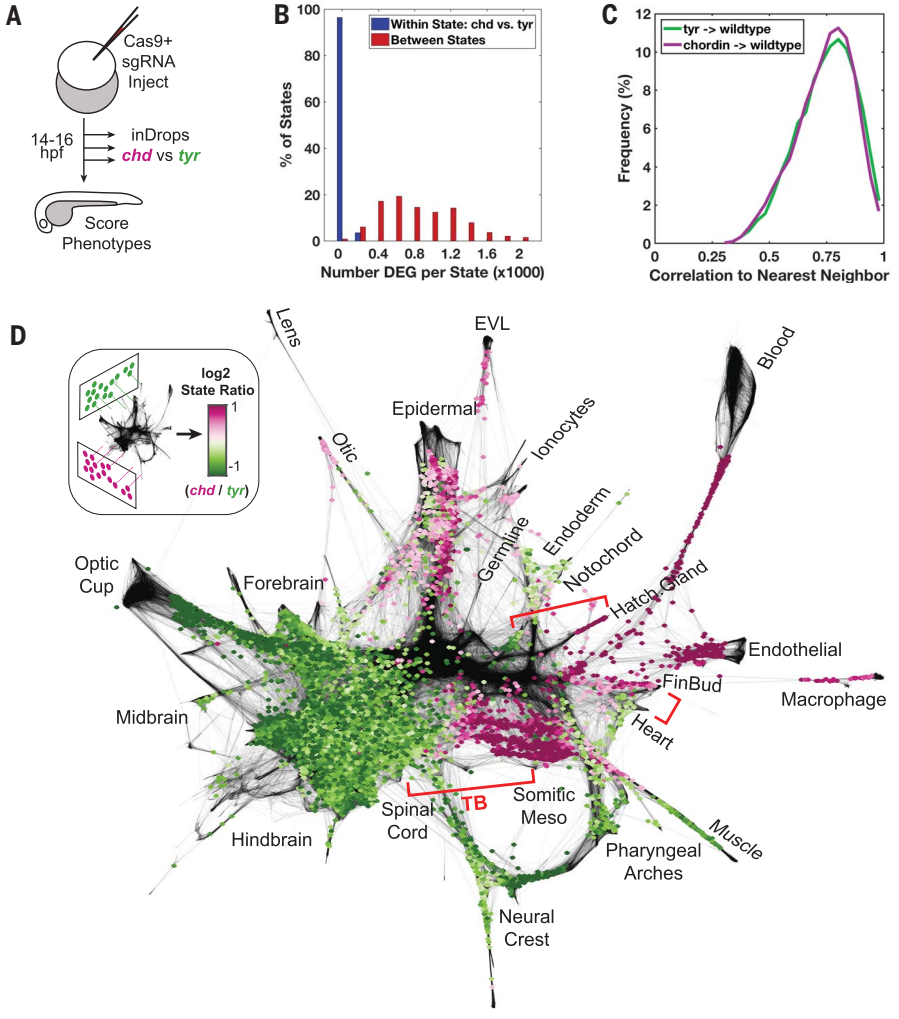

Fig. 6. Regulatory features of the developmental landscape identified by genetic perturbation. (**A**) Overview of the CRISPR experiment. Three pairs of *chordin*- and *tyrosinase* (control)–targeted samples were prepared and processed by inDrops at ~14 to 16 hpf. (**B**) Histogram depicting numbers of differentially expressed genes (DEGs) identified in *chordin* versus control (*tyrosinase*) cells for each state (blue bars), compared to DEG numbers when comparing between all state pairs (red bars). DEGs were identified by Wilcoxon rank sum test (adjusted *P* value < 0.01, absolute $\log_2$ fold change > 1, average expression > 25 transcripts per million). (**C**) Histogram of Pearson correlation similarities (after PCA projection) between each *chordin* or *tyrosinase* cell and its nearest neighbor from 10-, 14-, and 18-hpf wild-type datasets (see methods). (**D**) $\log_2$ ratios of cell states with significant differential abundance (false discovery rate < 0.25) in the *chordin* versus *tyrosinase* samples. Purple and green regions correspond to wild-type cell states that are over- or underrepresented in the *chordin* mutant, respectively. Adjacent graph domains with opposing *chordin* sensitivity are highlighted by brackets. TB, tailbud region (see *cdx4* expression in fig. S3).

used to reveal the complete signaling logic of the embryo, as cells are specified toward their final fates. Together, these studies demonstrate the power, modularity, and quantitative benefits of unbiased scRNA-seq–based interrogations of embryonic development. We anticipate that similar large-scale datasets will facilitate explorations of additional developmental stages, tissues, and species.

REFERENCES AND NOTES

1. A. F. Schier, W. S. Talbot, *Annu. Rev. Genet.* **39**, 561–613 (2005).
2. T. Hashimshony *et al.*, *Genome Biol.* **17**, 77 (2016).
3. S. Islam *et al.*, *Nat. Methods* **11**, 163–166 (2014).
4. A. M. Klein *et al.*, *Cell* **161**, 1187–1201 (2015).
5. E. Z. Macosko *et al.*, *Cell* **161**, 1202–1214 (2015).
6. L. Mazutis *et al.*, *Nat. Protoc.* **8**, 870–891 (2013).
7. R. Zilionis *et al.*, *Nat. Protoc.* **12**, 44–73 (2017).
8. B. Thisse, S. Pflumio, M. Fürthauer, B. Loppin, V. Heyer, A. Degrave, R. Woehl, A. Lux, T. Steffan, X. Q. Charbonnier, C. Thisse, Expression of the zebrafish genome during embryogenesis, ZFIN Direct Data Submission, (2001); http://zfin.org.
9. C. Trapnell *et al.*, *Nat. Biotechnol.* **32**, 381–386 (2014).
10. S. C. Bendall *et al.*, *Cell* **157**, 714–725 (2014).
11. J. Shin *et al.*, *Cell Stem Cell* **17**, 360–372 (2015).
12. L. Haghverdi, M. Büttner, F. A. Wolf, F. Buettner, F. J. Theis, *Nat. Methods* **13**, 845–848 (2016).
13. C. B. Kimmel, R. M. Warga, T. F. Schilling, *Development* **108**, 581–594 (1990).
14. A. E. Melby, R. M. Warga, C. B. Kimmel, *Development* **122**, 2225–2237 (1996).
15. R. M. Warga, C. Nüsslein-Volhard, *Development* **126**, 827–838 (1999).
16. K. Woo, S. E. Fraser, *Development* **121**, 2595–2609 (1995).
17. K. Kawakami, *Genome Biol.* **8** (suppl. 1), S7 (2007).
18. D. G. Gibson *et al.*, *Nat. Methods* **6**, 343–345 (2009).
19. A. McKenna *et al.*, *Science* **353**, aaf7907 (2016).
20. J. P. Junker *et al.*, bioRxiv 056499 [Preprint]. 4 January 2017.
21. R. M. Warga, D. A. Kane, R. K. Ho, *Dev. Cell* **16**, 744–755 (2009).
22. K. E. Whitlock, M. Westerfield, *Development* **127**, 3645–3653 (2000).
23. E. Tzouanacou, A. Wegener, F. J. Wymeersch, V. Wilson, J.-F. Nicolas, *Dev. Cell* **17**, 365–376 (2009).
24. R. L. Davis, M. W. Kirschner, *Development* **127**, 255–267 (2000).
25. J. P. Kanki, R. K. Ho, *Development* **124**, 881–893 (1997).
26. N. M. Le Douarin, E. Dupin, *Curr. Opin. Genet. Dev.* **13**, 529–536 (2003).
27. N. M. Le Douarin, S. Creuzet, G. Couly, E. Dupin, *Development* **131**, 4637–4650 (2004).
28. C. S. Le Lièvre, N. M. Le Douarin, *J. Embryol. Exp. Morphol.* **34**, 125–154 (1975).
29. Y. Sasai *et al.*, *Cell* **79**, 779–790 (1994).
30. M. Hammerschmidt *et al.*, *Development* **123**, 95–102 (1996).
31. S. Schulte-Merker, K. J. Lee, A. P. McMahon, M. Hammerschmidt, *Nature* **387**, 862–863 (1997).
32. Y. Sasal, B. Lu, H. Steinbelsser, E. M. De Robertis, *Nature* **378**, 419 (1995).
33. S. Piccolo, Y. Sasai, B. Lu, E. M. De Robertis, *Cell* **86**, 589–598 (1996).
34. J. A. Gagnon *et al.*, *PLOS ONE* **9**, e98186 (2014).
35. A. Y. Leung *et al.*, *Dev. Biol.* **277**, 235–254 (2005).
36. V. E. Miller-Bertoglio, S. Fisher, A. Sánchez, M. C. Mullins, M. E. Halpern, *Dev. Biol.* **192**, 537–550 (1997).
37. R. H. Row, D. Kimelman, *Dev. Biol.* **329**, 55–63 (2009).
38. R. H. Row, S. R. Tsotras, H. Goto, B. L. Martin, *Development* **143**, 244–254 (2016).
39. M. Gouti *et al.*, *Dev. Cell* **41**, 243–261.e7 (2017).
40. P. Gönczy, *Nat. Rev. Mol. Cell Biol.* **9**, 355–366 (2008).

ACKNOWLEDGMENTS

We thank A. Ratner for technical support and T. W. Hiscock, V. Savova, S. L. Wolock, S. Mekhoubad, and R. M. Wagner for helpful discussions. **Author contributions:** D.E.W. designed and performed all single-cell experiments, processed and analyzed data, and generated figures. D.E.W., A.M.K., and S.G.M. conceived the study and wrote the manuscript. C.W. generated the web portal for viewing single-cell and coarse-grained graphs. Z.M.C designed single-guide RNA sequences and performed CRISPR-Cas9 injections. J.A.B. shared access to unpublished single-cell data. **Funding:** D.E.W. acknowledges support from a Howard Hughes Medical Institute–Life Sciences Research Foundation postdoctoral fellowship and NIH grant 1K99GM121852. A.M.K. was supported by an Edward J. Mallinckrodt Foundation Grant and a Burroughs Wellcome Fund CASI Award. S.G.M. was supported by NIH grants R01GM107733 and R01DC015478. **Competing interests:** S.G.M., D.E.W., C.W., Z.M.C., and J.A.B. declare no competing interests. A.M.K. is a founder of 1CellBio, Inc. **Data and materials availability:** A web portal providing access to the single-cell and coarse-grained graphs is available at www.tinyurl.com/scZfish2018. Single-cell counts matrices and FASTQ files have been deposited in the National Center for Biotechnology Information's Gene Expression Omnibus under accession number GSE112294.

SUPPLEMENTARY MATERIALS

www.sciencemag.org/content/360/6392/981/suppl/DC1
Materials and Methods
Figs. S1 to S17
Tables S1 to S3
References (*41*–*56*)

7 November 2017; accepted 29 March 2018
Published online 26 April 2018
10.1126/science.aar4362

SUSTAINABILITY

Reducing food's environmental impacts through producers and consumers

J. Poore[1,2]* and T. Nemecek[3]

Food's environmental impacts are created by millions of diverse producers. To identify solutions that are effective under this heterogeneity, we consolidated data covering five environmental indicators; 38,700 farms; and 1600 processors, packaging types, and retailers. Impact can vary 50-fold among producers of the same product, creating substantial mitigation opportunities. However, mitigation is complicated by trade-offs, multiple ways for producers to achieve low impacts, and interactions throughout the supply chain. Producers have limits on how far they can reduce impacts. Most strikingly, impacts of the lowest-impact animal products typically exceed those of vegetable substitutes, providing new evidence for the importance of dietary change. Cumulatively, our findings support an approach where producers monitor their own impacts, flexibly meet environmental targets by choosing from multiple practices, and communicate their impacts to consumers.

With current diets and production practices, feeding 7.6 billion people is degrading terrestrial and aquatic ecosystems, depleting water resources, and driving climate change (*1*, *2*). It is particularly challenging to find solutions that are effective across the large and diverse range of producers that characterize the agricultural sector. More than 570 million farms produce in almost all the world's climates and soils (*3*), each using vastly different agronomic methods; average farm sizes vary from 0.5 ha in Bangladesh to 3000 ha in Australia (*3*); average mineral fertilizer use ranges from 1 kg of nitrogen per ha in Uganda to 300 kg in China (*4*); and although four crops provide half of the world's food calories (*4*), more than 2 million distinct varieties are recorded in seed vaults (*5*). Further, products range from minimally to heavily processed and packaged, with 17 of every 100 kg of food produced transported internationally, increasing to 50 kg for nuts and 56 kg for oils (*4*).

Previous studies have assessed aspects of this heterogeneity by using geospatial data sets (*6*–*8*), but global assessments using the inputs, outputs, and practices of actual producers have been limited by data. The recent rapid expansion of the life cycle assessment (LCA) literature is providing this information by surveying producers around the world. LCA then uses models to translate producer data into environmental impacts with sufficient accuracy for most decision-making (*9*–*11*).

To date, efforts to consolidate these data or build new large-scale data sets have covered greenhouse gas (GHG) emissions only (*8*, *12*, *13*), agriculture only (*13*–*16*), small numbers of products (*8*, *14*–*16*), and predominantly Western European producers (*12*–*16*) and have not corrected for important methodological differences between LCAs (*12*–*16*). Here, we present a globally reconciled and methodologically harmonized database on the variation in food's multiple impacts. Our results show the need for far-reaching changes in how food's environmental impacts are managed and communicated.

Building the multi-indicator global database

We derived data from a comprehensive meta-analysis, identifying 1530 studies for potential inclusion, which were supplemented with additional data received from 139 authors. Studies were assessed against 11 criteria designed to standardize methodology, resulting in 570 suitable studies with a median reference year of 2010 (*17*). The data set covers ~38,700 commercially viable farms in 119 countries (fig. S2) and 40 products representing ~90% of global protein and calorie consumption. It covers five important environmental impact indicators (*18*): land use; freshwater withdrawals weighted by local water scarcity; and GHG, acidifying, and eutrophying emissions. For crops, yield represents output for a single harvest. Land use includes multicropping (up to four harvests per year), fallow phases (uncultivated periods between crops), and economic allocation to crop coproducts such as straw. This makes it a stronger indicator of both farm productivity and food security than yield.

The system we assess begins with inputs (the initial effect of producer choice) and ends at retail (the point of consumer choice) (fig. S1). For each study, we recorded the inventory of outputs and inputs (including fertilizer quantity and type, irrigation use, soil, and climatic conditions). Where data were not reported, for example, on climate, we used study coordinates and spatial data sets to fill gaps. We recorded environmental impacts at each stage of the supply chain. For GHG emissions, we further disaggregated the farm stage into 20 emission sources. We then used the inventory to recalculate all missing emissions. For nitrate leaching and aquaculture, we developed new models for this study (*17*).

Studies included provided ~1050 estimates of postfarm processes. To fill gaps in processing, packaging, or retail, we used additional meta-analyses of 153 studies providing 550 observations. Transport and losses were included from global data sets. Each observation was weighted by the share of national production it represents, and each country by its share of global production. We then used randomization to capture variance at all stages of the supply chain (*17*).

We validated the global representativeness of our sample by comparing average and 90th-percentile yields to Food and Agriculture Organization (FAO) data (*4*), which reconcile to within ±10% for most crops. Using FAO food balance sheets (*4*), we scaled up our sample data. Total arable land and freshwater withdrawals reconcile to FAO estimates. Emissions from deforestation and agricultural methane fall within ranges of independent models (*17*).

Environmental impacts of the entire food supply chain

Today's food supply chain creates ~13.7 billion metric tons of carbon dioxide equivalents (CO_2eq), 26% of anthropogenic GHG emissions. A further 2.8 billion metric tons of CO_2eq (5%) are caused by nonfood agriculture and other drivers of deforestation (*17*). Food production creates ~32% of global terrestrial acidification and ~78% of eutrophication. These emissions can fundamentally alter the species composition of natural ecosystems, reducing biodiversity and ecological resilience (*19*). The farm stage dominates, representing 61% of food's GHG emissions (81% including deforestation), 79% of acidification, and 95% of eutrophication (table S17).

Today's agricultural system is also incredibly resource intensive, covering ~43% of the world's ice- and desert-free land. Of this land, ~87% is for food and 13% is for biofuels and textile crops or is allocated to nonfood uses such as wool and leather. We estimate that two-thirds of freshwater withdrawals are for irrigation. However, irrigation returns less water to rivers and groundwater than industrial and municipal uses and predominates in water-scarce areas and times of the year, driving 90 to 95% of global scarcity-weighted water use (*17*).

Highly variable and skewed environmental impacts

We now group products by their primary dietary role and express impacts per unit of primary nutritional benefit (Fig. 1 and fig. S3). Immediately apparent in our results is the high variation in impact among both products and producers. Ninetieth-percentile GHG emissions of beef are 105 kg of CO_2eq per 100 g of protein, and

[1]Department of Zoology, University of Oxford, New Radcliffe House, Oxford OX2 6GG, UK. [2]School of Geography and the Environment, University of Oxford, South Parks Road, Oxford OX1 3QY, UK. [3]Agroscope, Agroecology and Environment Research Division, LCA Research Group, CH-8046 Zürich, Switzerland.
*Corresponding author. Email: joseph.poore@queens.ox.ac.uk

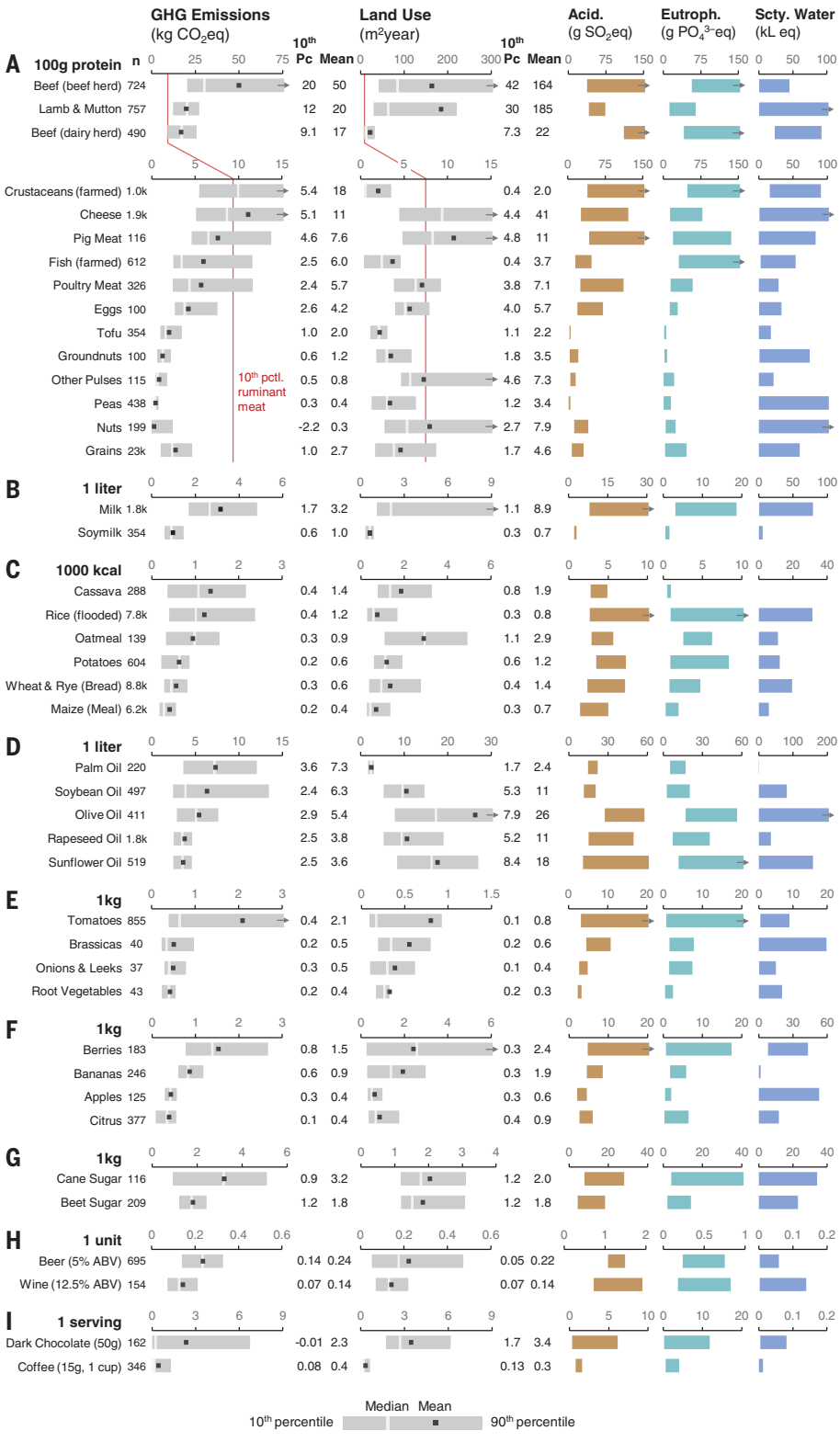

Fig. 1. Estimated global variation in GHG emissions, land use, terrestrial acidification, eutrophication, and scarcity-weighted freshwater withdrawals, within and between 40 major foods. (**A**) Protein-rich products. Grains are also shown here given that they contribute 41% of global protein intake, despite lower protein content. (**B**) Milks. (**C**) Starch-rich products. (**D**) Oils. (**E**) Vegetables. (**F**) Fruits. (**G**) Sugars. (**H**) Alcoholic beverages (1 unit = 10 ml of alcohol; ABV, alcohol by volume). (**I**) Stimulants. *n* = farm or regional inventories. Pc and pctl., percentile; scty., scarcity.

land use (area multiplied by years occupied) is 370 m^2·year. These values are 12 and 50 times greater than 10th-percentile dairy beef impacts (which we report separately given that its production is tied to milk demand). Tenth-percentile GHG emissions and land use of dairy beef are then 36 and 6 times greater than those of peas. High variation within and between protein-rich products is also manifest in acidification, eutrophication, and water use.

Within the major crops wheat, maize, and rice, 90th-percentile impacts are more than three times greater than 10th-percentile impacts on all five indicators. Within major growing areas for these crops (the Australian wheat belt, the U.S. corn belt, and the Yangtze river basin), land use becomes less variable, but we observe the same high levels of variation in all other indicators. This variability, even among producers in similar geographic regions, implies substantial potential to reduce environmental impacts and enhance productivity in the food system.

For many products, impacts are skewed by producers with particularly high impacts. This creates opportunities for targeted mitigation, making an immense problem more manageable. For example, for beef originating from beef herds, the highest-impact 25% of producers represent 56% of the beef herd's GHG emissions and 61% of the land use (an estimated 1.3 billion metric tons of CO_2eq and 950 million ha of land, primarily pasture). Across all products, 25% of producers contribute on average 53% of each product's environmental impact (fig. S3). For scarcity-weighted freshwater withdrawals, the skew is particularly pronounced: Producing just 5% of the world's food calories creates ~40% of the environmental burden. We will now explore how to access these mitigation opportunities through heterogenous producers.

Mitigation through producers

Enable producers to monitor multiple impacts

The first step in mitigation is estimating producer impacts. Prior research [e.g., (*7, 8, 14*)] has suggested that readily measurable proxies predict farm-stage impacts, avoiding the need for detailed assessment. From our larger data set, which includes more practices and geographies than prior studies, we assess the predictive power of common proxies, including crop yield, nitrogen use efficiency, milk yield per cow, liveweight gain, pasture area, and feed conversion ratios. Although most proxies significantly covary with impact, they make poor predictors when used alone, explaining little of the variation among farms (coefficient of determination R^2 = 0 to 27% in 47 of 48 proxy-impact combinations assessed) (fig. S4).

Prior research has also suggested using one impact indicator to predict others (*20*). We find weakly positive and sometimes negative relationships between indicators. For similar products globally, correlations between indicators are low (R^2 = 0 to 30% in 26 of 32 impact-impact combinations assessed) (fig. S4). Pork, poultry meat,

and milk show higher correlations between acidification and eutrophication ($R^2 \leq 54\%$), explained by the dominant role of manure in these impacts, but this does not generalize to other products or indicators. The same conclusion holds for farms in similar geographies or systems (fig. S5).

Monitoring multiple impacts and avoiding proxies supports far better decisions and helps prevent harmful, unintended consequences. However, two recent studies suggest that data on practices and geography, required to quantify impacts, must come directly from producers (*11*, *21*), that quantifying impacts with the use of satellite or census data misses much of the variation among farms.

Set and incentivize mitigation targets

When land use or emissions are low, we find trade-offs between indicators for many crops (fig. S5). This reflects diminishing marginal yield with increasing inputs as crops tend toward their maximum yields (*22*). For example, for already low-emission Northern European barley farms, halving land use can increase GHG emissions per kilogram of grain by 2.5 times and acidification by 3.7 times. To explore trade-offs further, we pair observations from the same study, location, and year that assess a practice change (fig. S6). Of the nine changes assessed, only two (changing from monoculture to diversified cropping and improving degraded pasture) deliver statistically significant reductions in both land use and GHG emissions.

Geography influences these trade-offs. For example, in the Australian wheat belt, where farmers practice low-rainfall, low-input farming, we find that both output per hectare and GHG emissions are in the bottom 15% globally. The environmental and social importance of different impacts also varies locally, given land scarcity, endemic biodiversity, and water quality, among other factors. Setting regional and sector-specific targets will help producers navigate trade-offs and make choices that align with local and global priorities.

Meet targets by choosing from multiple practice changes

To meet these targets, policy might encourage widespread adoption of certain practices. However, the environmental outcomes of many practices, such as conservation agriculture (*23*), organic farming (fig. S6), and even integrated systems of best practice (*24*), are highly variable. Using our data set, we can generalize these findings. To do this, we disaggregate each environmental indicator into its sources or drivers. We consider practice change as a package of measures that targets one or more of these sources. If producers have different impact sources, the effects of practice change will be variable.

We find that sources of impact vary considerably among farms producing the same product (Fig. 2 and figs. S7 to S9). Priority areas for reducing impact for one farm may be immaterial for another. For example, measures to reduce direct nitrous oxide emissions from synthetic and organic fertilizer, such as biochar application, are included in many mitigation estimates (*25*). However, for a third of global crop calorie production,

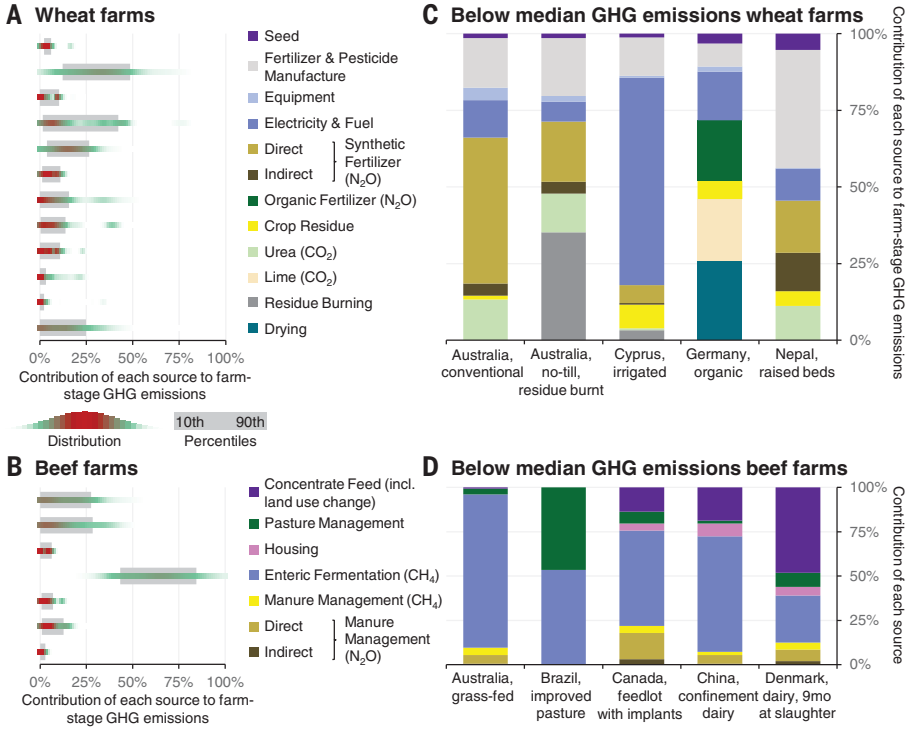

Fig. 2. Contributions of emission sources to total farm-stage GHG emissions. (**A** and **B**) Gray bars show 10th- and 90th-percentile contributions. Shaded bars represent the distribution. For example, the 90th-percentile contribution of organic fertilizer N_2O to farm-stage emissions is 16%, but for most wheat producers the contribution is near 0%. Density is estimated using a Gaussian kernel with bandwidth selection performed with biased cross-validation. (**C** and **D**) Contributions of emission sources for example producers with below-median GHG emissions.

these emissions represent less than 5% of farm-stage GHGs. It may be the case that low-impact farms have similar impact drivers. We again find variable sources of impact, even for low-impact farms (Fig. 2, C and D). Reducing impacts means focusing on different areas for different producers and, by implication, adopting different practices.

To explore this further, we use sensitivity analysis (*26*) to decompose the variance in each product's impact into its sources. Numerous sources contribute to variance (fig. S10). Most notably, for all crop calorie production globally, differences in fallow duration and multiple cropping drive 40% of the variance in land use. This is important as most strategies to increase productivity are focused on increasing single crop yields (*27*). But for many producers, increasing cropping intensity through the use of early-maturing varieties, intercropping, catch crops, and enhanced irrigation can provide more economically viable and trade-off–free ways to boost productivity and reduce impacts (*27*).

Geography plays a major role in this variation and affects the economic and environmental desirability of different practices (*28*). However, at the heart of agriculture is changing site conditions to enhance productivity (such as liming, terracing, or installing drainage), meaning that statements on the importance of geography have limitations. Nevertheless, some impact sources stand out. We find that freshwater aquaculture ponds create 0 to 450 g of methane per kg of liveweight (for context, enteric fermentation in dairy cows creates ~30 to 400 g per kg of liveweight). Of this variation, a third is explained by temperature (*17*), which accelerates methanogenesis and net primary production. Improving aeration and limiting addition of surplus feed to ponds can abate these emissions, particularly important in warm countries. Further, for every kilogram of nitrogen applied to crops, between 60 and 400 g is lost in reactive forms. Of this wide range, ~40% is explained by site conditions, including soil pH, temperature, and drainage (*17*). Prior research has also found that the potential of soil to store carbon varies significantly with soil properties, slope, and prior practice (*29*).

Providing producers with multiple ways to reduce their environmental impacts recognizes the variability in sources and drivers of impact but requires a step change in thinking: that practices such as conservation agriculture or organic farming are not environmental solutions in themselves but options that producers choose from to achieve environmental targets.

However, some practice changes can be pursued across all producers. Methane from flooded rice, enteric methane from ruminants, and concentrate feed for pigs and poultry are sizeable globally, representing 30% of food's GHG emissions; are material for all producers, contributing at least 17% of farm-stage emissions (Fig. 2B and fig. S7); and can be mitigated with relatively trade-off–free approaches such as shorter and shallower rice flooding (*30*), improving degraded pasture

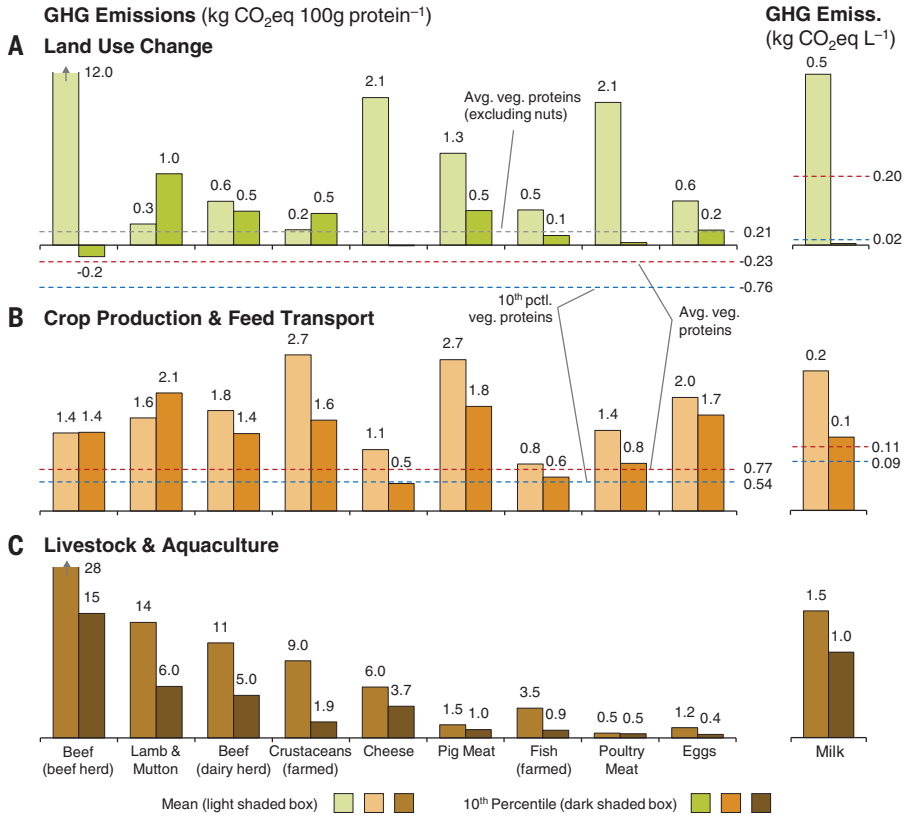

Fig. 3. Mean and 10th-percentile GHG emissions of protein-rich products across three major production stages. (**A** to **C**) Red lines represent average vegetable protein emissions, and blue lines represent 10th-percentile emissions. The gray line represents 10th-percentile emissions excluding nuts, which can temporarily sequester carbon if grown on cropland or pasture. To calculate 10th-percentile emissions by stage, we averaged across farms that have total emissions between the 5th and 15th percentiles, controlling for burden shifting between stages.

(fig. S6), and improving lifetime animal productivity (*8*). Further, emissions from deforestation and cultivated organic soils drive on average 42% of the variance in each product's agricultural GHG emissions (fig. S10) and dominate the highest-impact producers' emissions (fig. S11), further justifying ongoing efforts to curb forest loss and limit cultivation on peatlands.

Communicate impacts up the supply chain

Processors, distributors, and retailers can substantially reduce their own impacts. For any product, 90th-percentile postfarm emissions are 2 to 140 times larger than 10th-percentile emissions, indicating large mitigation potential (fig. S12). For example, returnable stainless steel kegs create just 20 g of CO_2eq per liter of beer, but recycled glass bottles create 300 to 750 g of CO_2eq, and bottles sent to landfills create 450 to 2500 g of CO_2eq.

Processing, more durable packaging, and greater usage of coproducts can also reduce food waste. For example, wastage of processed fruit and vegetables is ~14% lower than that of fresh fruit and vegetables, and wastage of processed fish and seafood is ~8% lower (*24*). Providing processors and retailers with information about the impacts of their providers could encourage them to reduce waste where it matters most. For products such as beef, distribution and retail losses contribute 12 to 15% of emissions (fig. S13), whereas the sum of emissions from packaging, transport, and retail contributes just 1 to 9%. Here, reducing losses is a clear priority.

As a third strategy, procurement could source from low-impact farms. Although this strategy is important, and possible only with information about the impacts of providers, it has clear limitations. To be effective, it relies on high-impact production not simply being purchased elsewhere in the market. The case of the Roundtable on Sustainable Palm Oil (RSPO) shows that this is hard to achieve: despite one-fifth of 2017 palm oil production being certified, there remains virtually no demand in China, India, and Indonesia (*31*). Alternatively, this strategy would be effective if higher prices for sustainable production incentivized low-impact producers to increase output or high-impact producers to change practices. The case of organic food shows how passing premiums to consumers limits total market size and widespread practice change.

However, processors and retailers routinely demand that products meet taste, quality, and food safety standards. These markets are concentrated, with just 10 retailers representing 52% of U.S. grocery sales and 15% of global sales (*32*). This sometimes means that standards achieve market transformation (*33*), where virtually all producers adhere to gain market access. A fourth strategy for producers is setting environmental standards. These are particularly important: Although many environmental issues can be monitored and mitigated in a flexible way, issues such as harmful pesticide usage and deforestation require strict controls, and issues such as on-farm biodiversity are hard to quantify (*28*). Procurement, farming organizations, and international policy-makers must come together to implement a safety net for global agriculture—comprehensive standards to manage the worst and hardest-to-quantify environmental issues, extending the successes of existing schemes and enabling a flexible mitigation approach to operate effectively.

Producer mitigation limits and the role of consumers

Though producers are a vital part of the solution, their ability to reduce environmental impacts is limited. These limits can mean that a product has higher impacts than another nutritionally equivalent product, however it is produced.

In particular, the impacts of animal products can markedly exceed those of vegetable substitutes (Fig. 1), to such a degree that meat, aquaculture, eggs, and dairy use ~83% of the world's farmland and contribute 56 to 58% of food's different emissions, despite providing only 37% of our protein and 18% of our calories. Can animal products be produced with sufficiently low impacts to redress this vast imbalance? Or will reducing animal product consumption deliver greater environmental benefits?

We find that the impacts of the lowest-impact animal products exceed average impacts of substitute vegetable proteins across GHG emissions, eutrophication, acidification (excluding nuts), and frequently land use (Fig. 1 and data S2). These stark differences are not apparent in any product groups except protein-rich products and milk.

Although tree crops can temporarily sequester carbon and reduce nutrient leaching, the impact of nuts is dominated by low-yielding cashews and water-, fertilizer-, and pesticide-intensive almonds. Production of nuts doubled between 2000 and 2015 (*4*), and more work is required to improve their resource use efficiency. Although aquaculture can have low land requirements, in part by converting by-products into edible protein, the lowest-impact aquaculture systems still exceed emissions of vegetable proteins. This challenges recommendations to expand aquaculture (*1*) without major innovation in production practices first. Further, though ruminants convert ~2.7 billion metric tons of grass dry matter, of which 65% grows on land unsuitable for crops (*34*), into human-edible protein each year, the environmental impacts of this conversion are immense under any production method practiced today.

Using GHG emissions (Fig. 3), we identified five primarily biophysical reasons for these results. These reasons suggest that the differences between

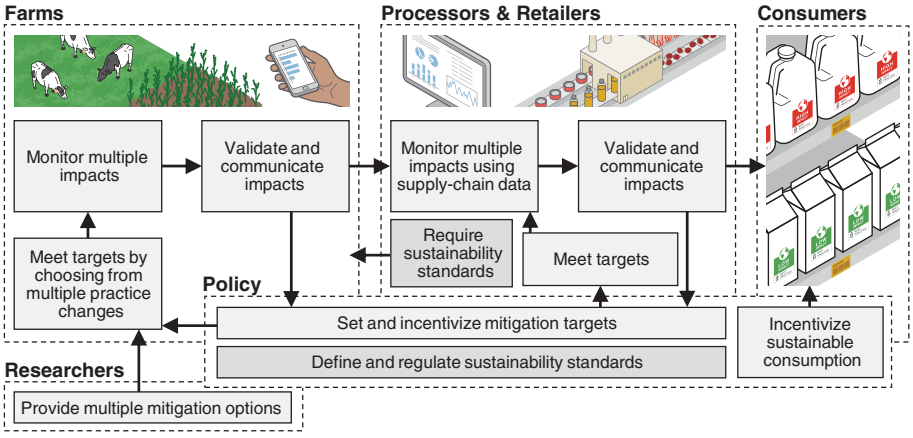

Fig. 4. Graphical representation of the mitigation framework.

animal and vegetable proteins will hold into the future unless major technological changes disproportionately target animal products. First, emissions from feed production typically exceed emissions of vegetable protein farming. This is because feed–to–edible protein conversion ratios are greater than 2 for most animals (*13*, *34*); because high usage of low-impact by-products is typically offset by low digestibility and growth; and because additional transport is required to take feed to livestock. Second, we find that deforestation for agriculture is dominated (67%) by feed, particularly soy, maize, and pasture, resulting in losses of above- and below-ground carbon. Improved pasture management can temporarily sequester carbon (*25*), but it reduces life-cycle ruminant emissions by a maximum of 22%, with greater sequestration requiring more land. Third, animals create additional emissions from enteric fermentation, manure, and aquaculture ponds. For these emissions alone, 10th-percentile values are 0.4 to 15 kg of CO_2eq per 100 g of protein. Fourth, emissions from processing, particularly emissions from slaughterhouse effluent, add a further 0.3 to 1.1 kg of CO_2eq, which is greater than processing emissions for most other products. Last, wastage is high for fresh animal products, which are prone to spoilage.

Mitigation through consumers

Today, and probably into the future, dietary change can deliver environmental benefits on a scale not achievable by producers. Moving from current diets to a diet that excludes animal products (table S13) (*35*) has transformative potential, reducing food's land use by 3.1 (2.8 to 3.3) billion ha (a 76% reduction), including a 19% reduction in arable land; food's GHG emissions by 6.6 (5.5 to 7.4) billion metric tons of CO_2eq (a 49% reduction); acidification by 50% (45 to 54%); eutrophication by 49% (37 to 56%); and scarcity-weighted freshwater withdrawals by 19% (−5 to 32%) for a 2010 reference year. The ranges are based on producing new vegetable proteins with impacts between the 10th- and 90th-percentile impacts of existing production. For the United States, where per capita meat consumption is three times the global average, dietary change has the potential for a far greater effect on food's different emissions, reducing them by 61 to 73% [see supplementary text (*17*) for diet compositions and sensitivity analyses and fig. S14 for alternative scenarios].

Consumers can play another important role by avoiding high-impact producers. We consider a second scenario where consumption of each animal product is halved by replacing production with above-median GHG emissions with vegetable equivalents. This achieves 73% of the previous scenario's GHG reduction and 67, 64, and 55% of the land use, acidification, and eutrophication reductions. Further, lowering consumption of more discretionary products (oils, sugar, alcohol, and stimulants) by 20% by avoiding production with the highest land use reduces the land use of these products by 39% on average. For emissions, the reductions are 31 to 46%, and for scarcity-weighted freshwater withdrawals, 87%.

Communicating average product impacts to consumers enables dietary change and should be pursued. Though dietary change is realistic for any individual, widespread behavioral change will be hard to achieve in the narrow timeframe remaining to limit global warming and prevent further, irreversible biodiversity loss. Communicating producer impacts allows access to the second scenario, which multiplies the effects of smaller consumer changes.

An integrated mitigation framework

In Fig. 4 we illustrate a potential framework implied by our findings, prior research, and emerging policy (*9*). First, producers would monitor their impacts using digital tools (*36*). Data would be validated against known ranges for each value (e.g., maximum yields given inputs) and validated or certified independently. In the United States these tools have already been integrated with existing farm software (*31*); in Africa and South Asia they are in trials with 2G mobile phones (*37*); and in China they have been operated by extension services with extremely successful results (*24*).

Second, policy-makers would set targets on environmental indicators and incentivize them by providing producers with credit or tax breaks or by reallocating agricultural subsidies that now exceed half a trillion dollars a year worldwide (*38*). Third, the assessment tools would provide multiple mitigation and productivity enhancement options to producers. Ideally these tools would become platforms that consolidate the vast amounts of research conducted by scientists around the world, while also sharing producer best practices. In particular, practice sharing offers a very effective way to engage producers (*24*). Maximum flexibility also ensures least-cost mitigation (*39*) and supports producer-led innovation (*24*).

Finally, impacts would be communicated up the supply chain and through to consumers. For commodity crops that are hard to trace (*31*), this may not be feasible and mitigation efforts may have to focus on producers. For animal products, stringent traceability is already required in many countries (*40*), suggesting that communicating impacts is most feasible where it matters the most. Communication could occur through a combination of environmental labels, taxes or subsidies designed to reflect environmental costs in product prices (*35*), and broader education on the true cost of food.

We have consolidated information on the practices and impacts of a wide range of producers. From this research, we have provided a unified exposition of the environmental science for making major changes to the food system. We hope this stimulates progress in this crucially important area.

REFERENCES AND NOTES

1. H. C. J. Godfray *et al.*, *Science* **327**, 812–818 (2010).
2. J. A. Foley *et al.*, *Nature* **478**, 337–342 (2011).
3. FAO, "The state of food and agriculture" (FAO, 2014).
4. FAOSTAT; www.fao.org/faostat.
5. FAO, "The second report on the state of the world's plant genetic resources for food and agriculture" (FAO, 2010).
6. K. M. Carlson *et al.*, *Nat. Clim. Change* **7**, 63–68 (2016).
7. P. C. West *et al.*, *Science* **345**, 325–328 (2014).
8. P. J. Gerber, H. Steinfeld, B. Henderson, A. Mottet, C. Opio, J. Dijkman, A. Falcucci, G. Tempio, "Tackling climate change through livestock: A global assessment of emissions and mitigation opportunities" (FAO, 2013).
9. European Commission, "Recommendation 2013/179/EU on the use of common methods to measure and communicate the life cycle environmental performance of products and organisations" (European Commission, 2013).
10. S. Hellweg, L. Milà i Canals, *Science* **344**, 1109–1113 (2014).
11. K. Paustian, *Environ. Res. Lett.* **8**, 021001 (2013).
12. S. Clune, E. Crossin, K. Verghese, *J. Clean. Prod.* **140**, 766–783 (2017).
13. D. Tilman, M. Clark, *Nature* **515**, 518–522 (2014).
14. M. Clark, D. Tilman, *Environ. Res. Lett.* **12**, 064016 (2017).
15. M. de Vries, I. J. M. de Boer, *Livest. Sci.* **128**, 1–11 (2010).
16. D. Nijdam, T. Rood, H. Westhoek, *Food Policy* **37**, 760–770 (2012).
17. See the supplementary materials.
18. W. Steffen *et al.*, *Science* **347**, 1259855 (2015).
19. A. F. Bouwman, D. P. Van Vuuren, R. G. Derwent, M. Posch, *Water Air Soil Pollut.* **141**, 349–382 (2002).
20. E. Röös, C. Sundberg, P. Tidåker, I. Strid, P.-A. Hansson, *Ecol. Indic.* **24**, 573–581 (2013).
21. E. Beza, J. V. Silva, L. Kooistra, P. Reidsma, *Eur. J. Agron.* **82**, 206–222 (2017).
22. Z. Cui *et al.*, *Biogeosciences* **11**, 2287–2294 (2014).
23. J. K. Ladha *et al.*, *Global Change Biol.* **22**, 1054–1074 (2016).
24. Z. Cui *et al.*, *Nature* **555**, 363–366 (2018).
25. P. Smith *et al.*, in *Climate Change 2014: Mitigation of Climate Change* (Cambridge Univ. Press, 2015), pp. 811–922.
26. E. Song, B. L. Nelson, J. Staum, *SIAM/ASA J. Uncertain. Quantif.* **4**, 1060–1083 (2016).
27. Q. Yu *et al.*, *Agric. Syst.* **153**, 212–220 (2017).
28. R. N. German, C. E. Thompson, T. G. Benton, *Biol. Rev. Cambridge Philos. Soc.* **92**, 716–738 (2017).

29. R. Lal, *Global Chang. Biol.* 10.1111/gcb.14054 (2018).
30. P. Smith *et al.*, *Agric. Ecosyst. Environ.* **118**, 6–28 (2007).
31. K. B. Waldman, J. M. Kerr, *Annu. Rev. Resour. Econ.* **6**, 429–449 (2014).
32. Euromonitor; www.euromonitor.com
33. D. C. Nepstad, W. Boyd, C. M. Stickler, T. Bezerra, A. A. Azevedo, *Philos. Trans. R. Soc. London Ser. B* **368**, 20120167 (2013).
34. A. Mottet *et al.*, *Global Food Sec.* **14**, 1–8 (2017).
35. M. Springmann *et al.*, *Nat. Clim. Change* **7**, 69–74 (2016).
36. K. Denef, K. Paustian, S. Archibeque, S. Biggar, D. Pape, "Report of greenhouse gas accounting tools for agriculture and forestry sectors" (Interim report to U.S. Department of Agriculture under contract no. GS23F8182H, ICF International, 2012).
37. GSM Association (GSMA), "Creating scalable, engaging mobile solutions for agriculture" (GSMA, 2017).
38. Organisation for Economic Co-operation and Development (OECD), "Agriculture policy monitoring and evaluation 2017" (OECD, 2017).
39. K. Segerson, *Annu. Rev. Resour. Economics* **5**, 161–180 (2013).
40. European Parliament and Council, "Establishing a common organization of the markets in agricultural products" [Regulation (EU) 1308/2013, European Union, 2013].

ACKNOWLEDGMENTS

We thank the many researchers who provided us with additional data, acknowledged in data S1. We are grateful to R. Grenyer, P. Smith, E. J. Milner-Gulland, C. Godfray, G. Gaillard, L. de Baan, Y. Malhi, D. Thomas, K. Javanaud, and K. Afemikhe for comments on the manuscript and Tyana for illustrations. **Funding:** This work was unfunded. **Author contributions:** J.P. conducted the analysis and wrote the manuscript. J.P. and T.N. contributed to the study design and data interpretation and reviewed the manuscript.

Competing interests: The authors declare no competing interests. **Data and materials availability:** A Microsoft Excel file allowing full replication of this analysis, containing all original and recalculated data, has been deposited in the Oxford University Research Archive (doi.org/10.5287/bodleian:0z9MYbMyZ).

SUPPLEMENTARY MATERIALS

www.sciencemag.org/content/360/6392/987/suppl/DC1
Materials and Methods
Supplementary Text
Figs. S1 to S14
Tables S1 to S17
References (*41–150*)
Data S1 and S2

5 October 2017; resubmitted 8 December 2017
Accepted 17 April 2018
10.1126/science.aaq0216

PLANETARY SCIENCE

Dunes on Pluto

Matt W. Telfer,[1]*† Eric J. R. Parteli,[2]† Jani Radebaugh,[3]† Ross A. Beyer,[4,5] Tanguy Bertrand,[6] François Forget,[6] Francis Nimmo,[7] Will M. Grundy,[8] Jeffrey M. Moore,[5] S. Alan Stern,[9] John Spencer,[9] Tod R. Lauer,[10] Alissa M. Earle,[11] Richard P. Binzel,[11] Hal A. Weaver,[12] Cathy B. Olkin,[12] Leslie A. Young,[9] Kimberly Ennico,[5] Kirby Runyon,[12] The New Horizons Geology, Geophysics and Imaging Science Theme Team‡

The surface of Pluto is more geologically diverse and dynamic than had been expected, but the role of its tenuous atmosphere in shaping the landscape remains unclear. We describe observations from the New Horizons spacecraft of regularly spaced, linear ridges whose morphology, distribution, and orientation are consistent with being transverse dunes. These are located close to mountainous regions and are orthogonal to nearby wind streaks. We demonstrate that the wavelength of the dunes (~0.4 to 1 kilometer) is best explained by the deposition of sand-sized (~200 to ~300 micrometer) particles of methane ice in moderate winds (<10 meters per second). The undisturbed morphology of the dunes, and relationships with the underlying convective glacial ice, imply that the dunes have formed in the very recent geological past.

Dunes require a supply of particulate material on a surface and a fluid boundary layer to entrain the grains (i.e., wind, for dunes on a planet's surface). They have been identified in some surprising locations: Contrary to predictions (*1*), Saturn's moon Titan has a broad belt of linear dunes encircling its equatorial latitudes (*2*), and despite the lack of a persistent atmosphere, eolian landforms (i.e., those related to wind) have also been suggested to occur on comet 67P/Churyumov-Gerasimenko (*3*). On 14 July 2015, NASA's New Horizons spacecraft flew past Pluto, which provided spectral data and imagery of the surface at resolutions as detailed as 80 m/pixel (*4*). The combination of Pluto's low gravity (0.62 m s^{-1}, or $^1/_{16}$ that of Earth), sparse atmosphere [1 Pa (*5*)], extreme cold [~45 K (*5*)], and surface composition [N_2, CO, H_2O, and CH_4 ices (*6*)] made pre-encounter predictions of surface processes challenging. However, pre-encounter speculation included that eolian processes, and potentially dunes, might be found on Pluto (*7*), because, despite the relatively thin atmosphere, the winds could possibly sustain saltation (i.e., particle movement by ballistic hops) in the current surface conditions. We examined images from the Long Range Reconnaissance Imager (LORRI) instrument (*8*) on New Horizons, taken during the probe's closest approach to Pluto, to search for landforms with the morphological and distributional characteristics of dunes. We also searched spectroscopic data from the Multispectral Visible Imaging Camera [MVIC (*9*)] for evidence of sufficient sand-sized ice particles to form dunes, and discuss how sublimation may play a role in lofting these particles, enabling them to be saltated into dunes.

Observations from New Horizons

The surface of Pluto, as revealed by New Horizons, is diverse in its range of landforms, composition, and age (*4*, *10*). One of the largest features, Sputnik Planitia (SP), is a plain of N_2, CO, and CH_4 ice [(*6*) and fig. S1] that extends across Pluto's tropics and at its widest point covers 30° of longitude (Fig. 1A). Polygonal features on the surface of SP, tens of kilometers across and bounded by trenches up to 100 m deep (Fig. 1, B and C) have been interpreted as the result of thermally driven, convective overturning of the ice (*11*, *12*), which, together with the uncratered surface of SP (*4*), suggests a geologically young [<500 thousand years (ka)] (*11*, *12*) and active surface. Much of the western edge of the ice is bounded by the Al-Idrisi Montes (AIM), a mountainous region with relief of up to 5 km. On the SP plain bordering these mountains, distinct, regularly spaced, linear ridges are evident within a belt of ~75 km from the mountain margin (Fig. 2A). They have positive relief as evident from shadows consistent with the mountains. The ridges show pronounced spatial regularity (~0.4 to 1 km wavelength), substantial length/width ratios (sometimes >20 km length), consistent shape along these lengths, and the presence of merging and bifurcation junctions (Figs. 1, C and D, and 2, D and E). These junctions are approximately evenly spread between 47 north-facing bifurcations and 42 south-facing splits, and there is no clear spatial patterning to the direction of junctions. Farther from the mountain margin, toward the southeast, the ridges become more widely spaced and generally larger, while still in isolated fields or patches. Dark streaks are also found across the surface of the ice, typically behind topographic obstacles, and have been interpreted as wind streaks (*4*). These features indicate that there are loose particles near and on the surface, as the streaks are thought to result from the deposition of suspended, fine particles in the lee of obstacles to wind flow (*4*, *5*, *13*) (Fig. 1, C and E).

We have identified 357 pale-colored, linear ridges on SP adjacent to the AIM (Fig. 2, A to C), as well as six darker wind streaks in addition to the seven previously identified (*4*). The ridges closest to the SP/AIM mountain front are oriented approximately parallel with it, and ridges farther to the southeast shift orientation clockwise by ~30° over a distance of ~75 km (Fig. 2, A and B); the ridges farther from the SP/AIM margin are significantly (Mann-Whitney U = −7.41; $p < 0.0001$) more widely spaced (Fig. 2C). Beyond the ~75-km-wide belt in which the linear ridges are predominantly found, the morphology of the surface changes, with preferential alignment of the ridges gradually disappearing (fig. S2), until the landscape is dominated by weakly aligned or unaligned, but still regularly dispersed, pits likely caused by sublimation of the ice (*14*). Wind streaks adjacent to the SP/AIM border are perpendicular to the ridges and mimic the shift in orientation shown by the ridges (Fig. 3, A and B). Streaks within the zone in which the ridges are found (i.e., <75 km from the SP/AIM border) are geographically (i.e., clockwise from north) oriented 113 ± 4° (1 standard deviation, σ, with sample number $n = 4$), while more distant wind streaks are oriented significantly [(heteroscedastic Student's $t = 9.912$; $p < 0.001$ (Fig. 3B)] differently at 153 ± 10° (1σ, $n = 9$).

Interpretation as dunes

The ridges found on western SP have morphological similarities to dunes (Figs. 1, C and D, and 4, A to C). In addition to analog similarities, we argue that these landforms are most consistent with an initial eolian depositional origin (i.e., dunes) on the grounds that (i) a depositional origin is favored by the superimposition of many of the dunes on the trenches bordering SP's convective cells (Figs. 1D and 2, D and E); (ii) the distribution of the dunes with pattern coarsening (enlarging toward the southeast), away from the mountains (Fig. 4C), is characteristic of dunefields; (iii) their orientation, and systematic regional changes to this orientation, are more readily explained by the wind regime than variations in incoming solar radiation; (iv) the presence of pronounced wind streaks, orthogonal to the dunes, demonstrates the potential efficacy of Pluto's winds; (v) their location, on a methane- and nitrogen-dominated ice cap adjacent to mountains, is where the strongest winds and a supply of sediment might be expected; and

[1]School of Geography, Earth and Environmental Sciences, Plymouth University, Drake Circus, Plymouth, Devon PL4 8AA, UK. [2]Department of Geosciences, University of Cologne, Pohligstraße 3, 50969 Cologne, Germany. [3]Department of Geological Sciences, College of Physical and Mathematical Sciences, Brigham Young University, Provo, UT 84602, USA. [4]Sagan Center at the SETI Institute, Mountain View, CA 94043, USA. [5]NASA Ames Research Center, Moffett Field, CA 94035, USA. [6]Laboratoire de Météorologie Dynamique, Université Pierre et Marie Curie, Paris, France. [7]University of California Santa Cruz, Santa Cruz, CA, USA. [8]Lowell Observatory, Flagstaff, AZ, USA. [9]Southwest Research Institute, Boulder, CO, USA. [10]National Optical Astronomy Observatory, Tucson, AZ 85726, USA. [11]Department of Earth, Atmosphere, and Planetary Science, Massachusetts Institute of Technology, Cambridge, MA 02139, USA. [12]Johns Hopkins University Applied Physics Laboratory, Laurel, MD, USA.
***Corresponding author. Email: matt.telfer@plymouth.ac.uk**
†These authors contributed equally to this work. ‡The New Horizons Geology, Geophysics and Imaging Science Theme Team authors and affiliations are provided in the supplementary materials.

(vi) their differing morphologies and undeformed regular alignment differ from the randomly aligned, shallow pits that border on the dune regions of SP (Fig. 4E and fig. S2) and the deeply incised, discrete, aligned pits that can be found toward SP's southern and eastern margins (Fig. 4D). These pit-like features are morphologically distinct from the dune-like ridges farther north near the AIM that we discuss here (Fig. 4, A and D). To test this hypothesis, we use a model (*15*) to examine the saltation of sand-sized (in this case, ~200 to 300 μm) particles on Pluto. Once initiated, the model indicates that saltation can be sustained even under the low (Earth-like; 1 to 10 m s^{-1}) wind speeds predicted at the surface today (*16*). However, the model also suggests that an additional process may be necessary to initially loft particles (*15*). This can be accomplished by sublimation, which is capable of lofting particles, and we model this process to find that particles can be entrained. This function of sublimation is in addition to the role sublimation may play in eroding mature dunes to more altered forms, which is also discussed in more detail below. Thus, under the current conditions, if there are sufficiently noncohesive sand-sized particulates on the surface of Pluto, we should expect to find dunes.

Terrestrial and planetary dunes that form straight ridges can occur either perpendicular to the wind, forming transverse dunes, or parallel to the net local wind regime, forming longitudinal (or linear) dunes, and regional variation in the alignment of such dunes on Earth is typically associated with meso- or large-scale atmospheric patterns (*17*). Wind streaks are well known on Venus and Mars, are present even under the tenuous atmosphere of Triton, and are generally considered to represent the wind direction (*13*). The presence of pronounced wind streaks (Fig. 1C) within the dunefield, very nearly orthogonal to the dune trends, suggests that the observed dunes are transverse forms (Fig. 3A). The transverse nature of the dunes is further supported by the lack of consistency in bifurcation orientation; within dunefields oriented parallel to net sediment-transporting winds, such defects tend to cluster in terms of their orientation (*18*). The transverse orientation also shows that these ridges cannot be sastrugi (erosional snow ridges that form parallel to net winds) (*19*), or other erosional features analogous to yardangs (wind-carved ridges). The dunes in the northwestern portion of SP/AIM (Fig. 4A) are even more regularly spaced and parallel than many transverse dunes on Earth. Possible explanations for this include a highly consistent wind regime, lack of topographic deflection of winds, or a smooth substrate.

Conditions for the formation of dunes and sublimation pits

The existence of dunes on the surface of Pluto requires three necessary criteria to be met. First, there must be a fluid atmosphere of sufficient density to make eolian transport possible. Second, there must be a granular material of a size and density, and with sufficiently low cohesion, that it can be entrained by winds. On Earth, this role is typically played by sand-sized mineral grains of a variety of compositions, including snow and ice. Third, given the high wind speeds needed to lift surface particles against cohesion forces (*20*) (Fig. 5), a specific mechanism must exist to loft large quantities of ice particles into the atmosphere where they are available for eolian transport. The presence of these criteria alone is necessary but not sufficient to identify the surface features as dunes. To justify our interpretation of these features as being dunes, we also examine the conditions required for the other most likely candidate: aligned sublimation pits.

Winds

The orientations of the dunes and the wind streaks change locally, and consistently; in the case of the dunes, over a distance on the order of 10 to 10^2 km. This implies that the topography and/or surface composition has influenced the local wind regime, as was anticipated (*21*). These orientations are consistent with sublimation-driven and topographic mechanisms for the horizontal displacement of the atmosphere, as winds are generated by a gravity-driven flow toward lower regions. Modeling of Pluto's current atmosphere suggests that surface winds on the order of 1 to 10 ms^{-1} are possible; they should be strongest where there are topographic gradients and when driven by sublimation of surface ices by sunlight (*15*). The location of the dunes at the western margins of the SP and AIM should thus be among the windiest locations on the known regions of Pluto. As with Earth and Mars, once grain transport along the surface of Pluto has begun, increased efficacy of grain-splash (the ejection of new particles due to grains in saltation colliding with the ground) promotes a hysteretic effect that further sustains sediment flux (*22*, *23*). We use a numerical model (*15*) to

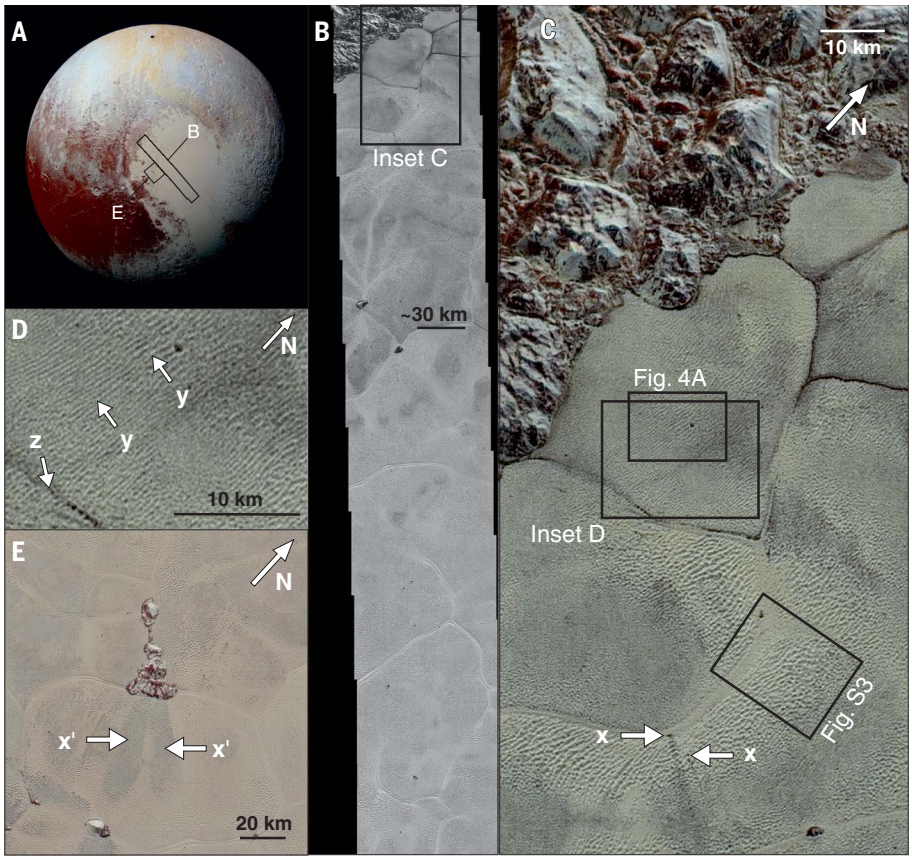

Fig. 1. New Horizons flyby imagery of landforms attributed to eolian origins. All images are unrectified, and thus all scales are approximate. Color-composite MVIC images are shown here for context; dune identification was performed on grayscale LORRI images (shown below). (**A**) Overview of Pluto centered on ~25° latitude, ~165° longitude, showing the locations of images (B) and (E) and Fig. 3A and fig. S3 (*47*). (**B**) The spatial context for SP and the AIM mountains to the west (*48*). Insets (**C**) and (**D**) show details of the highly regular spatial patterning, which we attribute to eolian dune formation, and two newly identified wind streaks (arrows x), along the margins of the SP/AIM border. Here the dunes show characteristic bifurcations (arrows y) and a superposition with SP's polygonal patterning (arrow z), suggesting a youthful age for these features (*49*). (**E**) Two further wind streaks on the surface (x'), downwind of the Coleta de Dados Colles (*4*). These wind streaks, farther from the SP/AIM margin, are oriented differently than those close to the icefield's edge and are still roughly orthogonal to the dunes there (*50*).

demonstrate that despite the high wind speeds needed for initial eolian entrainment, eolian transport can, once established, be sustained with wind speeds of ~10 m s^{-1} (Fig. 5).

Sediment supply

Although terrestrial dunes are typically associated with quartz, basalt, or gypsum sand, other materials can form the grains for dune development. Snow dunes of a very large scale are observed in the center of the Antarctic continent (*24*); on Titan, it is generally assumed to be atmosphere-derived organics, perhaps initially tholins, which form the equatorial belt of giant dunes (*25*). Whereas tholins are thought to form the dark patches of Pluto's equatorial regions (*6*), the dunes evident on SP are light in color and are thus not formed from the same complex, organic, photochemically derived haze seen in Pluto's atmosphere (*4*). The most likely candidates are thus N_2 and CH_4 ices. The surface of SP has generally been interpreted as predominantly composed of N_2 ice (*4*, *5*), just as solidified nitrogen snows are believed to account for Triton's ice-covered surface (*26*, *27*). The zone in which the ridges occur is coincident with the latitudes in which net N_2 condensation occurs over the course of a Pluto year (*16*, *28*) (fig. S3). However, recent analyses suggest that the composition may be a more complex mix of N_2, CH_4, and CO ices (*29*). Our analysis of data from the MVIC instrument, using a CH_4 filter (*15*), suggests that the location of the ridges and streaks coincides with a region of enhanced CH_4 ice content (fig. S4). To the west of SP, the Enrique Montes in Cthulhu Macula (CM) have been shown to be capped with methane, presumably as the result of condensation or precipitation (*29*, *30*). CH_4 ice retains hardness and rigidity under Pluto surface conditions, which is ideal for saltation and dune formation, whereas N_2 ice is likely to be softer. These constraints lead us to conclude that the dunes are formed predominantly of grains of methane ice, though we do not rule out that there could also be a nitrogen ice component. The presence of transverse forms, indicating sediment-rich local conditions, as opposed to more sediment-starved isolated barchans (discrete, crescentic dunes), suggests that locally, the sediment supply to this region of SP must be, or must have been, abundant. Given the strength of the color and boundary delineations of methane in the AIM (fig. S3), the methane ice may be quite thick and perhaps similar to valley glaciers in these isolated regions. If such high-altitude methane snowpack is a regular, seasonal occurrence, this may be a substantial reservoir from which to derive the abundant sand across the northwestern surface of SP required to form these transverse dunes.

Grain size

Credible sediment sizes are required for dune formation under the likely eolian regime. The grain sizes proposed for nitrogen ices (e.g., on Triton) have varied from micrometer (*31*, *32*) to meter scale (*33*). We develop a method (*15*) to approximately constrain average grain size (d) and formative wind speed (U) from the mean crest-to-crest distance, or wavelength (λ), of the transverse dunes. For eolian dunes, the relevant length scale controlling this wavelength is the saturation length (L_{sat}) of the sediment flux, which is the distance needed by the flux to adapt to a change in local flow conditions. By combining theory (*34*), which predicts L_{sat} as a function of wind speed and attributes of sediment and atmosphere, with a mathematical model (*35*) for λ as a function of L_{sat} and U, we obtain the values of d and U that are consistent with λ. These values are shown in fig. S5, for $\lambda \approx 700$ m and $\lambda \approx 560$ m, which correspond to the transverse dunes far from and near to the mountainous area of Fig. 1, respectively. Given that expected formative wind speeds on Pluto are not larger than 10 m s^{-1} (*16*), fig. S5 implies that grain size does not exceed ~370 μm and is most probably in the range between 210 and 310 μm. The spectral response of the MVIC CH_4 filter offers an additional constraint on the possible grain sizes observed, as Hapke modeling of the scattering within a granular medium provides a grain size–dependent control on the equivalent width of the absorption band. We find (*15*) that the observed response is consistent with a granular medium of ~200 to 300 μm.

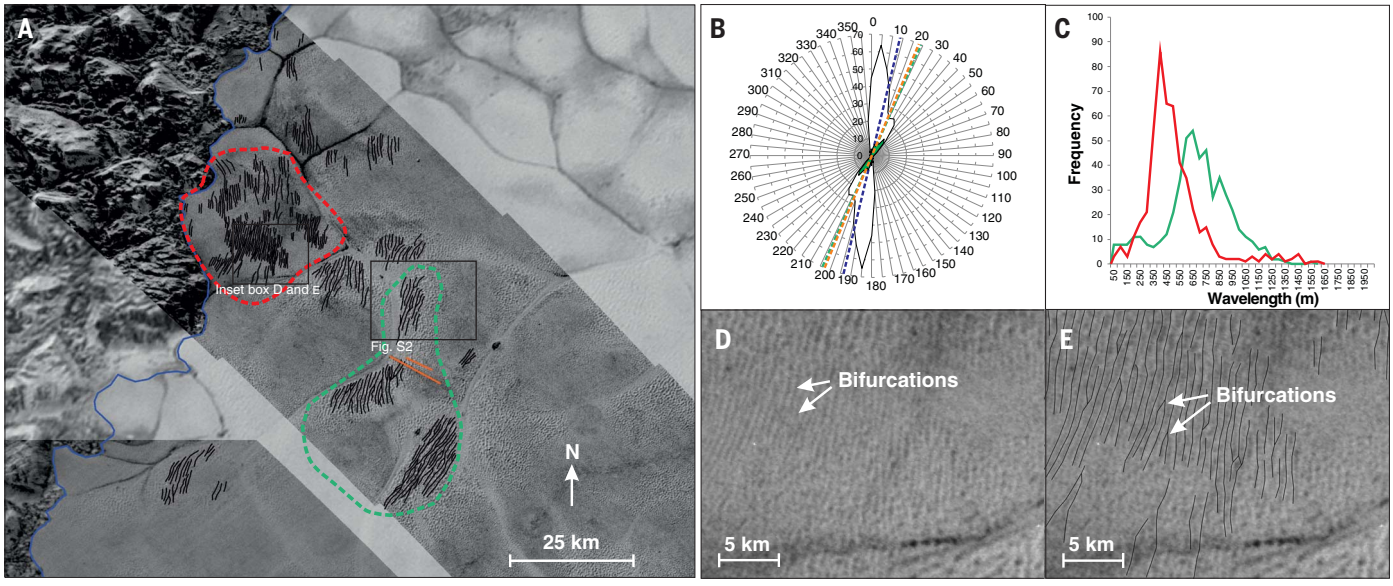

Fig. 2. Identified features. (**A**) Dunes (black lines) at the margins of western Sputnik Planitia. Prominent wind streaks are marked with orange lines. (**B**) Radial plot of the orientation of the dunes (n = 331), and the direction orthogonal to the wind implied by the wind streaks close to the SP/AIM margin (orange dashed line; n = 4; arithmetic mean, $\bar{x}$ = 203°). Because the dunes have a distinct shift in orientation (fig. S1), the distribution of dunes in the three patches closest to the wind streaks within the dunefield [outlined in dashed green in (A)] has been separately highlighted on the radial plot, in green. These have a mean orientation of 204° (n = 77), highlighted by the dashed green line. The dark blue line indicates the mean trend of the border of SP and the Al-Idrisi Montes in this area (194°). (**C**) Frequency of dune spacings in clusters close to [red line representing dunes within the red dashed line of (A)] and far from [green line representing dunes within the green dashed line of (A)] the icefield/mountain interface. Dunes farther from the mountains are more widely spaced ($\bar{x}$ = 700 m) than those close to the mountains ($\bar{x}$ = 560 m). (**D**) Detail of the image interpretation process of the highest-resolution swath, showing linear ridges, which sometimes bifurcate but are otherwise notable for their regularity. (**E**) The same image with ridge lines highlighted.

Lofting

Although eolian transport can be maintained under Pluto's current wind regime, the speeds necessary for initial entrainment are orders of magnitude greater than those believed to be present at Pluto's surface (Fig. 5). An additional process is thus likely to be necessary to initiate eolian activity. In Sputnik Planitia, this process may be related to the intense, solar-driven sublimation of surface ices that injects more than 10^3 m^3 m^{-2} of gas into the atmosphere every afternoon [figure 8 of (*16*)]. When sunlight penetrates through, the upper layers of semi-transparent ice particles are lofted, sometimes at high vertical velocities, due to a mechanism often referred to as a solid-state greenhouse (*36*). Therefore, initial entrainment of ice grains that eventually form dunes may result from sublimating subsurface ice, as has been observed in the thin atmospheres of Mars' northern polar region (*37*) and proposed for comet 67P/Churyumov-Gerasimenko (*38*, *39*) and Triton (*24*, *25*). Modeling (*15*) suggests that subsurface N_2 sublimation under Pluto surface conditions is capable of lofting even the densest candidate particles [N_2 ice, at 1030 kg m^{-3}, is denser than CH_4 ice, at 494 kg m^{-3} (*40*)] with sizes ~200 μm, even at 0.1 Pa; within the range of both Pluto's atmospheric pressure and the solid N_2 vapor pressure. Surface ices of mixed composition offer an additional potential mechanism for facilitating grain lofting. At the nitrogen frost point temperature of 63 K (*11*), pure methane ice particles mixed with nitrogen should not sublimate at all. As methane particles are slightly heated by the Sun, they should enable the sublimation of the nitrogen ice that they touch and thus be readily lofted into the atmosphere. Similar processes have recently been suggested for the migration of tholin deposits on the surface of Pluto (*41*). Past periods of higher atmospheric pressures, which have been suggested (*42*), could facilitate initial entrainment due to increased efficacy of eolian processes.

Sublimation

The landscape of SP contains evidence of sublimation-driven landforms (*4*, *7*, *14*), and this process is important in shaping parts of Pluto's surface. We consider whether the landforms described here are more consistent with origins attributable to eolian or sublimation processes. Locally, sublimation pits are deeply incised and may align to form linear troughs up to tens of kilometers long and up to ~1 km deep (*4*, *7*). Frequently, and especially toward the southern and eastern margins of SP, any alignment is subsequently heavily deformed, presumably driven by glacial flow and convective overturning. Analog landforms on Earth are provided by sublimation-driven textures of snow and ice surfaces: ablation hollows (suncups) and penitentes (*14*, *43*). On Earth, ablation hollows on snow may become aligned to leave ridges (penitentes), which align themselves to within ±30° of east-west (i.e., the annual mean net Sun path) (*44*). Although the orientation of any penitentes on Pluto is likely to be more complex and seasonally dependent, they are only likely to form wavelengths in excess of ~1000 m (*45*). It is possible that sublimation has acted upon already formed dunes in some regions (Fig. 2A). In polar regions on Earth, wind-driven snow or ice grains can produce dunes, which then become hardened by sintering and begin to undergo modification by wind and sublimation processes, thus changing from depositional to erosional landforms (*44*, *45*). Given the tendency of ices to sinter together under the right conditions, this could also happen in the CH_4 or N_2 ices of Pluto's dunes. Sublimation erosion of Pluto's dunes may enlarge and round the areas between the dunes, and sharpen the dune crests while preserving the overall dune orientation and spacing. This morphology may be seen just at the resolution limit in the features farthest from the mountains in Fig. 2A (enlarged view in fig. S2). This is supported by modeling (*15*) of the net accumulation of ices across Pluto's surface during the past two (Earth) centuries (fig. S4), which suggests that for the past ~30 Earth years, the dunefield has been experiencing net sublimation. Some of these features may have progressed so far toward being erosional that we have not identified them as dunes (fig. S2).

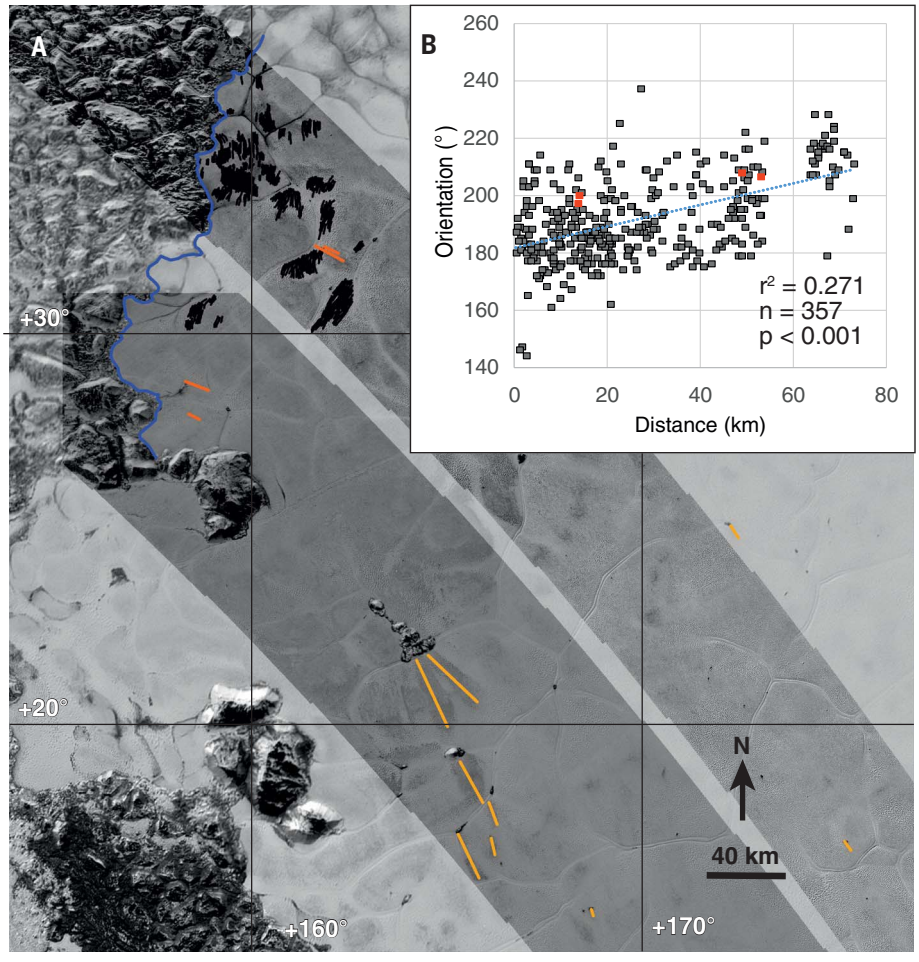

Fig. 3. The western margin of Sputnik Planitia. (**A**) Transverse dunes are shown in black, the margin of the icefield and neighboring Al-Idrisi Montes to the northwest in blue, wind streaks close to this margin in orange, and further wind streaks farther from the mountains in yellow. There is an orientation shift between the two sets of wind streaks, matching the correlation between the distance to the margin of the icefield and mountains, and the orientation of the transverse dunes [(**B**); wind streaks in orange]. We interpret this as topography and/or surface composition influencing regional wind regimes.

Age

An upper limit on the age of the dunes, which sit atop the ice of the western margins of SP, is imposed by the recycling rate of the upper surface of the convectional cells within the ice (i.e., <500 ka) (*11*, *12*). This overturning of the substrate, inferred from the complete absence of identified craters on SP, provides an age constraint for superficial landforms that is not available for dunes on other solar system bodies and implies a geologically and/or geomorphologically active surface (*4*, *10*, *46*). Surface features, undistorted by the convectional overturning within the ice, must be much younger than the time scales of convection, and therefore closer to the time scales of Pluto's strong seasons (i.e., terrestrial decades to centuries). Further evidence that the dunes form on a time scale substantially shorter than that of the convection is suggested

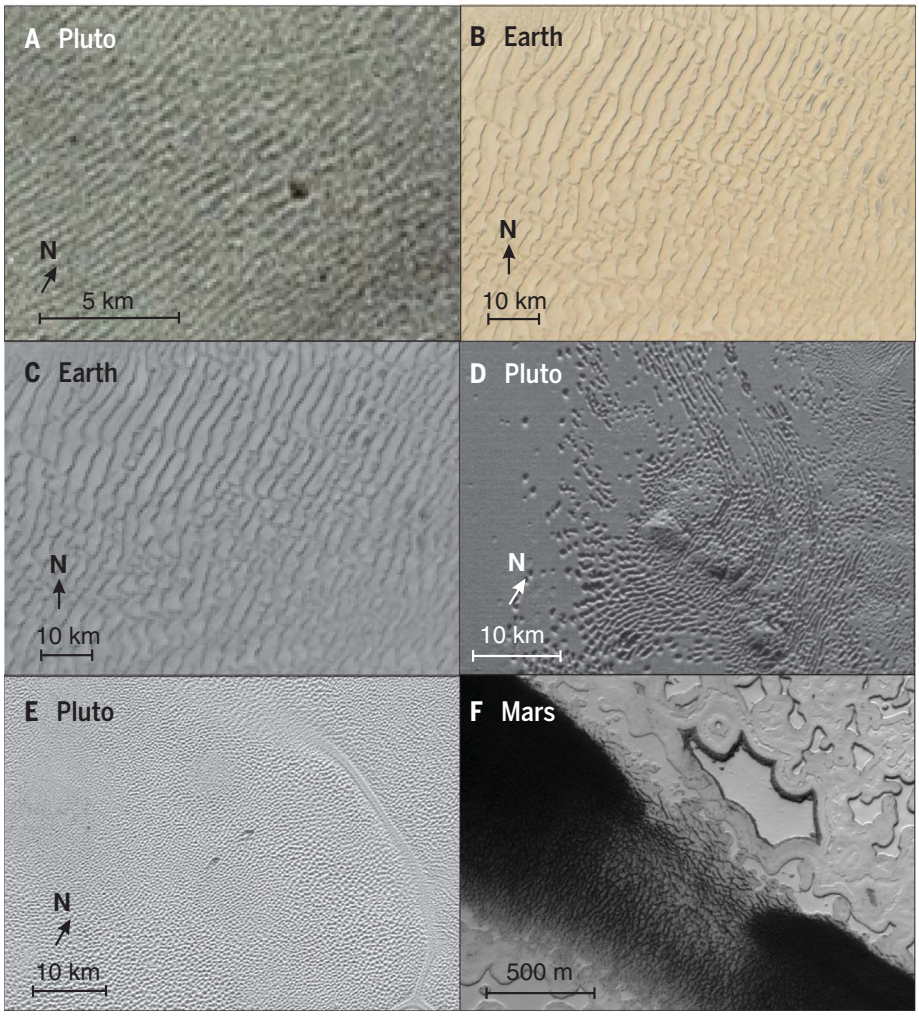

Fig. 4. Analogs and comparison with sublimation features. (**A**) Details of the dunes on western Sputnik Planitia, centered on 34.35° 159.84° (location shown in Fig. 1). (**B**) Analogous terrestrial transverse dunes of the Taklamakan Desert, western China [Image credit: image CNRS/SPOT, DigitalGlobe and courtesy of Google Earth], and (**C**) the same location down-sampled to a relative resolution similar to that of the Pluto dunes (i.e., ~5 to 10 pixels per crest-crest spacing). (**D**) The aligned and distorted sublimation features abundant on southern and eastern SP (image centered on −4.78° 189.48°) and (**E**) weakly aligned to randomly oriented, shallow sublimation pits. (**F**) An example of a landscape revealing both eolian and sublimation-derived landforms at Mars' southern polar ice cap from the Mars Reconnaissance Orbiter reveals both dark eolian bedforms (dunes and ripples), as well as sublimation pits developing in the underlying CO_2 ice. [Image credit: NASA/JPL/University of Arizona, ESP_014342_0930_RED]

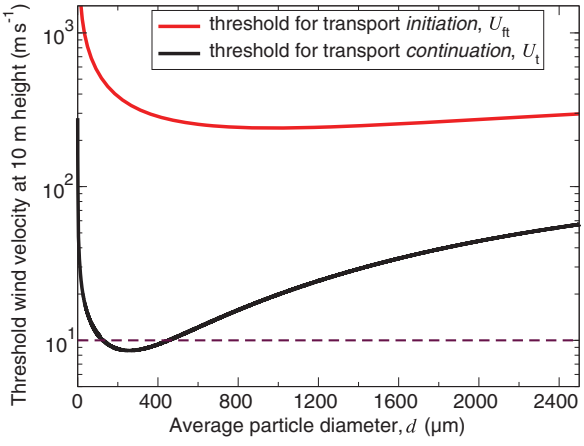

Fig. 5. Minimal threshold wind speeds. The wind speeds required for initiation (U_{ft}, orange line) and continuation (U_t, black line) of saltation on Pluto, at a reference height of 10 m above the soil, were computed for different values of the average particle diameter (*15*). The dashed horizontal line indicates maximum likely wind speeds at Pluto's surface.

by the superposition of the dunes over the depressions at the cell margins (Fig. 1G).

Summary and conclusions

We have presented evidence that the highlands adjacent to SP accumulate methane. The ridged, dune-like landforms nearby, and accompanying wind streaks, are rich in methane relative to their underlying substrate. Although the wind speeds needed for eolian entrainment are higher than the likely wind speeds present on the surface, sublimation provides a credible mechanism for lofting grains. Numerical sediment transport and spectral modeling suggest that these methane grains are ~200 to 300 μm. Our models suggest that eolian transport is highly effective under Pluto surface conditions once initiated. An ample sediment supply appears to be available from a seasonally abundant snowpack in the adjacent mountains. The result is the formation of transverse dunes, as we identify in the images from New Horizons. The orientation of the dunes perpendicular to the wind is supported by the local topography and surface, and accompanying wind streaks. The presence of these dunes indicates an active atmosphere that produces geologically young landforms.

REFERENCES AND NOTES

1. R. D. Lorenz, J. I. Lunine, J. A. Grier, M. A. Fisher, *J. Geophys. Res. Planets* **100**, 26377–26386 (1995).
2. R. D. Lorenz *et al.*, *Science* **312**, 724–727 (2006).
3. N. Thomas *et al.*, *Science* **347**, aaa0440 (2015).
4. S. A. Stern *et al.*, *Science* **350**, aad1815 (2015).
5. G. R. Gladstone *et al.*, *Science* **351**, aad8866 (2016).
6. W. M. Grundy *et al.*, *Science* **351**, aad9189 (2016).
7. J. M. Moore *et al.*, *Icarus* **246**, 65–81 (2015).
8. A. F. Cheng *et al.*, *Space Sci. Rev.* **140**, 189–215 (2008).
9. D. C. Reuter *et al.*, *Space Sci. Rev.* **140**, 129–154 (2008).
10. J. M. Moore *et al.*, *Science* **351**, 1284–1293 (2016).
11. W. B. McKinnon *et al.*, *Nature* **534**, 82–85 (2016).
12. A. J. Trowbridge, H. J. Melosh, J. K. Steckloff, A. M. Freed, *Nature* **534**, 79–81 (2016).
13. C. Sagan, C. Chyba, *Nature* **346**, 546–548 (1990).
14. J. M. Moore *et al.*, *Icarus* **287**, 320–333 (2017).
15. Materials and methods are available as supplementary materials.
16. F. Forget *et al.*, *Icarus* **287**, 54–71 (2017).
17. R. A. Bagnold, in *The Physics of Blown Sand and Desert Dunes* (Chapman and Hall, London, 1941), p. 16.
18. M. W. Telfer *et al.*, *Geomorphology* **290**, 85–100 (2017).
19. S. G. Warren, R. E. Brandt, P. O'Rawe Hinton, *J. Geophys. Res. Planets* **103**, 25789–25807 (1998).
20. R. Greeley, J. D. Iversen, *Wind as a Geological Process: On Earth, Mars, Venus and Titan* (Cambridge Univ. Press, 1985), vol. 4, pp. 67–106.
21. A. D. Toigo *et al.*, *Icarus* **254**, 306–323 (2015).
22. J. F. Kok, *Geophys. Res. Lett.* **37**, L12202 (2010).
23. J. F. Kok, *Phys. Rev. Lett.* **104**, 074502 (2010).
24. M. Frezzotti, S. Gandolfi, S. Urbini, *J. Geophys. Res. D Atmospheres* **107**, 4344 (2002).
25. L. A. Soderblom *et al.*, *Planet. Space Sci.* **55**, 2025–2036 (2007).
26. C. J. Hansen, A. S. McEwen, A. P. Ingersoll, R. J. Terrile, *Science* **250**, 421–424 (1990).
27. L. A. Soderblom *et al.*, *Science* **250**, 410–415 (1990).
28. T. Bertrand, F. Forget, *Nature* **540**, 86–89 (2016).
29. B. Schmitt *et al.*, *Icarus* **287**, 229–260 (2017).
30. A. D. Howard *et al.*, *Icarus* **287**, 287–300 (2017).
31. J. Eluszkiewicz, *J. Geophys. Res. Planets* **96** (S01), 19217–19229 (1991).
32. J. Eluszkiewicz, D. J. Stevenson, *Geophys. Res. Lett.* **17**, 1753–1756 (1990).
33. A. P. Zent, C. P. McKay, J. B. Pollack, D. P. Cruikshank, *Geophys. Res. Lett.* **16**, 965–968 (1989).
34. T. Pähtz, J. F. Kok, E. J. R. Parteli, H. J. Herrmann, *Phys. Rev. Lett.* **111**, 218002 (2013).
35. A. Fourrière, P. Claudin, B. Andreotti, *J. Fluid Mech.* **649**, 287–328 (2010).

36. E. Kaufmann, N. I. Kömle, G. Kargl, . *Icarus* **185**, 274–286 (2006).
37. N. Thomas, C. J. Hansen, G. Portyankina, P. S. Russell, *Icarus* **205**, 296–310 (2010).
38. N. Thomas *et al*., *Astron. Astrophys.* **583**, A17 (2015).
39. P. Jia, B. Andreotti, P. Claudin, *Proc. Natl. Acad. Sci. U.S.A.* **114**, 2509–2514 (2017).
40. N. Fray, B. Schmitt, *Planet. Space Sci.* **57**, 2053–2080 (2009).
41. D. Cruikshank, paper presented 49th Division of Planetary Sciences meeting, Provo, UT, 15 October 2017. Abstract ID 102.06.
42. S. A. Stern *et al*., *Icarus* **287**, 47–53 (2017).
43. S. Filhol, M. Sturm, *J. Geophys. Res. Earth Surf.* **120**, 1645–1669 (2015).
44. L. M. Cathles, D. S. Abbot, D. R. MacAyeal, *J. Glaciol.* **60**, 147–154 (2014).
45. J. E. Moores, C. L. Smith, A. D. Toigo, S. D. Guzewich, *Nature* **541**, 188–190 (2017).
46. S. J. Robbins *et al*., *Icarus* **287**, 187–206 (2017).
47. NASA/Johns Hopkins University Applied Physics Laboratory/South West Research Institute, The Rich Colour Variations of Pluto; https://photojournal.jpl.nasa.gov/catalog/PIA19952 (accessed 27 September 2016).
48. NASA/Johns Hopkins University Applied Physics Laboratory/South West Research Institute, Pluto's Icy Plains Captured in Highest-Resolution Views from New Horizons; https://photojournal.jpl.nasa.gov/catalog/PIA20336 (accessed 27 September 2016).
49. NASA/Johns Hopkins University Applied Physics Laboratory/South West Research Institute, Pluto's Close-up, Now in Color; https://photojournal.jpl.nasa.gov/catalog/PIA20213 (accessed 27 September 2016).
50. NASA/Johns Hopkins University Applied Physics Laboratory/South West Research Institute, Ice Mountains and Plains; https://photojournal.jpl.nasa.gov/catalog/PIA19954 (accessed 27 September 2016).

ACKNOWLEDGMENTS

We thank everyone involved, from concept to data retrieval, with the New Horizons mission. This research has made use of the USGS Integrated Software for Imagers and Spectrometers (ISIS). **Funding:** E.J.R.P. thanks the German Research Foundation for grant RI2497/3-1. All New Horizons team member authors are funded by the NASA New Horizons Project. **Author contributions:** M.W.T. conducted the spatial analysis and image interpretation, coordinated the research, and co-wrote the paper. E.J.R.P. developed and conducted the numerical modeling and co-wrote the paper. J.R. coordinated the research and co-wrote the paper. R.A.B. produced and provided LORRI mosaicking. T.B. and F.F. provided data on surface/atmosphere exchanges. F.N. performed calculations on the effectiveness of sublimation modeling. W.M.G. conducted the Hapke modeling. J.M.M., S.A.S., and J.S. contributed to the manuscript. T.R.L. produced and provided LORRI mosaicking. R.P.B. and A.M.E. provided circulation model data. H.A.W., C.B.O., L.A.Y., and K.E. are project scientists and contributed to the manuscript. K.R. provided discussion of ideas. **Competing interests:** There are no competing interests to declare. **Data and materials availability:** The LORRI data are archived in the Planetary Data System (PDS) Small Bodies Node at https://pds-smallbodies.astro.umd.edu/holdings/nh-p-lorri-3-pluto-v2.0/. MVIC data are available via the PDS at https://pds-smallbodies.astro.umd.edu/holdings/nh-p-mvic-3-pluto-v2.0/

SUPPLEMENTARY MATERIALS

6 July 2017; accepted 19 April 2018
10.1126/science.aao2975

REPORT

BIOMATERIALS

A bioinspired flexible organic artificial afferent nerve

Yeongin Kim,[1]* Alex Chortos,[2]* Wentao Xu,[3,4]*† Yuxin Liu,[5] Jin Young Oh,[6,7] Donghee Son,[6] Jiheong Kang,[6] Amir M. Foudeh,[6] Chenxin Zhu,[1] Yeongjun Lee,[3] Simiao Niu,[6] Jia Liu,[6] Raphael Pfattner,[6] Zhenan Bao,[6]† Tae-Woo Lee[3]†

The distributed network of receptors, neurons, and synapses in the somatosensory system efficiently processes complex tactile information. We used flexible organic electronics to mimic the functions of a sensory nerve. Our artificial afferent nerve collects pressure information (1 to 80 kilopascals) from clusters of pressure sensors, converts the pressure information into action potentials (0 to 100 hertz) by using ring oscillators, and integrates the action potentials from multiple ring oscillators with a synaptic transistor. Biomimetic hierarchical structures can detect movement of an object, combine simultaneous pressure inputs, and distinguish braille characters. Furthermore, we connected our artificial afferent nerve to motor nerves to construct a hybrid bioelectronic reflex arc to actuate muscles. Our system has potential applications in neurorobotics and neuroprosthetics.

Whereas classical von Neumann–based computing systems rely on centralized and sequential operations determined by a clock, neurons and synapses in biological nervous systems process information on the basis of distributed, parallel, and event-driven computation (*1*). As a result, classical systems exhibit the advantages of high speed and accuracy for well-defined problems, and biological systems are compact, fault tolerant, and power efficient for complex real-world problems, such as visual information processing, speech recognition, and movement control. Biological systems have influenced many fields of science and engineering, such as neuromorphic computing (*2*–*5*), bioinspired sensing systems (*6*–*9*), control theory for legged robots (*10*, *11*), and prosthetics (*12*–*14*).

Biologically inspired systems have been implemented at the software level in classical von Neumann–based systems to distinguish braille characters (*15*) and control actuators in legged robots (*10*, *11*). Alternatively, complex silicon circuits have been developed to mimic the spike-based information processing in biological systems, in which the function of a synapse was emulated by several conventional silicon transistors and a capacitor (*16*).

Device structures that emulate the functionality and signal processing of biological components may potentially simplify complex circuits by mimicking multiple synapses with a single device. Organic devices are attractive because their characteristics can be tuned through chemical design (*17*, *18*), they are compatible with printing methods that enable large-area coverage at a low cost (*13*), and they have relatively low elastic moduli, similar to those of soft biological systems.

The development of neuromorphic systems that mimic the sense of touch can benefit from the improved understanding of information processing in somatosensory peripheral nerves. The branched structure of slowly adapting type I (SA-I) afferent (sensory) neurons, which leads to a complex receptive field with many hotspots, is critical for sensing at a spatial resolution smaller than the spacing between the receptive field centers (fig. S1) (*19*), discerning the movement of objects, and distinguishing the orientation of edges on objects (*19*). The interneurons in the spinal cord have also been found to form synapses with multiple afferent neurons to encode and separate input features before tactile information is delivered to the cortex (*20*, *21*).

Here we describe an artificial afferent nerve based on flexible organic electronics (*22*–*25*). The bioinspired artificial afferent nerve emulates the functions of biological SA-I afferent nerves (Fig. 1A) by collecting data from multiple tactile receptors and conveying this information to biological efferent (motor) nerves, completing a hybrid bioelectronic reflex arc. Our artificial afferent nerve (Fig. 1, B and C, and fig. S2) consists of three core components: resistive pressure sensors, organic ring oscillators, and a synaptic transistor. Artificial mechanoreceptors consisting of a cluster of pressure sensors (each pressure sensor corresponds to a hotspot in the receptive field) are connected to an artificial nerve fiber (a ring oscillator) that converts external tactile stimuli into voltage pulses. The electrical signals from multiple artificial nerve fibers are then integrated and converted into postsynaptic currents by a synaptic transistor. The synaptic transistor can be subsequently used to interface with biological efferent nerves to form a complete monosynaptic reflex arc.

The resistive pressure sensors (*13*), with a sensitivity and working range comparable to those of biological receptors, are composed of a conducting pyramid-structured elastomer that forms a resistive pathway between CNT (carbon nanotube) and Au electrodes (Fig. 1B and fig. S3). An increase in pressure increases the contact area and therefore decreases the resistance between the CNT electrode and the Au electrodes (Fig. 2A).

The organic ring oscillator (figs. S4 and S5) was made of odd numbers of pseudo–complementary metal-oxide semiconductor (CMOS) inverters (figs. S6 and S7). The ring oscillator was designed to oscillate at frequencies that match the action potentials of sensory neurons (0 to 100 Hz) (supplementary text) (*26*). Frequency-encoded information can be more robust to voltage degradation and parasitic resistances than amplitude-encoded information. The supply voltage to the ring oscillator increased with the pressure on the sensor (Fig. 2A). The oscillation of the ring oscillator is "off" and the power consumption decreases (though not to 0 W because of the pseudo-CMOS design) when there is no pressure on the sensor. A constant nonzero pressure input leads to a fixed supply voltage to the ring oscillator, resulting in a constant frequency output that can be easily used to calculate the pressure input on the basis of a 1-to-1 relationship between pressure inputs and concurrent ring oscillator outputs, but this constant input also increases power consumption compared with that of biological SA-I afferent nerves, which have slow sensory adaption (supplementary text). An increase in pressure intensity resulted in an increase in both the frequency and the peak amplitude of electrical impulses from the oscillator (Fig. 2B). This is slightly different from the case in biology, in which the amplitudes of action potentials are usually the same (supplementary text).

The synaptic transistor (*17*, *27*, *28*) was fabricated with the use of a solution-processed conjugated polymer (the compound **P1**) (fig. S8B) as the hole-transporting semiconductor and an ion gel as the gate dielectric (figs. S8 to S11). Although the synaptic transistor was more limited in its capacity for run-time tuning of the temporal dynamics during operation (fig. S12) than the rather complex silicon synapse consisting of several transistors and a capacitor (*16*), we were able to obtain decay times for postsynaptic currents (typically 2 to 3 ms) (fig. S13) in a range comparable

[1]Department of Electrical Engineering, Stanford University, Stanford, CA, USA. [2]Department of Materials Science and Engineering, Stanford University, Stanford, CA, USA. [3]Department of Materials Science and Engineering, Seoul National University, Seoul, South Korea. [4]Institute of Photoelectronic Thin Film Devices and Technology, Nankai University, Tianjin, China. [5]Department of Bioengineering, Stanford University, Stanford, CA, USA. [6]Department of Chemical Engineering, Stanford University, Stanford, CA, USA. [7]Department of Chemical Engineering, Kyung Hee University, Yongin, South Korea.
*These authors contributed equally to this work.
†Corresponding author. Email: wentao@nankai.edu.cn (W.X.); zbao@stanford.edu (Z.B.); twlees@snu.ac.kr (T.-W.L.)

to that of decay times for synapses of biological afferent nerves (1.5 to 5 ms) (*21*, *29*) by choosing a specific polymer semiconductor during fabrication (table S1). The large variation in decay times within a material should have minimal effect on the output (*30*). The voltage outputs from the ring oscillators were connected to the gate electrodes of the synaptic transistor. The frequency of the current output from the synaptic transistor (Fig. 2C) matched the frequency of the voltage output from the ring oscillator (Fig. 2B). However, the pressure-current output from the synaptic transistor (Fig. 2C) was more linear than the pressure-voltage output of the ring oscillator (Fig. 2B). Our artificial afferent neuron consumes ~8 μW in the "off" state and ~25 μW in the "on" state (fig. S14). An array of our artificial afferent neurons can lead to a flexible artificial afferent nervous system—one of spiking neural networks (supplementary text)—with lower power consumption than the system consisting of a conventional flexible one-transistor–one-resistor pressure sensor array connected to Si-integrated circuit chips, which consume additional power for readout and control (fig. S15 and table S2).

Prolonged presynaptic voltage spikes can lead to more anion accumulation near or in the organic semiconductor and then increase the amplitude of postsynaptic currents (*31*). The peak postsynaptic currents are influenced by not only the magnitude of the pressure stimulus (Fig. 2, C and D) but also the duration of the pressure stimulus (Fig. 2, E and F). The duration of the pressure stimulus does not change voltage outputs from the ring oscillator. When we applied 500 cycles of 2-s pressure stimulation every 10 s (fig. S12), we detected slight increases in the postsynaptic currents and the decay times.

The synaptic transistor can combine signals from multiple ring oscillators because the ion gel allows the active channel to be gated by multiple electrodes (Fig. 3A and fig. S10C). The postsynaptic currents resulting from the pressures simultaneously applied to two pressure sensors (Fig. 3D) were comparable to the sum of the currents resulting from a pressure applied to two individual sensors (Fig. 3E = Fig. 3B + Fig. 3C). In the Fourier transform of each case (Fig. 3F), the synaptic transistor could combine signals from two pressure sensors and generate postsynaptic currents consisting of two frequency components corresponding to those from the two pressure sensors. Analogous to the way in which dendrites of a postsynaptic neuron in connection with a number of biological synapses add action potentials from multiple presynaptic neurons, a single synaptic transistor can add voltage inputs coming

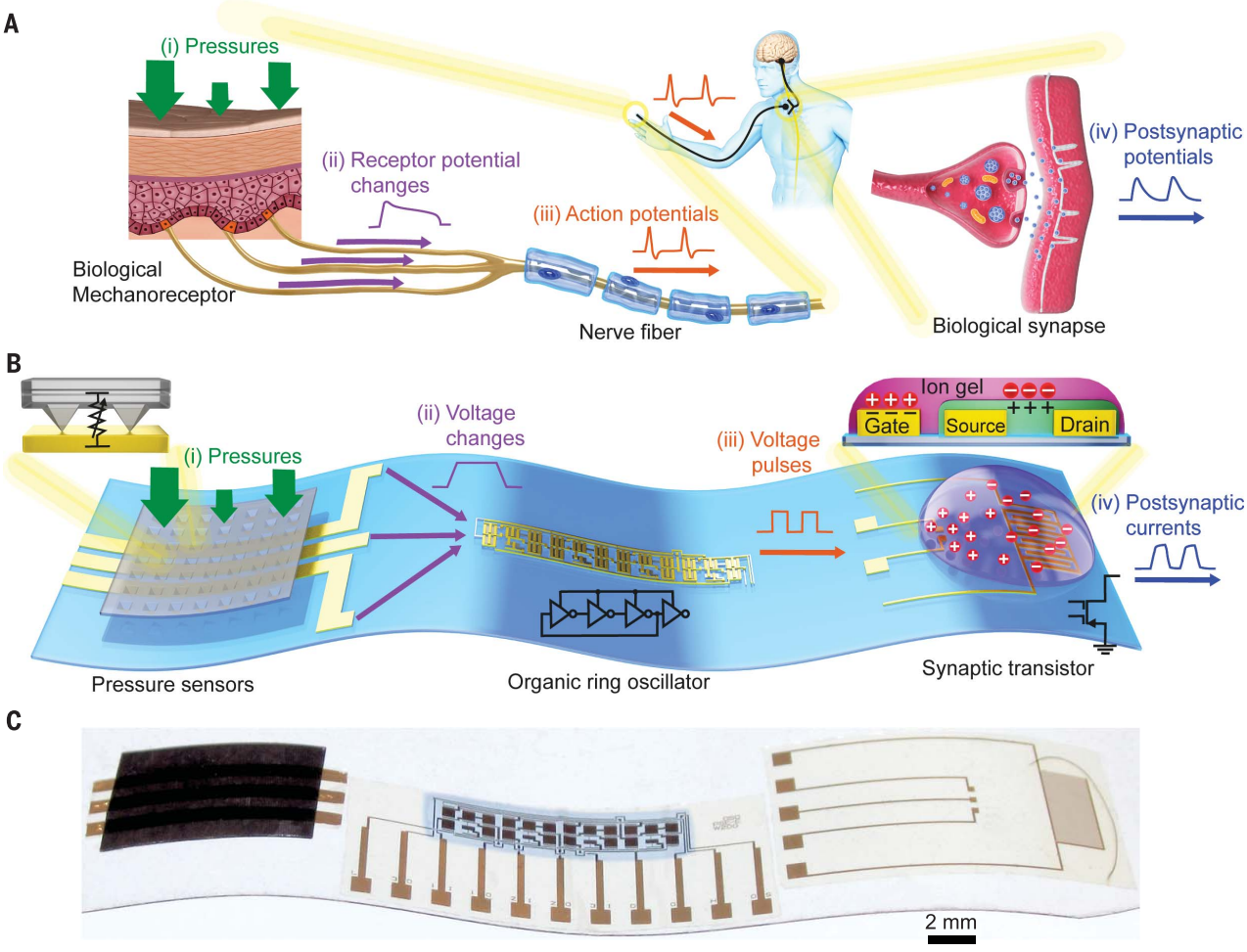

Fig. 1. An artificial afferent nerve system in comparison with a biological one. (**A**) A biological afferent nerve that is stimulated by pressure. Pressures applied onto mechanoreceptors change the receptor potential of each mechanoreceptor. The receptor potentials combine and initiate action potentials at the heminode. The nerve fiber forms synapses with interneurons in the spinal cord. Action potentials from multiple nerve fibers combine through synapses and contribute to information processing. (**B**) An artificial afferent nerve made of pressure sensors, an organic ring oscillator, and a synaptic transistor. Only one ring oscillator connected to a synaptic transistor is shown here for simplicity. However, multiple ring oscillators with clusters of pressure sensors can be connected to one synaptic transistor. The parts with the same colors in (A) and (B) correspond to each other. (**C**) A photograph of an artificial afferent nerve system.

from multiple ring oscillators. The synaptic transistor thus integrates signals more simply than the traditional synapse circuit made of several transistors and a capacitor, which needs separate circuits per input (*16*), although the decay time and the synaptic weight of each gate input in our synaptic transistor can be individually tuned only during fabrication, not during operation. Compared with uniformly applied pressures (80 kPa in fig. S16, D and F), pressures of different magnitudes (20 and 80 kPa in Fig. 3, D and F) led to different temporal and spectral patterns of postsynaptic currents. Such patterns could be used to encode information about large-scale textures measured by SA-I afferents.

One ring oscillator can combine signals from a cluster of pressure sensors, similar to a biological heminode (the beginning of the myelinated part of a nerve fiber) (*26*). When multiple pressure sensors are connected in parallel (Fig. 3G), the highest pressure will have a dominant effect on the output of the ring oscillator. This behavior mimics the branched structures and heminodes of afferent nerves that give rise to a sophisticated sense of touch in higher-order animals (*26*). A rodlike object was moved across two branches of pressure sensors in two different directions (Fig. 3G). When the object moved in the directions of the red and blue arrows, the postsynaptic current outputs had one valley corresponding to the object position between the two pressure sensors (Fig. 3H) and a monotonic increase without any local minimum (Fig. 3I), respectively. Analysis of the temporal profiles of postsynaptic currents in these two cases demonstrates the possibility of a bioinspired approach to recognize the direction and potentially the speed of object movement, which can be estimated from the duration of the valley of postsynaptic currents.

We used our artificial afferent nerves to identify braille characters pressed on an array of three pixels by two pixels (Fig. 3J and fig. S17). Six synaptic transistors accepted inputs from one oscillator, and 11 synaptic transistors each accepted inputs from two different oscillators. The peak frequencies of postsynaptic currents connected to one pixel (marked with a single number, from 1 to 6, and a blue box in fig. S17, A and B) are shown for all six pixels (Fig. 3K and fig. S18A). To quantify the difference in postsynaptic responses between different letters, we used Victor-Purpura spike train metrics (*32*) to calculate the Victor-Purpura distances (D_{VP}) between the characters (fig. S18, B and C). A larger D_{VP} means more dissimilarity between two spike trains. Compared with the smallest D_{VP} between different letters with the use of only pressure sensors and ring oscillators (i.e., without the signal integration of two pixels), the synaptic signal integration led to an increase in the smallest D_{VP} between different alphabets, which means that braille letters became more distinguishable because of the synaptic integration (Fig. 3L). Thus, this approach mimics the process of tactile information processing in a biological somatosensory system, where the signals of multiple tactile inputs from first-order neurons are integrated by synapses to partially process the information before delivery to the brain (*20*, *21*).

We connected our artificial afferent nerve to biological efferent nerves of a discoid cockroach (*Blaberus discoidalis*) (Fig. 4A) to complete a hybrid monosynaptic reflex arc (Fig. 4B), emulating a biological reflex arc (fig. S19). We used this hybrid system to demonstrate the flow of information from multiple pressure sensors through a neuromorphic circuit to deliver biomimetic postsynaptic oscillating signals into the biological efferent nerves in a detached cockroach leg (Fig. 4C), leading to the actuation of the tibial extensor muscle in the leg (Fig. 4D). The oscillating signals from our artificial afferent nerve elicit action potentials in nerves better than constant voltages (*33*). An increase in the amplitude and frequency of stimulation signals increases the number of activated muscle fibers and the forces generated by each muscle fiber, respectively (*33*, *34*). When we increased the intensity and

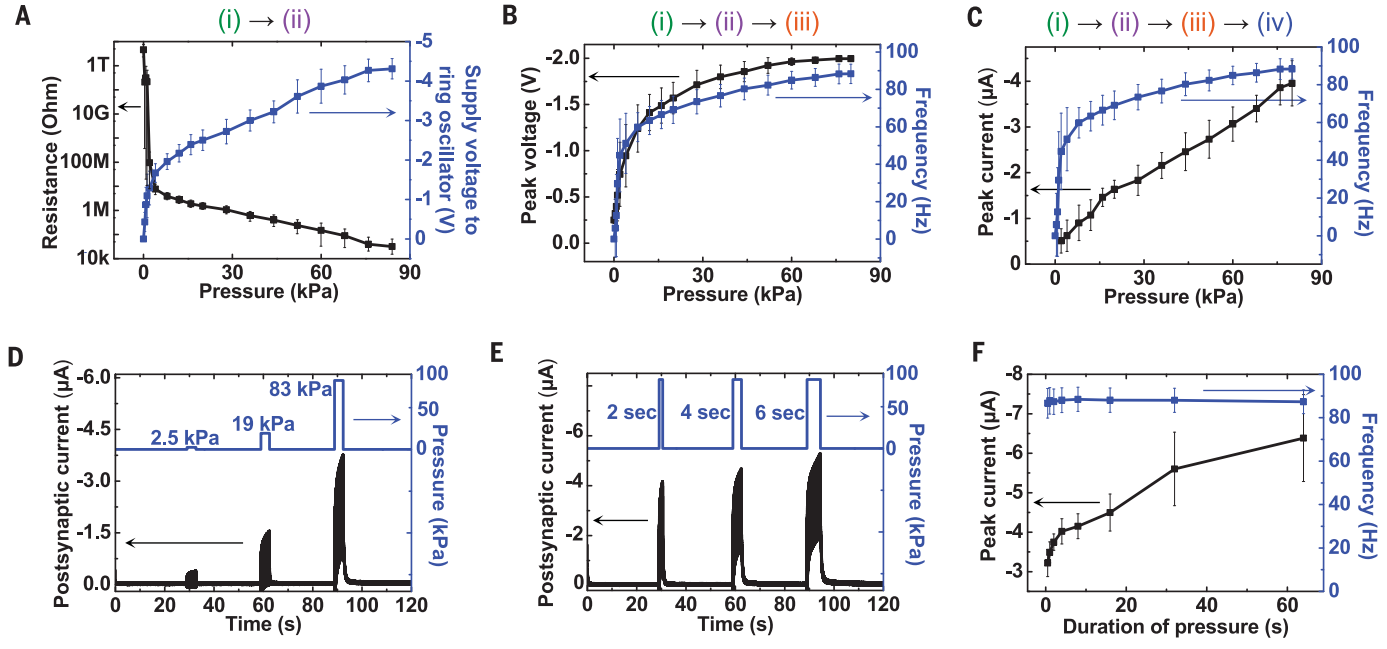

Fig. 2. Characteristics of an artificial afferent nerve system with one branch. (**A**) Resistance of a resistive pressure sensor and the corresponding change in the supply voltage of an organic ring oscillator in response to the change of pressure. The pressure sensor and the organic ring oscillator formed a voltage divider between a dc power supply voltage and the ground (fig. S2). (**B**) Peaks and oscillating frequencies of output voltages of ring oscillators as a function of pressures applied to pressure sensors. (**C**) Peak values and oscillating frequencies of postsynaptic currents of synaptic transistors depending on pressures. The gate voltage of the synaptic transistor was supplied from the ring oscillator output. (**D**) Postsynaptic current output of an artificial afferent nerve for three different pressure intensities. The duration of the stimulus application was 4 s for all three cases. (**E**) Response to three different durations of the pressure stimulus with a constant pressure intensity of 80 kPa. (**F**) The peak amplitude and frequency of the postsynaptic current depending on the duration of the stimulus application for the fixed amplitude of pressure (80 kPa). All error bars in (A) to (F) show 1 SD. (i) to (iv) correspond to the signals in Fig. 1. Arrows indicate the conversion of the signals by pressure sensors, organic ring oscillators, and synaptic transistors.

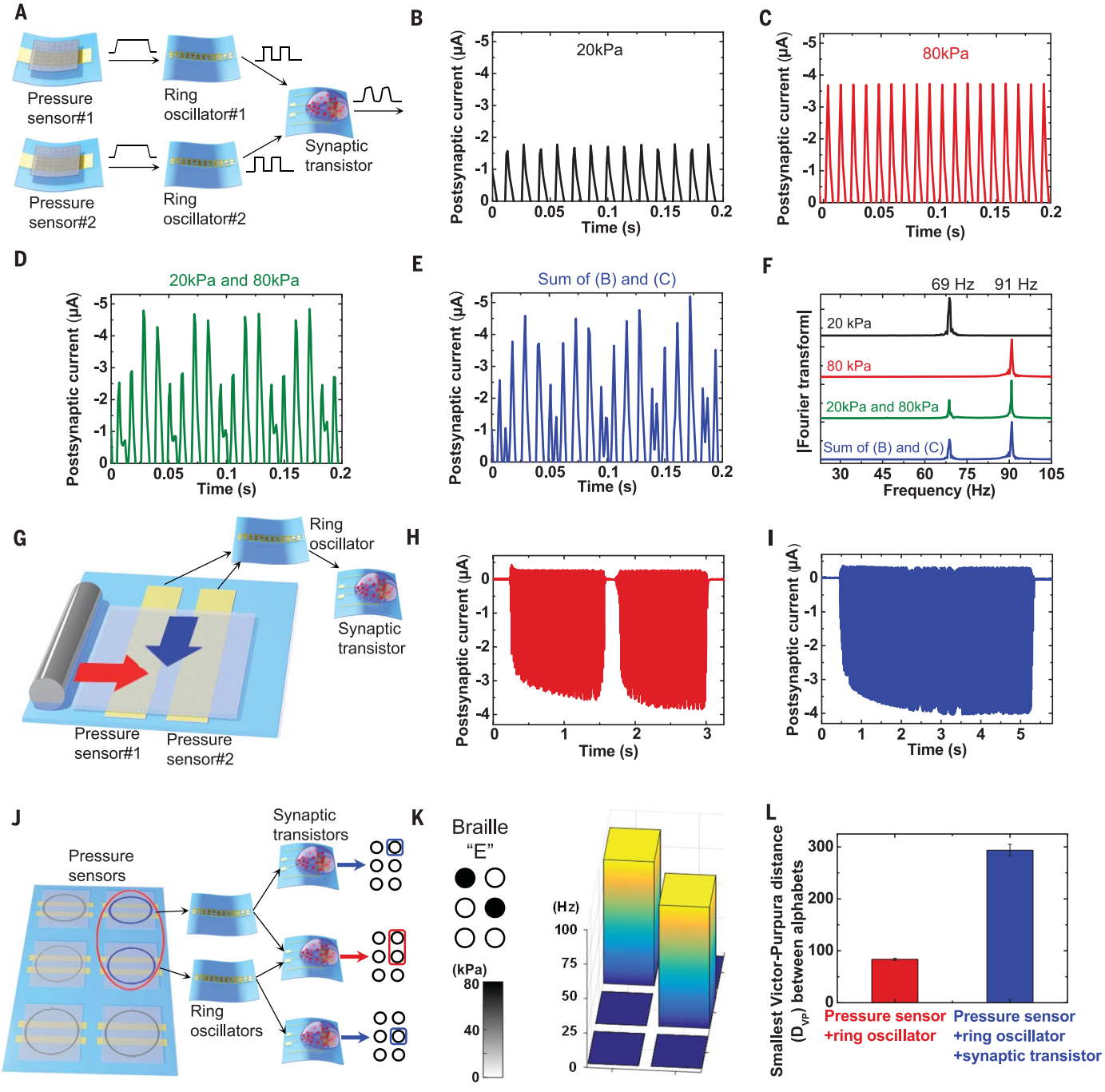

Fig. 3. Characterization of an artificial afferent nerve system with multiple branches. (**A**) Artificial afferent nerve with two branches of ring oscillators and pressure sensors measured in (B) to (F). (**B** and **C**) Postsynaptic currents when only one pressure sensor was pressed with 20 kPa (B) and 80 kPa (C), respectively. (**D**) Postsynaptic current when pressures of 20 and 80 kPa were simultaneously applied to two pressure sensors. (**E**) Plot of the sum of currents from (B) and (C). Our synaptic transistor functions as an adder so that (D) and (E) are almost the same. (**F**) The amplitude of Fourier transform of the cases in (B) to (E). Frequency components corresponding to pressures are maintained after the pressure information is combined by a synaptic transistor. Each transform was done for 4 s of data and normalized to its maximum peak. (**G**) Artificial afferent nerve with a cluster of two pressure sensors used for movement recognition in (H) and (I). The width of electrodes was 800 μm, and the distance between the two electrodes was 400 μm. (**H** and **I**) Postsynaptic currents when an object is moved in the direction of the red arrow (H) and the direction of the blue arrow (I) in (G). (**J**) Portion of the connections used for braille reading in (K) and (L). Ring oscillators and synaptic transistors were connected to an array of three pixels by two pixels of pressure sensors. A synaptic transistor was connected to either one or two ring oscillators. The complete combinations of connections used are shown in fig. S17, A and B. (**K**) (Left) Applied pressures on the pressure sensor array. (Right) Peak frequencies of postsynaptic currents from synaptic transistors connected to only one pixel (the synaptic transistors in blue boxes in fig. S17A). The results from all the braille characters are shown in fig. S18A. (**L**) The smallest Victor-Purpura distance (the metric used to quantify the difference between postsynaptic currents) between the postsynaptic currents of different alphabets. The integration of signals from two pixels by synaptic transistors improves the discrimination among the braille characters.

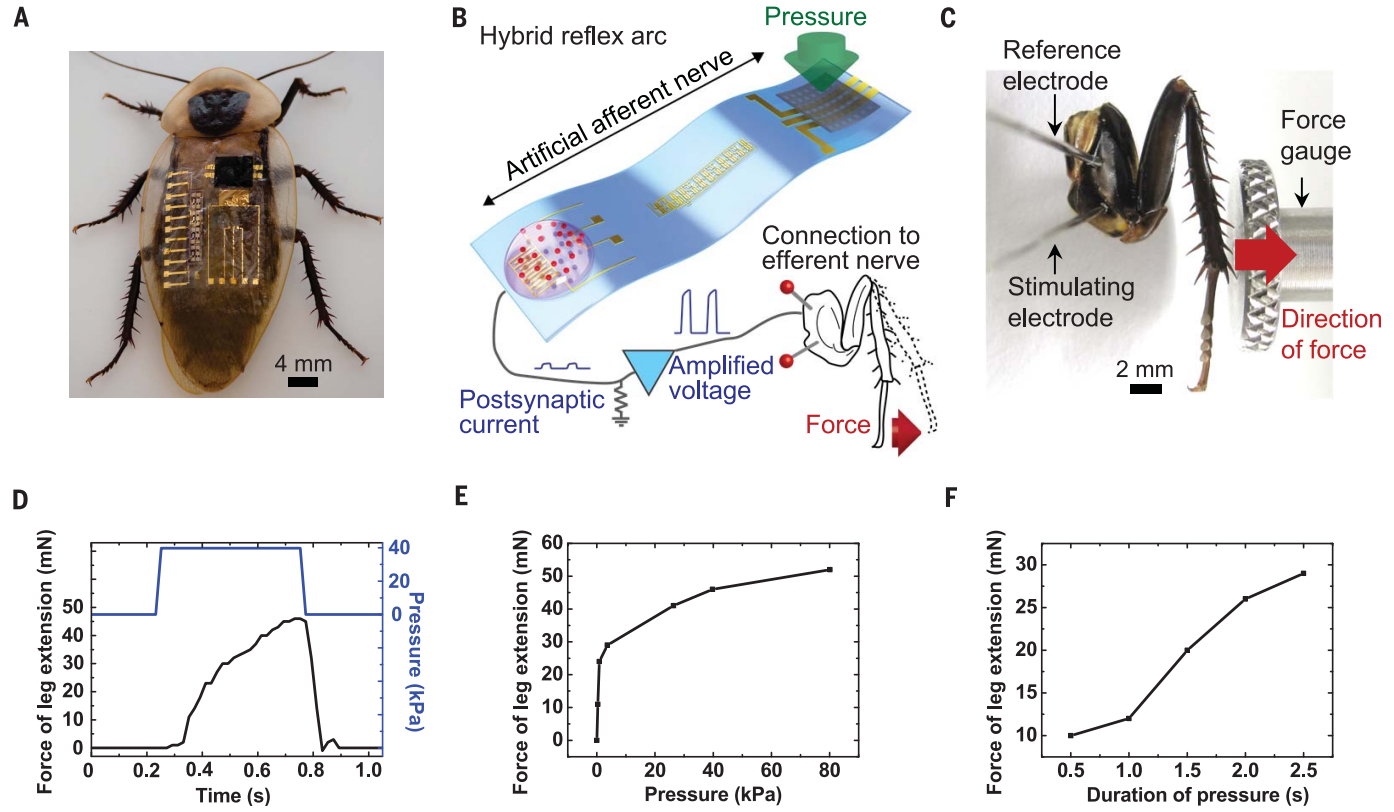

Fig. 4. Hybrid reflex arc. (**A**) Discoid cockroach with an artificial afferent nerve on its back. (**B**) Hybrid reflex arc made of an artificial afferent nerve and a biological efferent nerve. This experimental setup was used for measurements in (D) to (F). Pressure stimuli from multiple spots can be combined by an artificial afferent nerve and can be converted into postsynaptic currents. Postsynaptic currents are amplified to stimulate biological efferent nerves and muscles to initiate movement. (**C**) Photograph of reference and stimulating electrodes, a detached cockroach leg, and a force gauge used for (D) to (F). The tibial flexor muscle was dissected to remove its disturbance. (**D**) Isometric contraction force of the tibial extensor muscle in response to pressure on the artificial afferent nerve in (B). The pressure intensity and duration were 39.8 kPa and 0.5 s, respectively. (**E**) Summary of the maximum isometric contraction force of the tibial extensor muscle depending on the intensities of pressures. The duration of the stimulus application was 0.5 s for all measurements. (**F**) Effects of the duration of the pressure stimulus on the maximum isometric contraction force of the tibial extensor muscle. The amplitude of pressure was fixed at 360 Pa.

duration of the stimulus application on the artificial afferent nerve, the maximum isometric contraction force of the tibial extensor muscle increased accordingly (Fig. 4, E and F, respectively; additional data are in fig. S20). Isotonic contractions are shown in fig. S21 and movie S1.

Inspired by state-of-the-art understanding of biological afferent nerves, we fabricated an artificial afferent nerve based on organic devices that have multiple hotspots in the receptive field, generate action potentials depending on the combined pressure inputs, and integrate action potentials at a synaptic transistor. The biomimetic hierarchical structures were used to detect the shape and movement of an object in simple cases and to distinguish braille characters. Finally, our artificial afferent nerve was connected to biological efferent nerves to demonstrate a hybrid bioelectronic reflex arc and control biological muscles.

REFERENCES AND NOTES

1. S. Furber, *J. Neural Eng.* **13**, 051001 (2016).
2. S. B. Furber, F. Galluppi, S. Temple, L. A. Plana, *Proc. IEEE* **102**, 652–665 (2014).
3. J. Schemmel, D. Briiderle, A. Griibl, M. Hock, K. Meier, S. Millner, paper presented at the 2010 IEEE International Symposium on Circuits and Systems (ISCAS2010), Paris, France, 30 May to 2 June 2010.
4. N. Qiao *et al.*, *Front. Neurosci.* **9**, 141 (2015).
5. C. Mead, *Analog VLSI and Neural Systems* (Addison-Wesley Longman, 1989).
6. T. Delbrück, B. Linares-Barranco, E. Culurciello, C. Posch, paper presented at the 2010 IEEE International Symposium on Circuits and Systems (ISCAS2010), Paris, France, 30 May to 2 June 2010.
7. S.-C. Liu, A. Van Schaik, B. A. Mincti, T. Delbruck, paper presented at the 2010 IEEE International Symposium on Circuits and Systems (ISCAS2010), Paris, France, 30 May to 2 June 2010.
8. L. Osborn, R. Kaliki, A. Soares, N. Thakor, *IEEE Trans. Haptics* **9**, 196–206 (2016).
9. S. Caviglia, L. Pinna, M. Valle, C. Bartolozzi, paper presented at the 2016 IEEE International Symposium on Circuits and Systems (ISCAS2016), Montreal, QC, Canada, 22 to 25 May 2016.
10. R. D. Beer, R. D. Quinn, H. J. Chiel, R. E. Ritzmann, *Commun. ACM* **40**, 30–38 (1997).
11. D. Goldschmidt, F. Wörgötter, P. Manoonpong, *Front. Neurorobot.* **8**, 3 (2014).
12. K. A. Zaghloul, K. Boahen, *J. Neural Eng.* **3**, 257–267 (2006).
13. B. C.-K. Tee *et al.*, *Science* **350**, 313–316 (2015).
14. C. M. Oddo *et al.*, *eLife* **5**, e09148 (2016).
15. L. L. Bologna, J. Pinoteau, R. Brasselet, M. Maggiali, A. Arleo, *J. Physiol. (Paris)* **105**, 25–35 (2011).
16. C. Bartolozzi, G. Indiveri, *Neural Comput.* **19**, 2581–2603 (2007).
17. W. Xu, S.-Y. Min, H. Hwang, T.-W. Lee, *Sci. Adv.* **2**, e1501326 (2016).
18. Y. van de Burgt *et al.*, *Nat. Mater.* **16**, 414–418 (2017).
19. J. A. Pruszynski, R. S. Johansson, *Nat. Neurosci.* **17**, 1404–1409 (2014).
20. H. Jörntell *et al.*, *Neuron* **83**, 1444–1452 (2014).
21. F. Bengtsson, R. Brasselet, R. S. Johansson, A. Arleo, H. Jörntell, *PLOS ONE* **8**, e56630 (2013).
22. M. Park *et al.*, *Nat. Nanotechnol.* **7**, 803–809 (2012).
23. D. Khodagholy *et al.*, *Nat. Commun.* **4**, 1575 (2013).
24. D. T. Simon *et al.*, *Nat. Mater.* **8**, 742–746 (2009).
25. S. Lee *et al.*, *Nat. Nanotechnol.* **11**, 472–478 (2016).
26. D. R. Lesniak *et al.*, *eLife* **3**, e01488 (2014).
27. C. Qian *et al.*, *ACS Appl. Mater. Interfaces* **8**, 26169–26175 (2016).
28. J. Lee *et al.*, *J. Phys. Chem. C* **113**, 8972–8981 (2009).
29. Y. Takeuchi *et al.*, *J. Neurosci.* **32**, 6917–6930 (2012).
30. D. Querlioz, O. Bichler, C. Gamrat, paper presented at the 2011 International Joint Conference on Neural Networks (IJCNN), San Jose, CA, 31 July to 5 August 2011.
31. L. Herlogsson *et al.*, *Adv. Mater.* **19**, 97–101 (2007).
32. J. D. Victor, K. P. Purpura, *J. Neurophysiol.* **76**, 1310–1326 (1996).
33. J. Malmivuo, R. Plonsey, *Bioelectromagnetism: Principles and Applications of Bioelectric and Biomagnetic Fields* (Oxford Univ. Press, 1995).
34. J. W. S. Pringle, *J. Exp. Biol.* **16**, 220–231 (1939).

ACKNOWLEDGMENTS

We thank Y. Park, J. H. Jang, and J. Kim for theoretical background; J. Lopez for suggestions; and M. He for providing the conjugated polymer **P1**. **Funding:** This work was supported by a National Research Foundation of Korea (NRF) grant (NRF-2016R1A3B1908431) funded by the Korean government (Ministry of Science and ICT); the Center for Advanced Soft-Electronics, funded by the Ministry of Science and ICT as a Global Frontier Project (CASE-2013M3A6A5073175); and the Creative-Pioneering Researchers Program through Seoul National University (SNU). Research carried out at Stanford University is funded by Samsung Electronics. Y.Li. acknowledges NSS funding support from the Agency for Science, Technology and Research (A*STAR), Singapore. A.M.F. acknowledges postdoctoral fellowship support from the Natural Sciences and Engineering Research Council (NSERC) of Canada. R.P. acknowledges support from a Beatriu de Pinós fellowship (AGAUR 2014 BP-A 00094) from the Marie Curie Cofund. Part of this work was performed in the nano@Stanford labs (part of the National Nanotechnology Coordinated Infrastructure) and at the Stanford Nano Shared Facilities (SNSF), both of which are supported by the NSF under award ECCS-1542152. **Author contributions**: Y.K., A.C., W.X., Z.B., and T.-W.L. conceived of and designed the overall experiments. Y.K., A.C., and W.X. carried out experiments and collected related data. Y.Li. contributed to cockroach stimulation experiments. J.Y.O. helped fabricate pressure sensors. D.S. and A.M.F. aided in transfers of thin-film devices. J.K., Y.Le., and J.L. contributed to analyses of synaptic transistors. C.Z., S.N., and R.P. helped with electrical measurements. Z.B. and T.-W.L. initiated the study. Y.K., A.C., W.X., Z.B., and T.-W.L. analyzed all the data and cowrote the paper. All authors discussed the results and commented on the manuscript. **Competing interests:** Patents related to this work are planned. **Data and materials availability:** All data are available in the article or the supplementary materials.

SUPPLEMENTARY MATERIALS

www.sciencemag.org/content/360/6392/998/suppl/DC1
Materials and Methods
Supplementary Text
Figs. S1 to S21
Tables S1 and S2
References (*35*–*37*)
Movie S1

5 June 2017; accepted 18 April 2018
10.1126/science.aao0098

INDUCED SEISMICITY

The November 2017 M_w 5.5 Pohang earthquake: A possible case of induced seismicity in South Korea

F. Grigoli,[1]* S. Cesca,[2] A. P. Rinaldi,[1] A. Manconi,[3] J. A. López-Comino,[2] J. F. Clinton,[1] R. Westaway,[4] C. Cauzzi,[1] T. Dahm,[2,5] S. Wiemer[1]

The moment magnitude (M_w) 5.5 earthquake that struck South Korea in November 2017 was one of the largest and most damaging events in that country over the past century. Its proximity to an enhanced geothermal system site, where high-pressure hydraulic injection had been performed during the previous 2 years, raises the possibility that this earthquake was anthropogenic. We have combined seismological and geodetic analyses to characterize the mainshock and its largest aftershocks, constrain the geometry of this seismic sequence, and shed light on its causal factors. According to our analysis, it seems plausible that the occurrence of this earthquake was influenced by the aforementioned industrial activities. Finally, we found that the earthquake transferred static stress to larger nearby faults, potentially increasing the seismic hazard in the area.

Deep geothermal resources can provide a valuable contribution to the production of renewable energy. Through enhanced geothermal systems (EGSs), geothermal energy production is no longer confined to volcanic or hydrothermal regions. Unlike the conventional geothermal systems, EGS technologies exploit geothermal resources through hydraulic stimulation—which involves the injection of high-pressure cold water to increase the permeability of the target formation at a few kilometers of depth—by creating new fractures or enhancing existing ones. Although the potential for deep geothermal energy is indisputably large, in urban areas the problem of induced seismicity associated with such operations is often not adequately addressed.

On 15 November 2017, a moment magnitude (M_w) 5.5 earthquake struck South Korea, injuring ~70 people and causing extensive damage in and around the city of Pohang. This earthquake was preceded by the M_w 5.5 Gyeongju event of 12 September 2016, which occurred ~30 km farther south on a major right-lateral fault, the Yangsan fault, which continues northward through the Pohang area (*1*, *2*) (Fig. 1, A and B). These earthquakes are the largest recorded in South Korea since instrumental monitoring of seismicity began in 1903 (*2*). The proximity of the 2017 Pohang earthquake to an EGS site (Fig. 1B), where hydraulic stimulation operations had recently taken place, has led to a public debate in South Korea regarding the potential anthropogenic origin of this event. At this EGS site between early 2016 and September 2017, many thousands of cubic meters of water were injected under pressure into wells reaching ~4 km of depth (*3*). Although an investigation by the South Korean government is currently ongoing, here we present observations that suggest a causal connection between the EGS activity and the most recent large earthquake.

The Korean Peninsula is generally considered stable with low to moderate intraplate seismic activity, but the historical seismicity of this region indicates large long-term variations in earthquake rate and energy release (*4*, *5*). The relatively low rate of activity since 1904 was preceded by much higher activity between the 15th to 18th centuries, with a peak of 1000 reported historical earthquakes between 1500 and 1600 CE (*5*). The largest events reached magnitude ~7 (*4*, *5*). The historic earthquakes were likely associated with the major fault systems of the area, such as the Yangsan fault, and highlight that these structures are active (*4*, *5*). In principle, given the historically varying rates of seismicity and prevalence of faults in this region, the increase in seismic activity represented by the 2016 Gyeongju and 2017 Pohang earthquakes is not completely inconsistent with the historically varying rates of seismicity. This line of reasoning preserves the possibility that the occurrence of earthquakes close to the EGS site is a coincidence.

We applied full-waveform seismological methods to regional and teleseismic data (Fig. 1A) (*6*), as we do not have access to open data from a local seismic network (with the exception of two accelerometers deployed in the epicentral area). We analyzed 15 days of continuous waveform data spanning from 15 to 30 November. We detected and relocated 46 events, most with magnitude M >2. The trend of these 46 epicenters indicates a west-southwest (WSW)–to–east-northeast (ENE) strike of the fault that ruptured in the mainshock (Fig. 2A). We determined 3- to 7-km hypocentral depths for most of these events (Fig. 2, A and B). These depths are shallower than the depths of typical seismic events in the area (~12 to 15 km) (Fig. 2C) (*2*, *4*). For the Pohang earthquake, we determined the depth of both the mainshock and the largest aftershock to be 4.0 to 4.5 km (Fig. 2B). Depth is a critical parameter for discrimination between natural and induced seismicity (*7*), so we obtained independent estimates (by using array analysis at teleseismic distances and two accelerometers located in the epicentral region) that confirm the shallow depth (*6*). Our moment tensor inversion indicated that the mainshock had a reverse-to-oblique double-couple (DC) mechanism, with a WSW-to-ENE striking nodal plane, subparallel to the aftershock zone and dipping north-northwest at ~66°. The full moment tensor had a large non-DC term. Conversely, the M_w 4.3 aftershock indicated reverse faulting on a WSW-to-ENE striking fault (Figs. 1B and 2A). On the basis of many previous analyses [e.g., (*8*, *9*)], we inferred that the non-DC component (Fig. 2A) is caused by a complex rupture process that includes the (near-)simultaneous activation of differently oriented faults. By mapping the azimuthal distribution of the apparent source durations, maximum energy peaks, and centroid time delays, we detected a common pattern, which we interpret as the failure of two subevents at close origin times and separated by a short distance along the azimuth of rupture directivity. We estimated a distance of 3.5 to 4.0 km between the two subevents, indicative of a dynamic triggering process (*6*). We thus hypothesize that the earthquake involved the failure of two different faults with slightly different orientations, which might, in principle, explain the non-DC term of the moment tensor (*9*), as well as the complexity of *P*-wave signals for the mainshock (*6*). A potential alternative source model, characterized by a complex rupture along a single fault, with heterogeneous slip directions, cannot explain the non-DC component of the moment tensor and results in a substantially worse fit for the pattern of the relative hypocentral centroid location (*6*).

We also used satellite radar interferometry [differential interferometric synthetic aperture radar (DInSAR)] to map and measure the coseismic surface deformation associated with the mainshock and to independently model its source geometry (*6*, *10*). Our InSAR analysis indicated a maximum surface deformation of ~5 cm, with a fault location and area consistent with the seismological analysis (Fig. 3A). Despite the moderate event size and complex rupture resolved by seismological data, we can fit the observed deformation with a simple elastic dislocation model (*11*) based on a single fault plane with shear displacement and opening (Fig. 3B). The fault dimensions (length ~5 km and width ~1.6 km) and the apparent slip, derived from this inversion of geodetic data, are compatible with a magnitude of M_w 5.5 (*12*) and consistent with our seismological analysis. However, DInSAR data cannot resolve the small-scale complexities associated with the

[1]Swiss Seismological Service, ETH-Zurich, Zurich, Switzerland. [2]Section 2.1: Physics of Earthquakes and Volcanoes, German Research Centre for Geosciences (GFZ), Potsdam, Germany. [3]Engineering Geology Group, Department of Earth Sciences, ETH-Zurich, Zurich, Switzerland. [4]School of Engineering, University of Glasgow, Glasgow, UK. [5]Institute of Earth and Environmental Sciences, University of Potsdam, Potsdam, Germany.
*Corresponding author. Email: francesco.grigoli@sed.ethz.ch

progressive rupture of adjacent fault patches. Nonetheless, our geodetic analysis confirmed that the earthquake nucleation and main slip on the fault occurred at very shallow depth (4 to 5 km), on a reverse fault striking WSW-to-ENE and with a ~75° dip toward the NW (Fig. 2B). The average residuals are ~0.05 cm and within the measurement accuracy (Fig. 3C). The DInSAR results are in good agreement with the aftershock locations and the focal mechanisms of the largest events, placing strong independent constraints on the location and extent of a previously unmapped fault system.

Natural and induced earthquakes are not distinguishable by their waveform characteristics. It is generally necessary to build a convincing chain of evidence to differentiate induced earthquakes from naturally occurring events (*7*, *13*–*16*). For instance, the hypothesis that the Pohang earthquake sequence is anthropogenic is supported by the spatial correlation between the mainshock and its aftershocks and the injections. Our seismological and geodetic analyses indicate that the activated fault passes directly beneath the EGS site (Fig. 2B), within ~1 km of the termination of the injection wells (Fig. 2B). The combined evidence from the hypocentral locations, the DInSAR data inversion, the observed interval between *P*- and *S*-wave arrival times at the borehole and surface stations, and the observed strong motion and damage patterns is consistent with this interpretation (*6*). Another piece of evidence supporting that this seismicity is induced is our relocation of the local magnitude 3.1 earthquake on 15 April 2017, which occurred during hydraulic stimulation operations at the EGS site: This event was very close to the 15 November mainshock (Fig. 2A). No stimulation activities occurred in the 2 months preceding this mainshock, but induced earthquakes can be delayed by days, weeks, or even months after the start or end of injection (*14*). Our techniques (using regional and teleseismic data from the public domain, thus restricted to earthquakes of magnitude ≥~2) demonstrate the extent to which a candidate case study of induced seismicity can be investigated using public data, without proprietary data from site operators.

We also studied the relation between the seismic moment (M_o ~ 1.7 × 10^{17} N·m) of the mainshock (*6*) and the volume (V) of fluid injected. Assuming that unreported injections are similar to initial stimulation (*3*), we estimated an upper bound to the total volume of ~10,000 m^3. The limitation of water supply and storage capacity of the EGS justifies our assumption. We approximated an upper bound to M_o by using the product of net injected volume and the shear modulus (*17*). For V = 10,000 m^3, this relation implies an upper bound of M_o ~ 2 × 10^{14} N·m, or M_w ~ 3.5. On this basis, an induced earthquake of M_w 5.5 would require three orders of magnitude more volume (V ~ 10^7 m^3). However, several counterexamples to this scaling relation exist [(*18*, *19*) and references therein], and the

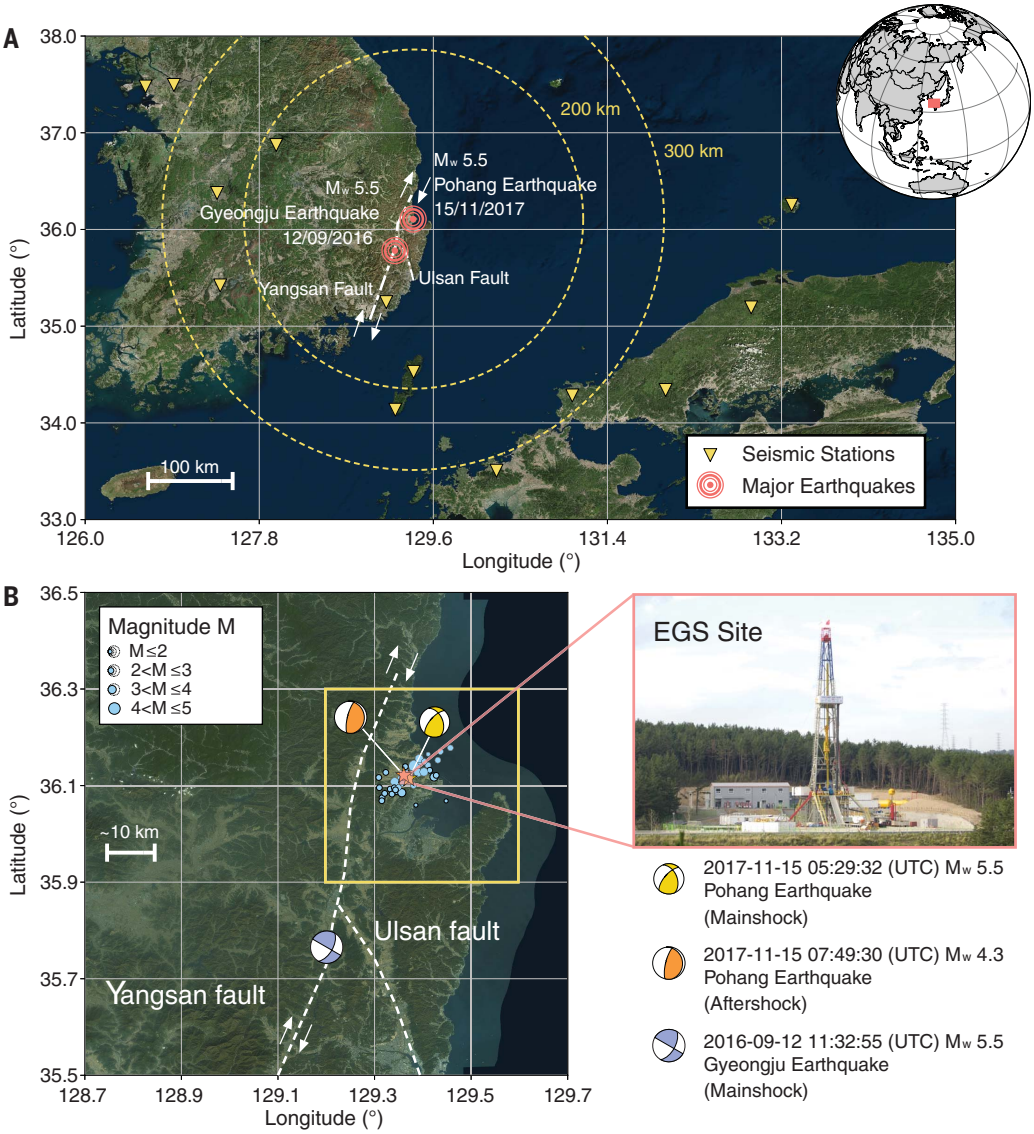

Fig. 1. The 2016 and 2017 M_w 5.5 earthquakes in South Korea. (**A**) Regional map showing locations of the Gyeongju and Pohang earthquakes, the Yangsan fault, and the available open seismic stations. (**B**) Map of the study area showing the main faults of the area, the distribution of seismicity with respect to the EGS site, and the mechanisms of the largest events. A more detailed map of the area of study (outlined by the yellow square) is shown in Fig. 2A. UTC, universal time coordinated.

EGS SITE PHOTO: COURTESY OF THE DESTRESS PROJECT TEAM

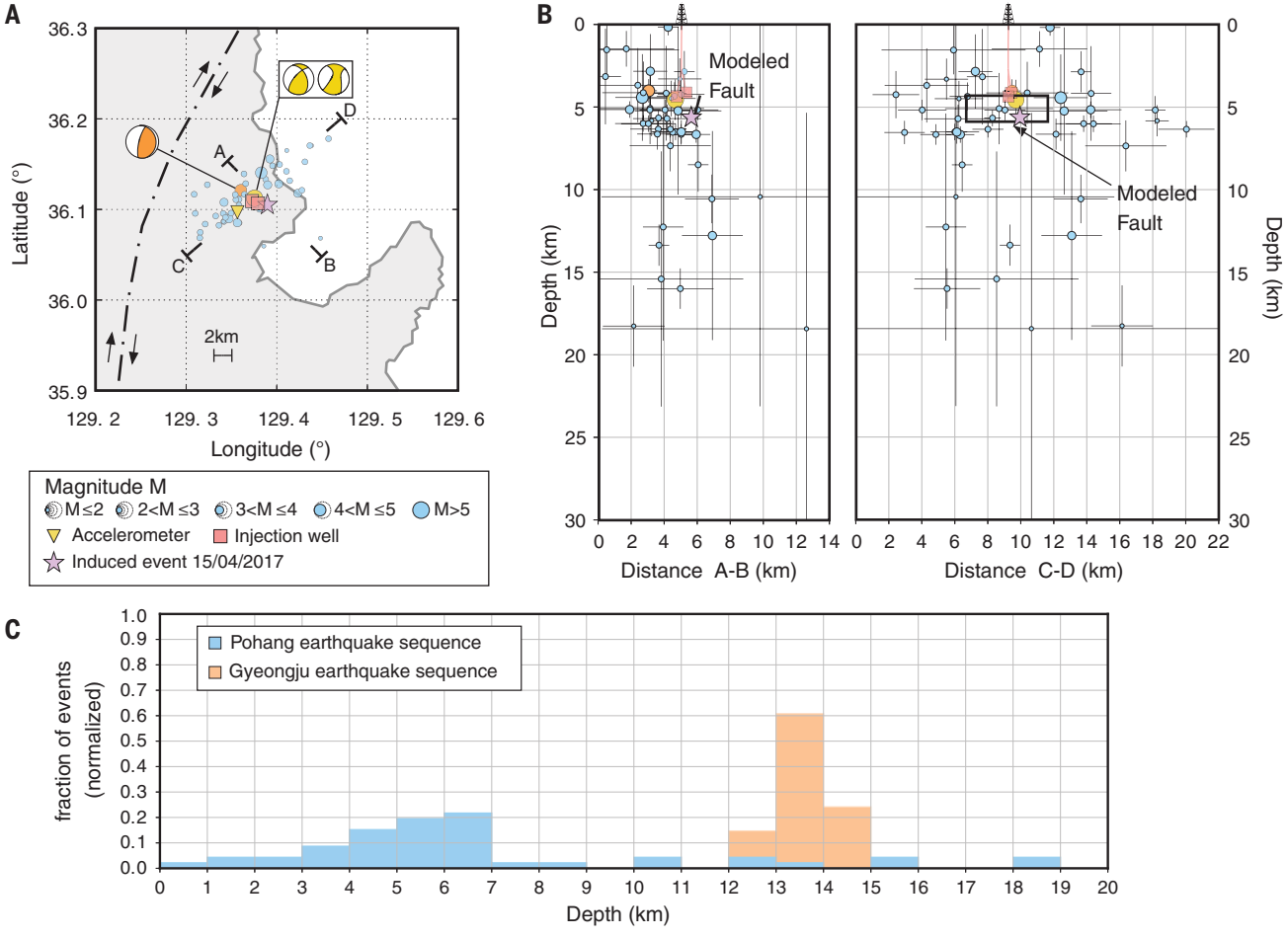

Fig. 2. Spatial distribution of the 2017 Pohang seismic sequence. (**A**) Detailed map showing the epicentral distribution of seismicity and (**B**) two cross sections displaying the depth distribution of seismicity (including location uncertainties) and the fault as inferred by geodetic analysis. The EGS site is located at 36°06′23.34″N, 129°22′46.08″E and includes the two injection wells that reach depths of 4127 and 4348 m (*3*). (**C**) Focal depth distribution of earthquakes in the study region and comparison with the 2016 Gyeongju seismic sequence.

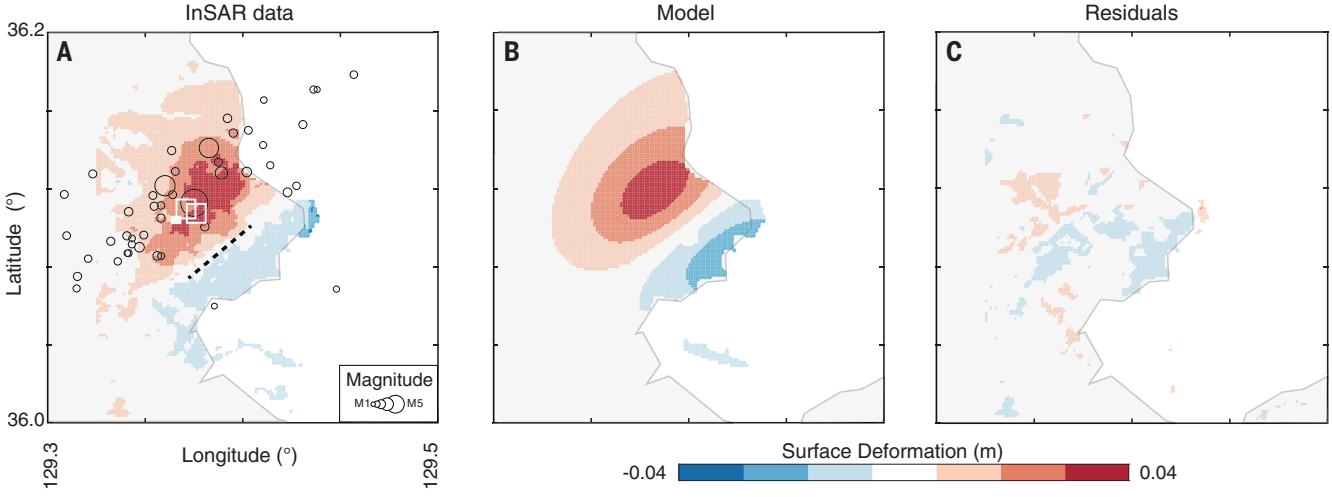

Fig. 3. DInSAR data and model. (**A**) Surface deformation (satellite line-of-sight displacements) obtained with InSAR. Seismicity and the extrapolated fault trace are indicated by black circles and a dashed line, respectively. (**B**) Modeled surface deformation using a rectangular fault plane with the following parameters: latitude = 36.100° ± 0.005°, longitude = 129.383° ± 0.003° (center of the rectangular fault), depth = 4.3 ± 0.3 km (upper edge of the fault), strike (from north) = 225° ± 12°, dip (from horizon) = 75° ± 11°, length = 5.0 ± 0.7 km, width = 1.6 ± 0.4 km, slip = 1 ± 0.22 m, and rake = 123° ± 35°. (**C**) Difference between InSAR data and model. The standard deviation is <0.5 cm, which is below the accuracy threshold of the measurements.

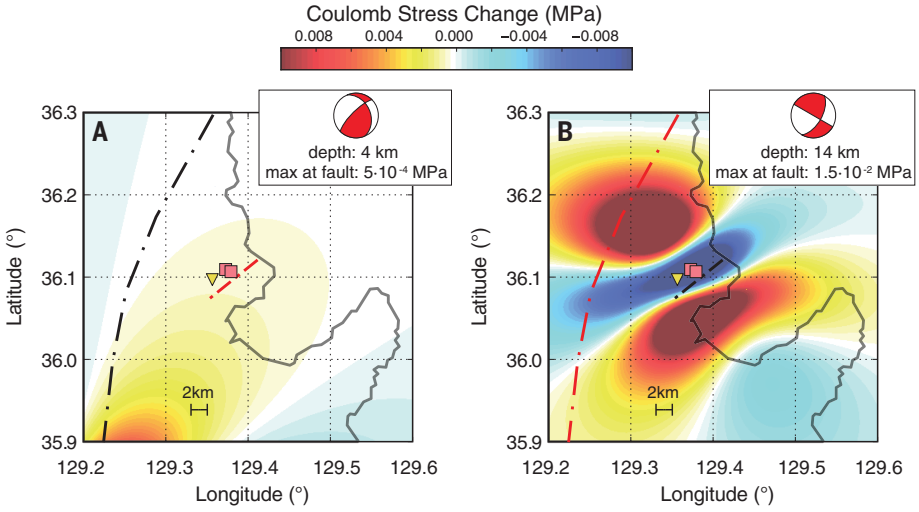

Fig. 4. Coulomb stress modeling. (**A**) Static coulomb failure stress showing the effect of the 2016 Gyeongju earthquake at 4 km of depth on the fault activated by the 2017 Pohang event and (**B**) the effect of this latter event on the Yangsan fault at 14 km of depth. Receiver faults are denoted by red dot-dashed lines. The triangle represents the local accelerometer, and the squares denote the injection wells.

Pohang earthquake provides much clearer evidence that the use of this relation should be subject to caution.

Although none of our observations exclude the possibility that the Pohang earthquake was induced by industrial activity at the EGS site, our seismological and geodetic analyses (Figs. 2 and 3) rule out a reactivation of the Yangsan fault. Our hypocenter is <1 km southeast of the injection point, at the same depth as the injection. The coseismic deformation and source model derived from the DInSAR analysis confirm this location (Figs. 2 and 3). Aftershock locations and focal mechanisms consistently indicate activation of a previously unmapped fault system. This case thus highlights the importance of a preliminary seismotectonic assessment of the area surrounding any future EGS project site, aimed at identifying potentially active faults. Along with real-time analysis and control systems (*20*), this evaluation may mitigate the risk associated with induced seismicity.

We also investigated whether the September 2016 M_w 5.5 Gyeongju earthquake might have contributed to triggering the 2017 Pohang event. Coulomb stress modeling (*6*) indicates that the Gyeongju earthquake caused a slight (~0.0005 MPa) increase in static stress on the fault that ruptured in the subsequent Pohang earthquake. This value is small, but it is feasible to propose the occurrence of a clock advance on the subsequent fault. In turn, the M_w 5.5 Pohang earthquake transferred static stress of 0.015 MPa onto the northern part of the Yangsan fault (Fig. 4B), potentially increasing the seismic hazard in this area.

In accordance with our findings, it is plausible that the occurrence of the 2017 Pohang earthquake was influenced by the nearby stimulation activities. If so, the Pohang event was the largest and most damaging earthquake ever to have been associated with an EGS, making it a potential "game changer" for the geothermal industry worldwide.

REFERENCES AND NOTES

1. Y. Kim, X. He, S. Ni, H. Lim, S. C. Park, *Bull. Seismol. Soc. Am.* **107**, 2525–2531 (2017).
2. K. H. Kim *et al.*, *Bull. Seismol. Soc. Am.* **108**, 517–523 (2017).
3. S. Park *et al.*, *Procedia Eng.* **191**, 829–837 (2017).
4. M. Han, K. H. Kim, M. Son, S. Y. Kang, *Tectonophysics* **694**, 414–423 (2017).
5. K. Lee, W. S. Yang, *Bull. Seismol. Soc. Am.* **96**, 846–855 (2006).
6. See supplementary materials.
7. S. D. Davis, C. Frohlich, *Seismol. Res. Lett.* **64**, 207–224 (1993).
8. C. Frohlich, K. D. Apperson, *Tectonics* **11**, 279–296 (1992).
9. G. P. Hayes *et al.*, *Nat. Geosci.* **3**, 800–805 (2010).
10. D. Massonnet *et al.*, *Nature* **364**, 138–142 (1993).
11. Y. Okada, *Bull. Seismol. Soc. Am.* **75**, 1135–1154 (1985).
12. D. L. Wells, K. J. Coppersmith, *Bull. Seismol. Soc. Am.* **84**, 974–1002 (1994).
13. W. L. Ellsworth, *Science* **341**, 1225942 (2013).
14. K. M. Keranen, M. Weingarten, G. A. Abers, B. A. Bekins, S. Ge, *Science* **345**, 448–451 (2014).
15. R. Westaway, *Pure Appl. Geophys.* **159**, 7–62 (2002).
16. F. Grigoli *et al.*, *Rev. Geophys.* **55**, 310–340 (2017).
17. A. McGarr, *J. Geophys. Res. Solid Earth* **119**, 1008–1019 (2014).
18. G. M. Atkinson *et al.*, *Seismol. Res. Lett.* **87**, 631–647 (2016).
19. R. Westaway, in *Environmental and Health Issues in Unconventional Oil and Gas Development* (Elsevier, 2016), pp. 175–210.
20. A. Mignan, M. Broccardo, S. Wiemer, D. Giardini, *Sci. Rep.* **7**, 13607 (2017).

ACKNOWLEDGMENTS

We thank F. Bethmann, T. Kraft, and D. Giardini for information, comments, and suggestions that helped to improve the paper. **Funding:** This work was funded by the EU projects DESTRESS (EU H2020 research and innovation program, grant agreement 691728) and SHEER (EU H2020 research and innovation program, grant agreement 640896). A.P.R. is currently funded by a Swiss National Science Foundation, Ambizione Energy grant (PZENP2-160555). **Author contributions:** F.G. performed the analysis of the seismic sequence. S.C. performed moment tensor inversion. A.P.R. performed coulomb stress failure analysis. A.M. processed and inverted geodetic data. J.A.L.-C. performed the rupture directivity analysis. J.F.C. and C.C. analyzed the local strong motion data. F.G., R.W., T.D., and S.W. interpreted the results. All the authors contributed to writing and reviewing the paper. **Competing interests:** The authors declare no competing interests. **Data and materials availability:** The waveform data used in this study are publicly available and can be downloaded from the NIED (www.bosai.go.jp; for the Japanese network) and IRIS (www.iris.edu; for the Korean network) websites. The data from the local accelerometer are available in the supplementary materials. Sentinel-1 radar data can be downloaded from the ESA website (https://earth.esa.int).

SUPPLEMENTARY MATERIALS

www.sciencemag.org/content/360/6392/1003/suppl/DC1
Supplementary Text
Figs. S1 to S12
Waveform and Local Accelerometer Data
References (*21*–*39*)

14 February 2018; accepted 13 April 2018
Published online 26 April 2018
10.1126/science.aat2010

Corrected 31 May 2018. See full text.

INDUCED SEISMICITY

Assessing whether the 2017 M_w 5.4 Pohang earthquake in South Korea was an induced event

Kwang-Hee Kim,[1]* Jin-Han Ree,[2]* YoungHee Kim,[3] Sungshil Kim,[2] Su Young Kang,[1] Wooseok Seo[1]

The moment magnitude (M_w) 5.4 Pohang earthquake, the most damaging event in South Korea since instrumental seismic observation began in 1905, occurred beneath the Pohang geothermal power plant in 2017. Geological and geophysical data suggest that the Pohang earthquake was induced by fluid from an enhanced geothermal system (EGS) site, which was injected directly into a near-critically stressed subsurface fault zone. The magnitude of the mainshock makes it the largest known induced earthquake at an EGS site.

The injection of fluid into reservoir rocks, which facilitates oil and gas recovery, enhances geothermal systems, and aids in the disposal of wastewater and CO_2 gas, also has a small chance of inducing earthquakes [e.g., (*1*–*4*)]. Empirical and theoretical relationships exist to connect the maximum magnitude of an induced earthquake and the injected fluid volume (*2*, *5*). The magnitude of an induced earthquake may be tectonically controlled—for example, owing to the presence of a fault suitably oriented for slip under a given stress field that is also located adjacent to one or more injection or production wells (*6*, *7*). The earthquake nucleation itself might be controlled by the injection (*6*). Previously observed magnitudes of induced seismicity at enhanced geothermal system (EGS) sites have been relatively small (*8*); the largest local magnitude (M_L) reported was 3.4, in Basel, Switzerland (*9*), although a much larger, possibly induced earthquake has been reported in the Cerro Prieto geothermal field, Mexico, a tectonically active area (*10*).

A moment magnitude (M_w) 5.4 earthquake occurred at the Pohang EGS site in southeastern Korea on 15 November 2017. The earthquake was the most damaging and the second-largest in magnitude in South Korea since the first seismograph was installed in 1905. The earthquake injured 90 people, and the estimated property damage was US$52 million (*11*). We present evidence that the Pohang earthquake was the largest induced event to have occurred at any EGS site worldwide. Moreover, this event indicates that injected fluid volumes much smaller than predicted by theory can trigger a relatively large earthquake, at least under the right set of conditions.

[1]Department of Geological Science, Pusan National University, Busan 46241, Republic of Korea. [2]Department of Earth and Environmental Sciences, Korea University, Seoul 02841, Republic of Korea. [3]School of Earth and Environmental Sciences, Seoul National University, Seoul 08826, Republic of Korea.
*Corresponding author. Email: kwanghee@pusan.ac.kr (K.-H.K.); reejh@korea.ac.kr (J.-H.R.)

The Korean Peninsula lies within the Eurasian Plate (Fig. 1), although it was composed of continental magmatic arcs at a plate boundary until the early Tertiary period (~30 million years ago) (*12*). North-northeast (NNE)–striking strike-slip faults and NNE- to NE-striking normal faults developed predominantly in southeastern Korea and adjacent offshore areas when the East Sea (or Japan Sea) opened as a back-arc basin in the early to middle Tertiary (~30 to 15 million years ago), with the coetaneous formation of smaller-scale basins, including the Pohang (*12*–*14*). Some of these faults have been reactivated as strike-slip and thrust faults in the current compressional regime (*13*–*15*). The axes of compression determined by focal mechanism solutions indicate shallow plunges to the ENE throughout the southern Korean Peninsula (*15*, *16*).

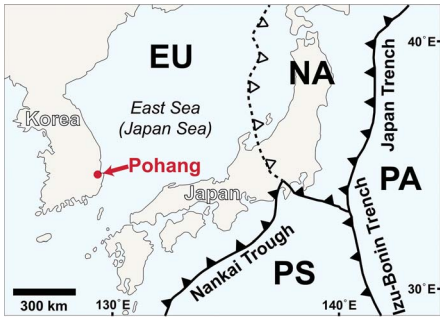

Fig. 1. Tectonic map of northeast Asia. Saw-toothed lines with solid teeth denote subduction zones. The broken line with open teeth represents an incipient subduction zone (*30*). EU, Eurasian Plate; NA, North American Plate; PS, Philippine Sea Plate; PA, Pacific Plate.

The Pohang basin consists of nonmarine to deep marine sedimentary strata dating to the Miocene (~20 million years ago), with a basement composed of Cretaceous to Eocene sedimentary and volcanic rocks and late Paleozoic to Eocene granitoids (*17*–*19*) (Fig. 2A). The geology of the Pohang EGS site comprises (from top to bottom) Quaternary alluvia (<10 m thick), Miocene semi-consolidated mudstone (200 to 400 m thick), Cretaceous to Eocene sedimentary and igneous rocks (~1000 m thick), and Permian granodiorite with gabbroic dykes (*19*–*21*) (Fig. 2B).

One vertical injection well (4346 m deep; PX2) and another deviated production well (4362 m deep; PX1) were drilled into Permian granodiorite with gabbroic dykes for the EGS, with an expected electricity production of 1.2 MW (*21*). The PX1 well, only 6 m from PX2 at the surface, is 600 m northwest of PX2 at the bottom (Fig. 3). The drilling began in September 2012 and was completed in November 2015. No earthquakes with M_L > 2.0 were recorded within 10 km of the Pohang EGS site between 1978 and 2015 (*22*); a total of six earthquakes with M_L 1.2 to 1.9 were detected in the area between 2006 and 2015. To further examine the seismicity around the EGS site, we improved the earthquake catalog by applying a matched filter to continuous waveforms (*23*) recorded by a permanent seismic station (PHA2; Fig. 2A), located about 10 km north of the EGS site, during the period between 1 January 2012 and 14 November 2017. Once detected, waveforms were visually inspected for time differences between *P*- and *S*-wave arrivals consistent with a source at Pohang (~1.54 s). The matched-filter analysis found no noticeable earthquakes at the EGS site before the completion of drilling. We detected a total of 148 earthquakes by the match filtering that all occurred after the completion of the drilling, including four earthquakes with M_L > 2.0.

Hydraulic stimulation began on 29 January 2016 and comprised four phases of injection with a total volume of 12,800 m^3 at injection rates of 1.00 to 46.83 liter s^{-1} (Fig. 4). Fluid was injected into both PX1 (phases 2 and 4) and PX2 (phases 1, 3, and 4). To investigate the relationship between seismicity and fluid injection, we used data on regional earthquakes detected by the matched filter together with earthquake data provided by the Ministry of Trade, Industry, and Energy (MTIE), Republic of Korea (*23*). We did not detect noticeable microearthquakes before the drilling. The timing of the earthquakes coincides with that of fluid injections. The first reported hydraulic stimulation (phase 1) was carried out between 29 January 2016 and 20 February 2016, followed by three additional phases of fluid injection (Fig. 4). Each injection phase was accompanied by intense seismic activity that started only a few days after injection. Microseismic activity decreased rapidly after the termination of fluid injection. The magnitudes of induced earthquakes tend to increase with the net volume of injected fluid. After a M_L 3.1 earthquake on 15 April 2017, which was the largest felt event near the EGS site before the M_L 5.4 Pohang earthquake, we deployed eight temporary seismic stations around the EGS site. Each standalone station was equipped with a three-component velocity–type short-period sensor. These sensors record continuous seismic

Corrected 31 May 2018. See full text.

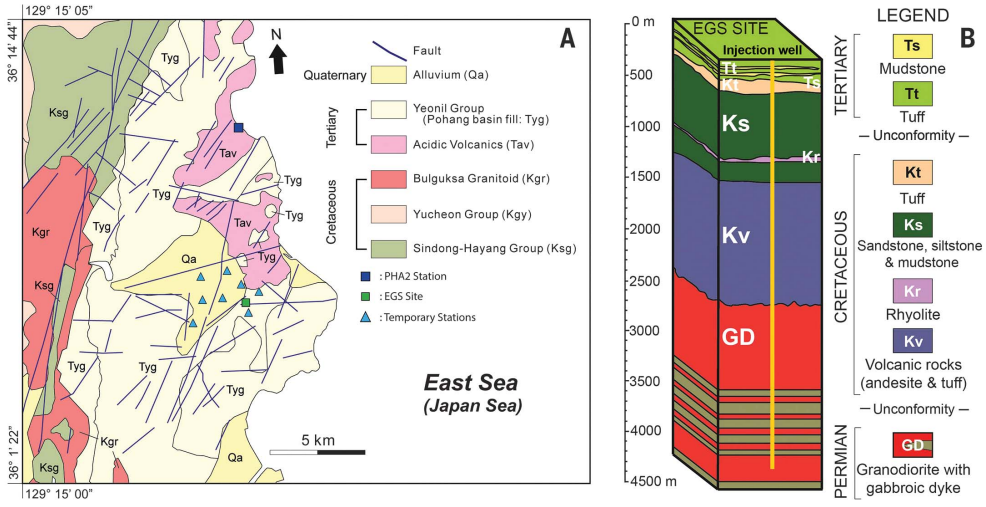

Fig. 2. Geologic map and column of the Pohang basin. (**A**) Map showing rocks and faults of the Pohang basin and adjacent area. One permanent seismic station operated by the Korea Meteorological Administration (PHA2) and our eight temporary seismic stations are represented by a dark blue square and green triangles, respectively. The green square denotes the site of the Pohang enhanced geothermal system (EGS). The geologic map was compiled from (*18*, *19*). (**B**) Geologic column of the Pohang EGS site with injection well. The geologic column was compiled from (*19*, *20*).

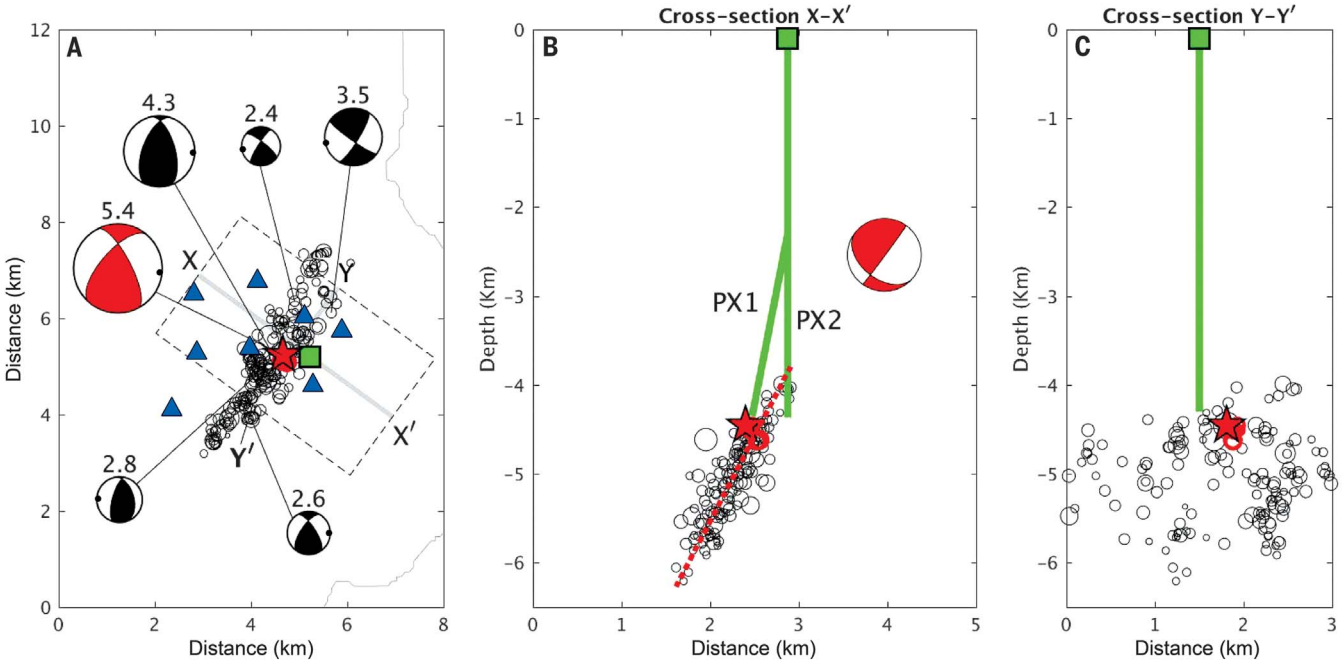

Fig. 3. Spatial distribution of epicenters and hypocenters of the 2017 Pohang earthquake sequence. (**A**) Epicenters of six foreshocks (red circles), mainshock (red star), and 210 aftershocks (black open circles) recorded in the first 3 hours after the mainshock. The location of the Pohang EGS is indicated by a green square. Blue triangles represent our eight temporary seismic stations. The red beach ball represents the source mechanism of the mainshock. Black beach balls show the focal mechanism solutions of representative aftershocks. Numbers above beach balls are local magnitudes. The black beach balls of the M_L 2.4 and 3.5 aftershocks, recorded 1 and 3 days after the mainshock, respectively, show strike-slip faulting. X–X′ and Y–Y′ denote the locations of the cross sections shown in (B) and (C), respectively. (**B** and **C**) Hypocentral distributions of earthquakes, projected onto vertical planes along the lines X–X′ (B) and Y–Y′ (C) shown in (A). The red beach ball in (B) represents the focal mechanism of the mainshock projected onto a vertical cross section. PX1 and PX2 denote production and injection wells, respectively. Other symbols are the same as for (A).

data at a sampling frequency of 200 Hz. Installation was completed on 10 November 2017. All of them are still in active operation.

The M_L 5.4 mainshock occurred at the Pohang EGS site on 15 November 2017 and was preceded and followed by foreshocks and aftershocks, respectively, all of which were well recorded by our local seismic array at distances of 0.6 to 2.5 km from the mainshock epicenter (Figs. 2A and 3). We precisely relocated this earthquake sequence with the hypoDD software package (*23*, *24*) (fig. S2). We plotted the spatial distribution of six foreshocks ($M_L \leq 2.6$), the mainshock, and 210 aftershocks that occurred within 3 hours of the mainshock (Fig. 3). The first two foreshocks occurred about 9 hours before the mainshock; the remaining four preceded it by 6 to 7 min. Most hypocentral depths fell in the range of 4 to 6 km, and the mainshock depth was about 4.5 km. Of note, the hypocenters of the foreshocks and mainshock were located immediately adjacent to the bottom of PX1. The hypocentral depths of the Pohang earthquake sequence are shallower than those of most earthquakes in the

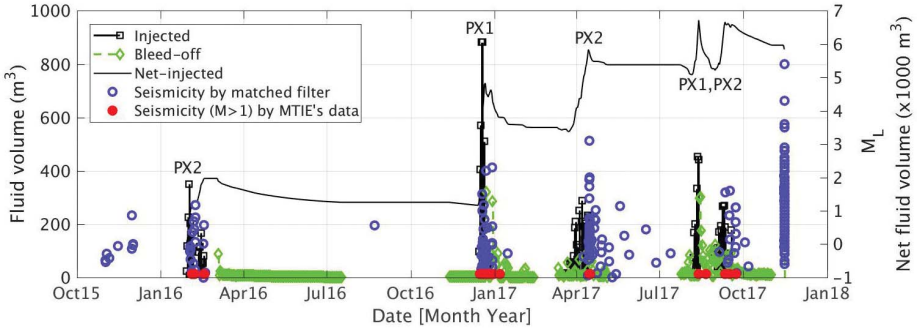

Fig. 4. History of fluid injection volume. Volume of injected and bleed-off fluid (left axis) and net fluid volume (right axis) as a function of time. Red circles denote times of seismic events from data provided by the MTIE (63 events; magnitude information is only available for $M > 1$). Dark blue circles denote seismic events determined by matched-filter analysis (148 events). The right axis also gives the local magnitudes of seismic events.

Korean Peninsula, which tend to occur at depths of 10 to 20 km (*25*). For comparison, the largest instrumentally recorded earthquake in South Korea, the 2016 Gyeongju event (M_L 5.8), had a hypocentral depth of about 14 km (*26*). The spatiotemporal distribution of hypocenters indicates that the rupture plane consisted of two segments, a main southwestern segment and a subsidiary northeastern segment (Fig. 3 and fig. S3). The aftershocks tended to occur earlier on the main segment than on the subsidiary segment (fig. S4). This observation, together with the locations of the foreshocks and mainshock on the main segment, suggests that the main segment ruptured earlier than the subsidiary one. By statistical plane-fitting using MATLAB software (Mathworks), we determined the best-fit orientations of the main and subsidiary rupture planes to be N36°E (strike)/65°NW (dip) and N19°E/60°NW, respectively (fig. S3). These orientations are consistent with the nodal planes determined by focal mechanism solutions (Fig. 3). The main segment shows thrust faulting with a minor strike-slip component, whereas the subsidiary segment is dominated by strike-slip faulting with a minor dip-slip component. The compression axis trends E–W or ENE–WSW with a shallow plunge, similar to that of other earthquakes in South Korea (*15*, *16*). The locations of the foreshocks and mainshock, at the bottom of the injection well, suggest that fluid was injected directly into the fault zone.

The temporal relationship between seismicity and fluid injection, the spatial relationship between the hypocenters and the EGS site, and the lack of seismicity in the area before the EGS was established all suggest that the Pohang earthquake was induced. Furthermore, the immediate response of seismicity to fluid injection and the locations of the foreshocks and mainshock at the bottom of the injection well suggest that fluid was injected directly into a fault zone. The fault plane inferred from the spatial distribution of hypocenters and focal mechanism solutions strikes NE and dips to the NW (fig. S4A), similar to Quaternary thrust faults in southeastern Korea. In fact, a magnetotelluric survey of the EGS site detected a low-resistivity feature that could be the fault zone, striking NE and dipping to the NW (*23*, *27*) (fig. S5). Reverse slip along a subsurface fault is consistent with the current stress field. All of these lines of evidence indicate that the Pohang earthquake was "almost certainly induced" in Frohlich *et al.*'s system of assessment (*28*). If we use McGarr's (*2*) equation for the relationship between the maximum magnitude and the total volume of injected fluid, about 4.7×10^6 m^3 of injected fluid would be required to induce an M_w 5.4 earthquake, which is more than 810 times the fluid volume injected at the Pohang EGS site. The permeability structure of fault zones is highly heterogeneous, and patches or layers of clay-rich gouge within the fault core act as barriers to fluid flow (*29*). The pore pressure thus can locally reach a critical value for earthquake nucleation after a relatively small volume of fluid is injected, depending on fault zone structure. Our results imply that if fluid is injected directly into a near-critically stressed fault, it can induce a larger earthquake than current theory predicts. Detailed investigation of the geological, geochemical, and geophysical properties of the Pohang EGS site will improve our understanding of earthquake-inducing processes.

REFERENCES AND NOTES

1. W. L. Ellsworth, *Science* **341**, 1225942 (2013).
2. A. McGarr, *J. Geophys. Res. Solid Earth* **119**, 1008–1019 (2014).
3. A. Zang *et al.*, *Geothermics* **52**, 6–21 (2014).
4. M. D. Zoback, S. M. Gorelick, *Proc. Natl. Acad. Sci. U.S.A.* **109**, 10164–10168 (2012).
5. A. McGarr, *J. Geophys. Res. Solid Earth* **81**, 1487–1494 (1976).
6. N. J. van der Elst, M. T. Page, D. A. Weiser, T. H. W. Goebel, S. M. Hosseini, *J. Geophys. Res. Solid Earth* **121**, 4575–4590 (2016).
7. E. L. Majer *et al.*, *Geothermics* **36**, 185–222 (2007).
8. G. Grünthal, *Geothermics* **52**, 22–35 (2014).
9. M. O. Häring, U. Schanz, F. Ladner, B. C. Dyer, *Geothermics* **37**, 469–495 (2008).
10. D. T. Trugman, A. A. Borsa, D. T. Sandwell, *Geophys. Res. Lett.* **41**, 8767–8774 (2014).
11. National Disaster and Safety Status Control Center, Ministry of the Interior and Safety, Republic of Korea, press release (6 December 2017).
12. S. K. Chough, S.-T. Kwon, J.-H. Ree, D. K. Choi, *Earth Sci. Rev.* **52**, 175–235 (2000).
13. J.-H. Ree *et al.*, *Isl. Arc* **12**, 1–12 (2003).
14. S. H. Yoon, Y. K. Sohn, S. K. Chough, *Mar. Geol.* **352**, 70–88 (2014).
15. H. Choi, T.-K. Hong, X. He, C.-E. Baag, *Tectonophysics* **572–573**, 123–133 (2012).
16. J.-C. Park, W. Kim, T. W. Chung, C.-E. Baag, J.-H. Ree, *Geophys. J. Int.* **169**, 1103–1114 (2007).
17. Y. K. Sohn, C. W. Rhee, H. Shon, *Sediment. Geol.* **143**, 265–285 (2001).
18. Y. K. Sohn, M. Son, *Sedimentology* **51**, 1387–1408 (2004).
19. T. J. Lee, Y. Song, D.-W. Park, J. Jeon, W. S. Yoon, "Three dimensional geological model of Pohang EGS pilot site, Korea," in *Proceedings of the World Geothermal Congress*, Melbourne, Australia, 19 to 25 April 2015; https://pangea.stanford.edu/ERE/db/WGC/papers/WGC/2015/31025.pdf.
20. K.-S. Yoon, J.-S. Jeon, H.-K. Hong, H.-G. Kim, A. Hakan, J.-H. Park, W.-S. Yoon, "Deep drilling experience for Pohang Enhanced Geothermal Project in Korea," in *Proceedings of the World Geothermal Congress*, Melbourne, Australia, 19 to 25 April 2015; https://pangea.stanford.edu/ERE/db/WGC/papers/WGC/2015/06034.pdf.
21. M. Kim, B. Yoon, C. Lee, K. G. Park, W.-S. Yoon, Y. Song, T. J. Lee, "Microseismic monitoring during hydraulic stimulation in Pohang (Korea) for EGS pilot project" [abstract S23B-0804], American Geophysical Union Fall Meeting, New Orleans, LA, USA, 11 to 15 December 2017.
22. The Korea Meteorological Administration catalog is available at http://necis.kma.go.kr/.
23. Supplementary materials.
24. F. Waldhauser, W. L. Ellsworth, *Bull. Seismol. Soc. Am.* **90**, 1353–1368 (2000).
25. Korea Meteorological Administration earthquake data service; www.weather.go.kr/weather/earthquake_volcano/domesticlist.jsp.
26. K.-H. Kim *et al.*, *Geosci. J.* **20**, 753–757 (2016).
27. T. J. Lee, Y. Song, T. Uchida, *Mulli-tamsa* **8**, 145–155 (2005).
28. C. Frohlich *et al.*, *Seismol. Res. Lett.* **87**, 1022–1038 (2016).
29. J. S. Caine, J. P. Evans, C. B. Forster, *Geology* **24**, 1025–1028 (1996).
30. T. Seno, S. Stein, A. E. Gripp, *J. Geophys. Res. Solid Earth* **98**, 17941–17948 (1993).

ACKNOWLEDGMENTS

We thank Representative S. S. Kim of the National Assembly and the Ministry of Trade, Industry and Energy, Republic of Korea, for providing fluid injection data. We are grateful to the Korea Meteorological Administration for providing continuous waveforms used in the study. We also thank two anonymous reviewers for their constructive comments. **Funding:** This work was supported by the Nuclear Safety Research Program through the Korea Foundation of Nuclear Safety (KoFONS) using financial resources granted by the Nuclear Safety and Security Commission (NSSC) of the Republic of Korea (no. 1705010). **Author contributions:** K.-H.K.: conceptualization, formal analysis, funding acquisition, methodology, original draft, and review and editing. J.-H.R.: conceptualization, formal analysis, funding acquisition, methodology, original draft, and review and editing. Y.K.: investigation, methodology, validation, and review and editing. S.K.: data curation, formal analysis, investigation, and software. S.Y.K.: data curation, formal analysis, investigation, and software. W.S.: data curation, formal analysis, investigation, and software. **Competing interests:** The authors declare no conflicts of interest. **Data and materials availability:** Our earthquake catalog, including the earthquake source parameters (locations and times) and waveforms used in this paper, is available at https://zenodo.org/record/1218738#.WtPQROTEaRE. Earthquake waveform data recorded at PHA2 can be acquired from the National Earthquake Comprehensive Information System, Korea Meteorological Administration (http://necis.kma.go.kr/; last accessed April 2018). Continuous data may be obtained from the website on request.

SUPPLEMENTARY MATERIALS

www.sciencemag.org/content/360/6392/1007/suppl/DC1
Materials and Methods
Figs. S1 to S5
References (*31–38*)

18 March 2018; accepted 16 April 2018
Published online 26 April 2018
10.1126/science.aat6081

ORGANIC CHEMISTRY

A radical approach to the copper oxidative addition problem: Trifluoromethylation of bromoarenes

Chip Le,* Tiffany Q. Chen,* Tao Liang,* Patricia Zhang, David W. C. MacMillan†

Transition metal–catalyzed arene functionalization has been widely used for molecular synthesis over the past century. In this arena, copper catalysis has long been considered a privileged platform due to the propensity of high-valent copper to undergo reductive elimination with a wide variety of coupling fragments. However, the sluggish nature of oxidative addition has limited copper's capacity to broadly facilitate haloarene coupling protocols. Here, we demonstrate that this copper oxidative addition problem can be overcome with an aryl radical–capture mechanism, wherein the aryl radical is generated through a silyl radical halogen abstraction. This strategy was applied to a general trifluoromethylation of aryl bromides through dual copper-photoredox catalysis. Mechanistic studies support the formation of an open-shell aryl species.

The development of fragment coupling transformations by transition metal catalysis has substantially expanded access to valuable, complex organic molecules (*1*). Major efforts in this field have been devoted toward the use of aryl halides, stable and highly accessible building blocks, as coupling partners for the construction of functionalized arenes (*2*). The success of these transformations generally relies on the transition metal catalyst to activate haloarenes through an oxidative addition step and, thereafter, forge the desired bond by a reductive elimination step. This paradigm is exemplified in modern palladium and nickel catalysis, wherein catalyst design over four decades has rendered these elementary steps generically efficient, thereby enabling the development of a vast array of coupling manifolds that convert (hetero)aryl C–X bonds to C_{sp^2}-carbon, -nitrogen, -sulfur, and -oxygen bonds (*3*, *4*). In contrast, copper catalysis has been less successful than Pd or Ni with respect to diverse applications in cross-coupling chemistry, despite its potential for economical and operational benefits. Indeed, the most robust copper cross-coupling reactions are limited to transmetalling reagents such as organoboronic acids, specifically to bypass the challenge of oxidative addition (*5*).

The limited capacity of copper to participate in haloarene functionalizations has been attributed to its relatively low rate of oxidative addition in comparison to nickel and palladium. Formation of the key Cu(III)-arene intermediate has been calculated to possess a high kinetic barrier and is typically the rate-determining step in such catalytic cycles (*6*–*8*). Although elegant studies in ligand design have allowed for improvements in the rates of oxidative addition for certain substrate classes, functionalization of aryl halides by copper catalysis remains largely restricted to aryl iodides and activated aryl bromides (*9*–*11*). The need to overcome this oxidative addition problem is further underscored by the knowledge that the subsequent reductive elimination step from high-valent Cu(III) complexes is extremely facile for a wide range of coupling partners (*12*). In many cases, the reductive elimination of highly electronegative groups such as C_{sp^2}-CF_3, C_{sp^2}-F, and C_{sp^2}-N bonds is more favorable and more facile with Cu than Pd and Ni (Fig. 1) (*5*, *13*, *14*). As such, the invention of a mechanistic paradigm that bypasses the Cu-haloarene oxidative addition problem should enable a range of catalytic cross-coupling reactions of scope and utility that has not been broadly realized using other forms of metal catalysis (including Pd, Ni, or Cu). Here, we describe a silyl radical/halogen abstraction/copper capture mechanism that effectively functions as a surrogate for this elementary oxidative addition step and, in doing so, allows copper-mediated bromoarene functionalization in a general format and under mild conditions (visible light and room temperature). Moreover, this catalytic strategy has been exploited to deliver a general approach to the trifluoromethylation of heteroaryl and aryl bromides through the combination of copper and photoredox catalysis.

Trifluoromethylarenes are valuable structural motifs in the area of drug discovery due to the enhancement of desired physicochemical properties upon the introduction of the trifluoromethyl group (*15*, *16*). Among synthetic strategies, transition metal–catalyzed conversion of aryl halides to the corresponding trifluoromethylarenes is considered one of the most attractive approaches (*9*, *17*). Despite extensive effort, nickel catalysis of this transformation has not been achieved, and only a single report of palladium-catalyzed trifluoromethylation of aryl chlorides has been disclosed (*18*). Such diminished catalytic reactivity in comparison to other well-known coupling reactions is ascribed to the C_{sp^2}–CF_3 reductive elimination step, a well-documented challenge for both palladium and nickel catalysts (*17*, *19*, *20*). In contrast, copper complexes have been shown to generally undergo facile C_{sp^2}–CF_3 reductive elimination (*21*, *22*). This realization has propelled

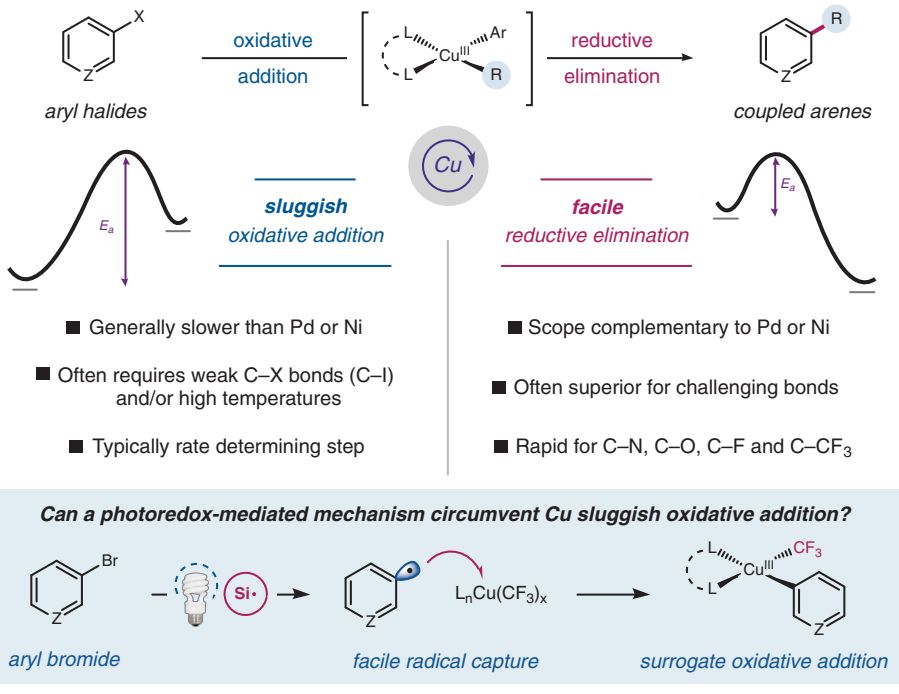

Fig. 1. Trifluoromethylation with dual copper/photoredox catalysis. Aryl radical capture by copper catalysts can bypass oxidative addition. Ar, (hetero)aryl.

Merck Center for Catalysis at Princeton University, Princeton, NJ 08544, USA.
*These authors contributed equally to this work.
†Corresponding author. Email: dmacmill@princeton.edu (D.W.C.M.)

extensive research efforts to develop copper-catalyzed trifluoromethylation protocols with haloarenes. Although recent examples of copper-mediated (*23*–*25*) and copper-catalyzed (*26*–*28*) methodologies have provided promising results for the construction of aryl–CF_3 motifs, the limited capacity of Cu(I) to participate in oxidative addition has restricted the application of these elegant systems to mostly aryl iodides or activated aryl bromides, often employing elevated temperatures. As such, a mechanistic pathway that can bypass the copper oxidative addition problem, while benefiting from the facility of Cu(III) to engage in difficult reductive elimination, might enable a mild and broadly general strategy toward the trifluoromethylation of aryl bromides.

We recently developed a metallaphotoredox-catalyzed (*29*) cross-electrophile coupling protocol in which alkyl radicals were generated by a silyl radical–mediated halogen abstraction (*30*). This manifold was shown to provide facile access to a wide range of alkyl radicals from the corresponding alkyl bromides, a feature that has been found to be remarkably general. Literature precedents indicate that this facile silane-mediated halogen abstraction mechanism should also function broadly with aryl bromides ($k \approx 5 \times 10^6$ $M^{-1}s^{-1}$ to 1.1×10^8 $M^{-1}s^{-1}$ for bromobenzene with a range of silyl radicals) to generate the corresponding aryl radicals under mild conditions (*31*, *32*). Given that aryl radicals are known to be captured by Cu(II) species at a rate approaching diffusion (*33*, *34*), we questioned whether this light-driven halogen abstraction mechanism might be exploited to forge Cu(III)-arene intermediates from a diverse range of aryl halides at room temperature (Fig. 1), effectively overcoming the copper oxidative addition problem. The successful execution of this mechanistic concept would solve a long-standing challenge in copper catalysis, thereafter providing a general platform to catalytically access trifluoromethylarenes.

Our proposed mechanism for the light-enabled trifluoromethylation protocol is outlined in Fig. 2A. Upon exposure to visible light, photocatalyst $Ir(dFFppy)_2$ (4,4´-dCF_3bpy)PF_6 [dFFppy = 2-(2,4-difluorophenyl)-5-fluoropyridine; 4,4´-dCF_3bpy = 4,4´-di(trifluoromethyl)-2,2´-bipyridyl)] (**1**) should produce excited triplet state species **2**. This highly oxidizing Ir complex [$E_{1/2}^{red}$ ($^*Ir^{III}/Ir^{II}$) = +1.55 V versus saturated calomel electrode (SCE) in CH_3CN] can undergo single-electron transfer (SET) with tris-(trimethylsilyl) silanol (**4**) [supersilanol, E_p ($\mathbf{4}^{+\bullet}/\mathbf{4}$) = +1.54 V versus SCE in CH_3CN] to give Ir(II) complex **3** (*35*). We hypothesize that supersilanol **4**, upon oxidation and deprotonation, would then undergo rapid silyl migration (Fig. 2B) to yield species **5** as the catalytically relevant silyl radical (*36*). Subsequent bromine atom abstraction from aryl bromide **6** would then yield the corresponding aryl radical **7**. Concurrently, Ir(II) complex **3** [$E_{1/2}^{red}$ (Ir^{III}/Ir^{II}) = −0.83 V versus SCE in CH_3CN] could facilitate the formation of the CF_3 radical (**9**) through a SET event with electrophilic CF_3 reagent **8** [E_p ($\mathbf{8}/\mathbf{8}^{\bullet-}$) = −0.52 V versus SCE in CH_3CN]. At this time, we believe the Cu(II)–CF_3 adduct (**11**) should be generated through interaction between the CF_3 radical (**9**) and the active Cu(I) complex (**10**), formed in situ by SET reduction of a Cu(II) catalyst precursor by the photocatalyst. Aryl radical **7** should quickly undergo radical trapping by Cu(II) complex **11** to yield the key aryl–Cu(III)–CF_3 adduct **12** (*37*, *38*). Reductive elimination from this high-valent Cu(III) intermediate would yield the desired product **13** and simultaneously regenerate Cu(I) catalyst **10** (*39*).

A survey of various combinations of different electrophilic CF_3 reagents, copper sources, and solvents revealed that blue light-emitting diode (LED) irradiation of a mixture of 4-bromobenzonitrile, supersilanol (**4**), dMesSCF$_3$ (**8**), $CuBr_2$•2LiBr [20 mole % (mol %)], and Ir(III) photocatalyst **1** (0.25 mol %) in acetone at room temperature afforded the desired trifluoromethylarene in 89% yield (Fig. 2C). The use of supersilanol in place of hydrosilanes was found to be crucial, because it minimizes unproductive protodehalogenation of the bromoarene, which presumably proceeds through hydrogen atom abstraction

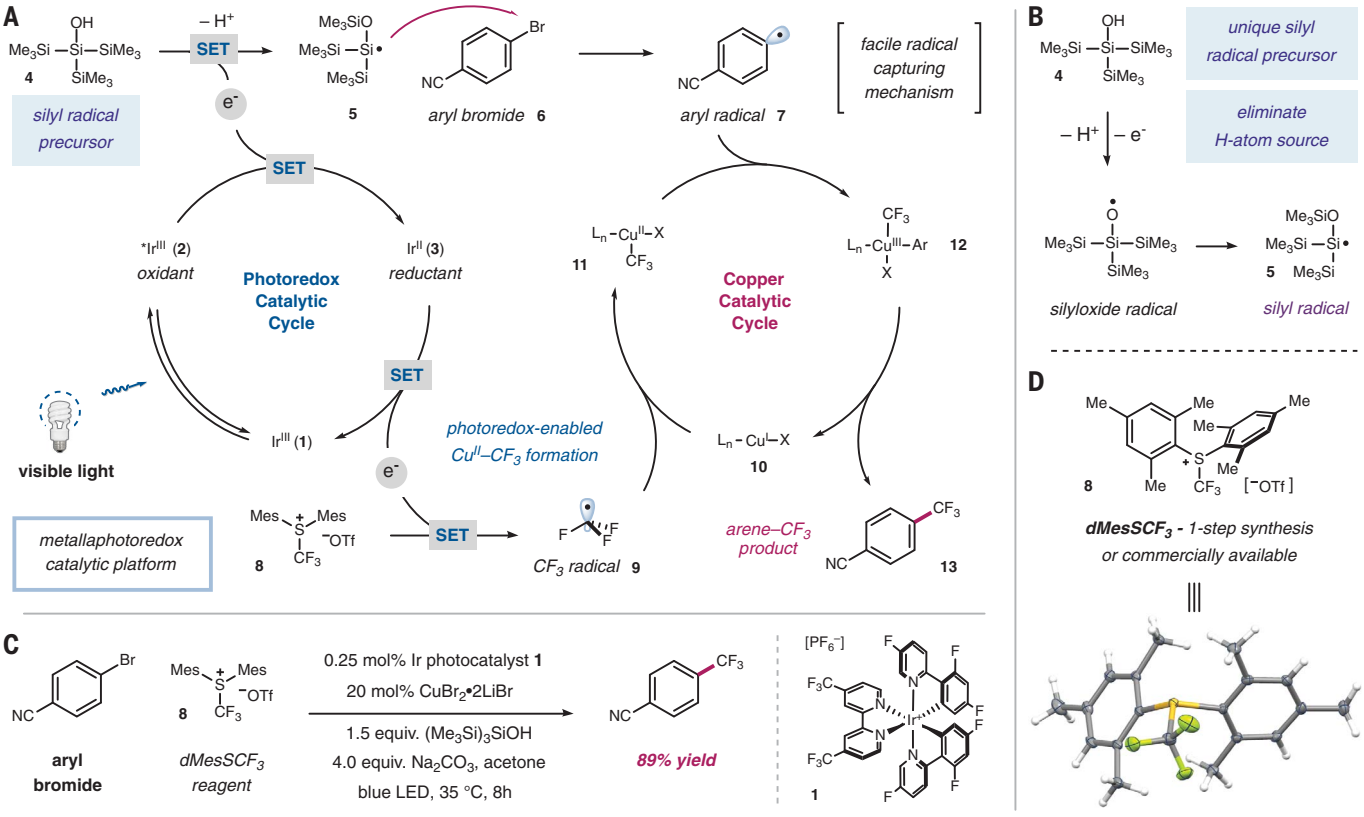

Fig. 2. Reaction design. (**A**) Proposed mechanism for the trifluoromethylation of aryl bromides with dual copper/photoredox catalysis. (**B**) Proposed mechanism for the generation of the active silyl radical. (**C**) Optimized conditions. (**D**) Reagent dMesSCF$_3$ and its solid-state structure. Ellipsoids are drawn at 50% probability. The triflate counterion is omitted. Me, methyl; LED, light-emitting diode; SET, single-electron transfer; Mes, 2,4,6-trimethylphenyl; $^-$OTf, trifluoromethanesulfonate.

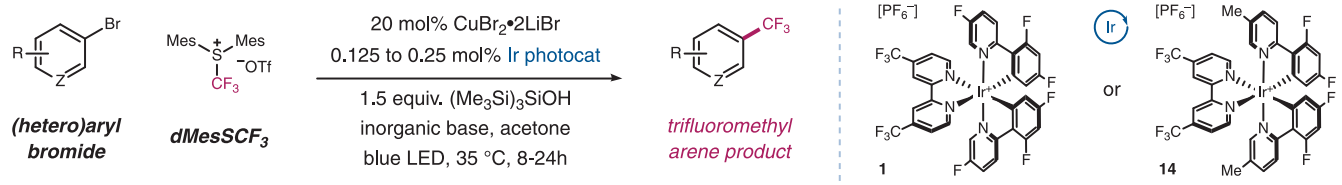

aryl bromides

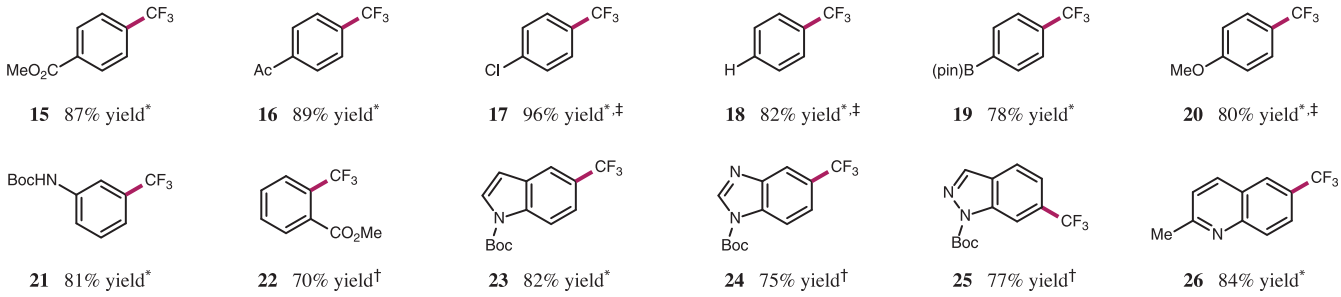

15 87% yield*; **16** 89% yield*; **17** 96% yield*,‡; **18** 82% yield*,‡; **19** 78% yield*; **20** 80% yield*,‡

21 81% yield*; **22** 70% yield†; **23** 82% yield*; **24** 75% yield†; **25** 77% yield†; **26** 84% yield*

heteroaryl bromides

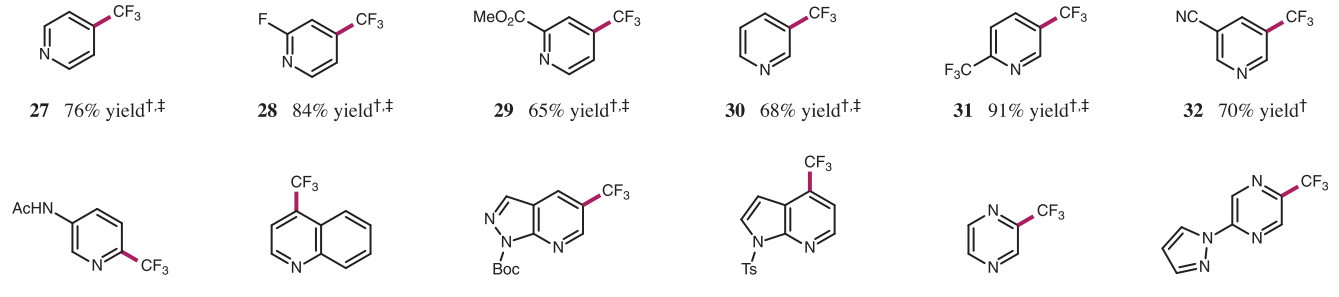

27 76% yield†,‡; **28** 84% yield†,‡; **29** 65% yield†,‡; **30** 68% yield†,‡; **31** 91% yield†,‡; **32** 70% yield†

33 82% yield†; **34** 72% yield†; **35** 66% yield†; **36** 71% yield†; **37** 70% yield†,‡; **38** 66% yield†

39 91% yield†,§; **40** 90% yield†,‡; **41** 79% yield†,‡; **42** 64% yield†,‖; **43** 64% yield*,‡; **44** 51% yield*

45 47% yield*,‡,‖; **46** 38% yield†; **47** 63% yield*,‖,¶; **48** 61% yield*,‖,¶; **49** 62% yield†; **50** 60% yield†,¶

trifluoromethylation of biorelevant molecules

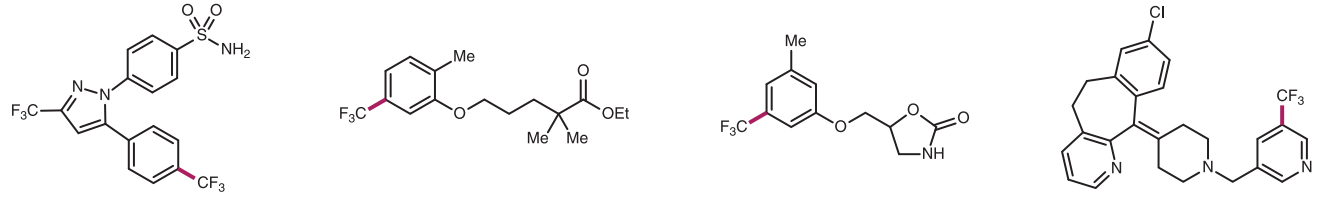

Celebrex CF_3 derivative **51** 77% yield†

Lopid Ester CF_3 derivative **52** 66% yield*

Skelaxin CF_3 derivative **53** 72% yield*

Rupatadine CF_3 derivative **54** 42% yield†

Fig. 3. Synthesis of trifluoromethyl(hetero)arenes. Substrate scope for the metallaphotoredox-catalyzed trifluoromethylation of (hetero)aryl bromides. All yields are isolated unless noted otherwise. See the supplementary materials for experimental details and more examples. *With photocatalyst **14**. †With photocatalyst **1**. ‡Yield determined by ^{19}F or proton nuclear magnetic resonance (^1H NMR) of crude reaction mixture with respect to an internal standard. §With 20 mol % 1,10-phenanthroline. ‖Copper(I)-thiophene-2-carboxylate as catalyst. ¶With 20 mol % 4,7-dimethoxy-1,10-phenanthroline. Ac, acetyl; Pin, pinacolato; Boc, *tert*-butoxycarbonyl; Et, ethyl; Ts, 4-toluenesulfonate.

by aryl radicals from weak Si–H bonds (*31*). In addition, a variety of diaryl sulfonium CF_3 salts were found to be compatible with the coupling protocol. However, the dimesityl sulfonium triflate salt (**8**) provided the highest efficiency of the desired product. We attribute this efficiency to suppression of unproductive CF_3 radical addition to the corresponding diaryl sulfide (*40*). No reactivity was observed between sulfonium **8** and a variety of Cu(I) and Cu(II) complexes, which further supports a photoredox-catalyzed generation of a CF_3 radical. Electrophilic CF_3 reagent **8** is a bench-stable, crystalline solid, which allows for ease in purification and handling (Fig. 2D). Moreover, optimization in the preparation procedure allowed for a one-step, scalable synthesis of this now-commercial trifluoromethylating reagent.

With the optimized conditions in hand, we sought to examine the scope of the trifluoromethylation protocol (Fig. 3). A broad range of electronically differentiated parasubstituted bromoarenes were found to give good to excellent yields of the desired product (**15** to **20**, 78 to 96% yield). Functionalities with coupling capability, such as chloro and pinacolborato, remain intact, potentially allowing for subsequent orthogonal functionalization (**17** and **19**, 96 and 78% yield). Substituents at the meta and ortho positions were also well tolerated (**21** and **22**, 81 and 70% yield). Without the implementation of extensive optimization studies, the functionalization of dibromobenzenes provided the bis(trifluoromethyl)arene adduct product in good yield with the para-case and moderate to low yields with the ortho and meta adducts (figs. S28 to S30). The monotrifluoromethylated product could be achieved in good yield for all cases using our standard conditions. Aryl bromides with fused cyclic motifs were converted to the desired trifluoromethylarenes in good yields (**23** to **26**, 75 to 84% yield). Additional examples of bromoarene trifluoromethylation can be found in fig. S31. Regarding the scope of heteroarylbromides, pyridine-derived substrates were functionalized in good to excellent yields (**27** to **36**, 65 to 91% yield), and the trifluoromethylation of bromopyrazines, -pyrimidines, and -pyridazines was also accomplished in generally high efficiency (**37** to **42**, 64 to 91% yield). We were pleased to find that a wide range of five-membered heteroaryl bromides, such as imidazoles, pyrazoles, and thiazoles, were competent substrates, providing the desired products in useful to good yields (**43** to **50**, 38 to 64% yield). Finally, the compatibility of the trifluoromethylation protocol with biorelevant molecules was also examined. Indeed, CF_3-derivatives of Celebrex, Lopid, Skelaxin, and Rupatadine were readily synthesized from the corresponding aryl bromide precursors (**51** to **54**, 42 to 77% yield).

We next turned our attention to investigating the intermediacy of an aryl radical under this dual copper/photoredox platform. First, generation of an aryl radical under copper-free conditions was examined by exposure of a mixture of bromoarene (**6**), supersilanol (**4**), dMesSCF$_3$ reagent (**8**), and photocatalyst (**1**) to blue LEDs

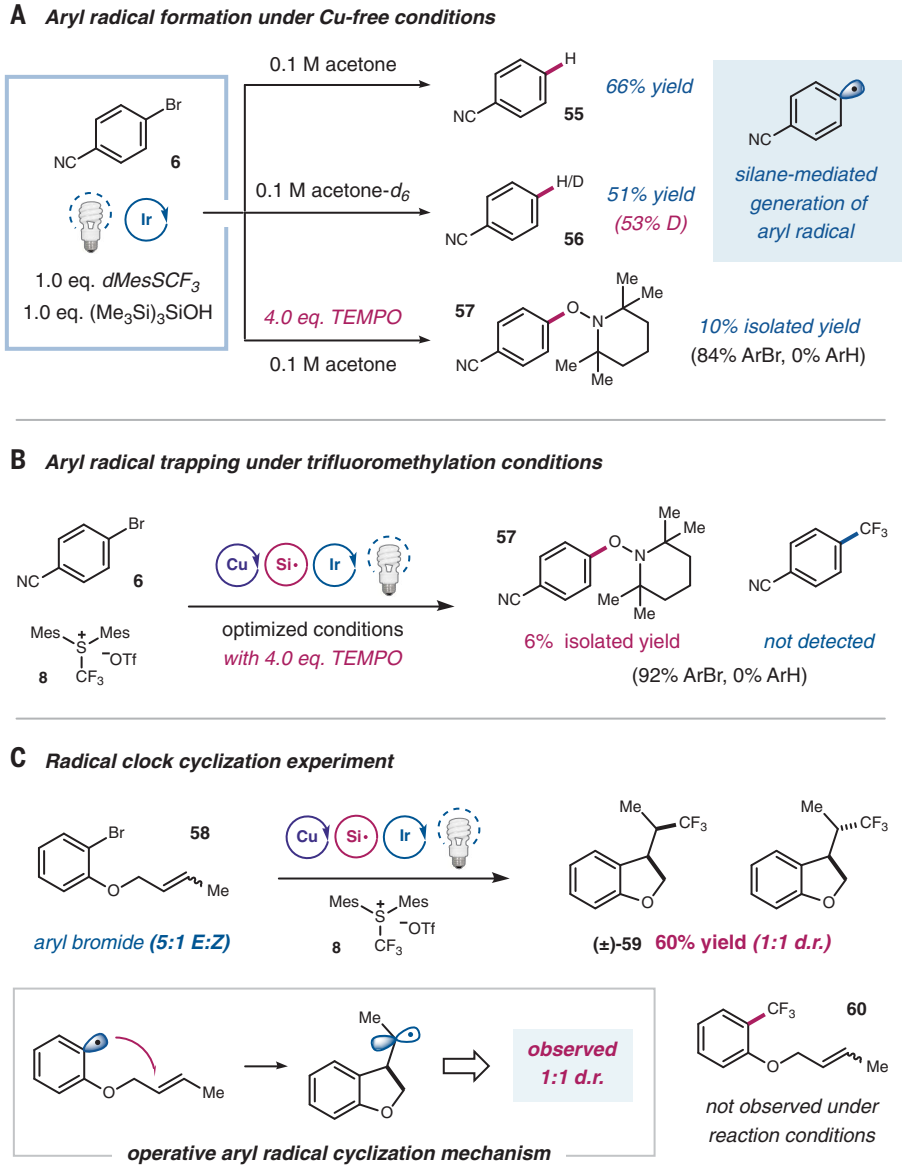

Fig. 4. Evidence for an aryl radical mechanism. (**A**) Under copper-free conditions, silane-mediated generation of aryl radical was observed through hydrogen/deuterium trapped product and TEMPO-trapped adduct. (**B**) Similar behavior was observed under the optimized reaction condition when TEMPO was used as a radical trap. (**C**) Exclusive cyclized product formation, along with the observed diastereoselectivity, served as strong indications for an aryl radical mechanism being operative. TEMPO, (2,2,6,6-Tetramethylpiperidin-1-yl)oxyl; d.r., diastereomeric ratio.

(Fig. 4A). When acetone was employed as the reaction medium, 66% yield of the protodehalogenation product (**55**) was observed. This product is proposed to arise from a hydrogen atom transfer event between an aryl radical and a solvent molecule. When the same reaction was carried out in acetone-d_6, a similar yield was observed with 53% deuterium incorporation at the para position (**56**, 51% yield). Furthermore, conducting the identical reaction in the presence of 2,2,6,6-tetramethylpiperidin-1-oxyl (TEMPO) resulted in complete shutdown of formation of the reduced product, and, more important, aryl-trapped TEMPO adduct **57** was isolated, further supporting the intermediacy of an aryl radical (*41*, *42*). A similar result was observed when a TEMPO-trapping experiment was carried out with the optimized trifluoromethylation conditions. As shown in Fig. 4B, aryl-TEMPO adduct **57** was isolated, whereas the formation of the desired trifluoromethylarene was completely suppressed. Control experiments indicated that the aryl radical formation is not mediated by direct SET reduction of the aryl bromide by the photocatalyst (fig. S41). To lend additional support to our proposed mechanism, we next employed a radical clock experiment with *ortho*-*O*-(3-methyl-allyl)bromobenzene (5:1 trans:cis mixture) (**58**) as the substrate (Fig. 4C). Subjecting the olefin mixture to the standard conditions

yielded exclusively the cyclized alkyl-CF_3 product in good yield (**59**, 60% yield). The 1-to-1 diastereomeric ratio of the cyclized product **59**, along with the absence of the CF_3-arene product **60**, further support the hypothesis of aryl radical generation during the course of the reaction (*33*, *34*). Previously reported copper-mediated aryl halide trifluoromethylation protocols did not exhibit aryl radical characteristics when similar radical clock experiments were used as a mechanistic probe (*24*, *25*). In addition, whereas aryl radical generation has previously been shown to be operative under light-irradiated copper catalysis (*33*), the open-shell aryl species under our optimized conditions is generated by a silyl radical halogen abstraction, independent of the copper catalyst (*43*).

Use of aryl radical trapping to circumvent the sluggish nature of conventional oxidative addition in copper catalysis has allowed for the development of a general dual copper/photoredox-catalyzed trifluoromethylation protocol for aryl bromides. We expect this method to be widely adopted by the synthetic community as a complementary tool to existing trifluoromethylation platforms. Perhaps most important, we see this halide abstraction/radical capture mechanism (at room temperature) as an approach to overcome the copper oxidative addition problem and in doing so provide a general paradigm to the development of many, previously unknown, copper-catalyzed coupling reactions.

REFERENCES AND NOTES

1. L. S. Hegedus, B. C. G. Söderberg, *Transition Metals in the Synthesis of Complex Organic Molecules* (University Science Books, United States, ed. 3, 2010).
2. D. A. Petrone, J. Ye, M. Lautens, *Chem. Rev.* **116**, 8003–8104 (2016).
3. J. Tsuji, *Palladium Reagents and Catalysts: New Perspectives for the 21st Century* (John Wiley & Sons, 2005).
4. S. Z. Tasker, E. A. Standley, T. F. Jamison, *Nature* **509**, 299–309 (2014).
5. G. Evano, N. Blanchard, *Copper-Mediated Cross-Coupling Reactions* (John Wiley & Sons, 2014).
6. G. O. Jones, P. Liu, K. N. Houk, S. L. Buchwald, *J. Am. Chem. Soc.* **132**, 6205–6213 (2010).
7. H.-Z. Yu, Y.-Y. Jiang, Y. Fu, L. Liu, *J. Am. Chem. Soc.* **132**, 18078–18091 (2010).
8. R. Giri *et al*., *J. Am. Chem. Soc.* **140**, 793–806 (2018).
9. P. J. Amal Joseph, S. Priyadarshini, *Org. Process Res. Dev.* **21**, 1889–1924 (2017).
10. Systems competent for aryl chloride oxidative addition have recently been reported. See (*11*).
11. S. Bhunia, G. G. Pawar, S. V. Kumar, Y. Jiang, D. Ma, *Angew. Chem. Int. Ed.* **56**, 16136–16179 (2017).
12. A. Casitas, X. Ribas, *Chem. Sci.* **4**, 2301–2318 (2013).
13. T. Furuya, A. S. Kamlet, T. Ritter, *Nature* **473**, 470–477 (2011).
14. A. J. Hickman, M. S. Sanford, *Nature* **484**, 177–185 (2012).
15. K. Uneyama, *Organofluorine Chemistry* (Blackwell, Oxford, UK, 2006).
16. W. K. Hagmann, *J. Med. Chem.* **51**, 4359–4369 (2008).
17. O. A. Tomashenko, V. V. Grushin, *Chem. Rev.* **111**, 4475–4521 (2011).
18. E. J. Cho *et al*., *Science* **328**, 1679–1681 (2010).
19. J. R. Bour, N. M. Camasso, M. S. Sanford, *J. Am. Chem. Soc.* **137**, 8034–8037 (2015).
20. C. Alonso, E. M. de Marigorta, G. Rubiales, F. Palacios, *Chem. Rev.* **115**, 1847–1935 (2015).
21. A. I. Konovalov, A. Lishchynskyi, V. V. Grushin, *J. Am. Chem. Soc.* **136**, 13410–13425 (2014).
22. J. Jover, *ACS Catal.* **4**, 4389–4397 (2014).
23. G. G. Dubinina, H. Furutachi, D. A. Vicic, *J. Am. Chem. Soc.* **130**, 8600–8601 (2008).
24. A. Zanardi, M. A. Novikov, E. Martin, J. Benet-Buchholz, V. V. Grushin, *J. Am. Chem. Soc.* **133**, 20901–20913 (2011).
25. H. Morimoto, T. Tsubogo, N. D. Litvinas, J. F. Hartwig, *Angew. Chem. Int. Ed.* **50**, 3793–3798 (2011).
26. Q.-Y. Chen, S.-W. Wu,*J. Chem. Soc. Chem. Commun.* **11**, 705–706 (1989).
27. M. Oishi, H. Kondo, H. Amii, *Chem. Commun. (Camb.)* **14**, 1909–1911 (2009).
28. T. Schareina *et al*., *Top. Catal.* **55**, 426–431 (2012).
29. J. Twilton *et al*., *Nat. Rev. Chem.* **1**, 0052 (2017).
30. P. Zhang, C. C. Le, D. W. C. MacMillan, *J. Am. Chem. Soc.* **138**, 8084–8087 (2016).
31. C. Chatgilialoglu, *Organosilanes in Radical Chemistry* (Wiley, Chichester, UK, 2014).
32. J. J. Devery III, J. D. Nguyen, C. Dai, C. R. J. Stephenson, *ACS Catal.* **6**, 5962–5967 (2016).
33. S. E. Creutz, K. J. Lotito, G. C. Fu, J. C. Peters, *Science* **338**, 647–651 (2012).
34. M. W. Johnson, K. I. Hannoun, Y. Tan, G. C. Fu, J. C. Peters, *Chem. Sci.* **7**, 4091–4100 (2016).
35. Stern-Volmer studies confirmed quenching interaction between supersilanol **4** and the excited photocatalyst. See fig. S40.
36. M. Lucarini, E. Marchesi, G. F. Pedulli, C. Chatgilialoglu, *J. Org. Chem.* **63**, 1687–1693 (1998).
37. For reviews on radical-radical cross-coupling in the presence of a transition metal catalyst, see (*38*).
38. H. Yi *et al*., *Chem. Rev.* **117**, 9016–9085 (2017).
39. A. Lishchynskyi, G. Berthon, V. V. Grushin, *Chem. Commun. (Camb.)* **50**, 10237–10240 (2014).
40. See the supplementary materials for optimization studies.
41. Z. Xia, Q. Zhu, *Org. Lett.* **15**, 4110–4113 (2013).
42. D. A. Leas, Y. Dong, J. L. Vennerstrom, D. E. Stack, *Org. Lett.* **19**, 2518–2521 (2017).
43. Studies were carried out to rule out an aryl bromide activation by an excited Cu(I)-CF_3 species as the major pathway under the standard conditions. See the supplementary materials.

ACKNOWLEDGMENTS

The authors thank C. Kraml, N. Byrne, and L. Wilson (Lotus Separations) for compound purification and P. Jeffrey for assistance with x-ray structure determination. **Funding:** Research reported in this publication was supported by the NIH National Institute of General Medical Sciences (R01 GM103558-03) and gifts from Merck, Bristol-Myers Squibb, Eli Lilly, Genentech, Pfizer, and Johnson & Johnson. C. L. thanks Bristol-Myers Squibb for a graduate fellowship. **Author contributions:** D.W.C.M. conceived and directed the project. D.W.C.M., C.L., T.Q.C., T.L., and P.Z. designed the experiments. C.L., T.Q.C., and T.L. performed and analyzed the experiments. T.Q.C. obtained x-ray quality crystals for trifluoromethylating reagent **8**. P.Z. discovered silanol reagent **4** as a new silyl radical source. D.W.C.M., C.L., T.Q.C., T.L., and P.Z. prepared the manuscript. **Competing interests:** The authors declare no conflicts of interest. **Data and materials availability:** Crystallographic parameters for compound **8** are available free of charge from the Cambridge Crystallographic Data Centre under CCDC 1833832. Data are available in the supplementary materials.

SUPPLEMENTARY MATERIALS

www.sciencemag.org/content/360/6392/1010/suppl/DC1
Materials and Methods
Figs. S1 to S49
References (*44*–*51*)
NMR Spectra

23 February 2018; accepted 12 April 2018
10.1126/science.aat4133

PLANT SCIENCE

Feedback regulation of COOLAIR expression controls seed dormancy and flowering time

Min Chen and Steven Penfield*

Plants integrate seasonal signals, including temperature and day length, to optimize the timing of developmental transitions. Seasonal sensing requires the activity of two proteins, FLOWERING LOCUS C (FLC) and FLOWERING LOCUS T (FT), that control certain developmental transitions in plants. During reproductive development, the mother plant uses FLC and FT to modulate progeny seed dormancy in response to temperature. We found that for regulation of seed dormancy, *FLC* and *FT* function in opposite configuration to how those same genes control time to flowering. For seed dormancy, FT regulates seed dormancy through *FLC* gene expression and regulates chromatin state by activating antisense *FLC* transcription. Thus, in *Arabidopsis* the same genes controlled in opposite format regulate flowering time and seed dormancy in response to the temperature changes that characterize seasons.

In *Arabidopsis*, seasonal changes in temperature are sensed by the epigenetic state of the floral repressor gene *FLOWERING LOCUS C* (*FLC*) (*1*–*3*). Prolonged periods of cold promote the expression of antisense transcripts at *FLC* known as *COOLAIR*, which facilitate silencing of *FLC* mRNA transcription via recruitment of Polycomb repressive complex 2 (PRC2) and deposition of the trimethylated histone H3 Lys^{27} (H3K27me3) chromatin mark (*4*–*6*). A key target of FLC is *FLOWERING LOCUS T* (*FT*), and FT and FLC are believed to act sequentially to deliver seasonal information that promotes flowering (*7*–*9*).

After flowering, FLC and FT control plant architecture and progeny seed dormancy, the latter by regulation of seed coat development and seed hormone levels (*10*–*15*). Temperature changes applied to plants before buds are visible affect progeny seed dormancy in a process that requires maternal FLC and FT, which pass seasonal information to progeny (*12*). In this way, the mother plant exploits environmental temperature variation to create diversity in progeny seed behavior, which is important for bet-hedging reproductive strategies (*15*). Here, we investigated how FT controls seed dormancy.

To repress *FT* expression, FLC forms heterodimers with the transcription factor SHORT VEGETATIVE PHASE (SVP) (*16*, *17*). To determine the genetic architecture of maternal temperature signaling pathways controlling seed dormancy, we exposed *ft-1 svp-3* and *ft-1 flc-21* double mutant rosettes to high and low ambient temperatures and analyzed the effect on progeny dormancy relative to the wild type and single mutants (Fig. 1A). Restricting temperature treatments to the pre-anthesis period enables dormancy outcomes to be ascribed solely to parental responses (*12*). Genetic interactions showed that the effect of SVP requires *FT*, because mutation of *FT* suppressed the high germination of *svp-3* mutants (Fig. 1A). However, *ft-1 flc-21* double mutant plants produced seeds whose germination resembled that of *flc-21*, and *flc-21* reversed the stronger dormancy of *ft-1* mutants (Fig. 1A). Therefore, in the context of seed dormancy, the *FLC* locus acts genetically downstream of FT. To test whether FT requires maternal FLC for dormancy control, we made reciprocal crosses between *ft-1* and *ft-1 flc-21* double mutants. Maternal *FLC* was required for seed dormancy control by FT (fig. S1A) (*10*). FT is required for temperature regulation of seed coat development (*12*). Indeed, *flc-21* prevented increases in seed coat tannin content and decreases in seed coat permeability observed in *ft* mutant fruit tissue, and reversed the up-regulation of transcription factors controlling seed coat tannin deposition in *ft-1* (Fig. 1, B and C, and fig. S1, B and C).

Next, we tested whether FT controls *FLC* expression, focusing our analysis on female reproductive tissues. Relative to 16°C conditions, warm conditions (22°C) down-regulated *FLC* mRNA expression in wild-type carpels, as it does in leaves (*18*). Loss of FT strongly reduced the magnitude of this response (Fig. 2A). To locate the tissues in which FT regulates *FLC*, we crossed a translational GUS fusion containing the entire *FLC* locus (*3*) (*FLC-GUS*) into *ft-1* and analyzed the expression in reproductive tissues. In flowers at 22°C, *FLC* is expressed only in the stamen of wild-type plants, but in the *ft-1* mutant we observed ectopic expression of *FLC-GUS* in carpels (Fig. 2, B and C). We also tested the effect of *ft-1* on antisense *COOLAIR* expression in carpels (Fig. 2D). *COOLAIR* is transcribed into both short (proximal) and longer (distal) transcripts (*19*). We found that at 22°C, levels of distal *COOLAIR* were reduced in *ft-1* but levels of proximal *COOLAIR* transcript were unchanged (Fig. 2D).

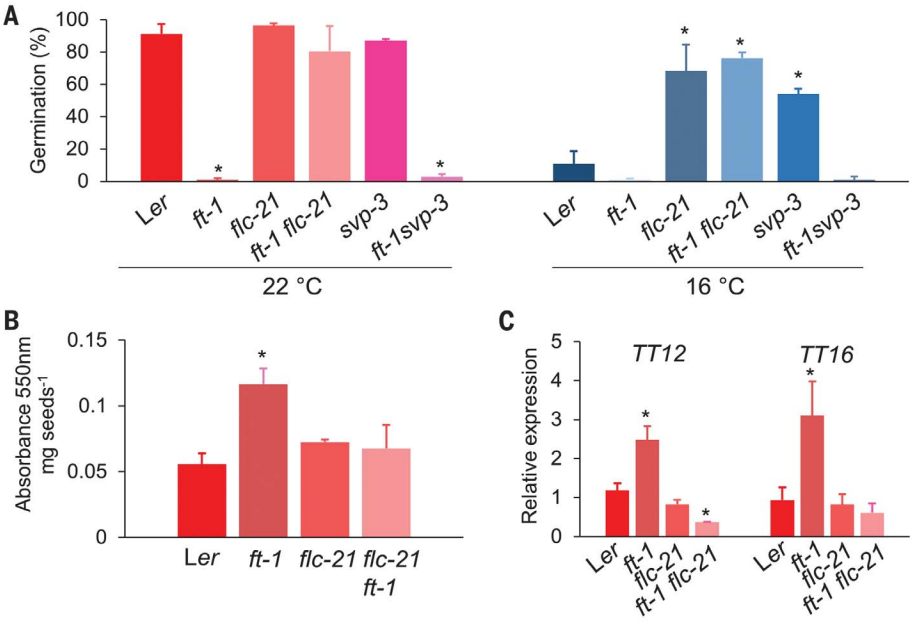

Fig. 1. *FT* acts upstream of *FLC* to regulate seed dormancy. (**A**) Germination of seeds from mother plants subjected to either 22° or 16°C before anthesis. Error bars represent SE ($n \geq 5$ biological replicates). (**B**) Insoluble tannin content in wild-type (Ler), *ft-1*, *flc-21*, and *ft-1 flc-21* double mutant seeds. Error bars represent SE ($n = 5$ biological replicates). (**C**) Quantitative reverse transcription PCR (qRT-PCR) shows that *FLC* is required for up-regulation of regulators of tannin synthesis *TRANSPARENT TESTA 12* (*TT12*) and *TT16* in *ft-1*. Error bars represent SE ($n = 3$ biological replicates). *$P < 0.05$ (difference from wild type).

Department of Crop Genetics, John Innes Centre, Norwich Research Park, Norwich NR4 7UH, UK.
***Corresponding author. Email: steven.penfield@jic.ac.uk**

Therefore, FT influences the balance of sense and antisense gene expression at the *FLC* locus. Further analysis of *FLC:GUS* in seed tissues during seed maturation showed no effect of FT on *FLC:GUS* expression in seeds themselves (fig. S2), consistent with the maternal action of FLC in seed dormancy control; this finding suggests that *FT* and *FLC* act to control dormancy either during carpel development or shortly after fertilization.

Because of the differences in *FLC* expression between wild-type and *ft-1* mutants, we used FT tagged with green fluorescent protein (GFP) to test whether *FLC* is a direct target of FT. Plants expressing FT-GFP from the phloem-specific *SUC2* promoter (*9*) were used to determine whether FT-GFP could be detected at the *FLC* locus by chromatin immunoprecipitation (ChIP). This construct is functional and complements the late-flowering *ft-7* mutation, and also increases germination of *ft-7* seeds (fig. S3). We could detect enrichment of FT-GFP toward the last exon and 3′ region of the *FLC* locus, corresponding to the promoter and first exon of *COOLAIR* transcripts (Fig. 3A) (*4*, *5*). Given that *COOLAIR* transcripts silence *FLC* mRNA expression (*5*), we asked whether FT affects the temperature-regulation of *FLC* mRNA levels by promoting *COOLAIR* transcription. We used strand-specific quantitative reverse transcription polymerase chain reaction (qRT-PCR) to compare *COOLAIR* expression in wild-type and *ft-1* siliques produced on plants that began reproductive development at either 22° or 16°C. We found no evidence that either temperature or FT regulated proximal *COOLAIR* transcripts (Fig. 3B). However, 22°C increased distal *COOLAIR* levels in wild-type fruits compared to 16°C, and this effect required FT (Fig. 3C). This down-regulation of distal *COOLAIR* in *ft-1* suggested that this transcript opposed *FLC* mRNA expression (*20*), which is higher in the *ft-1* mutant than in the wild type (Fig. 2).

We next tested whether the FT protein can activate transcription from an isolated *COOLAIR* promoter fused to the *LUCIFERASE* (*LUC*) reporter. After introgressing the *COOLAIR:LUC* transgene from L*er* to *ft-1*, we compared *LUC* activity between wild-type plants and *ft-1* mutants. In the wild type, we could detect *COOLAIR:LUC* activity in whole plants, carpels, and fruits, with LUC activity in fruits declining during fruit and seed maturation (Fig. 3D). In *ft-1* plants, *COOLAIR:LUC*

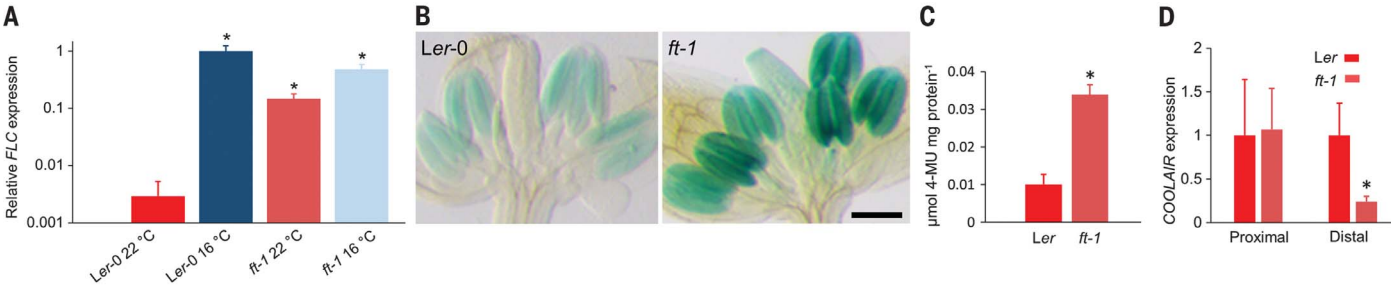

Fig. 2. Maternal temperature experience and FT affect *FLC* expression in carpels. (**A**) *FLC* mRNA transcripts in carpel tissue harvested from plants grown at either 16° or 22°C. Error bars represent SE (n = 3 biological replicates). (**B**) *FLC-GUS* expression in the stage 12 floral organs of representative L*er* and *ft-1* flowers. Scale bar, 1 mm. (**C**) Quantitative measurement of *FLC-GUS* activity in wild-type and *ft-1* isolated carpels at 22°C. Error bars represent SE (n = 3 biological replicates). (**D**) *COOLAIR* transcripts in wild-type and *ft-1* carpels at 22°C. Error bars represent SE (n = 3 biological replicates). *P < 0.05 (difference from wild type).

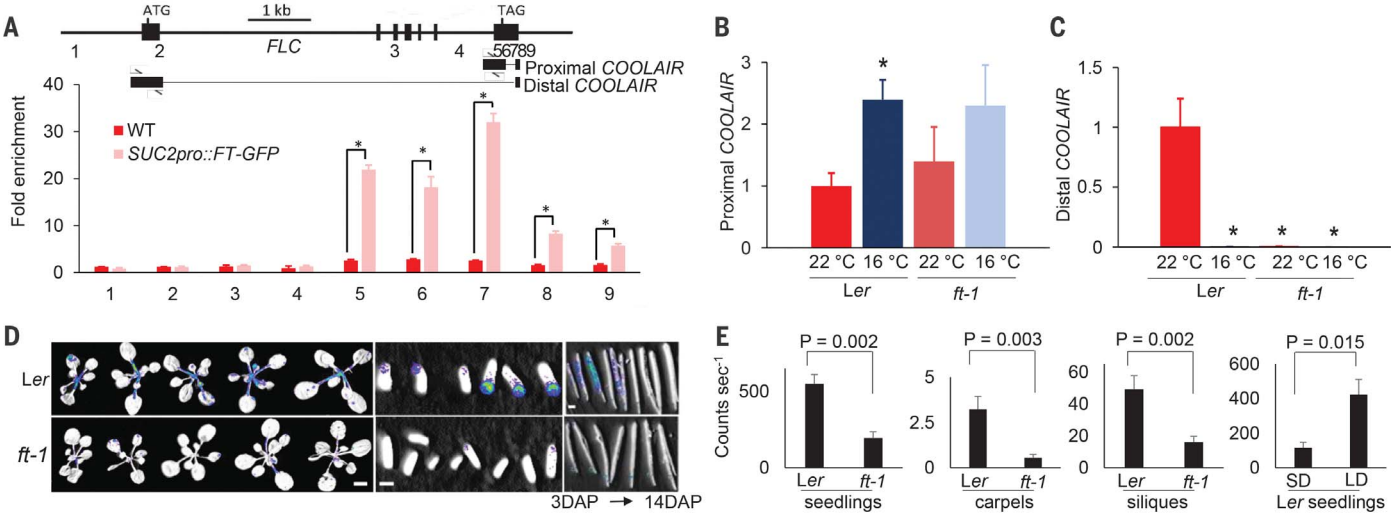

Fig. 3. Maternal temperature experience affects *FLC* antisense transcription in fruit tissue. (**A**) FT-GFP ChIP performed across the *FLC* locus in silique tissues. Data are represented relative to the negative control *ACTIN2*. Numbers indicate positions of primers used. Error bars represent SE (n = 3 biological replicates). *P < 0.05 (difference from wild type). (**B** and **C**) Proximal and distal *COOLAIR* levels in silique tissues from plants growing at either 16° or 22°C. Error bars represent SE (n = 3 biological replicates). Primers used are indicated by arrows in (A). *P < 0.05 (difference from wild type). (**D**) *COOLAIR:LUC* expression imaged in wild-type and *ft-1* seedlings, carpels, and developing siliques from 3 to 14 days after pollination (DAP; left to right). Scale bars, 5 mm (seedlings and siliques), 1 mm (carpels). (**E**) Quantitative analysis of *COOLAIR:LUC* expression at 22°C in the indicated organs in long days, and the effect of 16-hour days (LD) and 8-hour days (SD) on *COOLAIR:LUC* expression in L*er* seedlings. Data are means ± SE (n ≥ 5 biological replicates). P values were calculated by two-tailed Student t test between genotypes or treatments.

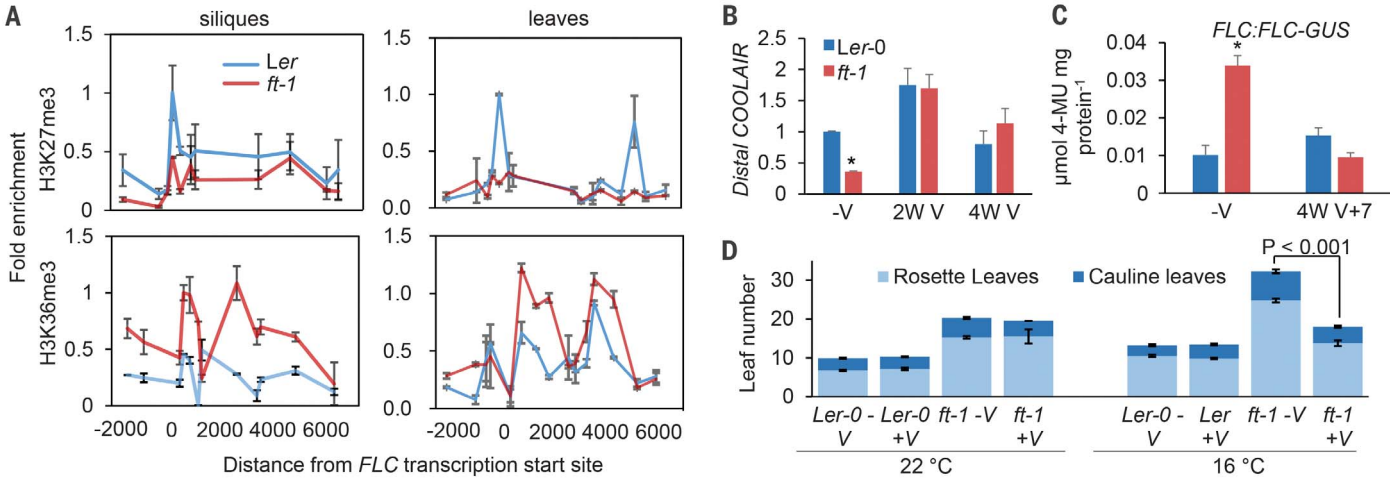

Fig. 4. FT affects *FLC* chromatin state in leaves and siliques. (**A**) ChIP comparing L*er* and levels of H3K27me3 and H3K36me3 across the *FLC* locus in silique and *ft-1* leaf tissues. Data are means ± SE ($n \geq 2$ biological replicates). (**B**) The effect of vernalization (V) at 4°C for the indicated number of weeks (W) on distal *COOLAIR* transcript levels in L*er* and *ft-1*. Data are means ± SE ($n = 3$ biological replicates). *$P < 0.05$ (difference from L*er* control levels without vernalization). (**C**) GUS activity from *FLC:GUS*-expressing L*er* and *ft-1* plants in seedlings without vernalization (–V) versus 7 days after vernalization for 4 weeks (4W V+7). Data are means ± SE ($n = 3$ biological replicates). *$P < 0.05$ (difference from L*er* control levels without vernalization). (**D**) Rosette and cauline leaf numbers at flowering in L*er* and *ft-1* plants grown at either 22° or 16°C with or without prior vernalization. Data are means ± SE ($n \geq 5$ biological replicates). Significant differences in response to vernalization are indicated.

expression was reduced to 20 to 30% of wild-type levels in all organs tested (Fig. 3, D and E). Moving wild-type *COOLAIR:LUC* plants from long days to short days reduced *LUC* expression (Fig. 3E), consistent with the known role of FT in photoperiod responses (*9*). Because FT bound the *FLC* locus close to the *COOLAIR* transcription start site, and because FT was required for *COOLAIR* promoter activity in plants grown at 22°C in long days, we conclude that FT suppresses *FLC* mRNA expression by activating *COOLAIR* transcription.

During vernalization, changes in *COOLAIR* expression precede stable chromatin state changes at *FLC* (*4*, *5*). To test whether FT regulation of *FLC* is chromatin-based, we analyzed histone methylation at the *FLC* locus in wild-type and *ft-1* plants at 22°C. Wild-type plants showed more H3K27me3 at the nucleation region (*6*) in siliques and leaves and less H3K36me3 than did *ft-1* plants (Fig. 4A). This shows that FT can switch *FLC* between active and passive transcription states. The effect of *ft-1* on *FLC* expression in leaves could be overcome by vernalization (Fig. 4, B and C). We also found that an FLC-dependent effect of *FT* on flowering time can be observed if plants are grown at 16°C (Fig. 4D). The *ft-1* mutant is later-flowering at 16°C than at 22°C, and this effect can also be overcome by vernalization. This is reminiscent of *fca* and *fy* mutants, which are also affected in *COOLAIR* processing (*21*). Therefore, the feedback regulation of FLC by FT has a general relevance, controlling both flowering time and seed dormancy processes.

REFERENCES AND NOTES

1. C. C. Sheldon, D. T. Rouse, E. J. Finnegan, W. J. Peacock, E. S. Dennis, *Proc. Natl. Acad. Sci. U.S.A.* **97**, 3753–3758 (2000).
2. S. D. Michaels, R. M. Amasino, *Plant Cell* **13**, 935–941 (2001).
3. R. Bastow *et al.*, *Nature* **427**, 164–167 (2004).
4. S. Swiezewski, F. Liu, A. Magusin, C. Dean, *Nature* **462**, 799–802 (2009).
5. T. Csorba, J. I. Questa, Q. Sun, C. Dean, *Proc. Natl. Acad. Sci. U.S.A.* **111**, 16160–16165 (2014).
6. J. I. Qüesta, J. Song, N. Geraldo, H. An, C. Dean, *Science* **353**, 485–488 (2016).
7. S. D. Michaels, E. Himelblau, S. Y. Kim, F. M. Schomburg, R. M. Amasino, *Plant Physiol.* **137**, 149–156 (2005).
8. P. A. Wigge *et al.*, *Science* **309**, 1056–1059 (2005).
9. L. Corbesier *et al.*, *Science* **316**, 1030–1033 (2007).
10. G. C. Chiang, D. Barua, E. M. Kramer, R. M. Amasino, K. Donohue, *Proc. Natl. Acad. Sci. U.S.A.* **106**, 11661–11666 (2009).
11. M. Niwa *et al.*, *Plant Cell* **25**, 1228–1242 (2013).
12. M. Chen *et al.*, *Proc. Natl. Acad. Sci. U.S.A.* **111**, 18787–18792 (2014).
13. T. Imaizumi, G. Auge, K. Donohue, *Am. J. Bot.* **104**, 516–526 (2017).
14. G. A. Auge, L. K. Blair, H. Neville, K. Donohue, *New Phytol.* **216**, 388–400 (2017).
15. V. Springthorpe, S. Penfield, *eLife* **4**, e05557 (2015).
16. J. L. Mateos *et al.*, *Genome Biol.* **16**, 31 (2015).
17. D. Li *et al.*, *Dev. Cell* **15**, 110–120 (2008).
18. M. A. Blázquez, J. H. Ahn, D. Weigel, *Nat. Genet.* **33**, 168–171 (2003).
19. S. Marquardt *et al.*, *Mol. Cell* **54**, 156–165 (2014).
20. S. Rosa, S. Duncan, C. Dean, *Nat. Commun.* **7**, 13031 (2016).
21. F. Liu, S. Marquardt, C. Lister, S. Swiezewski, C. Dean, *Science* **327**, 94–97 (2010).

ACKNOWLEDGMENTS

We thank C. Dean for *FLC:GUS* seeds and *COOLAIR:LUC* construct, G. Coupland for *ft-7 pSUC2:FT-GFP*, and G. Calder and E. Wegel for microscopy support. **Funding:** Supported by BBSRC grant BB/P013511/1 to the John Innes Centre. **Author contributions:** Experimental design by M.C. and S.P. Experimental work was conducted by M.C. Data analysis by M.C. and S.P. S.P. wrote the manuscript. **Competing interests:** None declared. **Data and materials availability:** All data needed to evaluate the conclusions in the paper are present in the paper or the supplementary materials.

SUPPLEMENTARY MATERIALS

www.sciencemag.org/content/360/6392/1014/suppl/DC1
Materials and Methods
Figs. S1 to S3
Table S1
References (*22*–*30*)

18 December 2017; accepted 13 April 2018
10.1126/science.aar7361

EVOLUTION

Predator-driven natural selection on risk-taking behavior in anole lizards

Oriol Lapiedra,[1]* Thomas W. Schoener,[2] Manuel Leal,[3] Jonathan B. Losos,[1]† Jason J. Kolbe[4]†

Biologists have long debated the role of behavior in evolution, yet understanding of its role as a driver of adaptation is hampered by the scarcity of experimental studies of natural selection on behavior in nature. After showing that individual *Anolis sagrei* lizards vary consistently in risk-taking behaviors, we experimentally established populations on eight small islands either with or without *Leiocephalus carinatus*, a major ground predator. We found that selection predictably favors different risk-taking behaviors under different treatments: Exploratory behavior is favored in the absence of predators, whereas avoidance of the ground is favored in their presence. On predator islands, selection on behavior is stronger than selection on morphology, whereas the opposite holds on islands without predators. Our field experiment demonstrates that selection can shape behavioral traits, paving the way toward adaptation to varying environmental contexts.

Understanding the role of behavior in adaptation of animals to new environmental circumstances remains a major challenge in biology. Research has long addressed the debate about whether behavior spurs or impedes evolution (*1*–*3*) on phenotypic dimensions such as morphology (*4*, *5*) or physiology (*6*). To unravel the process by which behavior shapes adaptation, we must examine how natural selection operates among individuals in a population (*7*, *8*). Recent growth in the study of interindividual variation in behavior (*9*–*11*) has revealed that behavior often varies consistently among individuals within a population (*12*). These studies have also suggested that this variation has fitness consequences (*13*–*16*). These results set the stage to investigate the hypothesis that natural selection on interindividual variation in behavior could drive different ecological and evolutionary trajectories for populations under distinct selective regimes (*7*, *8*, *17*–*20*). Assessing a hypothesis like this one under natural conditions requires controlled experiments in which natural selection is quantified under contrasting selective regimes generated by manipulating well-known selective pressures (*21*). Here, we used small Caribbean islands as replicates to test directly whether and how natural selection operates on lizards with different behaviors and morphologies under different selective regimes.

We conducted this experiment on a well-studied predator-prey system involving the small lizard *Anolis sagrei*—commonly found on or near the ground (*22*, *23*)—and its ground-dwelling predator, the larger lizard *Leiocephalus carinatus* (*24*) (Fig. 1A). We focused on individual variation in two behaviors of *A. sagrei* (Fig. 1B) that are consistently repeatable across time and in different contexts within individuals of this species (*25*) (see repeatability scores from this study in table S1). Specifically, we measured the rapidity of individuals to explore new and potentially dangerous environments and the time individuals spend on the ground and are thereby potentially exposed to ground-dwelling predators (*26*). The ecological relevance of these risk-taking behaviors in *A. sagrei* is illustrated by a simple cost-benefit trade-off (*27*, *28*). *Anolis sagrei* individuals more willing to explore new environments should survive better in the absence of terrestrial predators (*17*) because they are more likely to obtain resources. In contrast, *A. sagrei* individuals that spend more time exposed on the ground are more vulnerable to ground predators as compared with individuals that spend less time exposed on the ground (*22*, *25*, *29*). Previous studies have reported differences in habitat use and modulation of social signals in *A. sagrei* populations in the presence or absence of *L. carinatus* (*30*, *31*), leading us to hypothesize that variation in risk-taking behavior might be adaptive.

To experimentally examine natural selection on these risk-taking behaviors under natural conditions, we translocated 273 adult *A. sagrei* individuals onto eight small islands in the Bahamas (fig. S2). Lizards were captured from source islands in the study area that generally have higher vegetation and host more complex biological communities (*32*) than our experimental islands, which have scrubbier, shorter vegetation and do not support resident populations of any known lizard predator (see table S2).

Before translocation, we used outdoor laboratory behavioral assays [following (*25*, *26*)] to

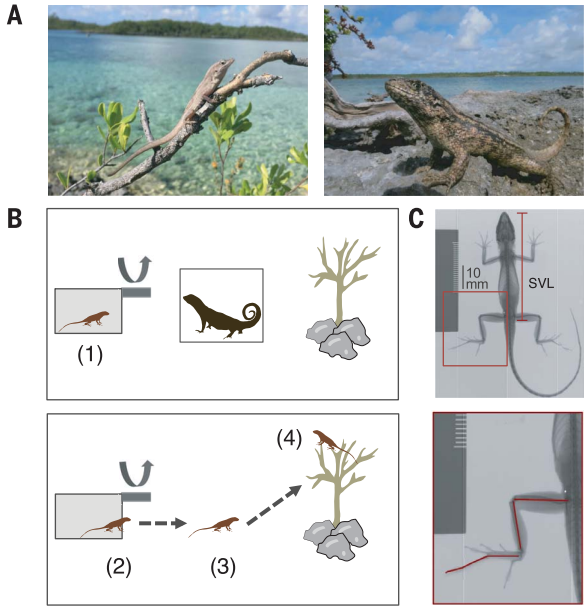

Fig. 1. Assessment of risk-taking behavior and morphological characterization of *A. sagrei* individuals. (**A**) *Anolis sagrei* (left) and *Leiocephalus carinatus* (right) photographed on the experimental islands. (**B**) Experimental assessment of behavioral traits (*26*). Following (*25*), an *A. sagrei* individual was gently placed into a wooden refuge inside a butterfly cage. During a 3-min habituation period, we placed a clear plastic cage that contained a live adult *L. carinatus* between the refuge and a natural perch. Then, we remotely opened the door of the refuge and the *A. sagrei* individual was able to see the predator for 5 min (1). At the end of this period, we closed the door of the refuge and removed the plastic container with the *L. carinatus* from the experimental cage. After another 5-min habituation period, we again opened the refuge cover and measured the "time to initiation of exploration in a new environment" (2), defined as the time interval between the time we opened the refuge cover and the time when the lizard started exploring the experimental cage by poking its head out of the refuge. We defined "time exposed on the ground" as the interval between the "exposed time start" (3)—defined as the time when the experimental lizard went out of the refuge (i.e., all its body, excluding the tail)—and the "exposed time end" (4), the time when the lizard either climbed the perch or hid underneath the rocks. See (*26*) for details. (**C**) Example of an x-ray image from which we measured the morphological traits in this study (i.e., SVL and hindlimb length).

[1]Museum of Comparative Zoology and Department of Organismic and Evolutionary Biology, Harvard University, Cambridge, MA, USA. [2]Department of Evolution and Ecology, University of California, Davis, CA 95616, USA. [3]Division of Biological Sciences, University of Missouri, Columbia, MO, USA. [4]Department of Biological Sciences, University of Rhode Island, Kingston, RI, USA.
*Corresponding author. Email: olapiedragonzalez@fas.harvard.edu
†These authors contributed equally to this work.

characterize interindividual variation in two behaviors known to consistently vary among individuals (*25*) (table S1). After being exposed to the presence of an individual *L. carinatus* (position 1 in Fig. 1B), "time to initiation of exploration in a new environment" was defined as the amount of time until the lizard started exploring the experimental cage by poking its head out of the wooden refuge (position 2 in Fig. 1B). "Time exposed on the ground" corresponded to the interval of time during which the lizard was out of the refuge (position 3 in Fig. 1B) until it climbed on the perch or hid underneath the rocks (position 4 in Fig. 1B). Each lizard was x-rayed (Fig. 1C) and individually tagged before translocation onto experimental islands. We randomly assigned individuals to islands. Each island received lizards in proportion to its vegetated area, which was determined by conducting vegetation transects [following (*26*, *32*)]. One week later, we added *L. carinatus* on four randomly selected islands, while the other four islands remained as predator-free controls. Four months later, we recaptured lizards on each of the experimental islands and identified surviving adult lizards from their individually unique subcutaneous tags.

On the basis of recapture data, we found that survival was lower on predator islands than on predator-free islands (mixed-effects model including island ID as a random factor and modeled following the binomial distribution; $P < 0.001$; fig. S3A). We also observed that *A. sagrei* from predator islands used the ground less frequently (16.9% of observations) than those from predator-free islands (41.4% of observations), and mean perch height was more than twice as high on predator islands (33.9 cm) than on predator-free islands (14.4 cm) ($t = -4.9$, df = 102.5, $P < 0.001$; fig. S3B).

Because *A. sagrei* is a sexually dimorphic species in which males and females differ in both morphology and behavior (*23*, *33*) (figs. S8 and S9), we hypothesized that natural selection on interindividual variation in behavior could operate differently between sexes under different environmental conditions. On predator-free islands, natural selection favored females that took less time to initiation of exploration in the experimental trials conducted before release—a pattern not observed on predator islands (Fig. 2A). On predator islands, females that spent less time exposed on the ground had a greater chance of survival (Fig. 2B). Behavior was not a significant predictor of survival for males (fig. S3A). Whether or not *A. sagrei* were initially captured from islands with *L. carinatus* present did not significantly affect their chances of survival during the experiment (table S3).

That we only found significant selection on time spent on the ground on predator islands for females, but not males, suggests a greater effect from predatory lizards on females than on males. In support of this possibility, female mortality was higher on predator islands than on predator-free ones ($\chi^2 = 9.7$, $P = 0.002$), whereas for males there was no difference ($\chi^2 = 2.9$, $P = 0.086$; Fig. 3A). In addition, on predator islands, use of the ground was also lower in females than in males (11.9% versus 22.9%, respectively; $\chi^2 = 41.9$, $P < 0.001$; Fig. 3B). Because *A. sagrei* feeds primarily on the ground (*23*), the observed patterns of ground use suggest that females could be having more difficulties obtaining food resources on the predator islands. Indeed, 4 months after experimental translocation, females were in poorer body condition on predator islands than on predator-free islands ($P < 0.001$), a pattern not observed in males ($P = 0.68$) (fig. S3). Together, these results suggest that differences in habitat use between sexes influence natural selection on behavioral traits.

A long-standing debate in evolutionary biology concerns the association between behavioral and morphological evolution (*1*, *2*, *34*). Our study design allowed us to investigate whether selection on morphological traits occurs simultaneously with selection on behavioral traits and to assess whether selection on both phenotypic dimensions was correlated. Specifically, we tested a well-established morphological pattern in *Anolis* lizards: that the use of the ground or other broad surfaces favors longer limbs, which provide greater sprinting abilities [reviewed in (*23*)]. We found

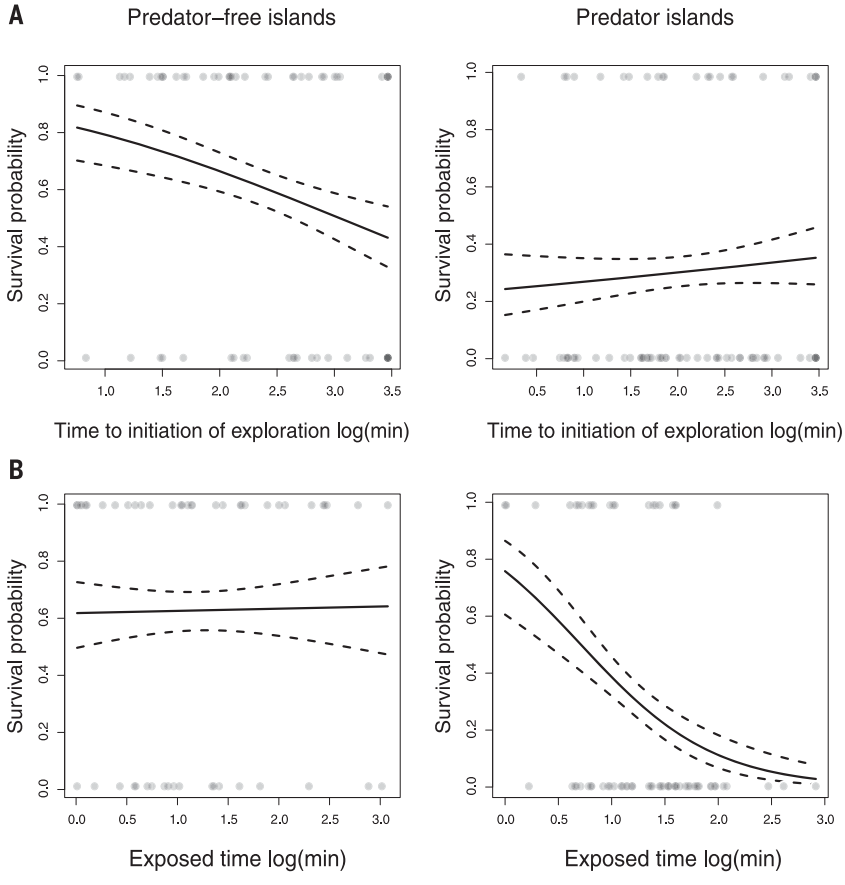

Fig. 2. Association between individual variation in behavior and survival of *A. sagrei* females after the 4-month experimental period. (**A** and **B**) Time to initiation of exploration in a new environment (A) and time exposed on the ground (B) are represented separately for predator-free versus predator islands. Solid lines represent the fitted model logistic regression; dashed lines denote 95% confidence intervals. Dots represent individual values for both survivors (dots at top of each panel) and nonsurvivors (dots at bottom of each panel); darker dots are indicative of several individuals having similar values. See table S4 for a representation of results pooling both sexes together.

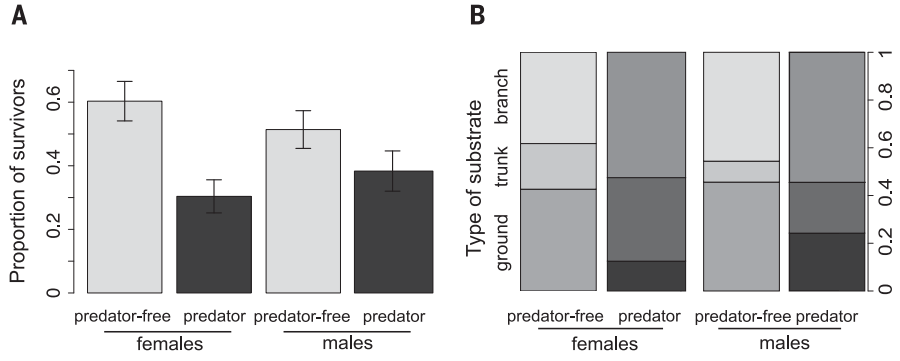

Fig. 3. Comparison of survival frequencies and habitat use between sexes and experimental treatments. (**A**) The proportion of females surviving was higher on predator-free islands than on predator islands, but this difference was marginally nonsignificant for males. Error bars indicate SEM. (**B**) Both sexes used the ground less on predator islands, but this difference was greater for females than for males.

Table 1. Best mixed-effects models describing female survival on the experimental islands.

		Estimate	SE	*z*	*P* value
	Predator-free islands (n = 63)				
	(Intercept)	2.82	1.05	2.7	0.007
Random effects	Island	0.18	0.423	0.43	0.669
Fixed effects	Time to initiation of exploration	–1.03	0.4	–2.55	0.011
	Relative hindlimb length	48.7	15.78	3.08	0.002
	Predator islands (n = 68)				
	(Intercept)	14.68	5.55	2.65	0.008
Random effects	Island	0	0	0	1
Fixed effects	Exposed time on ground	–1.27	0.61	–2.1	0.035
	Body size (SVL)	–0.34	0.14	–2.48	0.013

that females with longer hindlimbs relative to their body size survived better than shorter-limbed individuals on predator-free islands (P = 0.002; Table 1 and fig. S6). This is consistent with our observation that females used the ground more often on predator-free islands than on predator islands (Fig. 3B). On predator islands, relative hindlimb length did not affect survival (P = 0.26; fig. S6). We did not find selection on the relative hindlimb length for males (P > 0.80) in either experimental treatment. In addition, we found that on predator islands, smaller females survived better than larger females (P = 0.013; Table 1). Finally, selection on behavior and morphology was not correlated. For females from predator-free islands, selection for longer hindlimbs was independent of selection for increased exploratory behavior (shown by the lack of a significant interaction term in mixed models shown in Table 1). On predator islands, selection for smaller females was also independent of selection favoring individuals that spent less time exposed on the ground (Table 1). Overall, these results indicate that natural selection on behavior can occur simultaneously with, and independent of, selection on morphology.

Given that selection operated on both morphology and behavior, we asked which of these factors explained a higher proportion of the variation in mortality in females (no significant factors were detected in males). An analysis of the proportion of variation in mortality explained by behavior versus morphology (*26*) revealed that on predator-free islands, selection on hindlimb length explained 19.1% of the variation in mortality, whereas selection for more exploratory females accounted for 13.9%. Conversely, on predator islands, the proportion of variance in mortality explained by time exposed on the ground was 22.5%, whereas body size [snout-vent length (SVL)] accounted for 9.8%. These findings suggest that although both behavior and morphology can simultaneously contribute to survival, their importance is context-dependent and varies under different selective regimes.

Although behavior largely defines how animals interact with the environment, the evolutionary consequences of interindividual variation in behavior remain largely unknown (*7*, *8*). Our replicated field study provides evidence that natural selection operates differently on interindividual variation in behavior under different, experimentally manipulated selective pressures. Moreover, our results indicate that differences in habitat use between sexes likely influence the strength of natural selection on behavioral traits. By showing that selection can simultaneously and independently operate on behavior and morphology, we demonstrate that rapid environmental changes can shape different phenotypic dimensions at the same time; the evolutionary outcome of such selection will depend on the genetic basis of these traits and the extent to which they are correlated. Our results thus underscore the need to explicitly integrate interindividual variation in behavior as a relevant phenotypic dimension in studies of adaptation (*7*, *8*, *35*). Moreover, we found that under increased predation pressure, behavior is a more important factor explaining survival than the morphological traits that have been the subject of previous investigation (*22*); the extent to which these results can be generalized across species remains to be determined. Our results demonstrate that consistent behavioral variation among individuals can be an important focus of selection when populations experience novel environmental conditions—an increasingly common situation in the current context of global change.

REFERENCES AND NOTES

1. E. Mayr, *Animal Species and Evolution* (Harvard Univ. Press, 1963).
2. C. M. Bogert, *Evolution* **3**, 195–211 (1949).
3. R. B. Huey, P. E. Hertz, B. Sinervo, *Am. Nat.* **161**, 357–366 (2003).
4. D. Sol, D. G. Stirling, L. Lefebvre, *Evolution* **59**, 2669–2677 (2005).
5. O. Lapiedra, D. Sol, S. Carranza, J. M. Beaulieu, *Proc. R. Soc. B* **280**, 20122893 (2013).
6. M. M. Muñoz, J. B. Losos, *Am. Nat.* **191**, E15–E26 (2018).
7. S. R. X. Dall, S. C. Griffith, *Front. Ecol. Evol.* **2**, 1–7 (2014).
8. M. Wolf, F. J. Weissing, *Trends Ecol. Evol.* **27**, 452–461 (2012).
9. S. R. X. Dall, A. I. Houston, J. M. McNamara, *Ecol. Lett.* **7**, 734–739 (2004).
10. A. Sih, A. Bell, J. C. Johnson, *Trends Ecol. Evol.* **19**, 372–378 (2004).
11. D. Réale, S. M. Reader, D. Sol, P. T. McDougall, N. J. Dingemanse, *Biol. Rev. Camb. Philos. Soc.* **82**, 291–318 (2007).
12. A. M. Bell, S. J. Hankison, K. L. Laskowski, *Anim. Behav.* **77**, 771–783 (2009).
13. N. J. Dingemanse, C. Both, P. J. Drent, J. M. Tinbergen, *Proc. R. Soc. B* **271**, 847–852 (2004).
14. J. N. Pruitt, J. J. Stachowicz, A. Sih, *Am. Nat.* **179**, 217–227 (2012).
15. C. D. Santos *et al.*, *Sci. Rep.* **5**, 15490 (2015).
16. N. G. Ballew, G. G. Mittelbach, K. T. Scribner, *Am. Nat.* **189**, 396–406 (2017).
17. M. Wolf, G. S. van Doorn, O. Leimar, F. J. Weissing, *Nature* **447**, 581–584 (2007).
18. N. J. Dingemanse, M. Wolf, *Philos. Trans. R. Soc. B* **365**, 3947–3958 (2010).
19. D. Réale, N. J. Dingemanse, A. J. N. Kazem, J. Wright, *Philos. Trans. R. Soc. B* **365**, 3937–3946 (2010).
20. S. R. X. Dall, A. M. Bell, D. I. Bolnick, F. L. W. Ratnieks, *Ecol. Lett.* **15**, 1189–1198 (2012).
21. J. A. Endler, *Natural Selection in the Wild* (Princeton Univ. Press, 1986).
22. J. B. Losos, T. W. Schoener, D. A. Spiller, *Nature* **432**, 505–508 (2004).
23. J. B. Losos, *Lizards in an Evolutionary Tree: Ecology and Adaptive Radiation of Anoles* (Univ. of California Press, 2009).
24. T. W. Schoener, D. A. Spiller, J. B. Losos, *Nature* **412**, 183–186 (2001).
25. O. Lapiedra, Z. Chejanovski, J. J. Kolbe, *Glob. Change Biol.* **23**, 592–603 (2016).
26. See supplementary materials.
27. P. A. Bednekoff, S. L. Lima, *Proc. R. Soc. B* **271**, 1491–1496 (2004).
28. D. S. Wilson, A. B. Clark, K. Coleman, T. Dearstyne, *Trends Ecol. Evol.* **9**, 442–446 (1994).
29. M. Drakeley, O. Lapiedra, J. J. Kolbe, *PLOS ONE* **10**, e0138016 (2015).

30. M. López-Darias, T. W. Schoener, D. A. Spiller, J. B. Losos, *Ecology* **93**, 2512–2518 (2012).
31. D. S. Steinberg *et al*., *Proc. Natl. Acad. Sci. U.S.A.* **111**, 9187–9192 (2014).
32. J. J. Kolbe, M. Leal, T. W. Schoener, D. A. Spiller, J. B. Losos, *Science* **335**, 1086–1089 (2012).
33. T. W. Schoener, *Ecology* **49**, 704–726 (1968).
34. J. S. Wyles, J. G. Kunkel, A. C. Wilson, *Proc. Natl. Acad. Sci. U.S.A.* **80**, 4394–4397 (1983).
35. A. Sih, M. C. O. Ferrari, D. J. Harris, *Evol. Appl.* **4**, 367–387 (2011).

ACKNOWLEDGMENTS

We thank D. Fernández-Bellon and Q. Quach for field assistance; personnel from Friends of the Environment at Marsh Harbour; M. Melé, D. Spiller, and members of the Losos lab at Harvard University who provided valuable comments to improve the manuscript; personnel from the Museum of Comparative Zoology who helped to accession specimens; and the Bahamas Ministry of Agriculture and the Bahamas Environment, Science and Technology (BEST) Commission of the Ministry of the Environment for permission to conduct this research. **Funding:** Supported by the AGAUR in the form of Beatriu de Pinós postdoctoral fellowship 2014 BP-A 00116 (O.L.). Fieldwork was also funded with a Putnam Expedition Grant from the Museum of Comparative Zoology and a National Geographic Explorer Grant (O.L.) and funds from the University of Rhode Island. **Author contributions:** O.L. conceived the study; O.L., J.J.K., J.B.L., M.L., and T.W.S. designed the study; O.L. and J.J.K. collected the data; O.L. analyzed the data; and all authors extensively discussed results and contributed to manuscript preparation. **Competing interests:** The authors declare no competing interests. **Data and materials availability:** Data are available from the Dryad Digital Repository (doi:10.5061/dryad.9hn3dg7).

SUPPLEMENTARY MATERIALS

www.sciencemag.org/content/360/6392/1017/suppl/DC1
Materials and Methods
Figs. S1 to S9
Tables S1 to S5
References (*36*–*42*)

12 September 2017; accepted 23 April 2018
10.1126/science.aap9289

POLITICAL SCIENCE

The effect of partisanship and political advertising on close family ties

M. Keith Chen[1]*† and Ryne Rohla[2]*

Research on growing American political polarization and antipathy primarily studies public institutions and political processes, ignoring private effects, including strained family ties. Using anonymized smartphone-location data and precinct-level voting, we show that Thanksgiving dinners attended by residents from opposing-party precincts were 30 to 50 minutes shorter than same-party dinners. This decline from a mean of 257 minutes survives extensive spatial and demographic controls. Reductions in the duration of Thanksgiving dinner in 2016 tripled for travelers from media markets with heavy political advertising—an effect not observed in 2015—implying a relationship to election-related behavior. Effects appear asymmetric: Although fewer Democratic-precinct residents traveled in 2016 than in 2015, Republican-precinct residents shortened their Thanksgiving dinners by more minutes in response to political differences. Nationwide, 34 million hours of cross-partisan Thanksgiving dinner discourse were lost in 2016 owing to partisan effects.

American political partisanship has risen sharply over the past 25 years. More than 55% of Democrats and Republicans described "very unfavorable" feelings toward the opposing party in 2016, up from 17 to 21% in the mid-1990s; growing numbers of Independents express disfavor with both parties, and rising party defections increase polarization (*1*). Spatial partisan sorting produces increasingly homogeneous electoral "bubbles" at both state and local levels (*2*), and political minorities within these bubbles show reticence to participate in or reveal their party affiliation (*3*).

Animosity toward political rivals is not limited to the ballot box; implicit partisan biases manifest in discriminatory decisions even more frequently than racial or gender biases (*4*). Parents express intolerance of their children dating and marrying across partisan lines (*5*), and observed dating and marital choices segregate more strongly on politics than on physical attributes or personality characteristics (*6*). Political polarization affects decisions, such as where to work and shop, at higher rates than race, ethnicity, or religion (*7*).

We study whether politics strain close family ties by measuring family-gathering durations. After the historically divisive 2016 presidential election, 39% of American families avoided political conversations during the holidays, an aversion that spanned both party and socioeconomic lines (*8*). We examine Thanksgiving, which, in U.S. election years, may bring together family members with differing political views just weeks after votes are cast. Anecdotal evidence suggests that, in the wake of the 2016 election, many families canceled or otherwise cut short Thanksgiving plans with their most politically problematic relatives (*9*).

Several cognitive biases in social and political psychology explain why individuals might limit such interactions. A "partisan selective exposure" motivation occurs when individuals avoid counter-attitudinal political information that might engender cognitive dissonance or harm relationships (*10*). Numerous studies find "belief polarization," whereby individuals gravitate toward more extreme versions of their own initial positions during discussion of political issues (*11*). Exacerbating this effect, individuals also incorrectly expect others to respond to discussion and debate in the same direction as their own response, anticipating belief convergence rather than polarization (*12*), and attribute a lack of convergence to the bias and irrationality of others, while viewing themselves and copartisans as less ideological than cross-partisans (*13*). Our study examines whether these effects, which are well-studied in experimental settings among strangers, extend to close family gatherings.

We analyze how political differences affect the duration of Thanksgiving dinner by merging two datasets. Anonymized smartphone-location data from more than 10 million Americans allow observation of actual travel at extremely precise spatial and temporal levels. We combine this with a precinct-level database for the 2016 election to impute presidential voting at the finest spatial resolution possible. By comparing vote shares in an individual's home and Thanksgiving destination precincts, we test the relationship between political disagreement and time expenditure.

To isolate the particular effect of election-year political partisanship from a multitude of demographic and spatial confounds, we construct comparison sets of smartphone users that share the same home-destination pairs. Our measured effects are neither eliminated nor attenuated by comparing only matched users, suggesting that the measured time loss is not an artifact of politically correlated demographics or spatial sorting. Furthermore, because political advertising polarizes opinions (*14*) and heightens dislike for opposing parties (*15*), we compare partisan rifts between comparable users who fall just on opposite sides of media-market boundaries. Accounting for political advertising more than tripled our measured "Thanksgiving effect" in 2016, but not in 2015, before ads were run. This noneffect of yet-to-be-run ads acts as a political placebo test, further bolstering the argument that our measured Thanksgiving losses stem from political partisanship rather than from preexisting demographic or spatial confounds.

We collect precinct-level results for the 2016 presidential election through internet scraping and by contacting secretaries of state, boards of election, and individual county clerks via email, phone, or fax or in person. Finally, we match vote totals to precinct polygonal shapefiles using Geographic Information Systems (GIS) software. The resulting dataset covers 172,098 precincts across 99.9% of counties nationally (Fig. 1A).

Political advertising data are from Kantar Media's Campaign Media Analysis Group (*16*) and count every U.S. presidential television ad aired in all 210 Nielsen Designated Market Areas after 12 June 2016, including ads purchased directly by campaigns or outside groups such as political action committees. Data from the 2010 Decennial Census and the Census Bureau's 2012–2015 American Community Survey form the basis of demographic controls.

Location data rely on numerous smartphone apps and were aggregated by SafeGraph, a company that builds and maintains anonymized geospatial datasets for more than 10 million U.S. smartphones. These data consist of "pings," each identifying the coordinates of a particular smartphone at a moment in time. Our primary analysis includes 21 billion pings from November 2016 and 4.5 billion from November 2015.

To merge datasets, we infer the precinct and census block of each smartphone user's "home" on the basis of that user's pings between 1:00 a.m. and 4:00 a.m. over the 3 weeks before Thanksgiving. This procedure identifies more than 6 million approximate home locations in November 2016 (Fig. 1B), which we then link with precinct-level two-party vote shares and census demographics. Similarly, a user's Thanksgiving location is based on their modal location between 1:00 p.m. and 5:00 p.m. (24 November 2016 and 26 November 2015).

By construction, this sample is representative of the 77% of Americans who own smartphones, raising the question of whether our sample is politically representative of the American electorate as a whole. We test this by assigning to each resident a vote ratio proportional to the

[1]Anderson School of Management, University of California, Los Angeles, Los Angeles, CA 90095, USA. [2]School of Economic Sciences, Washington State University, Pullman, WA 99164, USA.
*These authors contributed equally to this work.
†Corresponding author. Email: keith.chen@anderson.ucla.edu

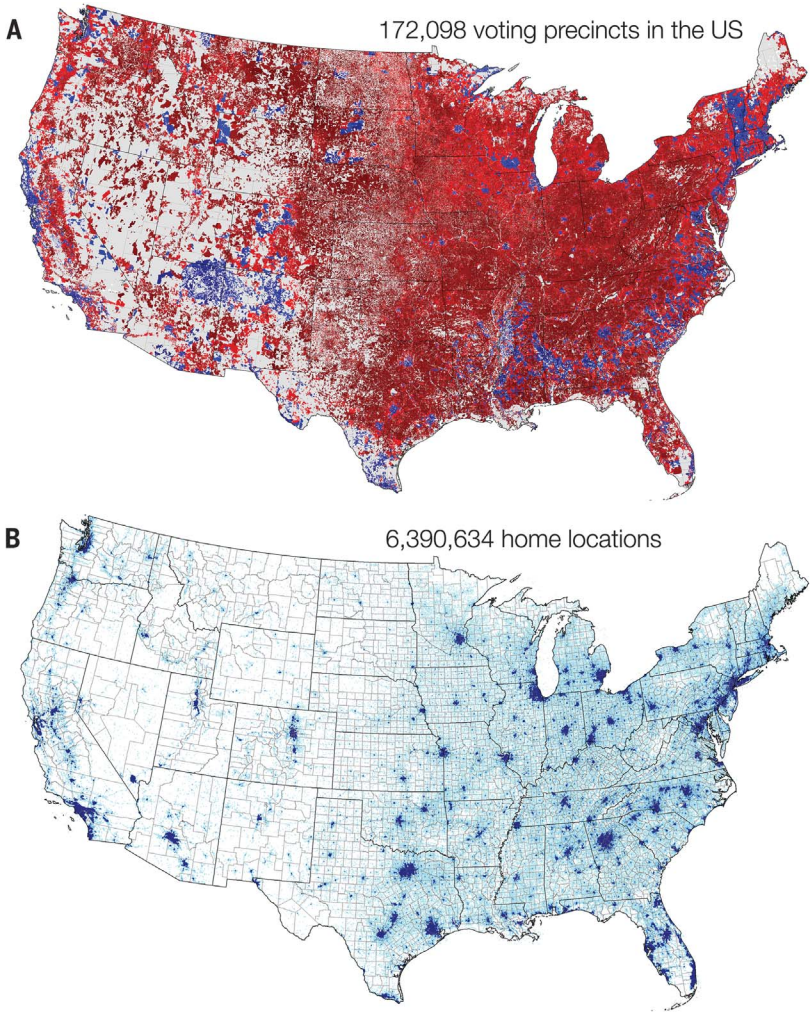

Fig. 1. Sampling and imputation validation. (**A**) Results of the 2016 U.S. presidential election by precinct (excludes unpopulated census blocks). (**B**) Home locations of smartphone users in the 2016 sample. (**C**) Correlation between actual two-party vote share by state and the District of Columbia (DC) (*x* axis) and predicted vote share (*y* axis) using each smartphone user's home precinct. Nationally, this predicts a 0.516 Clinton vote share, compared to an actual vote share of 0.511. Highlighted are the two most Democratic-leaning states (California and Massachusetts) and two most Republican-leaning states (Wyoming and West Virginia), as well as the states with the largest prediction error.

Table 1. Effect of political mismatch on Thanksgiving dinner duration. Each regression (column) estimates the effect of voting disagreement on 2016 Thanksgiving dinner duration. All results use linear regressions with fixed effects controlling for an individual's home location–cross–Thanksgiving destination. Stepwise regressions control for progressively finer pairs, culminating in a five-digit geohash, a square grid about 3 miles by 3 miles in size. The mean duration of Thanksgiving dinner was 257 min (SD = 162 min). The average probability of voting mismatch was 0.44 (SD = 0.10). Standard errors are reported in parentheses and clustered at the precinct-cross-precinct level. R^2, coefficient of determination. ***$P < 0.001$; **$P < 0.01$.

Independent variable	1	2	3	4
	Dependent variable: Duration of Thanksgiving dinner (min)			
Probability of political mismatch	−21.58***	−38.04***	−45.23**	−56.26**
	(2.226)	(2.952)	(8.696)	(14.55)
Observations	642,962	642,962	642,962	642,962
R^2	0.0003	0.0660	0.458	0.661
Fixed effects	None	County pairs	ZIP code pairs	Geohash-5 pairs
Number of fixed-effects groups	0	35,507	302,716	414,950

2016 two-party vote share of their home precinct. A resident of a precinct that recorded 150 Clinton and 50 Trump votes, for example, would be assigned 0.75 Clinton and 0.25 Trump votes. Figure 1C compares these votes against actual 2016 two-party vote shares for each state and Washington, D.C. The 45° line represents where states would lie if the SafeGraph sample politically matched the distribution of American voters. Our imputed votes are accurate to within 1 percentage point in 33 states and within 5 percentage points in all states. Nationally, the data suggest a two-party Democratic vote share of 0.516, compared to the actual share of 0.511.

We first examine whether, conditional on traveling for Thanksgiving dinner, the partisan distance between a home and destination affects that dinner's duration. We restrict our sample to residents who were home both in the morning and during the night of Thanksgiving, but who traveled for Thanksgiving dinner, to focus

Table 2. Asymmetric effects of political mismatch. Each regression (column) estimates the effect of voting disagreement between travelers and hosts [DPR traveler to RPR host (DPR→RPR) and RPR traveler to DPR host (RPR→DPR)] on 2016 Thanksgiving dinner duration. The *F*-test *P* value tests for equality between coefficients, to test for an asymmetric mismatch effect. The average probability of DPRs attending a RPR-hosted dinner and vice versa was 0.221 and 0.215, respectively (for both, SD = 0.10). Standard errors are reported in parentheses and clustered at the precinct-cross-precinct level. ***$P < 0.001$; **$P < 0.01$; *$P < 0.05$.

Independent variable	1	2	3	4
	Dependent variable: Duration of Thanksgiving dinner (min)			
Probability DPR→RPR	−5.60*	−23.44***	−30.16**	−44.53**
	(2.454)	(3.207)	(9.358)	(15.73)
Probability RPR→DPR	−38.74***	−53.47***	−60.23***	−69.20***
	(2.555)	(3.314)	(9.455)	(16.14)
F-test (RPR→DPR ≠ DPR→RPR)	0.0001	0.0001	0.0001	0.0572
Observations	642,962	642,962	642,962	642,962
R^2	0.0003	0.0662	0.458	0.661
Fixed effects	None	County pairs	ZIP code pairs	Geohash-5 pairs
Number of fixed-effects groups	0	35,507	302,716	414,950

Table 3. Political advertising heightens partisan effects. Each regression (column) estimates the effect of voting disagreement between travelers and hosts on 2016 Thanksgiving dinner duration. The second and fourth regressions explore whether political advertising heightens these effects. Media markets in swing states like Florida saw more than 26,000 ads in 2016. Standard errors are reported in parentheses and clustered at the precinct-cross-precinct level. A blank cell indicates that the variable was not included in this regression. ***$P < 0.001$; *$P < 0.05$.

Independent variable	1	2	3	4
	Dependent variable: Duration of Thanksgiving dinner (min)			
Probability of political mismatch	−21.58***	−14.40***		
	(2.226)	(2.588)		
Probability DPR→RPR			−5.604*	4.117
			(2.454)	(2.879)
Probability RPR→DPR			−38.74***	−33.68***
			(2.555)	(2.978)
Number of political ads		1.334***		1.349***
(1000 ads per market)		(0.185)		(0.185)
Probability of political mismatch		−2.645***		
times number of political ads		(0.393)		
Probability DPR→RPR times number				−3.237***
of political ads				(0.417)
Probability RPR→DPR times number				−2.122***
of political ads				(0.439)
Observations	642,962	642,962	642,962	642,962
R^2	0.0003	0.0004	0.0003	0.0004

our analysis on travelers who could control the duration of their visits. In Table 1, we estimate the following equation:

$$duration_{ij} = \alpha + \beta\ mismatch_{ij} + \gamma F_{ij} + \varepsilon_{ij}$$

where

$$mismatch_{ij} = P_i(1 - P_j) + (1 - P_i)P_j$$

In this specification, $duration_{ij}$ is the number of minutes traveler i spent with host j on Thanksgiving, F_{ij} is a set of fixed effects that form groups of people defined by pairs of home (i) and destination (j) locations, and β is the coefficient of interest. P_i and P_j are the two-party vote shares associated with home precincts for i and j, where $P_i = democratic_i/(democratic_i + republican_i)$. By using P_i and P_j, $mismatch_{ij}$ is the imputed probability that persons i and j voted for different candidates in 2016. In all tables, regressions control for progressively finer (i, j) location pairs, culminating in five-digit geohash (geohash-5) boxes, a global grid of rectangular areas, each about 3 miles by 3 miles in size.

To control for confounds including demographics, distance, and travel time, our regressions compare Thanksgiving dinner durations between travelers with the same home and destination areas. For example, regression 3 compares two travelers if and only if they both live in ZIP code X and visit ZIP code Y. The coefficient of interest β measures the reduction in Thanksgiving dinner duration between travelers within the same F_{ij} comparison groups but who likely voted differently than their Thanksgiving hosts. Standard errors are clustered at the home precinct–cross–destination precinct level. We use progressively tighter spatial controls to control for both demographics and travel distance simultaneously.

The results in Table 1 indicate that families that were likely to have voted for different presidential candidates spent about 30 to 50 fewer minutes together—subtracted from an average Thanksgiving dinner time of 4.2 hours—after controlling for both travel distance and location-correlated demographics. As we add finer spatial controls, our estimate of β remains fairly stable, with a point estimate of 56.3 ± 14.6 min under our tightest geohash-5 controls. In table S4, we report qualitatively identical results when demographics such as race, age, education, income, and employment are controlled for separately.

We examine the two components of $mismatch_{ij}$, $P_i(1 - P_j)$ and $(1 - P_i)P_j$, to separately measure the effect of voting disagreement among Democratic-precinct residents (DPRs) visiting Republican-precinct residents (RPRs) and vice versa. Table 2 demonstrates that, conditional on traveling, DPRs shortened their visits to RPR hosts by about 20 to 40 min, whereas RPRs shortened their visits to DPRs by about 50 to 70 min. *F*-test results indicate that these estimates are statistically different ($P < 0.0001$ in four of five specifications), with RPRs shortening their cross-party stays by more minutes than DPRs.

When investigating whether these effects interact with local political advertising, we find that cross-partisan Thanksgiving dinners are further shortened by around 2.6 min on average for every 1000 political advertisements aired in the traveler's home media market (Table 3). Some media markets in swing states saw more than 26,000 ads over the course of the campaign, implying a 69-min-shorter Thanksgiving dinner for vote-mismatched families in Orlando, for example, compared to those in markets without advertising. Although this effect may not be solely due to advertising, which may be correlated with other campaign activities such as rallies, campaign visits, and fundraising efforts, these results bolster the conclusion that measured effects on Thanksgiving dinner duration likely stem from an increased intensity and salience of partisan differences.

The results in table S1 support this finding and report the results of a placebo test concerning whether advertisements in 2016 affected Thanksgiving dinner behavior the year before

airing. Regardless of whether we pool smartphone users or split the sample into DPRs and RPRs, we find no evidence of preexisting partisan effects in regions that witnessed high advertising levels. Although our empirical results estimate briefer Thanksgiving dinners among cross-partisan gatherings in both years, the ad-related amplification of this effect is present only in 2016, both in statistical significance and magnitude, supporting our conjecture that the main effect is most likely political in nature.

An examination of destination choices suggests that travelers did not change plans to reduce political divisions from 2015 to 2016. Among travelers who traveled in both years—the strongest possible control for demographic and spatial confounds—we observe no appreciable difference in the distribution of likely political mismatch (fig. S1). This finding suggests that travelers were more likely to change the duration of Thanksgiving gatherings than to change the destination.

Finally, tables S2 and S3 estimate linear probability models for the choice of whether to travel for Thanksgiving, in both 2015 and 2016. When matched residents living within 1.5 miles of each other are compared, DPRs reduced their likelihood of travel between 2015 and 2016 by 2 percentage points more than comparable RPRs, an effect that increases substantially in areas with heavy political advertising.

Examining only those residents included in both the 2015 and 2016 data yields qualitatively similar results. Among residents at home on Thanksgiving morning in both years, 56.4% traveled for Thanksgiving in 2015, whereas 51.9% traveled in 2016 (n = 28,890; Fisher's exact text, $P < 0.0005$). Accompanying this difference is a reduction in Thanksgiving dinner duration for those cross-partisan dinners that still occurred. By comparing travelers who went to the same location both years (n = 1271), we estimate that politically mismatched gatherings declined by 42.1 ± 41.4 min. Although this small sample size precludes statistical significance, this estimate is very close to our findings shown in Table 1.

By aggregating across the 77% of American adults who own smartphones (*17*), our results suggest that partisan differences cost Americans 73.6 million hours of Thanksgiving time with others in 2016, 47.8% from DPRs and 52.2% from RPRs. Political advertising–related partisanship comprised 15.9 million of lost person-hours, 46.3% from DPRs and 53.7% from RPRs. Altogether, an estimated 33.9 million person-hours of cross-partisan discourse were eliminated, perhaps creating a feedback mechanism by which partisan segregation reduces opportunities for close cross-party conversations.

Our findings have several implications, both for the literature and for campaign policy. After the 2016 election, anecdotal media reports and online social-media behavior (*18*) demonstrated an avoidance of personal confrontations over political issues among Democratic voters, findings our study corroborates. RPRs, however, were more sensitive to partisan differences at Thanksgiving dinners, an effect that supports findings of greater partisan-selective exposure among Republicans in news-media consumption (*19*). Our results suggest that partisan polarization extends in quantitatively meaningful ways to close family settings and that political advertising and related campaign efforts can exacerbate these fissures. As abbreviated Thanksgiving gatherings tend to accumulate in regions with greater campaign activity, policies designed to shorten campaigns may reduce the private costs of political polarization.

REFERENCES AND NOTES

1. Pew Research Center, "Partisanship and political animosity in 2016," 22 June 2016; http://people-press.org/2016/06/22/partisanship-and-political-animosity-in-2016.
2. M. Motyl, R. Iyer, S. Oishi, S. Trawalter, B. Nosek, *J. Exp. Soc. Psychol.* **51**, 1–14 (2014).
3. R. Perez-Truglia, G. Cruces, *J. Polit. Econ.* **125**, 1208–1243 (2017).
4. S. Iyengar, S. Westwood, *Am. J. Pol. Sci.* **59**, 690–707 (2015).
5. S. Iyengar, G. Sood, Y. Lelkes, *Public Opin. Q.* **76**, 405–431 (2012).
6. J. Alford, P. Hatemi, J. Hibbing, N. Martin, L. Eaves, *J. Polit.* **73**, 362–379 (2011).
7. C. McConnell, Y. Margalit, N. Malhotra, M. Levendusky, *Am. J. Pol. Sci.* **61**, 5–18 (2017).
8. B. Oliphant, S. Smith, "How Americans are talking about Trump's election in 6 charts," Pew Research Center, 22 December 2016; www.pewresearch.org/fact-tank/2016/12/22/how-americans-are-talking-about-trumps-election-in-6-charts/.
9. S. Tavernise, K. Seelye, "Political divide splits relationships—and Thanksgiving, too," *The New York Times*, 15 November 2016; www.nytimes.com/2016/11/16/us/political-divide-splits-relationships-and-thanksgiving-too.html.
10. J. Frimer, L. Skitka, M. Motyl, *J. Exp. Soc. Psychol.* **72**, 1–12 (2017).
11. C. Sunstein, *J. Polit. Philos.* **10**, 175–195 (2002).
12. L. Ross, D. Greene, P. House, *J. Exp. Soc. Psychol.* **13**, 279–301 (1977).
13. R. Robinson, D. Keltner, A. Ward, L. Ross, *J. Pers. Soc. Psychol.* **68**, 404–417 (1995).
14. S. Ansolabenhere, S. Iyengar, *Going Negative: How Political Advertisements Shrink and Polarize the Electorate* (Free Press, 1996).
15. M. Levendusky, N. Malhotra, *Polit. Commun.* **33**, 283–301 (2016).
16. C. Zubak-Skees, "Tracking TV ads in the 2016 presidential race," The Center for Public Integrity, 25 October 2016; http://publicintegrity.org/2016/01/21/19164/tracking-tv-ads-2016-presidential-race.
17. L. Rainie, A. Perrin, "10 facts about smartphones as the iPhone turns 10," Pew Research Center, 28 June 2017; www.pewresearch.org/fact-tank/2017/06/28/10-facts-about-smartphones/.
18. E. Bakshy, S. Messing, L. A. Adamic, *Science* **348**, 1130–1132 (2015).
19. C. Rodriguez, J. Moskowitz, R. Salem, P. Ditto, *Transl. Issues Psychol. Sci.* **3**, 254–271 (2017).

ACKNOWLEDGMENTS

The authors thank seminar participants at UCLA, Washington State, Northwestern, Simon Fraser, and Stanford Universities, as well as E. Long, for helpful comments and A. Hoffman, R. Squire, and N. Yonack at SafeGraph for data access and technical assistance. **Funding:** There are no funding sources related to this study. **Author contributions:** M.K.C. and R.R. designed and implemented the study, acquired the data, and drafted and revised the manuscript. **Competing interests:** The authors declare no competing interests. **Data and materials availability:** All data and code are available at www.anderson.ucla.edu/faculty/keith.chen/datafilm.htm.

SUPPLEMENTARY MATERIALS

www.sciencemag.org/content/360/6392/1020/suppl/DC1
Fig. S1
Tables S1 to S4
References

5 October 2017; accepted 23 April 2018
10.1126/science.aaq1433

HUMAN EVOLUTION

Ancient human parallel lineages within North America contributed to a coastal expansion

C. L. Scheib,[1,2]* Hongjie Li,[3] Tariq Desai,[4] Vivian Link,[5] Christopher Kendall,[6] Genevieve Dewar,[6] Peter William Griffith,[1] Alexander Mörseburg,[1] John R. Johnson,[7] Amiee Potter,[8,9] Susan L. Kerr,[10] Phillip Endicott,[11] John Lindo,[12] Marc Haber,[13] Yali Xue,[13] Chris Tyler-Smith,[13] Manjinder S. Sandhu,[13] Joseph G. Lorenz,[14] Tori D. Randall,[15] Zuzana Faltyskova,[1] Luca Pagani,[2,16] Petr Danecek,[13] Tamsin C. O'Connell,[1] Patricia Martz,[17] Alan S. Boraas,[18] Brian F. Byrd,[19] Alan Leventhal,[20,21] Rosemary Cambra,[20] Ronald Williamson,[22] Louis Lesage,[23] Brian Holguin,[24] Ernestine Ygnacio-De Soto,[25] JohnTommy Rosas,[26] Mait Metspalu,[2] Jay T. Stock,[1,27] Andrea Manica,[28] Aylwyn Scally,[4] Daniel Wegmann,[5] Ripan S. Malhi,[3]* Toomas Kivisild[1,2]*

Little is known regarding the first people to enter the Americas and their genetic legacy. Genomic analysis of the oldest human remains from the Americas showed a direct relationship between a Clovis-related ancestral population and all modern Central and South Americans as well as a deep split separating them from North Americans in Canada. We present 91 ancient human genomes from California and Southwestern Ontario and demonstrate the existence of two distinct ancestries in North America, which possibly split south of the ice sheets. A contribution from both of these ancestral populations is found in all modern Central and South Americans. The proportions of these two ancestries in ancient and modern populations are consistent with a coastal dispersal and multiple admixture events.

An increasing body of archaeological (*1*–*3*) evidence shows that the initial peopling of the Americas occurred at least a few thousand years prior to the spread of the Clovis cultural complex ~13,000 years ago (all dates are calibrated) (*4*), with a majority of well-supported Pre-Clovis sites clustered in coastal areas and around glacial edges (*1*, *3*, *5*). Studies of ancient and modern genomes have uncovered four distinct ancestry components within the Americas arriving in three hypothesized waves: the most recent Thule-related Neo-Eskimo ~2000 years ago, the Saqqaq/Dorset Paleo-Eskimo ~4500 years ago (both restricted to the Arctic region), and a "First American" dispersal prior to 13,000 years ago that split within North America into a northern and a southern branch (*6*–*10*). The northern branch is ancestral to populations including Algonquian, Na-Dené, Salishan, and Tsimshian speakers from Canada (NAM), whereas the southern branch includes the ancestors of the Clovis individual (Anzick-1) and all Mexicans, Central Americans (CAM), and South Americans (SAM) (*9*–*12*). Within the southern branch there is some localized evidence of early population structure, as a few modern Amazonian populations show an excess genetic affinity to Australasians (*13*, *14*). The second oldest North American genome, The Ancient One (Kennewick Man, 8700 to 8400 years ago), is likely to have derived from the ancestral northern branch but is a poor proxy for modeling this ancestry, given its low sequencing depth (*10*).

Here, we investigated the ancestral relationship between the northern (NAM) and southern (Mexico, CAM, and SAM) branch populations. To do so, we sequenced 91 ancient whole genomes from North America, mainly from two geographic areas: the California Channel Islands in the west and Southwestern Ontario in the east, near modern Algonquian-speaking populations (Fig. 1A and table S1) (*15*). Both of these areas show evidence of occupation from at least 13,000 years ago (*5*, *16*) and are geographically located south of the known distribution of the ancient Neo- and Paleo-Eskimo dispersals (*6*). We radiocarbon-dated 27 individuals (table S2) (*15*) to between ~4800 and ~200 years ago and sequenced all genomes to an average depth of 0.007 to 13.6× (tables S1, S3, and S4) (*15*). Mitochondrial DNA (mtDNA) haplotypes were recovered from all samples (tables S1 and S5) (*15*) and Y chromosome haplotypes from 34 of the male individuals (fig. S1 and data S1) (*15*). In addition, a set of modern whole mitochondrial genomes (n = 45) were resequenced from a previous study to explore sex-specific migration patterns on the west coast of Southern California (tables S3 and S5) (*15*, *17*).

All ancient Native American individuals clustered with modern Native Americans on a worldwide principal components analysis (PCA) (Fig. 1B) (*15*, *18*). In a regional plot that includes Siberians, the northern and southern branches show clear distinction (Fig. 1B, inset). Ancient Californians cluster alongside southern branch populations near to Anzick-1, whereas the ancient Southwestern Ontario (ASO) population clusters with modern Algonquian speaking populations and The Ancient One (Fig. 1B). Modern and ancient Athabaskans map between ASO and Northeast Siberian populations (Chukchi/Koryak) (Fig. 1B). The Upper Sun River individuals (USR1 and USR2) map near to Shuká Kää, between Central Siberians and the northern branch populations (Fig. 1B).

Both PCA and ADMIXTURE (*19*) analysis of the ancient genomes within the context of a worldwide panel (Fig. 1, B and C, fig. S2, and data S2) (*15*) indicate that, relative to the ASO, extant NAM as well as ancient Pacific Northwest Coast (PNWC) and ancient Northern Athabaskans have up to 50% more Arctic-related ancestry, prominent in Greenland Inuits and also found in Siberian Eskimos (Fig. 1C) (*15*). These differences are further confirmed by significant Z ($Z > 3$) scores for D-statistics D(Mbuti,SiberianPop;Mixe, TestPop) (*20*) and f_3-statistics f(ASO,TestPop; Mbuti) (*21*, *22*) (table S6 and data S3) (*15*). We found no significant evidence of gene flow into the ASO from any non-American population (table S7 and data S3) (*15*).

All ancient Californian genomes clustered together with southern branch (Anzick-1, Mexico, CAM, SAM) populations on the regional PCA (Fig. 1B) (*15*). As suggested by the archaeological and osteological evidence (*23*–*25*), radiocarbon-dated individuals from San Nicolas Island from early (ESN) and late (LSN) periods (Fig. 1D)

[1]Department of Archaeology, University of Cambridge, Cambridge CB2 3DZ, UK. [2]Estonian Biocentre, Institute of Genomics, University of Tartu, Tartu 51010, Estonia. [3]Department of Anthropology and Carl R. Woese Institute for Genomic Biology, University of Illinois at Urbana-Champaign, Urbana, IL 61801, USA. [4]Department of Genetics, University of Cambridge, Cambridge CB2 3EH, UK. [5]Department of Biology, Université de Fribourg, Fribourg, Switzerland. [6]Department of Anthropology, University of Toronto, Toronto, Ontario M5S 2S2, Canada. [7]Santa Barbara Museum of Natural History, Santa Barbara, CA 93105, USA. [8]Department of Anthropology, Portland State University, Portland, OR 97232, USA. [9]Knight Diagnostics Laboratory, Oregon Health & Science University, Portland, OR 97239, USA. [10]Department of Anthropology, Modesto Junior College, Modesto, CA 95350, USA. [11]Department Hommes Natures Societies, Musée de l'Homme, Paris 75016, France. [12]Department of Anthropology, Emory University, Atlanta, GA 30322, USA. [13]Wellcome Sanger Institute, Wellcome Genome Campus, Hinxton CB10 1SA, UK. [14]Department of Anthropology and Museum Studies, Central Washington University, Ellensburg, WA 98926, USA. [15]Department of Anthropology, San Diego City College, San Diego, CA 92101, USA. [16]APE Lab, Department of Biology, University of Padova, Padova, Italy. [17]Department of Anthropology, California State University, Los Angeles, CA 90032, USA. [18]Kenai Peninsula College, Soldotna, AK 99669, USA. [19]Far Western Anthropological Research Group Inc., Davis, CA 95618, USA. [20]Muwekma Ohlone Tribe of the San Francisco Bay Area, P.O. Box 360791, Milpitas, CA 95036, USA. [21]Department of Anthropology, San Jose State University, San Jose, CA 95192, USA. [22]Archaeological Services Inc., Toronto, Canada. [23]Huron-Wendat Nation, Canada. [24]Department of Anthropology, University of California, Los Angeles, CA 90095, USA. [25]Barbareño Chumash, California Indian Advisory Committee, Santa Barbara Museum of Natural History, Santa Barbara, CA 93105, USA. [26]Tongva Nation, CA, USA. [27]Department of Anthropology, University of Western Ontario, London, Ontario N6A 3K7, Canada. [28]Department of Zoology, University of Cambridge, Cambridge CB2 3EJ, UK.
*Corresponding author. Email: cls83@ut.ee (C.L.S.); tk331@cam.ac.uk (T.K.); malhi@illinois.edu (R.S.M.)

clustered into two distinct genetic populations in both the autosomal and uniparental markers with evidence of 11% autosomal continuity between the early and late populations (Fig. 1E) (*15*). The genome-wide diversity estimates (*26*) of the earliest-dated LSN individuals are greater than those of the ESN individuals (fig. S3) (*15*), which is consistent with higher effective population sizes in the LSN source population and/or recent admixture. Outgroup f_3(Test,X;Mbuti) and D(Mbuti,Test;Mixe,X) tests show that the ESN shares more drift with SAM ($Z > 3$) than with geographically proximal populations (data S3) (*15*), which suggests that the ESN is related to a population that expanded into South America.

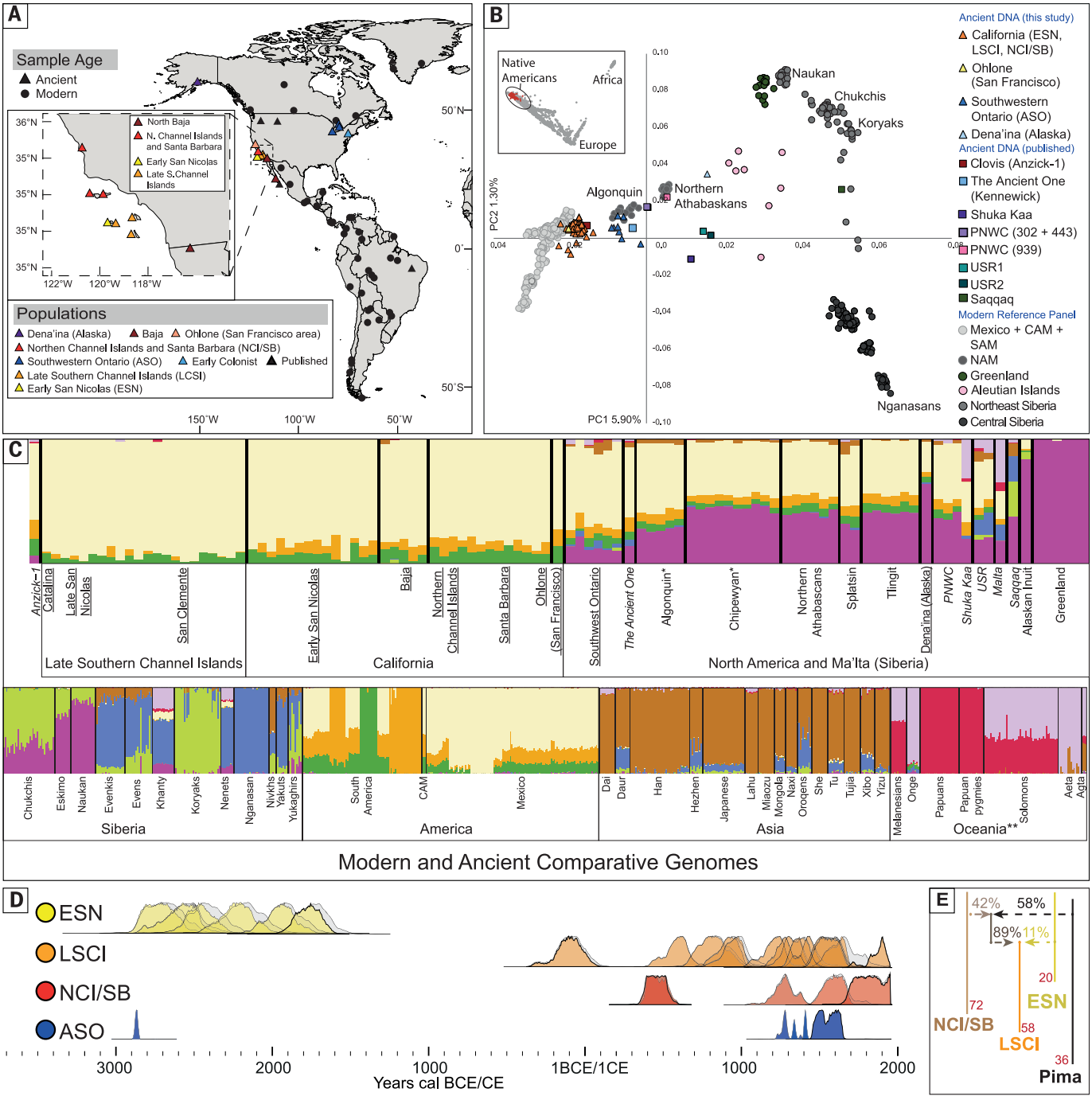

Fig. 1. Ancient individuals, population genetic analyses and modeling. (**A**) Sites of newly sequenced ancient individuals are designated by colored triangles. Comparative modern populations and ancient individuals are designated by black circles and triangles, respectively. (**B**) PCA with ancient individuals projected onto modern Native American and Siberian variation. Inset: Ancient genomes projected onto modern worldwide data. (**C**) Visualization of model-based ancestry analysis at fivefold cross-validation–supported $K = 9$ ancestral components (*15*). Underlines denote new and ancient genomes; italics, published ancient genomes; single asterisks, masked data; double asterisks, Oceanian populations including Onge, Aeta, and Agta (*15*). (**D**) Probability area of radiocarbon dates grouped by population and calibrated with IntCal13 (colored area) and Marine13 (light gray area) (*28*) where appropriate (*15*). (**E**) A model that explains genetic diversity in the Late Southern Channel Island populations through three-way admixture.

By contrast, the LSN population shares more drift and alleles with geographically proximal populations ($Z > 3$) (data S3) (*15*).

We modeled the population history of the Americas using qpGraph (*15*, *21*) and found that the ASO and Mexican (Pima) populations were consistently outgroups to sets of clades formed by Anzick-1, SAM (Surui), and ESN populations in analyses that did not involve admixture (fig. S4) (*15*, *21*). Fit between the data and the tree could be significantly improved when modeling ancient Californian, modern Pima, and Surui populations through admixture of two basal ancestries that we call ANC-A and ANC-B (Fig. 2A) (*15*). The ESN, Northern Channel Islands and Santa Barbara (NCI/SB), and Surui populations share similar proportions of both components, while the Pima have a higher ANC-B component (Fig. 2A) (*15*). We used qpGraph to estimate the ANC-B contribution in modern CAM and SAM populations and found it to vary within a range of 42 to 71% (average 53%; table S8) (*15*). In SAM populations, the lower end of the spectrum of contributions of ANC-B are found in the Amazonian Equatorial Tucanoan-speaking groups (including Surui) (40 to 53%) and the highest in the Andeans (50 to 71%) (Fig. 2B and table S8) (*15*), particularly in the Chilote and Huilliche (~70%) from locations overlapping the Monte Verde site (~18,500 to 14,500 years ago) (Fig. 2B).

The clear separation of ANC-A and ANC-B ancestries is further supported by the sharing of unambiguous, derived haplotype segments in modern Surui and Pima populations (*27*) with both the ASO (CK-13) and Anzick-1 individuals (fig. S5) (*15*). The results of this analysis are consistent with ancient substructure and a separation of at least a few thousand years between the ANC-A and ANC-B populations prior to merging (fig. S6) (*15*). The summary of evidence presented here allows us to reject models of a panmictic "first wave" population from which the ASO

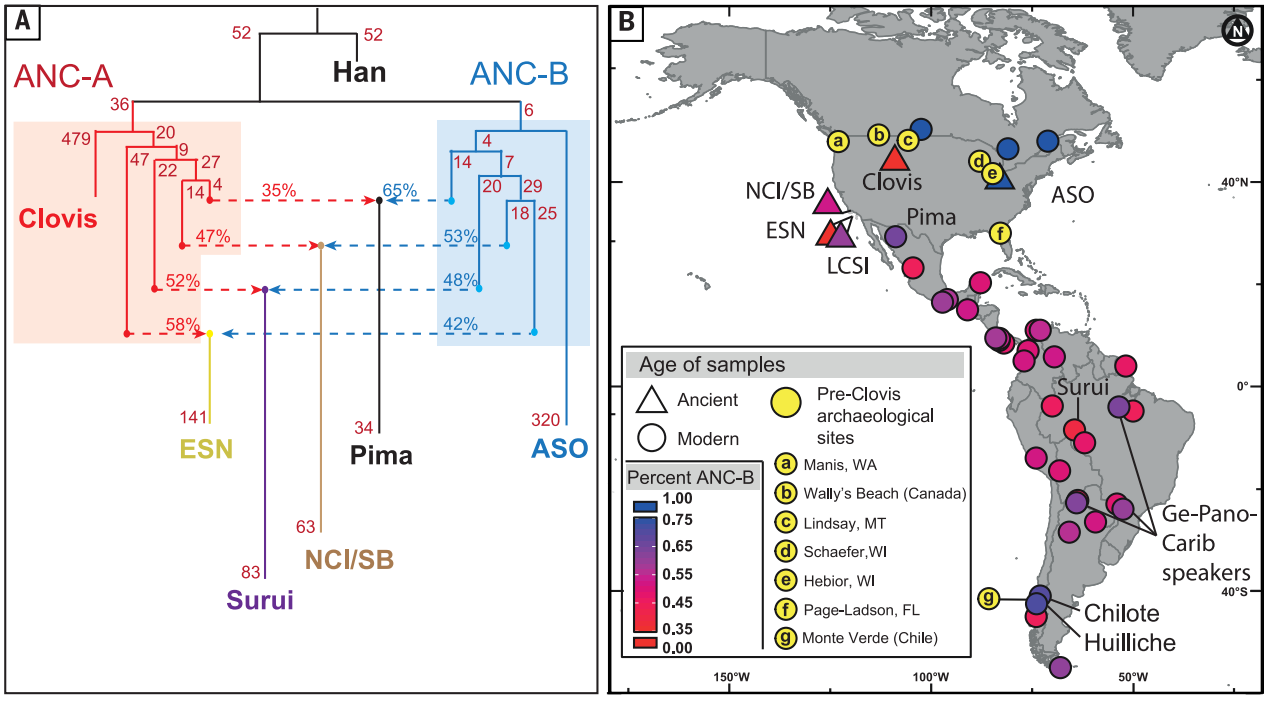

Fig. 2. Visual model of ancestry components and distribution of proportions in the Americas. (**A**) A model with four admixture events that offers a good fit to the data ($Z = 0.888$) (*15*). (**B**) Scale of ANC-B ancestry from 0% in Anzick-1 to 100% in the ASO and modern Algonquian-speaking populations.

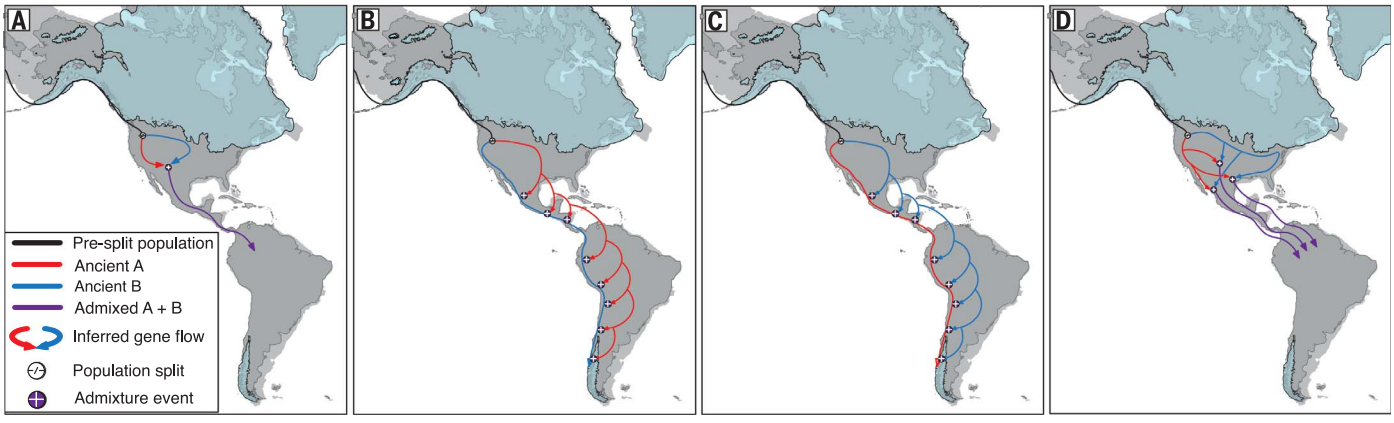

Fig. 3. Dispersal models that are consistent with the results of this study. Red and blue indicate ANC-A and ANC-B, respectively; symbols denote admixture event(s). Locations of admixture events are hypothetical. (**A**) A model with one admixture event in North America. (**B**) A model in which an ANC-B population first reached South America, followed by an ANC-A population with multiple admixture events. (**C**) The same model as (B), but reversing the populations. (**D**) A model with multiple admixture events and dispersals.

diverged after the peopling of South America or in which solely the ANC-A population contributed to modern southern branch populations. Because populations vary in ANC-A and ANC-B proportions but do not differ significantly in their affinity to non-American populations (table S7) (*15*), it is possible that ANC-A and ANC-B split within America as opposed to Beringia where there would have been ongoing gene flow with Siberia.

Four possible models can explain the contribution of both branches to CAM and SAM populations: (i) an admixture event in North America prior to the peopling of South America (Fig. 3A); (ii) ANC-B–related ancestral population(s) dispersing into South America first, followed by a dispersal of ANC-A–related population(s) and admixture of the two branches occurring in South America (Fig. 3B); (iii) ANC-A–related ancestral population(s) dispersing into South America first, followed by a dispersal of ANC-B–related population(s) and admixture of the two branches occurring in South America (Fig. 3C); and (iv) multiple admixture events occurring in North America, with multiple dispersals into South America (Fig. 3D). Additional ancient DNA from terminal Pleistocene human remains within the Americas is needed to determine which model best describes the sequence of events constituting the complex population history of the Americas.

REFERENCES AND NOTES

1. T. Goebel, M. R. Waters, D. H. O'Rourke, *Science* **319**, 1497–1502 (2008).
2. M. R. Waters *et al.*, *Science* **331**, 1599–1603 (2011).
3. T. D. Dillehay *et al.*, *PLOS ONE* **10**, e0141923 (2015).
4. M. R. Waters, T. W. Stafford Jr., *Science* **315**, 1122–1126 (2007).
5. M. R. Waters, T. W. Stafford Jr., B. Kooyman, L. V. Hills, *Proc. Natl. Acad. Sci. U.S.A.* **112**, 4263–4267 (2015).
6. M. Raghavan *et al.*, *Science* **345**, 1255832 (2014).
7. D. Reich *et al.*, *Nature* **488**, 370–374 (2012).
8. M. Rasmussen *et al.*, *Nature* **463**, 757–762 (2010).
9. M. Rasmussen *et al.*, *Nature* **506**, 225–229 (2014).
10. M. Rasmussen *et al.*, *Nature* **523**, 455–458 (2015).
11. J. Lindo *et al.*, *Proc. Natl. Acad. Sci. U.S.A.* **114**, 4093–4098 (2017).
12. P. Verdu *et al.*, *PLOS Genet.* **10**, e1004530 (2014).
13. M. Raghavan *et al.*, *Science* **349**, aab3884 (2015).
14. P. Skoglund *et al.*, *Nature* **525**, 104–108 (2015).
15. See supplementary materials.
16. J. R. Johnson, T. W. Stafford Jr., H. O. Ajie, D. P. Morris, in *Proceedings of the Fifth California Islands Symposium* (Santa Barbara Museum of Natural History, 2002), pp. 541–545.
17. J. R. Johnson, J. G. Lorenz, *J. Calif. Gt. Basin Anthropol.* **26**, 33–64 (2006).
18. N. Patterson, A. L. Price, D. Reich, *PLOS Genet.* **2**, e190 (2006).
19. D. H. Alexander, J. Novembre, K. Lange, *Genome Res.* **19**, 1655–1664 (2009).
20. R. E. Green *et al.*, *Science* **328**, 710–722 (2010).
21. N. Patterson *et al.*, *Genetics* **192**, 1065–1093 (2012).
22. D. Reich, K. Thangaraj, N. Patterson, A. L. Price, L. Singh, *Nature* **461**, 489–494 (2009).
23. J. A. Ezzo, "The Ancient Mariners of San Nicolas Island: A Bioarchaeological Analysis of the Burial Collections" (Tech. Rep. 01-64, Statistical Research Inc., Tucson, 2002).
24. S. L. Kerr, G. M. Hawley, in *Fifth California Islands Symposium*, D. R. Browne, K. L. Mitchell, H. W. Chaney, Eds. (Santa Barbara Museum of Natural History, 1999), pp. 546–554.
25. P. Martz, in *Proceedings of the Sixth California Islands Symposium* (Santa Barbara Museum of Natural History, 2008), pp. 65–82.
26. A. Kousathanas *et al.*, *Genetics* **205**, 317–332 (2017).
27. S. Mallick *et al.*, *Nature* **538**, 201–206 (2016).
28. P. Reimer *et al.*, *Radiocarbon* **55**, 1869–1887 (2013).

ACKNOWLEDGMENTS

We thank T. Biers, D. Bolnick, and M. Schillaci for providing NAGPRA-related counsel and tribal contacts; the Most Likely Descendant (MLD) appointed by the California Native American Heritage Commission for granting permission to test the tooth from the Carpinteria burial; A. (S.) Lindgren for her support and facilitating the partnership with the Kenaitze Tribe; and H. Schroeder for providing reagents and guidance for mtDNA target capture. **Funding:** Supported by European Research Council Starting Investigator grant FP7-261213 (T.K.); Natural Environment Research Council (NERC) Radiocarbon Facility grant NF/2016/1/6 (T.K. and C.L.S.); the Economic and Social Research Council Impact Accelerator Award RG76702 (C.L.S.); NSF grants BCS-1518026 and SMA-1620239 (R.S.M.); European Research Council Consolidator Grant FP7-617627 (J.T.S.); Wellcome grant 098051 (M.H., Y.X., C.T.-S., M.S.S., and P.D.); the European Union through European Regional Development Fund project no. 2014-2020.4.01.16-0024, MOBTT53 (L.P.); and European Research Council Consolidator Grant 647787 "Local Adaptation" (A.Ma.). **Author contributions:** C.L.S., T.K., and J.S. conceived the study; Z.F. contributed to the conception of the study and provided protocols/reagents/training necessary for extraction and analysis; T.R., P.E., S.L.K., J.R.J., A.P., and G.D. provided samples; R.S.M. provided data processed by H.L. and J.L.; C.L.S. and C.K. extracted the Lucier samples; C.L.S. extracted other samples; C.L.S., T.K., V.L., L.P., A.Mö., P.D., D.W., T.O.C., T.D., and G.D. analyzed data; J.R.J. and R.S.M. facilitated communication with indigenous representatives; A.S.B., A.S.L., B.F.B., A.L., R.C., R.W., L.L., J.R., B.E.H., and E.Y.-D.S. facilitated discussions with indigenous community members and tribal governments; P.W.G. made the figures; M.M. provided access to data; C.L.S., D.W., C.T.-S., Y.X., M.H., B.E.H., P.M., L.P., T.K., A.S., and A.Ma. contributed to interpretation of results; and C.L.S. and T.K. wrote the manuscript. **Competing interests:** The authors declare no competing financial interests. **Data and materials availability:** All data needed to evaluate the conclusions are present in the manuscript or supplementary materials. Genomic data used in this paper are publicly available. Scripts for calculating haplotype matching segments were written by T.D. and are available at https://github.com/td329/NA-hapmatch-2018. **Accession numbers:** Sequence data were deposited in the European Nucleotide Archive under accession PRJEB25445. **Ethics statement:** Human remains analyzed for this study from the Palm Site, Sii Túupentak, and the Teston Road and Turnbull Ossuaries were transferred to R.S.M. for destructive analysis by representatives of the Kenaitze, Muwekma Ohlone, and Huron-Wendat tribes, respectively. R.S.M. has visited the Kenaitze and the Muwekma Ohlone regularly and has formed mutually beneficial partnerships on genomics research with them. With support of First Nations, remains from the Lucier site were provided to G.D. with permission from the University of Toronto Office of Research Ethics. All other remains were housed in museums, and permission for destructive analysis was granted by the curator or loan committee. C.L.S. has visited and shared results of this study with representatives of Chumash and other Southern California communities. Some members of these communities have consented to collaborate on this work and have seen and contributed to the final version of this manuscript (*15*).

SUPPLEMENTARY MATERIALS

www.sciencemag.org/content/360/6392/1024/suppl/DC1
Supplementary Text
Figs. S1 to S14
Tables S1 to S12
Data S1 to S4
References (*29*–*99*)

10 December 2017; accepted 20 April 2018
10.1126/science.aar6851

HUMAN EVOLUTION

Ancient genomes from Iceland reveal the making of a human population

S. Sunna Ebenesersdóttir,[1,2]* Marcela Sandoval-Velasco,[3] Ellen D. Gunnarsdóttir,[1,2] Anuradha Jagadeesan,[1,2] Valdís B. Guðmundsdóttir,[1,2] Elísabet L. Thordardóttir,[1,2] Margrét S. Einarsdóttir,[1,2] Kristjan H. S. Moore,[1] Ásgeir Sigurðsson,[1] Droplaug N. Magnúsdóttir,[1] Hákon Jónsson,[1] Steinunn Snorradóttir,[1] Eivind Hovig,[4,5,6] Pål Møller,[4,7,8] Ingrid Kockum,[9] Tomas Olsson,[9] Lars Alfredsson,[10] Thomas F. Hansen,[11,12] Thomas Werge,[11,13,14] Gianpiero L. Cavalleri,[15] Edmund Gilbert,[15] Carles Lalueza-Fox,[16] Joe W. Walser III,[17,18] Steinunn Kristjánsdóttir,[17,18] Shyam Gopalakrishnan,[3] Lilja Árnadóttir,[17] Ólafur Þ. Magnússon,[1] M. Thomas P. Gilbert,[3,19] Kári Stefánsson,[1,20]* Agnar Helgason[1,2]*

Opportunities to directly study the founding of a human population and its subsequent evolutionary history are rare. Using genome sequence data from 27 ancient Icelanders, we demonstrate that they are a combination of Norse, Gaelic, and admixed individuals. We further show that these ancient Icelanders are markedly more similar to their source populations in Scandinavia and the British-Irish Isles than to contemporary Icelanders, who have been shaped by 1100 years of extensive genetic drift. Finally, we report evidence of unequal contributions from the ancient founders to the contemporary Icelandic gene pool. These results provide detailed insights into the making of a human population that has proven extraordinarily useful for the discovery of genotype-phenotype associations.

Historical sources (*1*) indicate that Iceland was settled by people from Norway and the British-Irish Isles between 870 and 930 CE (*2*, *3*). Throughout the preceding century, the Norse had raided, traded, and settled in the islands and coastal regions of Ireland, Scotland, and northern England (*4*). Settlers in Iceland are thought to number ~8,000 to 16,000 individuals, with the population rarely exceeding 50,000 until 1850 (*3*), after which there was a rapid expansion to its current size of 330,000.

Studies of mitochondrial DNA (mtDNA) and Y-chromosomes from contemporary Icelanders indicate that 62% of their matrilineal ancestry stems from Scotland and Ireland and 75% of their patrilineal ancestry is Scandinavian (*5*–*7*). Moreover, mtDNA control region sequences from 68 Icelandic skeletal remains (~1000 years old) are more similar to contemporary source populations in Scandinavia, Scotland, and Ireland than to contemporary Icelanders (*8*). This was explained by a loss of mtDNA haplotypes from the Icelandic gene pool due to extensive genetic drift (*8*), supported by findings from whole-genome sequencing (WGS), genome-wide association studies (*9*), and population genetics analyses (*10*).

To directly assess the formation and subsequent evolution of a human population, we selected 35 ancient Icelanders for WGS (Fig. 1), most of whom represent the first generations of settlement (*11*) (Table 1 and tables S1 and S2). The 27 individuals passing quality control (*11*) (tables S3 and S4) were sequenced to between 0.18× to 30.7× average read depth (median = 0.71) (Table 1). The data display characteristics of ancient DNA (aDNA), and their authenticity is supported by multiple analyses (*11*) (figs. S1 and S2 and tables S4 to S6).

The sex of 26 of individuals was confidently determined by calculating the proportion of sex chromosome reads that mapped to the Y-chromosome (R_y) (*12*) (fig. S3 and table S7). The result for one individual, YGS-B2, was ambiguous, as R_y = 0.055 exceeded the upper limit for females (0.016) but was below the lower limit for males (0.075). The read depth of sex chromosomes relative to autosomes indicates that YGS-B2, who died before adulthood, carried two X-chromosomes and one Y-chromosome (fig. S4). This is further supported by a clearly assigned Y-chromosome haplogroup and X-chromosome heterozygosity in the range observed for females (table S8). To our knowledge, Klinefelter syndrome has not been reported in aDNA studies to date. Of the 24 individuals from pre-Christian (<1000 CE) burials (Table 1), 19 (79%) were male (X^2 test against expectation of 50%, P = 0.008). As the

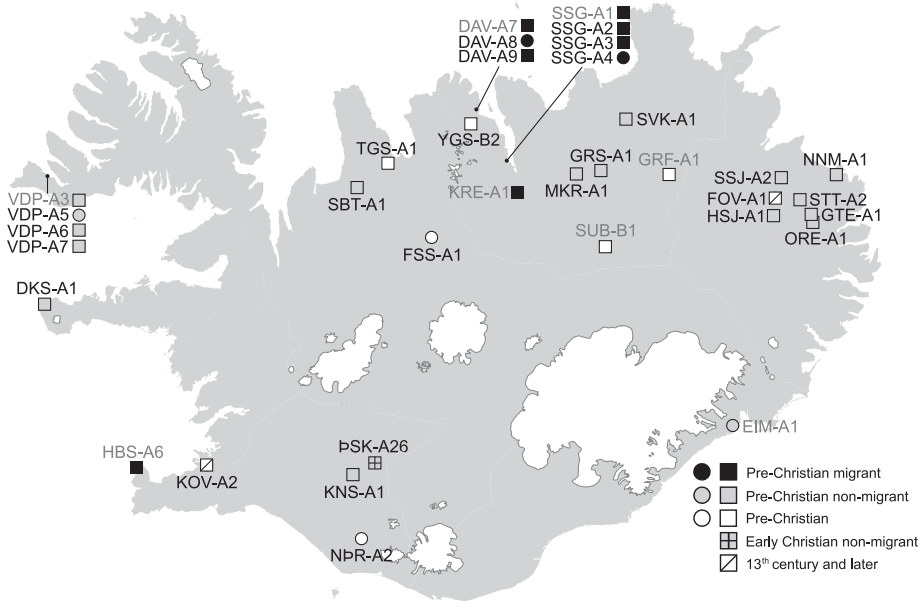

Fig. 1. A map of Iceland showing the locations of skeletal remains sampled for this study. Circles indicate females and squares, males. Eight samples (light gray labels) were ultimately excluded from further analysis.

[1]deCODE Genetics/AMGEN, Inc., Reykjavik Iceland. [2]Department of Anthropology, University of Iceland, Reykjavik, Iceland. [3]Natural History Museum of Denmark, University of Copenhagen, Øster Voldgade 5–7, 1350 Copenhagen K, Denmark. [4]Department of Tumor Biology, Institute for Cancer Research, Oslo University Hospital, Oslo, Norway. [5]Institute for Cancer Genetics and Informatics, Oslo University Hospital, Oslo, Norway. [6]Department of Informatics, University of Oslo, Oslo, Norway. [7]Department of Human Medicine, Universität Witten/Herdecke, Witten, Germany. [8]Research Group Inherited Cancer, Department of Medical Genetics, Oslo University Hospital, Oslo, Norway. [9]Center for Molecular Medicine, Department of Clinical Neuroscience, Neuroimmunology Unit, Karolinska Institutet, Stockholm, Sweden. [10]Institute of Environmental Medicine, Karolinska Institutet, Stockholm, Sweden. [11]Institute of Biological Psychiatry, Copenhagen Mental Health Services, Copenhagen, Denmark. [12]Danish Headache Center, Department of Neurology, Copenhagen University hospital, DK-2600 Glostrup, Denmark. [13]Department of Clinical Medicine, University of Copenhagen, Copenhagen, Denmark. [14]The Lundbeck Foundation Initiative for Integrative Psychiatric Research, iPSYCH, Copenhagen, Denmark. [15]Molecular and Cellular Therapeutics, Royal College of Surgeons in Ireland, 123 St. Stephen's Green, Dublin, Ireland. [16]Institut de Biologia Evolutiva (UPF-CSIC), Barcelona, Spain. [17]National Museum of Iceland, Reykjavik, Iceland. [18]Department of Archaeology, University of Iceland, Reykjavik, Iceland. [19]Norwegian University of Science and Techonology, University Museum, 7491 Trondheim, Norway. [20]Faculty of Medicine, University of Iceland, Reykjavik, Iceland.
*Corresponding author. Email: sunna@decode.is (S.S.E.); kstefan@deocde.is (K.S.); agnar@decode.is (A.H.)

individuals were not selected by morphologically predicted sex, this implies sex differences in burial practices during the period (*13*), such that female burials were either rarer or less likely to be discovered in our time.

Little can be inferred about the phenotypes of the ancient Icelanders. However, we report haploid genotypes for a set of rare disease-associated sequence variants discovered in the Icelandic population and variants thought to have been subject to positive selection in Europeans (tables S9 and S10).

We next examined the relationship between the ancient Icelanders and contemporary populations using single-nucleotide polymorphism (SNP) arrays (table S11). As the read depth for most ancient Icelanders was too low to call diploid genotypes, haploid genotypes were used in all analyses (*11*). We performed a principal components analysis (PCA) of 2139 contemporary individuals from 28 European populations. When projected onto the first two principal components (PCs), all ancient Icelanders plot within clusters of contemporary Scandinavians and British-Irish Islanders (fig. S5).

We also performed a PCA restricted to contemporary individuals from Scandinavia (n = 3118), the British-Irish Isles (n = 1436), and Iceland (n = 916) based on 404,066 SNPs. We observed a separation between contemporary Scandinavians and British-Irish Islanders on PC2 (Fig. 2A), reflecting allele frequency differences that have accumulated across several millennia of drift. PC1 reveals an even more marked separation of contemporary Icelanders from their source populations. This divergence is also seen in the distribution of genetic distances (F_{ST}) between Icelanders and their source populations (fig. S6A).

The most likely cause for this divergence of Icelanders is 1100 years of genetic drift resulting from an initial founder event and subsequent small population size (*8*–*10*, *14*). This interpretation is supported by PCA projections of 25 ancient Icelanders (24 pre-Christian and one early-Christian, <1104 CE), all of whom plot within the range of PC1 occupied by contemporary Scandinavians and British-Irish Islanders (Fig. 2A and fig. S7). Accordingly, F_{ST} distances show that allele frequencies in ancient Icelanders are more similar to those of the source populations than to those of contemporary Icelanders (fig. S6B). Furthermore, ancient Icelanders show no evidence of the geographic patterns of genetic variation found in contemporary Icelanders (fig. S8). The implication that source populations experienced much less drift than Icelanders (*8*) is supported by PCA projections of ancient individuals (n = 16) from the British-Irish Isles dating from ~4000 to 1100 calibrated years before the present (*11*) (table S12), who cluster within contemporary British and Irish populations (fig. S9).

Whereas some ancient Icelanders appear to be unadmixed Scandinavian or British-Irish Islanders, others resemble a mixture of these ancestral

Table 1. Summary of genomic sequence data from ancient Icelanders.

Time period	Classification based on $^{87}Sr/^{86}Sr$ values	Sample	Archaeological date	^{14}C dating (cal CE)	Auto. genome depth of coverage (×)	Auto. genome covered (%)	SNP overlap with European ref. (%)†	SNP overlap with North European ref. (%)‡	Sex chr. karyotype	mtDNA haplogroup	chrY haplogroup	$^{87}Sr/^{86}Sr$ ratio
Pre-Christian	**Migrant**	DA-V-A8	<1000	<1050	3.31	89.12	90.14	93.92	XX	H1	–	0.7121
		DAV-A9	<1000	980-1020	0.43	26.66	21.79	22.66	XY	H1	I1	0.7118
		SSG-A2*	<1000	NA§	10.56	94.96	95.58	99.8	XY	J1c3g	R1b1a1a2a1a2c1	0.7095
		SSG-A3*	<1000	NA	0.26	16.37	8.16	8.56	XY	T2b2b	I1	0.7093
		SSG-A4*	<1000	NA	7.26	94.08	94.92	99.08	XX	J1b1a1a	–	0.7117
	Non-migrant	DKS-A1	<1000	NA	0.56	36.43	28.38	29.59	XY	U5a1h	R1a1a1b1a3	0.7088
		GRS-A1	<1000	<1050	0.55	34.77	27.86	29	XY	K1a1b1b	R1a1a1b1a3b	0.7071
		GTE-A1	<1000	NA	0.25	13.54	12.73	13.18	XY	H4a1a4b	R1a1a1b1a3a1	0.7061
		HSJ-A1	<1000	NA	30.74	96.29	95.73	99.99	XY	H3g1	I1a1b3b	0.7074
		KNS-A1	<1000	NA	0.71	43.95	36.2	37.8	XY	H5	R1b1a1a2a1a2c	0.706
		MKR-A1	<1000	<1050	0.18	11.33	11.25	11.68	XY	K1c1b	R1a1a1b	0.7065
		NNM-A1	<1000	NA	0.48	32.83	22.23	23.3	XY	H2a2b5a	R1a1a1b1a3a	0.7062
		ORE-A1	<1000	NA	0.44	26.26	22.88	23.79	XY	K1a3a	R1b1a1a2a1a	0.7087
		SBT-A1	<1000	NA	6.01	93.72	94.36	98.46	XY	H3g1a	I1a2a1a2	0.7084
		SSJ-A2	<1000	NA	0.36	22.41	14.04	14.77	XY	U5a1a1	I1a1b3	0.7077
		STT-A2	<1000	975-1015	12.92	95.62	95.67	99.9	XY	U4b1b1	R1b1a1a2a1a2c1	0.7069
		SVK-A1	<1000	<1050	1.07	67.81	60.95	63.47	XY	I2	I1b	0.7078
		VDP-A5	<1000	NA	1.32	81.88	83.64	87.05	XX	H3	–	0.7085
		VDP-A6	<1000	NA	1.86	85.92	63.06	65.83	XY	H1c3a	R1a1a1b1a3a	0.7089
		VDP-A7	<1000	NA	0.83	70.07	83.15	86.68	XY	H4a1a1	R1b1a1a2a1a1b	0.7085
	Not available	FSS-A1	<1000	NA	0.94	58.92	56.28	58.54	XX	U4a2	–	NA
		NÞR-A2	<1000	NA	0.49	31.88	31.79	32.93	XX	K1a2a	–	NA
		TGS-A1	<1000	943-1024	1.01	59.32	54.86	57.14	XY	T2e1	R1b1a1a2a1a2d	NA
		YGS-B2	<1000	NA	0.27	18.37	14.99	15.67	XXY	J1c1a	R1b1a1a2a1a	NA
Early-Christian	**Non-migrant**	ÞSK-A26	1000–1104	1120	0.77	48.41	44.69	46.45	XY	J1b1a1a	R1a1	0.7061
13th century and later	**Not available**	FOV-A1	>1000	1246-1302	0.68	43.26	37.24	38.91	XY	HV17a	R1b1a1a2a1a2c1a1	NA
		KOV-A2	b. 1678	NA	0.57	36.05	34.03	35.42	XY	H1	R1b1a1a2a1a	NA

*Samples marked with an asterisk symbol (*) were excavated from the same site as samples that have been subjected to radiocarbon dating, yielding the date estimate 980 to 1020 cal CE. †N = 227,056 SNPs. ‡N = 404,066 SNPs. §NA, not available.

groups (*5*–*8*) (Fig. 2A). Contemporary genotyped individuals were grouped into Norse (n = 2138, Norway and Sweden) and Gaelic (n = 459, defined here as Ireland and Scotland, excluding Orkney), and their relationships were tested with *D*-statistics (*15*) in the form *D*(*Yoruba*, *X*; *Norse*, *Gaelic*) (Fig. 2B and table S13).

We ran ADMIXTURE in supervised mode separately for each ancient Icelander with the Norse and Gaelic reference populations, yielding results (Fig. 2C) consistent with both PC2 axis position in Fig. 2A and *D*-statistics (Fig. 2B) (Pearson's $|r| > 0.98$ between all three ancestry assessments). Table 1 shows that Y-chromosomes from the 22 ancient Icelandic males belong to haplogroups common in Norse (I1 and R1a) and in Gaels (R1b1) (*11*) (table S14). An association between I1/R1a status and autosomal Norse ancestry was observed in the 19 pre-Christian males (p = 0.02, one-sided t test, Fig. 2C), consistent with them dating to the first generations of settlement.

We estimated the mean Norse ancestry of the settlement population (24 pre-Christians and one early Christian) as 0.566 [95% confidence interval (CI) 0.431–0.702], with a nonsignificant difference between males (0.579) and females (0.521). Applying the same ADMIXTURE analysis to each of the 916 contemporary Icelanders, we obtained a mean Norse ancestry of 0.704 (95% CI 0.699–0.709). Although not statistically significant (t test p = 0.058), this difference is suggestive. A similar difference of Norse ancestry was observed with a frequency-based weighted least-squares admixture estimator (*16*), 0.625 [Mean squared error (MSE) = 0.083] versus 0.74 (MSE = 0.0037). Finally, the *D*-statistic test *D*(*YRI*, *X*; *Gaelic*, *Norse*) also revealed a greater affinity between Norse and contemporary Icelanders (0.0004, 95% CI 0.00008–0.00072) than between Norse and ancient Icelanders (−0.0002, 95% CI −0.00056–0.00015). This observation raises the possibility that reproductive success among the earliest Icelanders was stratified by ancestry, as genetic drift alone is unlikely to systematically alter ancestry at thousands of independent loci (fig. S10). We note that many settlers of Gaelic ancestry came to Iceland as slaves, whose survival and freedom to reproduce is likely to have been constrained (*17*). Some shift in ancestry must also be due to later immigration from Denmark, which maintained colonial control over Iceland from 1380 to 1944 (for example, in 1930 there were 745 Danes out of a total population of 108,629 in Iceland) (*18*).

For 20 of the 24 pre-Christian Icelanders, strontium isotopes 86 and 87 were measured from dental enamel (*11*), revealing whether they spent their first 6 years in Iceland (nonmigrants) or elsewhere (migrants). Three are deemed migrants on the basis of high $^{87}Sr/^{86}Sr$ ratios (>0.710). These likely first-generation settlers were unmixed; DAV-A8 and DAV-A9 (from the same site) were Norse, and SSG-A4 was Gaelic (Table 1 and Fig. 2C). SSG-A2 and SSG-A3 (from the same site as SSG-A4) have lower $^{87}Sr/^{86}Sr$ ratios, albeit too high for a childhood solely in Iceland. Notably, SSG-A3 is estimated to be an equal mix of Norse and Gaelic, indicating that some admixture occurred before arrival in Iceland, perhaps in Viking settlements in Scotland or Ireland.

One intriguing implication of the extensive drift that has accumulated in the Icelandic gene pool is that DNA samples from earlier generations could be dated through the proportion of drift shared with the contemporary population.

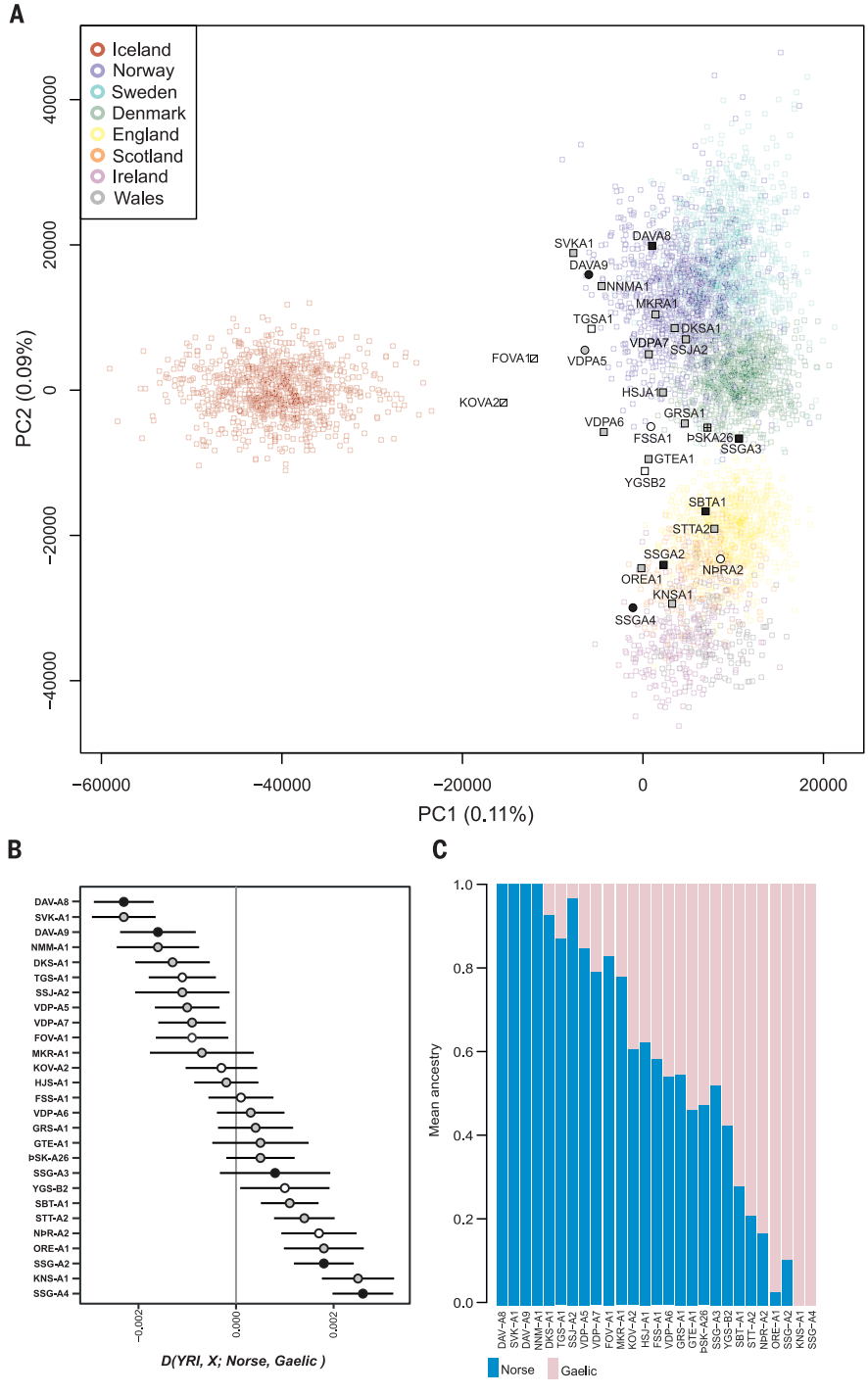

Fig. 2. Ancestry of ancient Icelanders. (**A**) Ancient Icelanders projected onto the first two eigenvectors of a PCA based on contemporary Scandinavians, British-Irish Islanders, and Icelanders. Proportion of variance explained is shown in parentheses. Symbols for ancient individuals are as specified in Fig. 1. (**B**) *D*-statistics reflecting the differential affinity of ancient Icelanders (*X*) to Norse and Gaelic reference populations, with the Yoruba from Nigeria (YRI) as an outgroup (n = 91). Symbols are shaded as in Fig. 1. (**C**) Estimated Norse and Gaelic ancestry proportions for ancient Icelanders using ADMIXTURE in supervised mode.

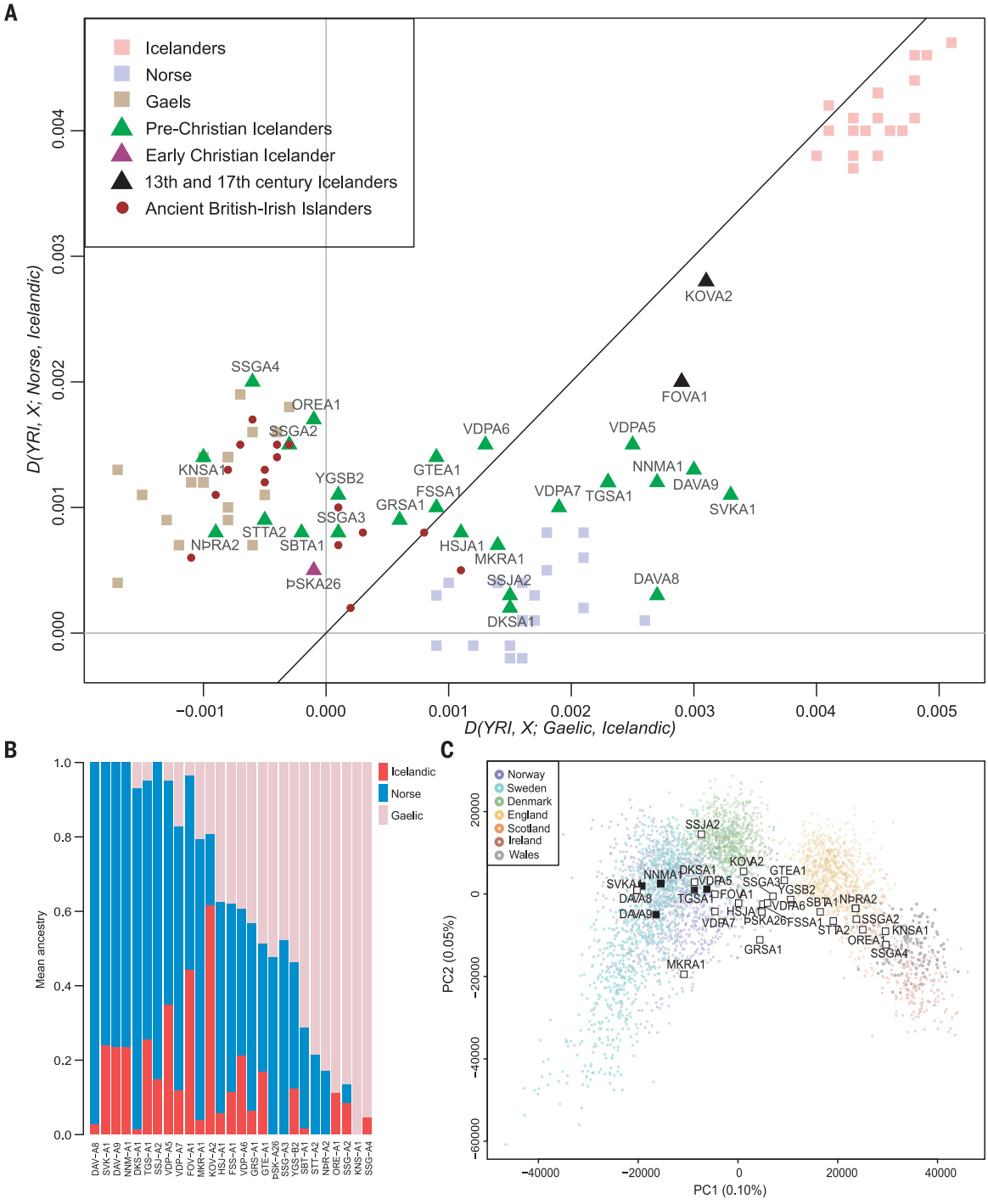

Fig. 3. Shared drift of ancient and contemporary Icelanders. (**A**) Scatterplot of *D*-statistics reflecting Iceland-specific drift. To aid interpretation, we included values for ancient British-Irish Islanders and a subset of contemporary individuals (who were correspondingly removed from the reference populations). (**B**) Estimated Norse, Gaelic, and Icelandic ancestry for ancient Icelanders using ADMIXTURE in supervised mode. (**C**) Ancient Icelanders projected onto a PCA of contemporary Scandinavians and British-Irish Islanders. Black squares denote the five individuals who may have contributed disproportionately to the Icelandic gene pool.

To test this hypothesis, we sequenced two Icelanders from the 13th (FOV-A1) and 17th (KOV-A2) centuries. Projection of their genotypes onto the PCA in Fig. 2A resulted in placement partway between contemporary Icelanders and their source populations, consistent with the genotypes of FOV-A1 and KOV-A2 being shaped by only part of the drift that characterizes modern Icelanders.

A scatterplot of two *D*-statistics, *D*(*YRI*, *X*; *Norse*, *Icelandic*) and *D*(*YRI*, *X*; *Gaelic*, *Icelandic*), for all 27 ancient Icelanders (table S15) effectively distinguishes the signature of Iceland-specific drift (an axis parallel to the diagonal line) from Norse-Gaelic ancestry (perpendicular deviation from that line) (Fig. 3A). Consistent with the PCA in Fig. 2A, pre-Christian Icelanders plot close to contemporary Norse and Gaels. Furthermore,

KOV-A2 is closer to contemporary Icelanders, whereas FOV-A1 plots roughly halfway between them and the contemporary Gaelic and Norse source populations.

Five pre-Christian Icelanders (VDP-A5, DAV-A9, NNM-A1, SVK-A1 and TGS-A1) fall just outside the space occupied by contemporary Norse in Fig. 3A. That these individuals show a stronger signal of drift shared with contemporary Icelanders is also apparent in the results of ADMIXTURE, run in supervised mode with three contemporary reference populations (Norse, Gaelic, and Icelandic) (Fig. 3B). The correlation between the proportion of Icelandic ancestry from this analysis and PC1 in Fig. 2A is $|r| = 0.913$. One possible explanation of this result is misclassification of these individuals as early Icelanders. However, this is doubtful, as they exhibit pre-Christian burial features, early radiocarbon dates (DAV-A9, SVK-A1 and TGS-A1), strontium isotopes inconsistent with being raised in Iceland (DAV-A9) (Table 1), and a high proportion (>87%) of Norse ancestry (DAV-A9, NNM-A1, SVK-A1, and TGS-A1, Fig. 2C).

Contamination from contemporary Icelanders could also affect our results but is negligible in all five individuals (table S4). Three factors could account for the greater shared drift of the five pre-Christian Icelanders with contemporary Icelanders. First, subtle genetic drift in the Norse gene pools might have shifted allele frequencies during the past 1100 years, making contemporary Norse less representative of their ancestors than is the case for Gaels. Second, they might originate from a subpopulation within Scandinavia that is poorly represented by contemporary populations or our reference samples. Third, these five individuals may have contributed disproportionately to the gene pool of contemporary Icelanders.

If genetic drift or population substructure in Scandinavian populations were responsible for their outlying positions (Figs. 2A and 3A), then the five individuals would also be outliers in a PCA generated only using contemporary individuals from Scandinavia and the British-Irish Isles. However, as the five ancient Icelanders fall well within the cluster of contemporary Scandinavians (Fig. 3C), we conclude that they, or close relatives, likely contributed more to the contemporary Icelandic gene pool than the other pre-Christians. We note that this observation is consistent with the inference that settlers of Norse ancestry had greater reproductive success than those of Gaelic ancestry.

Ancient genomes are key to answering questions about the formation and evolution of human populations during recent millennia. The settlement of Iceland occurred around 1100 years ago at the height of the Viking age. Our study reveals a highly admixed Norse and Gaelic gene pool of this founding population that was shaped by substantial genetic drift. The resultant founder events are one reason why the Icelandic population has contributed so much to the discovery of genotype-phenotype associations for rare sequence variants (*9*).

REFERENCES AND NOTES

1. *The Book of Settlements: Landnámabók* (Univ. of Manitoba, Winnipeg, 1972).
2. K. Eldjárn, *Kuml og haugfé*, A. Friðriksson, Ed. (Mál og menning, Reykjavík, ed. 3, 2016).
3. J. Steffensen, *Menning og meinsemdir: Ritgerðarsafn um mótunarsögu íslenskrar þjóðar og baráttu hennar við hungur og sóttir* (Ísafoldarprentsmiðja, Reykjavík, 1975).
4. G. Jones, *A History of the Vikings* (Oxford Univ. Press, Oxford, 1984).
5. S. Goodacre *et al*., *Heredity* **95**, 129–135 (2005).
6. A. Helgason, S. Sigurðardóttir, J. R. Gulcher, R. Ward, K. Stefánsson, *Am. J. Hum. Genet.* **66**, 999–1016 (2000).
7. A. Helgason *et al*., *Am. J. Hum. Genet.* **67**, 697–717 (2000).
8. A. Helgason *et al*., *PLOS Genet.* **5**, e1000343 (2009).
9. D. F. Gudbjartsson *et al*., *Nat. Genet.* **47**, 435–444 (2015).
10. A. Helgason, G. Nicholson, K. Stefánsson, P. Donnelly, *Ann. Hum. Genet.* **67**, 281–297 (2003).
11. See the supplementary materials.
12. P. Skoglund, J. Stora, A. Gotherstrom, M. Jakobsson, *J. Archaeol. Sci.* **40**, 4477–4482 (2013).
13. R. A. Maher, Kuml, kyn og kyngervi: athugun á íslenskum greftrunarsiðum á víkingaöld. *Árbók fornleifafélagsins* **2004-2005**, 151-168 (2007).
14. A. L. Price *et al*., *PLOS Genet.* **5**, e1000505 (2009).
15. N. Patterson *et al*., *Genetics* **192**, 1065–1093 (2012).
16. J. C. Long, *Genetics* **127**, 417–428 (1991).
17. R. M. Karras, *Slavery and Society in Medieval Scandinavia* (Yale Univ. Press, New Haven, CT, and London, 1998).
18. G. Jónsson, M. S. Magnússon, *Hagskinna: Icelandic Historical Statistics* (Hagstofa Íslands, Reykjavík, 1997).

ACKNOWLEDGMENTS

We thank the staff at the National Museum of Iceland for their help. **Funding:** S.S.E. and V.B.G. received grants from The Research Fund of University of Iceland for doctoral studies. M.S.-V. and A.J. received a grant from EUROTAST Marie Curie Framework Programme 7 Initial Training Network (290344). M.S.E. received a grant from the Icelandic Research Fund (163428-051). The work was partly funded (E.G. and G.L.C.) by a Career Development Award (13/CDA/2223) from Science Foundation Ireland and Swedish Research Council (Dnr 2016-02349), Swedish Research Council for Health, Working Life and Welfare (Dnr 2013-0194), and Swedish Brain Foundation (FO2017-0076). **Author contributions:** S.S.E., K.S., and A.H. designed and directed the research. S.S.E. and A.H. analyzed the data, with E.D.G., A.J., V.B.G., E.L.T., M.S.E., H.J., S.G., and M.T.P.G. providing assistance with particular tasks. S.S.E. and M.S.-V. generated the ancient genomic data with laboratory guidance and support from Á.S., D.N.M., S.S., C.L.-F., Ó.Þ.M., and M.T.P.G. Modern reference data sets were provided by E.H., P.M., I.K., T.O., L.A., T.F.H., T.W., G.L.C., and E.G. Archaeological and osteological context was provided by J.W.W., S.K., and L.Á., who also provided access to samples. S.S.E., K.S., and A.H. wrote the manuscript and supplements with input from M.S.-V., M.T.P.G., H.J., K.H.S.M., and S.G. **Competing interests:** Authors affiliated with deCODE Genetics are employed by the company, which is owned by Amgen, Inc.: S.S.E., E.D.G., A.J., V.B.G., E.L.T., M.S.E., K.H.S.M., Á.S., D.N.M., H.J., S.S., Ó.Þ.M., K.S., and A.H. **Data and materials availability:** The sequencing data (BAM files with reads mapped to NCBI build 38 of the human reference genome) for the 27 ancient Icelanders are available for download at the European Nucleotide Archive (ENA) under the accession number PRJEB26760. Also available for download as supplementary materials are eigenvector values, SNP loading values, and allele frequencies for the PCAs reported in Fig. 2A (data file S1), Fig. 3C (data file S2), fig. S5 (data file S3), and fig. S8A (data file S4). Microarray SNP genotypes and WGS data from contemporary Icelanders cannot be made publicly available, as Icelandic law and the regulations of the Icelandic Data Protection Authority prohibit the release of individual-level and personally identifying data. Access to these data can only be granted at the facilities of deCODE Genetics in Iceland, subject to Icelandic laws regarding data usage. Anyone wanting to gain access to Icelandic data should contact A.H. (agnar@decode.is) or K.S. (kstefans@decode.is). Microarray SNP genotypes from contemporary Scandinavian populations are not available for download, because of restrictions related to local institutional review board requirements. Genotypes related to the current article for the Swedish data are in principle available from K.S. under a material transfer agreement with Karolinska Institutet. However, to share genotype data from the Swedish cohort, a data transfer agreement (DTA) must be completed between Karolinska Institutet and the institution that wants to access the data. This is in accordance with new data protection legislation in Europe (GDPR). Anyone interested in getting access to the genotypes from the Swedish cohort can contact I.K. (ingrid.kockum@ki.se) to set up such a DTA. For more information about the genotype data from contemporary Norwegians, contact E.H. (ehovig@ifi.uio.no), and for genotype data from contemporary Danes, contact T.W. (thomas.werge@regionh.dk).

SUPPLEMENTARY MATERIALS

www.sciencemag.org/content/360/6392/1028/suppl/DC1
Materials and Methods
Supplementary Text
Figs. S1 to S10
Tables S1 to S16
Data Files S1 to S4
References (*19*–*64*)

27 October 2017; accepted 25 April 2018
10.1126/science.aar2625

eppendorf & Science

PRIZE FOR NEURO BIOLOGY

2017 Winner
Flavio Donato, Ph.D.
Kavli Institute
Norwegian University of
Science and Technology

For research on how neural networks mature during development to represent space in the brain

Application Deadline
June 15, 2018

Call for Entries

Eppendorf & Science Prize for Neurobiology
The annual Eppendorf & Science Prize for Neurobiology is an international award which honors young scientists for their outstanding contributions to neurobiological research based on methods of molecular and cell biology. The winner and finalists are selected by a committee of independent scientists, chaired by *Science's* Senior Editor, Dr. Peter Stern. To be eligible, you must be 35 years of age or younger.

As the Grand Prize Winner, you could be next to receive
> Prize money of US$25,000
> Publication of your work in *Science*
> Full support to attend the Prize Ceremony held in conjunction with the Annual Meeting of the Society for Neuroscience in the USA
> 10-year AAAS membership and online subscription to *Science*
> Complimentary products worth US$1,000 from Eppendorf
> An invitation to visit Eppendorf in Hamburg, Germany

It's easy to apply! Learn more at:

www.eppendorf.com/prize

eppendorf Science AAAS

Present your work to the world

Are you a representative of the upcoming generation of thought leaders in your field? Together we look forward to your application for the new Sartorius & *Science* Prize for Regenerative Medicine & Cell Therapy.

Apply now!

www.passionforscience.com/prize

The Sartorius & *Science* Prize for Regenerative Medicine & Cell Therapy

Awarded by sartorius Science

Gel-Imaging System

The InGenius3 gel documentation system is ideal for laboratories looking for a versatile, budget-friendly platform to accurately image both DNA and protein gels. It features a 3-megapixel CCD camera integrated to a compact, light-tight darkroom, and overhead Epi-LED white lighting for perfect gel positioning. The small darkroom has a slide-out drawer that can accommodate UV, blue, and white lighting options, allowing users the flexibility to image fluorescent and visibly stained gels. The system can be connected to the laboratory's choice of PC and is controlled by protocol-driven GeneSys software, which selects the best combination of filters and lighting available, making it easy to detect nanogram amounts of DNA and protein on gels of up to 20 cm x 20 cm.

Syngene
For info: 800-686-4407
www.syngene.com/gel-documentation-and-analysis-ingenius

Multispecies Toxicokinetic and Pharmacokinetic Kits

The Gyrolab Generic Toxicokinetic (TK) Kit adds to a growing menu of ready-to-use kits, and allows researchers to more efficiently quantify human therapeutic antibodies (IgG) in automated, nanoliter-scale Gyrolab xP and Gyrolab xPlore systems. The TK Kit complements the Gyrolab Generic Pharmacokinetic (PK) Kit, introduced in 2017 and based on the same reagents. The TK Kit addresses a higher concentration range than the PK Kit, making it more suited to toxicokinetic studies. Together, these kits more fully meet the needs of Gyrolab system users performing PK/TK assays in preclinical and clinical studies, and enable increased productivity, generating results in just 70 min. The two kits cover a combined range of 5 logs, minimizing dilution steps and repeats when performing human IgG quantification during early biotherapeutic development. They are designed for use with several species of preclinical animal models, including mouse and cynomolgus monkey.

Gyros Protein Technologies
For info: 800-477-6834
www.gyrosproteintechnologies.com

Protein Stain

InstantBlue is a ready-to-use Coomassie protein stain for polyacrylamide gels. Its unique mechanism of action stains proteins in 15 min, while leaving a clear background and eliminating the need to fix, wash, or destain. InstantBlue uses a one-step protocol and can be fully destained using standard procedures. Its acetic acid–free formulation doesn't methylate or acetylate protein during staining, making it fully compatible with mass spectrometry. InstantBlue is nontoxic and sink-disposable due to its methanol-free composition. Other stains require solvent-disposal procedures and can require microwaving, which produces dangerous fumes. The lack of methanol also means no gel shrinkage. Only 25 mL per mini-gel allows you to use less of the product. InstantBlue will stain at least 40 mini-gels per bottle.

Innova Biosciences
For info: 855-466-6821
www.innovabiosciences.com

Single Quadrupole Mass Spectrometer

The Thermo Scientific ISQ EC single quadrupole mass spectrometer seamlessly integrates with ion chromatography or liquid chromatography systems, so both novices and experts can quickly master mass spectrometry (MS) and get more information from every sample. Embedded in the spectrometer's instrument control is the Chromeleon Chromatography Data Software (CDS) platform, which enables users to minimize time spent on new MS user training. The ISQ EC also provides exceptional robustness, enabling users to analyze a range of simple and complex sample matrices.

Thermo Fisher Scientific
For info: 800-955-6288
www.thermofisher.com

SLE Microplate

Porvair Sciences' easy-to-use 96-well Supported Liquid Extraction (SLE) microplate is designed for high-recovery extraction of analytes from biological fluids such as blood, plasma, and serum. SLE is a separation technique in which the aqueous sample is immobilized on an inert support (such as diatomaceous earth), and the organic phase flows through the support, eliminating problems such as emulsion formation. The plate provides fast, reproducible, and economical sample cleanup when used with a simple vacuum manifold or positive pressure device. Its proprietary frit technology ensures samples will not drip or break through until the pressure or vacuum devices are applied, allowing longer dwell time in the plate wells. The SLE plate is the perfect sample cleanup device for physiological fluids prior to analysis by liquid chromatography/mass spectrometry. It has also been particularly helpful to environmental, food, and textile labs involved in sample cleanup prior to analysis.

Porvair Sciences
For info: +44-(0)-1978-666222
www.porvair-sciences.com

Double-Staining Immunofluorescence Kit

The VectaFluor Duet kit offers convenient, ready-to-use immunofluorescence double labeling. This kit is ideal for use on a wide range of frozen and FFPE tissue samples, combining primary and secondary antibodies to significantly streamline workflow. The kit includes a secondary reagent to detect mouse and rat primary antibodies with green and red DyLight fluorescent dyes and a normal blocking serum. With VectaFluor Duet, one protocol replaces several and reduces preparation time—in some cases by as much as a day or more.

Vector Laboratories
For info: 800-227-6666
vectorlabs.com

Electronically submit your new product description or product literature information! Go to www.sciencemag.org/about/new-products-section for more information.

Newly offered instrumentation, apparatus, and laboratory materials of interest to researchers in all disciplines in academic, industrial, and governmental organizations are featured in this space. Emphasis is given to purpose, chief characteristics, and availability of products and materials. Endorsement by *Science* or AAAS of any products or materials mentioned is not implied. Additional information may be obtained from the manufacturer or supplier.

want new technologies?

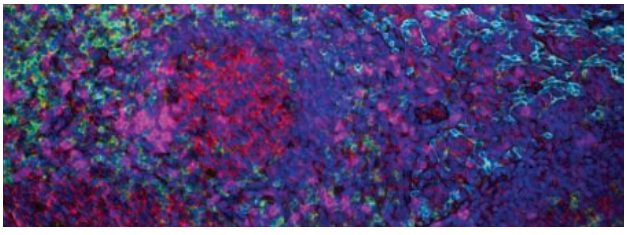

antibodies
apoptosis
biomarkers
cancer
cytometry
data
diseases
DNA
epigenetics
genomics
immunotherapies
medicine
microbiomics
microfluidics
microscopy
neuroscience
proteomics
sequencing
toxicology
transcriptomics

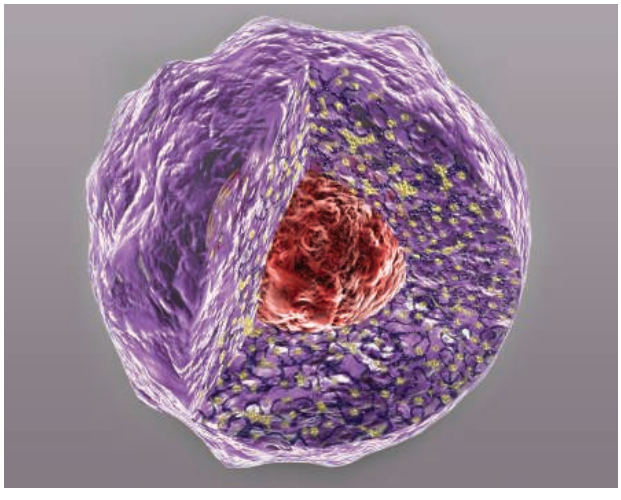

watch our webinars

Learn about the latest break-throughs, new technologies, and ground-breaking research in a variety of fields. Our expert speakers explain their quality research to you and answer questions submitted by live viewers.

VIEW NOW!
webinar.sciencemag.org

Science
AAAS

Brought to you by the *Science*/AAAS Custom Publishing Office

@SciMagWebinars

R&D SYSTEMS
a bio-techne brand

GMP-Grade Growth Factors

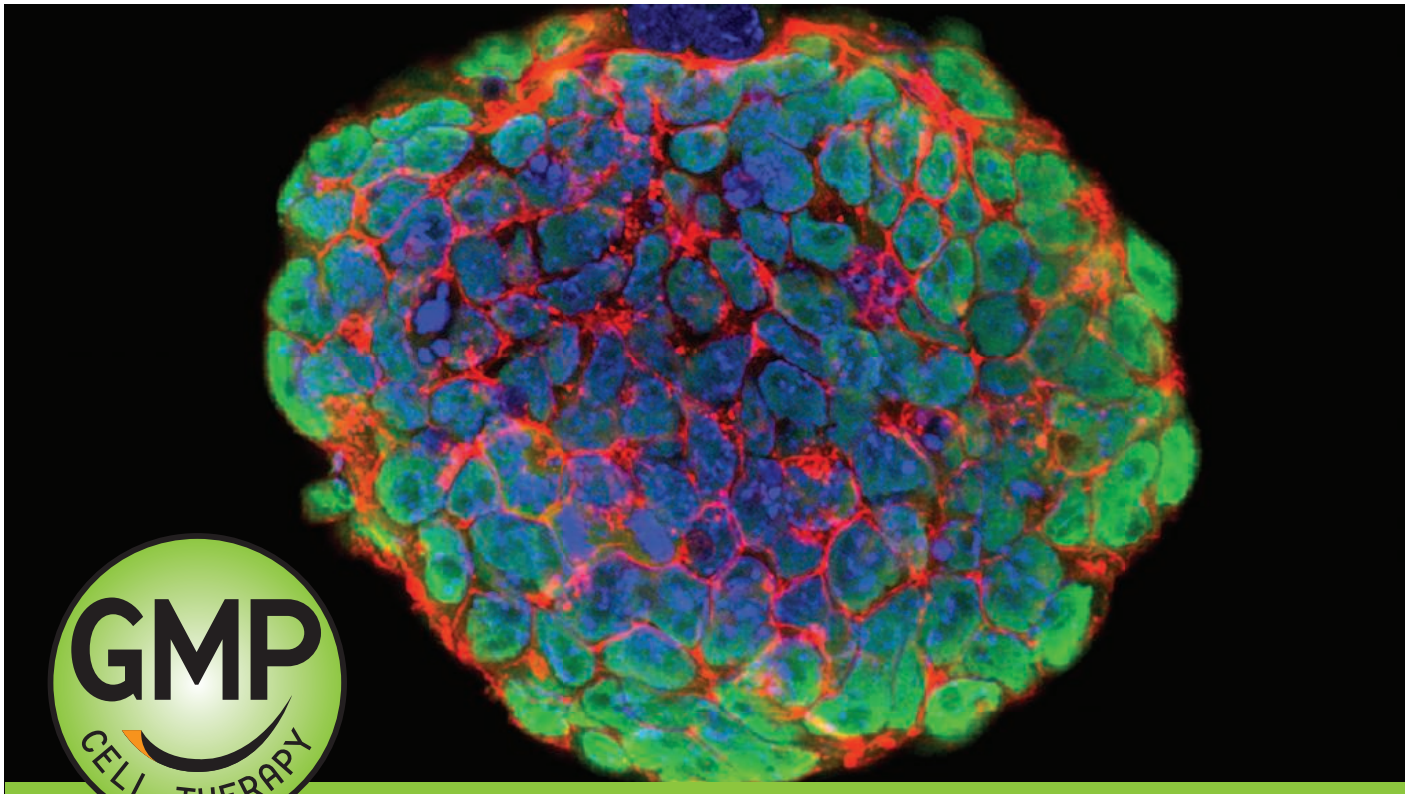

Dedicated to Consistent Proteins

The Widest Selection for

- Cell Manufacturing
- Immunotherapy
- Regenerative Medicine
- Stem Cell Therapy

Learn more | rndsystems.com/gmp

bio-techne®

Global bio-techne.com info@bio-techne.com TEL +1 612 379 2956 **North America** TEL 800 343 7475
Europe | Middle East | Africa TEL +44 (0)1235 529449 **China** info.cn@bio-techne.com TEL +86 (21) 52380373

Science Careers

SCIENCE CAREERS ADVERTISING

For full advertising details, go to ScienceCareers.org and click For Employers, or call one of our representatives.

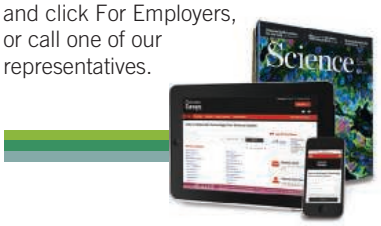

AMERICAS

+1 202 326-6577
+1 202 326-6578
advertise@sciencecareers.org

EUROPE, INDIA, AUSTRALIA, NEW ZEALAND, REST OF WORLD

+44 (0) 1223 326527
advertise@sciencecareers.org

CHINA, KOREA, SINGAPORE, TAIWAN, THAILAND

+86 131 4114 0012
advertise@sciencecareers.org

JAPAN

+81 3-6459-4174
advertise@sciencecareers.org

CUSTOMER SERVICE

AMERICAS

+1 202 326-6577

REST OF WORLD

+44 (0) 1223 326528

advertise@sciencecareers.org

All ads submitted for publication must comply with applicable U.S. and non-U.S. laws. *Science* reserves the right to refuse any advertisement at its sole discretion for any reason, including without limitation for offensive language or inappropriate content, and all advertising is subject to publisher approval. *Science* encourages our readers to alert us to any ads that they feel may be discriminatory or offensive.

ScienceCareers
FROM THE JOURNAL SCIENCE AAAS

ScienceCareers.org


INVENT.
IMPACT.
INSPIRE.
YOUR CHEMISTRY EXPERTISE CAN MAKE A BIG DIFFERENCE.
The world's greatest health challenges demand solutions from the most innovative minds in chemistry. That's who you'll find at Merck Research Laboratories South San Francisco, where our research spans exploratory biology through early clinical development. We need more visionaries like you to crack the code of life. Guide our incredible team as we discover the next big, life-changing drug or vaccine with world-class expertise in small molecules and biologics.
WANTED:
DIRECTOR, DISCOVERY PROCESS CHEMISTRY
To learn more, visit Merck.com/careers and search by job ID #RES002104.
MERCK
INVENTING FOR LIFE
merck.com/careers
Merck is proud to embrace diversity in all its manifestations | EOE M/F/D/V

10 ways that *Science* Careers can help advance your career

1. Register for a free online account on **ScienceCareers.org**.
2. Search thousands of job postings and find your perfect job.
3. Sign up to receive e-mail alerts about job postings that match your criteria.
4. Upload your resume into our database and connect with employers.
5. Watch one of our many webinars on different career topics such as job searching, networking, and more.
6. Download our career booklets, including Career Basics, Careers Beyond the Bench, and Developing Your Skills.
7. Complete an interactive, personalized career plan at "my IDP."
8. Visit our Career Forum and get advice from career experts and your peers.
9. Research graduate program information and find a program right for you.
10. Read relevant career advice articles from our library of thousands.

Visit **ScienceCareers.org** today — all resources are free

ScienceCareers
FROM THE JOURNAL SCIENCE AAAS

SCIENCECAREERS.ORG

INNOVATION AND TECHNOLOGY COMMISSION

Biotechnology Director

(Salary: HK$164,500 - HK$179,850 per month, depending on relevant experience)

Entry Requirements:

Candidates are required to have:

(a) a **PhD Degree** in the field of life science or biotechnology;

(b) a **minimum of 10 years' relevant post-qualification experience** at a senior management level in a scientific or corporate setting;

(c) strong research or technical background in biotechnology and related areas (preferably enjoy recognised international standing in his/her own specialist field); good scientific and/or business networks; competency in research and development and/or business and product development; and understanding of current trends in technology and market (familiarity with the development and commercial application of biotechnology in the Mainland will be an advantage); and

(d) strong command of both written and spoken English. Proficiency in written Chinese and spoken Cantonese and Putonghua will be an advantage.

Duties: Biotechnology Director is a non-civil service position responsible for providing expert technology-related advice in biotechnology and related fields to the Commissioner for Innovation and Technology. He/She is required to lead a team of professional staff to provide assistance to the Innovation and Technology Commission (the Commission) in developing solicitation themes, undertaking project assessment, monitoring progress and evaluating the programmes in related fields under the Innovation and Technology Fund and other funding schemes administered by the Commission. He/She is also expected to maintain contacts with academia, research institutes, industries and other relevant bodies, liaising and supporting the activities of other government departments/organizations in the biotechnology field, and undertaking ad hoc activities related to the Commission's operation and strategic development in this aspect.

Terms of Appointment: The successful candidate will be appointed on non-civil service agreement terms for three years.

Fringe Benefits:

(a) An end-of-contract gratuity may be granted upon satisfactory completion of the contract. The amount of gratuity payable will be the sum, which, when added together with the Government's contribution to the Mandatory Provident Fund scheme, equals 25% of the total basic salary drawn during the contract period; and

(b) vacation leave with leave passage allowance, housing benefits in the form of non-accountable cash allowance and other benefits subject to the meeting of the eligibility criteria as stipulated in the regulations relating to the provision of such benefits.

How to Apply: Candidates should apply in writing with a completed application form [G.F.340 (Rev.3/2013)] which can be downloaded from the Civil Service Bureau's website (**http://www.csb.gov.hk**)], **and** a full curriculum vitae giving a detailed account of employment records with description of duties and past experience in research/project administration/product development in related fields. Copies of academic qualification certificates and record of previous employment should also be provided. Applications should reach the following mailing or email address on or before the closing date for application (according to postmark). Candidates who are selected for interview will normally receive an invitation for interview in about eight to ten weeks after the closing date for application. Those who are not invited for interview may assume that their applications are unsuccessful. Interviews are tentatively scheduled to be conducted in Hong Kong during late August/ September 2018 (subject to change at the discretion of the Government without prior notification to applicants). Applicants should make themselves available for the interview during that period.

Application and Enquiries: Asianet Consultants (HK) Limited, 702-705, 7/F, Wilson House, 19 Wyndham Street, Central, Hong Kong. For enquiries, please call Mr Peter LIU at (852) 2530 0137 or send email to **itc-bd@asianetconsultants.com**.

Closing Date for Application: 15 June 2018

General Notes:

(a) As an Equal Opportunities Employer, the Government is committed to eliminating discrimination in employment. The vacancy advertised is open to all applicants meeting the basic entry requirement irrespective of their disability, sex, marital status, pregnancy, age, family status, sexual orientation and race.

(b) Non-civil service vacancies are not posts on the civil service establishment. Candidates appointed are not on civil service terms of appointment and conditions of service. Candidates appointed are not civil servants and will not be eligible for posting, promotion or transfer to any posts in the Civil Service.

(c) Persons who are not permanent residents of the Hong Kong Special Administrative Region may also apply for the post but will be appointed only when no suitable and qualified candidates who are permanent residents are available.

(d) Where a large number of candidates meet the specified entry requirements, shortlisting criteria may be devised to select the better qualified candidates for further processing. In these circumstances, only shortlisted candidates will be invited to attend the interview.

(e) It is Government policy to place people with a disability in appropriate jobs wherever possible. If a disabled candidate meets the entry requirements, he/she will be invited to attend the selection interview without being subject to any further shortlisting criteria.

(f) The entry pay, terms of appointment and conditions of service to be offered are subject to the provisions prevailing at the time the offer of appointment is made.

(g) Holders of academic qualifications other than those obtained from Hong Kong institutions/Hong Kong Examinations and Assessment Authority may also apply but their qualifications will be subject to assessments on equivalence with the required entry qualifications. They should submit copies of their official transcripts and certificates by post or email to the above mailing and email address.

(h) Non-civil service vacancy information contained in this advertisement is also available on the GovHK on the Internet at **http://www.gov.hk** and the Innovation and Technology Commission Homepage at **http://www.itc.gov.hk**.

By **Nathan Bradshaw**

Finding a community in the lab

It is a rite of passage for every college student: English 101. The class began with introductions. At 28 years old, I knew that I would be older than the average student. After almost failing out of high school, I had enlisted in the U.S. Navy and spent the next 8 years operating the nuclear reactor on an aircraft carrier. But I was not prepared for the six precocious high school students who were in the community college class with me, getting some exposure to higher education and earning college credit. They hammered home the feeling I had been trying to keep at bay: I was too old to be starting this journey. I only returned for the next class because the Department of Veterans Affairs was paying me a living allowance while I attended college. But when my studies led me to my first research lab, I found some much needed common ground.

I had started college with plans to become a pharmacist. In my introductory chemistry and biology courses, I found other "nontraditional" students—older students, veterans, students with kids, students who were also working full-time jobs—who grew into a cohort for me. The research I conducted as part of the class was challenging, but it offered an opportunity to apply some of the skills I had learned in the Navy, reassuring me that my experience had value. I enjoyed research so much that, before I completed my first year of college, I decided that I would go on to pursue a Ph.D.

When I transferred to a 4-year university, I regularly felt like an outsider among students 10 years younger than me with limited life experience. But again, research provided a place where I felt I belonged. When I started working in a lab on a project developing artificial muscles, a graduate student demonstrated how the muscles move when connected to an instrument called a Keithley source meter. The student had focused on synthesizing the muscles and wasn't very familiar with the meter, which both generates and measures voltage and current. I, on the other hand, had spent more than 6 years using an older version of this instrument for reactor maintenance in the Navy. I immediately felt at home. I could do this.

My undergraduate research adviser gave me free rein to pursue new directions with the meter and design my own experiments. This was just one way that she encouraged me to capitalize on my experience and helped me learn to be an undergraduate in my 30s. Her support helped me see college as a continuation of my career instead of starting over. The years I spent in the Navy became an asset instead of a gulf between me and my peers.

"I feel lucky to have found colleagues and mentors who make me feel that I belong."

I'm now pursuing my Ph.D., and I feel lucky to have found colleagues and mentors who make me feel that I belong. But I know that this is not everyone's experience, and that academia and labs can be alienating places. So, I do what I can to help foster a welcoming, supportive environment for the other researchers around me. I regularly share the difficulties I faced in school and lab with junior members of the lab to help them understand that everyone struggles. I also co-founded a speaker series where visiting professors share stories about their own roots in underrepresented communities or their efforts to reach out to other groups. My goal is to help graduate students see the humans behind the science and connect with the speakers at a deeper level.

These are just small steps. But they are based on the lesson that I learned through my years of struggling to find my place in academia: Community doesn't depend on age or background, but on appreciating one another's perspectives and skills and acknowledging that, despite differences, we face some common struggles. Taking the time and effort to build connections with other members of your lab and research community can help students of all backgrounds find success. It certainly did for me. ■

Nathan Bradshaw is a graduate student at Northwestern University in Evanston, Illinois. Do you have an interesting career story? Send it to SciCareerEditor@aaas.org.